# Attosecond imaging of molecular dynamics

Hartmut Ruf

UFR de Physique
Numéro d'ordre: 4651

# THÈSE

**présentée à**

## L'UNIVERSITÉ BORDEAUX 1

**soutenue publiquement le 6 décembre 2012**

École doctorale des Sciences Physiques et de l'ingénieur

Par Hartmut Ruf

pour obtenir le grade de

**Docteur**

**Spécialité: Laser, Matière et Nanoscience**

# Dynamique moléculaire par imagerie attoseconde

### Composition du jury

| | | |
|---|---|---|
| *Président*: | M. Jean Oberlé | Professeur des universités, Université Bordeaux 1 |
| *Rapporteurs*: | M. Olivier Faucher | Professeur des universités, Université de Bourgogne |
| | M. Christian Cornaggia | Ingénieur de recherche, CEA Saclay |
| *Examinateur*: | M. Fabien Quéré | Ingénieur de recherche, CEA Saclay |
| *Co-Directeur de thèse*: | M. Yann Mairesse | Chargé de recherche, Université Bordeaux 1 |
| *Directeur de thèse*: | M. Eric Mével | Professeur des universités, Université Bordeaux 1 |

---

**Centre Lasers Intenses et Applications - UMR 5107**

# Acknowledgement

The results presented in this thesis were carried out at CELIA in collaboration with many other groups around the world. A lot of persons contributed to this work:

I would like to thank Olivier Faucher and Christian Cornaggia for reviewing my thesis, as well as Jean Oberlé and Fabien Quéré for being members of my jury.

First and foremost, I would like to thank four persons of the group who closely followed my development since the beginning. Each of them contributed to the thesis in a complementary manner, and all of them were a huge source of inspiration and ideas.
A first big "Thank You" certainly belongs to Eric Mével and Yann Mairesse, my supervisors. I feel deeply indepted to their invested time for answering my questions, correcting my reports, posters, abstract-submissions, articles and talks. I also appreciated their personal commitment aside from work, like apéros, dinners, going out, demonstrations and many other activities. Eric not only guided me well through the doctoral program but often came by before leaving the lab for discussing physics. Especially Yann invested a lot of energy in my education, training me as scientist and a person. Most of what I learnt during the last three years, I learnt from him. He was more than a great mentor to me, but also succeeded in keeping my passion for science alive throughout the last three years. *Merci Beaucoup*!
Eric Constant was always there to share his knowledge with me in a very pedagogical manner. There is one important trait I especially learnt to appreciate: he always looked at new results with a critical eye and would not be satisfied with the first explanation. He was not only a great help inside the lab, but always give a hand when one of the students had to move. Baptiste Fabre was always ready to spend his nights with me in the lab. He's always been around to offer advice and motivation, what could happen quite often during those nights. I was certainly lucky to work alongside Baptiste and Yann in the lab.

There are four other persons I would like to mention next, Dominique Descamps, Valérie Blanchet, Fabrice Catoire and Bernard Pons. Dominique would not only take care of the laser if it refused to work as he was supposed to, but also gave me advice on the experimental setup, optical components etc. . I really appreciated his presence downstairs. Then there is of course Valérie who I really want to thank. Her enthusiasm and dynamism always kept us PhD students motivated, often quite long until late in the night. Valérie was a great teacher for femtochemistry. Her clear explications on molecules and all the movements they can perform, were very enriching. Thanks to Fabrice I got in touch with

TDSE, if he hadn't been I would probably still mix up all the different theories and the different gauges. Gladfully I will not only remember him for this, but also the nights having one or more drinks together. I owe Bernard most of my understanding about CTMC-QUEST and potential energy surfaces. I still find it incredible how Bernard and Baptiste were able to develop this novel approach to describe HHG and wish them and François good luck for further applications.

Being a PhD student also means sharing an office and life at the lab with other students. I would like to thank Julien for his warm welcome at the beginning and everything he tought and showed me in the lab; Charles for spending three enjoyable years together, you were great office- and labmate; Antoine for his conviviality, taking me swimming and giving us the notion how to *déchirer tout*; Nico for his support in the lab at Bordeaux and our visit to the U.S.; Ondrej for his humour and our visit to the olympic garden from Lausanne; David for his support, the sailing trip and our visit to Milan and Lausanne; grande Amélie for the visit to Lausanne; petite Amélie for the discussions about physics, I wish her good luck for the following two years and finally François and Mathieu for their kind accomodation at the new office.

A lot of people are responsible for keeping a lab running. I would like to thank Alain and Laurent from the mechanical workshop for all the pieces they built, their advice and making the workshop always an agreeable place to go to; Dominique, Stéphane, Capucine and Frédéric for taking care of the Laser and switching it on each morning; Rodrigue for the help with the planning of the new vacuum chamber; Anatoly for his programs and advice with Labview; Loïc and Elodie for resolving the "small" computer, printer and internet problems; Sophie, Fabienne, Céline and Emmanuelle for being a great help concerning the administration, it was certainly a lot I asked you for over the years and finally Philippe the director of the lab. I also would like to thank all the other members of CELIA, especially Patrick, Ghita, Nikita, Henry, Fabien, Joao, Claude, Sébastien and Eric Cormier. I was certainly lucky to do my PhD at CELIA in such a positive work atmosphere, keep it up.

This PhD thesis also involved several collaborations. Our closest one was certainly with Valérie, Raluca, Nico and David from the LCAR at Toulouse. I especially appreciated the conversations with Raluca about chiral molecules and clusters.
L. Bonnet, P. Larregaray and P. Halvick our collaborators from the ISM at Bordeaux calculated the evolution of the classical trajectory wave packet in excited $NO_2$. *Merci beaucoup*.
The experiment in Bordeaux was triggered by a collaboration that started at the NRC Steacie Institute at Ottawa. I would like to thank Hans, Julien and David for my three weeks in Ottawa, they made my stay very pleasant.
The experiments performed in linear molecules were performed in collaboration with Alex, Olga and Mischa from the MBI at Berlin. I appreciated their introduction how to calculate the high harmonic signal from a molecule, спасибо, thanks and *danke*.

I would also like to say спасибо to Vasily from the Russian Academy of Science at Moscow for his inspiring dicussions about clusters and autoionizing states.
At the Politecnico di Milano and afterwards in Bordeaux we exploded clusters togethter with Caterina, Salvatore, Matteo and Michele. *Grazie mille* for your kind accommodation in Milan, I enjoyed working with you.
I was glad to welcome Hadas, Oren and Barry from the Weizmann Institute of Science at Rehovot. תודה for your visit, the inspiring conversations and our reunion at Berlin and Lausanne.
In a last collaboration we installed the Even-Lavie jet at IRAMIS at Saclay. I had the pleasure to work with Antoine and Thierry in the lab and to discuss with Pascal and Bertrand the latest results. I especially owe a big *Merci* to Antoine for his kind invitation at his parents' house and the soccer matches each wednesday afternoon.

I would also like to thank all my friends for their moral support and my flatmates for their understanding.
*Vielen Dank* to my parents and my sister for everything they did for me, their trust, their support and their encouragement.
Finally a huge *Dieuredieuf* to Félicité for her understanding, her support during our ups and downs and who was always there when I needed her. *Demala beug*.

# Contents

# Introduction

Dear reader, you might still remember from high school the way electrons are arranged around an atom. In the Bohr model the electrons orbit around the atom nucleus (protons and neutrons) like the planets around the sun (Bohr, 1913). As in an antenna the electrons are subjected to an acceleration, leading to the emission of radiation and thus a loss of energy. Consequently the orbit radius is decreasing continuously until the electrons hit the nucleus. This process happens in less than a second, but in reality the lifetime of atoms is considerably longer. This contradiction was solved with the introduction of quantum mechanics at the beginning of the $20^{\text{th}}$ century, proposing an atomic orbital model. Electrons are not described as particles any more within the framework of this model. An orbital is assigned to each electron within which it can be found with a certain probability. Each orbital is occupied by electrons whose energy adopts a discrete value. The energies and orbitals can then be calculated by the time-independent Schrödinger equation. Thus the orbital structure of each atom in the periodic table and even molecular orbitals can be created.
But how can this structure be traced experimentally? The classical radius of an electron orbiting around an atomic core is 0.53 Å (1 Angström $= 1\,\text{Å} = 10^{-10}$ m). The resolution of a typical optical microscope is limited by the wavelength of visible light to several hundred nanometers ($1\,\text{nm} = 10^{-9}$ m) and is therefore insufficient. Owing to the wave-particle duality of matter, particles can be used instead of electromagnetic waves, e.g. visible light, for probing the sample of interest. Energetic electrons reaching low de Broglie wavelengths[1] (de Broglie, 1923) can resolve structures on the order of magnitude of several Angströms. The principle of the tunnel electron microscope is based on this idea (Knoll and Ruska, 1932).
We chose a similar approach, also taking advantage of the short wavelength of energetic matter waves. When atoms or molecules are subjected to a strong laser field ($\text{I} = 10^{14}\,\text{W/cm}^2$) an electron can escape by means of tunnel ionization. The wavefunction is thus split in two: a free electron wavepacket and a bound one. As the laser field is oscillating, the free electron is accelerated and can be driven back towards the parent ion. Both electron waves interfere with each other. The de Broglie wavelength of the recolliding electron is on the order of magnitude of one Angström and constitutes thus a sensitive probe for the orbital structure. Similar to an oscillating electron in an antenna, the oscillating electron wave packet resulting from the superposition from the bound and free wavefunctions creates a dipole emitting radiation: the high-order harmonics (McPherson et al., 1987; Ferray et al., 1988). The structural information of the probed orbital is

[1] De Broglie postulated matter waves and therewith introduced the concept of wave-particle duality.

encoded in the high harmonic spectrum that is measured in the experiment. This self-probing scheme of electronic structure is a fundamental principle in this manuscript. It has been first described by Corkum in terms of the three step model and demonstrated by the tomographic reconstruction of nitrogen ground state orbital (Corkum, 1993).
The second question addressed in this manuscript is, how can dynamics in electron orbitals be elucidated? The human eye is able to resolve movements on the timescale of $\approx 0.04\,\mathrm{s}$. At the end of the $19^{\mathrm{th}}$ century Muybridge first tackled this limit by using a camera with a fast shutter, taking pictures of a horse in motion. The time resolution was further improved by Edgerton tracing a bullet passing through an apple, and finally topped by tracing photons moving through space with a virtual slow motion camera (Velten et al., 2012)[2]. Electrons are certainly not moving faster than light, this technique can however not be applied in our case, remember a high spatial resolution is required. Indeed, as we will see in the following the self-probing scheme combines the two, spectral and spatial resolution.

## High Harmonic Generation leading to Attosecond Time Resolution

The basic mechanism of high harmonic generation (HHG) in atoms or molecules is described in the three step model: First, a bound electron escapes in the strong laser field through tunnel ionization. Second, the electron is driven away then accelerated back towards the parent ion. Third the electron recombines radiatively with the parent ion. At distinct times of the laser cycle, i.e. at different field amplitudes, the electrons follow well defined trajectories. The recombination time and electron momentum are given by the emission time of the electron (Shafir et al., 2012b). One photon is emitted per electron with an energy corresponding to the electron's kinetic energy plus the ionization potential. These photons can be resolved spectrally, thus allowing a distinction between different electron trajectories. The hole left behind after ionization moves during the time of flight, influencing the electron density in the orbital. The interference of the returning electron wavefunction depending on this orbital will thus be different. The electrons recombine and emit photons at distinct times with distinct energies, such that different photons correspond to different snapshots, encoding the electron-hole dynamics. Decoding the information hidden in the high harmonic spectra is however challenging (Smirnova et al., 2009a,b; Haessler et al., 2010). The time scale of the self-probing process is dictated by the duration of a laser cycle and therefore pushed to the sub-femtosecond regime ($1\,\mathrm{fs} = 10^{-15}\,\mathrm{s}$), i.e. to attoseconds ($1\,\mathrm{as} = 10^{-18}\,\mathrm{s}$).
Besides the self-probing scheme high harmonic generation exhibits another important aspect which allows access to extremely short pulses: the extremely large spectrum. If the phase is constant or linear over the entire spectrum (i.e. bandwidth-limited pulses), the lowest possible pulse durations can be reached. This is not the case for HHG, the

[2]The video is very impressive: www.mit.edu/~velten/.

phase varies non-linearly with frequency, limiting the duration of the generated pulses. Compression techniques can be used to decrase the pulse duration, the record being 63 as in attosecond pulse trains and 67 as in isolated attosecond pulses pulses with respective bandwidths of 83 eV and 75 eV (Ko et al., 2010; Zhao et al., 2012). Note that conventional pulsed laser technology is far from reaching this time scale, their spectra being too narrow. Recently it was possible to generate a 1.5 keV broad high harmonic spectrum, potentially enabling the production of even much shorter pulse durations (Popmintchev et al., 2012). Only further measurements will show. These pulses can be used in experiments for an ultra-high time resolution, as the opening time of a camera shutter determines the time resolution, the pulse duration sets this limit in an experiment (Krausz and Ivanov, 2009).

## Outline: High Harmonic Generation taking the Road from Atoms to Clusters

Chapter I: The basics of HHG are introduced for a single atom: the semiclassical three step model (Corkum, 1993) and the quantum model (Lewenstein et al., 1994). These two theories predict the main features of HHG, but still have drawbacks. At recombination they neglect the ionic potential of the core. Therefore a third theoretical approach is presented: Classical Trajectory Monte Carlo Quantum Electron Scattering Theory (CTMC-QUEST) (Higuet et al., 2011). This theory, developped by Fabre and Pons, is tested on the Cooper minimum of argon. This minimum originates from the atom's electronic orbital structure and is observed in the harmonic spectra. A direct comparison between theory and experiment can be drawn, allowing an outlook for the application of CTMC-QUEST in other, more complex systems.

Chapter II: As the orbital structure is well understood in the example of the argon atom, we move on to small linear molecules, nitrogen and carbon dioxide. Under experimental conditions this is not as trivial any more. As HHG is performed in a gas jet, the orientation of the molecules is arbitrary in this macroscopic target. Molecular alignment by laser pulses is however well established, which allows us to break this isotropy (Lavorel et al., 2000; Rosca-Pruna and Vrakking, 2001). Still the alignment distribution, i.e. the degree of alignment, crucially depends on the rotational temperature of the molecules in the gas. An Even-Lavie jet allows us to reach very low temperatures with an excellent alignment distribution meeting also a crucial condition for efficient HHG: a high gas density. Owing to the good alignment we are able to resolve the shape resonance in nitrogen recently predicted by (Jin et al., 2012). Furthermore another feature is observed depending on laser intensity and might thus be assigned to a dynamical behaviour originating from the interference of lower lying orbitals. This type of minimum is well established in carbon dioxide (Smirnova et al., 2009a) and shows a dependence on the alignment distribution in our measurements. Further details are resolved for high harmonic spectra from carbon dioxide taken at different alignment angles. These experiments were performed in collab-

oration with Harvey, Smirnova and Ivanov who will perform further calculations for the interpretation of our results.

Chapter III: In a next step a more complicated, namely non-linear molecule is studied: nitrogen dioxide. This molecule does not only play an important role in atmospheric chemistry but has also arisen much scientific interest. The photodissociation and the fs-relaxation between two potential energy surfaces (PES) is studied in this molecule with a sophisticated method: HHG combined with transient grating spectroscopy (Mairesse et al., 2008c). The experiments were performed in Ottawa and Bordeaux in collaboration with Wörner, Bertrand, Villeneuve and Corkum. The results obtained in Ottawa and Bordeaux are in agreement concerning the photodissociation of nitrogen dioxide on a picosecond timescale. The fs-dynamics observed in Ottawa are assigned to a population transfer between the two PES (Wörner et al., 2011). The experimental results from Bordeaux reveal a transient behaviour that is different however (Ruf et al., 2012). For getting a deeper understanding Halvick performed simulations based on trajectory surface hopping. The comparison between calculation and experiment leads to a different interpretation: oscillations of the bending wave packets and the coupling between the two PES is responsible for the fs-dynamics.

Chapter IV: A major effort was invested in this chapter of the thesis. It was initiated by the ambiguity on the nature of the generation media in a cold carbon dioxide gas jet: What is the contribution of clusters to HHG in strongly aligned molecules? Clusters are also considered as a promising light source, showing higher emission frequencies (Donnelly et al., 1996; Vozzi et al., 2005b). The exact mechanism of HHG remains still debated. We performed a detailed experimental study of HHG from clusters, which aimed at disentangling the harmonic signal from clusters and identifying the mechanism at play. The 2D spatio-spectral resolution of the harmonic signal allowed the identification of a region corresponding to emission from clusters. Furthermore we were able to assign a recollisional recombination mechanism to HHG from clusters (cluster-to-itself): ionization from and recombination to a delocalized electron cloud in the cluster. A crude model was developped which finally allowed an estimation of the electron correlation length within such an electron cloud.

## The End: A Table-Top XUV Light Source

Chapter V: The last chapter summarizes the planning, construction and first analysis of a XUV beamline provided by HHG. Therefore a new vacuum chamber had to be designed fulfilling the following criteria: spectral selectivity between harmonic 9 and harmonic 17, low budget, a photon flux of $10^6$ on target per pulse and harmonic and an easy switching between different setups. In order to meet these conditions the following three setups meeting different requirements were installed: First the high harmonic spectrum can

easily be imaged on the MCPs. Second the full harmonic spectrum can be used as a probe employing metallic filters for a spectral selection. Third a grating monochromator can be utilized for selecting single harmonic orders. The first setup allows us to continue experiments in the self-probing scheme whereas the last two permit to perform fs-XUV spectroscopy in a velocity map imaging (VMI) spectrometer (Handschin, 2012).

# 1. Paving the Road towards High Harmonic Generation

Since the observation of first high-order harmonic spectra in gases (McPherson et al., 1987; Ferray et al., 1988) until today, high harmonic generation (HHG) has demonstrated its importance, opening a door to the field of attosecond science. HHG is generally obtained by focusing an intense femtosecond laser pulse ($\approx 10^{14}\,\mathrm{W/cm^2}$) in a gas. The bandwidth of the emitted spectrum can reach up to 1.6 keV allowing transform-limited pulse durations of 2.5 as (Popmintchev et al., 2012). The radiation is coherent, has a limited divergence angle (2 mrad-12 mrad) and a well defined polarization. The attosecond pulses are emitted in form of pulse trains (Paul et al., 2001), but isolated pulses can be extracted (Goulielmakis et al., 2008; Feng et al., 2009; Ferrari et al., 2010; Vincenti and Quéré, 2012). The spectrum shows an evenly spaced frequency comb corresponding to the odd high harmonic orders of the fundamental laser frequency. In contrast to second order harmonic generation in solid state materials (Franken et al., 1961), HHG cannot be treated by a pertubative theory. Only the lowest harmonics strongly depend on the order of the multiphoton process wheras the conversion efficiency is almost constant in the plateau region (Ferray et al., 1988; Li et al., 1989). Finally the signal drops down dramatically in the cutoff region.

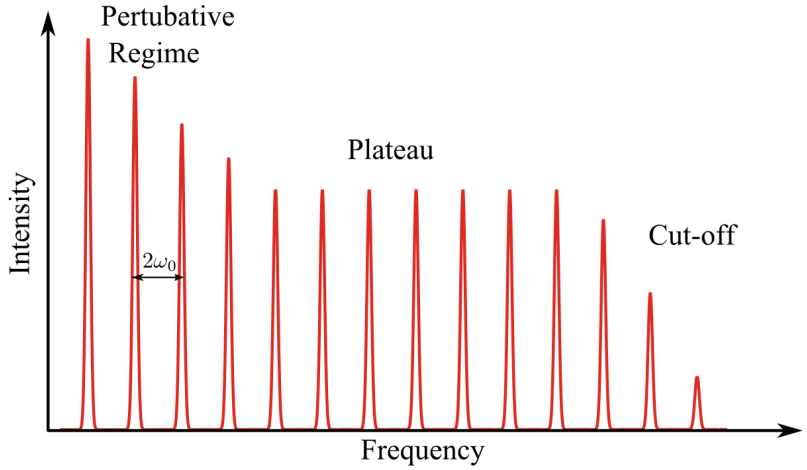


**Figure 1.1.:** Typical structure of a high order harmonic spectra generated in a gas (figure adopted from (Higuet, 2010)).

HHG is also a spectroscopic tool as it is possible to extract structural and dynamical information on the emitting medium from the properties of the harmonic radiation. Indeed

the molecular orbital of nitrogen was imaged by decoding the spectrum of the emitted VUV light (Itatani et al., 2004). This experiment triggered the tomographic reconstruction for other molecules. Also the phase (Smirnova et al., 2009a) and the polarization state (Levesque et al., 2007; Mairesse et al., 2008b) of the harmonic emission contain important information for the investigation of more complicated systems. Extreme non-linear optical spectroscopy (ENLOS) has transferred the techniques applied in conventional nonlinear spectroscopy to HHG.
This chapter summarizes the relevant and most important aspects of HHG in atoms. The fundamental process of HHG is explained in semiclassical approach and can be successfully complemented by a quantum mechanical description. To start with, both theories will be shortly presented, introducing the key parameters and a discussion on the related approximations. A third new theoretical approach, combining quantum rescattering theory and a statistical description, taking into account the ionic potential of the core neglected by the other two. Classical trajectory Monte Carlo quantum electron scattering theory (CTMC-QUEST) is finally applied in a first experiment. After a short presentation of the experimental setup the observation of the Cooper minimum (Higuet et al., 2011) is demonstrated and compared to results from CTMC-QUEST.

## 1.1. Motivation: Extreme Non-Linear Optical Spectroscopy

Before presenting the theoretical background of HHG the concept of extreme non-linear optical spectroscopy (ENLOS) is introduced. HHG can be used as a spectroscopic tool to extract structural and dynamical information of the emitting medium from the properties of the harmonic radiation. The exploited feature is the recollision mechanism in the last step of HHG (self-probing scheme). Owing to the wave-particle duality of matter the recolliding electrons can be considered as matter waves. The de Broglie wavelength $\lambda_{dB}$ is attributed to the electron: $\lambda_{dB} = h/p$, where h is the Planck constant and p the momentum of the particle. Recolliding electrons leading to the emission of harmonic 31 (fundamental wavelength: 800 nm) are assigned to a de Broglie wavelength of 2 Å. The order of magnitude of the recollision wavelength indicates that these matter waves can probe the structure of atomic and molecular orbitals.
In the self-probing scheme the recolliding electron wave packet interfers with the wavefunction of the parent ion. Similar to an oscillating electron in an antenna, the oscillating electron wave packet creates a dipole moment which emits radiation, the high-order harmonics. The structural information of the probed orbital is encoded in the high harmonic spectrum. A great breakthrough was the tomographic reconstruction of the highest occupied molecular orbital (HOMO) of nitrogen (Itatani et al., 2004). This experiment proved to be the herald of ENLOS. As depicted in figure 1.2 this technique can be used in combination with pump-probe spectroscopy for resolving dynamical information (Wagner et al., 2006). Electrons with different momenta recollide at different times, so that each emitted harmonic order corresponds to a different snapshot. The observation of

hole dynamics with a subfemtosecond resolution was proposed, first steps were undertaken in carbon dioxide (Smirnova et al., 2009a,b) and nitrogen (Haessler et al., 2010). Mairesse and coworkers transferred other techniques from nonlinear spectroscopy to the extreme nonlinear optical regime such as: polarization-resolved pump-probe spectroscopy (Levesque et al., 2007; Mairesse et al., 2008b), transient grating spectroscopy (Mairesse et al., 2008c) and high harmonic interferometry (Smirnova et al., 2009a).

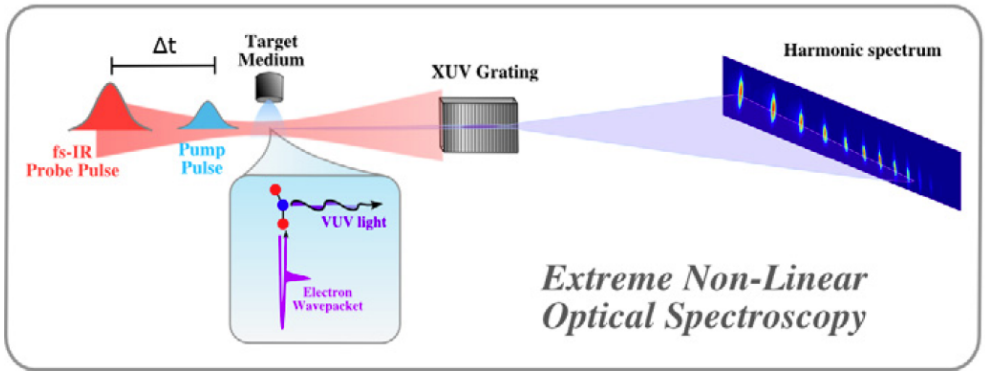


**Figure 1.2.:** Scheme for extreme non-linear optical spectroscopy. HHG is used in a self-probing scheme.

## 1.2. Three Step Model

A first simple model of HHG, called the three step model (Corkum, 1993; Schafer et al., 1993), was suggested six years after the first observation of high harmonic spectra in gases. It does not only provide a phenomenological understanding of many observations but very often also shows a good quantitative agreement. Most importantly, it disentangles the basic mechanisms at play allowing a more distinct treatment of HHG. The three steps are shown in figure 1.3:

**I)** The strong electric field bends the atomic potential and the electron tunnels through the potential barrier.

**II)** The electron is accelerated and driven back to the parent ion as the electric field reverses.

**III)** The electron recombines radiatively with its parent ion through emission of a photon.

### 1.2.1. First Step: Tunnel Ionization

When exposing an atom to a strong electric field, the most affected electrons by the electric field are the valence electrons. In a first approximation, only the outermost

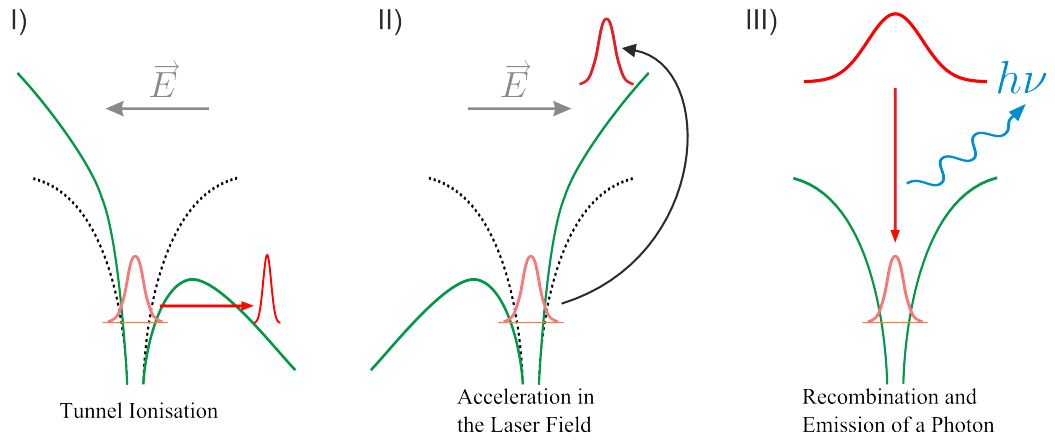


**Figure 1.3.:** The three step model.

electron will be considered in an effective atomic potential. The interaction of this bound electron with a linear polarized laser field $\vec{E} = E\vec{u}_x$ can be described by the following potential [1]:

$$V(x) = V_0(x) + E(t)x = \frac{-Z_{eff}}{|x|} + E_0 x \cos \omega_0 t \tag{1.1}$$

where $V_0$ is an effective ionic potential with a spherical symmetric potential with effective charge $Z_{eff}$. The electric field is oscillating with a period of $T_0 = 2\pi/\omega_0$ (typically 2.67 fs for a titanium-sapphire laser (Ti:Sa-Laser) at $\lambda_0 = 800$ nm). The three different cases in figure 1.4 only depict a snapshot at an extremum of the electric field.

In the presence of the external field, a barrier is created in the direction of the field. When the field is strong enough the height and the width of the barrier are small enough and an electron wave packet can tunnel through the barrier. As the tunnel probability depends exponentially on the field strength, tunnel ionization will mostly occur near the extrema of an oscillating laser field. But this picture holds, if the barrier can be considered as quasi static during the escape time of the tunneling electron. The Keldysh parameter $\gamma$ (Keldysh, 1965; Reiss, 1980) is the parameter dicriminating between different ionization regimes given by:

$$\gamma = \sqrt{\frac{I_p}{2U_p}} \tag{1.2}$$

with the ponderomotive energy $U_p = E_0^2/4\omega_0^2 \propto I\lambda^2$. The ponderomotive energy relates to the mean quiver energy which an electron initially at rest acquires during one laser cycle. The tunneling condition is fulfilled when $\gamma \ll 1$ corresponding to a situation in which the laser frequency $\omega_0$ is relatively low and the field $E_0$ relatively strong. This

[1] In atomic units.

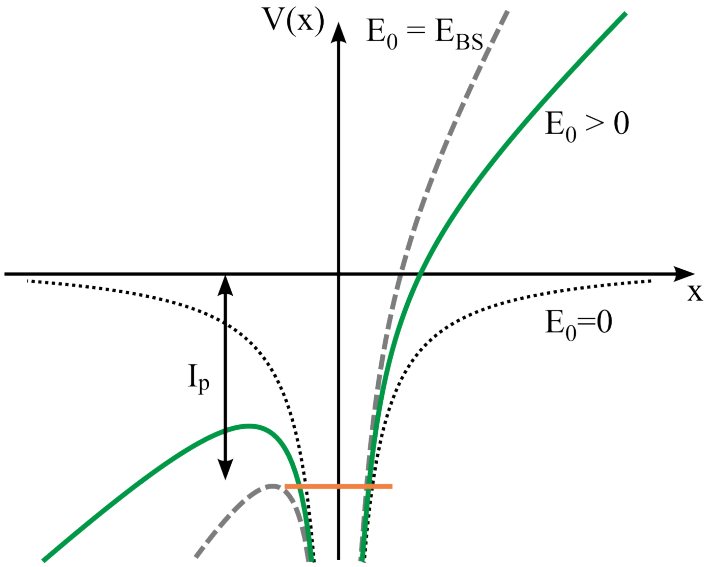


**Figure 1.4.:** Coulomb potential $V_0(x)$ without electric field (dotted line), in the tunnel-ionization regime (solid line) and in the BSI-regime (dashed line).

condition can also be understood in connection with the classical tunneling time $t_{tunnel}$. This is the time a classical particle needs to cross the barrier assuming that a direct passage through the barrier is allowed. The following relationship can be established (Keldysh, 1965):

$$\gamma = \omega_0 t_{tunnel} \tag{1.3}$$

Now the tunneling condition can be simply understood as $\gamma = \omega_0 t_{tunnel} \ll 1$ implying that the barrier remains quasi static during the tunneling process. If $\gamma > 1$ tunneling still takes place but becomes inefficient and another mechanism takes over. As the ponderomotive energy decreases $\gamma \gg 1$ this descripiton is no longer valid (Mével et al., 1993). One speaks of the multi-photon regime of ionization: the electron is taking the vertical ionization channel, it is shook up between the potential walls (Ivanov et al., 2005). Considering a typical experiment ($\lambda = 800\,\text{nm}$, $\text{I} = 10^{14}\,\text{W/cm}^2$) in krypton one obtains $\gamma = 1.08$. A Keldysh parameter around one still affirms tunnel ionization even though the barrier moves slightly during this process.
The tunnel ionization rate $\Gamma_{ADK}$ was first calculated by Ammosov-Delone-Krainov and depends exponentially on the field strength and the ionization potential (Ammosov et al., 1986):

$$\Gamma_{ADK}(t) \propto I_p^{0.25} \exp\left(\frac{-5.65\sqrt{I_p^3}}{3E(t)}\right) \tag{1.4}$$

The total probability of ionization $p$ is calculated by integrating over the pulse duration of the electric field:

$$p = 1 - \exp\left( - \int_{-\infty}^{+\infty} \Gamma(t) dt \right) \tag{1.5}$$

When increasing the laser intensity, the ionization probability increases exponentially. When the probability reaches the value of one, the atom is certainly ionized after the passage of the laser pulse. In other words saturation intensity is reached. Saturation intensity depends on several parameters such as pulse duration and spatial profile. Saturation intensity can be very well reached at the center of the beam, but not at the border. Saturation only affects HHG if the intensity is reached in a significant volume of the macroscopic medium. Also a pulse with relatively low peak intensity but long duration can significantly saturate a medium. This means that the medium is continuously ionized between the beginning and the end of each laser pulse. Pulses with the same maximum intensity containing less laser cycles, i.e. shorter pulses, will not reach saturation intensity in the same conditions. Saturation intensity is increasing with decreasing pulse length.

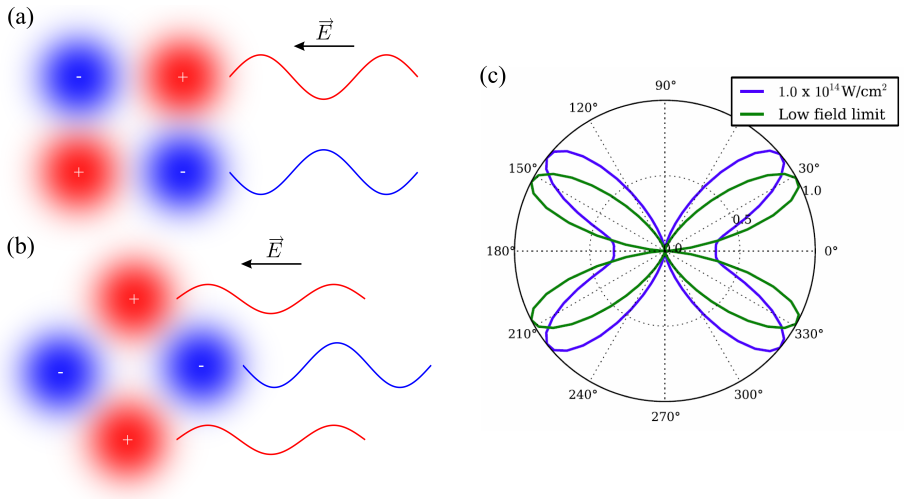


**Figure 1.5.:** Orientation of the orbital lobes leads to (a) suppression of ionization or to (b) enhanced ionization. (c) Tunnel ionization rate of $CO_2$ molecule with respect to its orientation to the electric field for low and high strength of the ionizing dc electric field (figure adopted from (Murray et al., 2011)).

In case of molecules, orbitals are spherically asymmetric and the ionization rate strongly depends on the orientation of the molecular axis relative to the polarization of the electric field (Murray et al., 2011). Figure 1.5(a) and 1.5(b) depicts the schematic orbital structure of the ground state of the $CO_2$ or the $O_2$ molecule. If the polarization direction constitutes a symmetry axis between the orbital lobes of inverse sign, ionization will be strongly suppressed (Muth-Böhm et al., 2000; Tong et al., 2002). Indeed, the contributions of each lobe have a $\pi$ phase difference and thus interfere destructively. If the orbital is rotated

by 45° ionization is not suppressed any more. This is a great difference to atoms, the quantization axis is imposed by the symmetry axis, and not by the polarization direction. For a typical non aligned sample, ionization is suppressed for a significant amount of molecules. This leads to an on average higher harmonic cutoff because higher intensities can applied till saturation of the entire sample is reached (Shan et al., 2002; Wong et al., 2010).
Right after tunneling, the electron velocity along the field direction $v_{\parallel}$ is zero as it has lost all its kinetic energy during the process. In the regime of tunnel ionization the initial velocity distribution transverse to the polarization of the electric field varies with the tunneling time $t_{tunnel}$. The width of the initial velocity distribution is approximated by the width of the electron wave packet $\psi(v_{\perp})$ (Ivanov et al., 2005):

$$\psi(v_{\perp}) = \psi(0)\exp(-v_{\perp}^2 t_{tunnel}/2) \tag{1.6}$$

This equation simply states that a short tunneling time leads to a strong transversal spread of initial electron velocities after tunneling. The electron tunnels out in the direction the potential is lowest. It is blocked on the sides by the higher potential which acts as a wall. The electron wave packet is diffracted from this boundary, which are closer when the tunneling time is short. The spatial spread of the electron wave packet after tunneling is obtained by the Fourier transform of this expression.

If the electric field overcomes a certain threshold $E_0 > E_{BS}$, the electron will immediately escape the potential. This case is also known as Barrier Suppression Ionization (BSI) (Augst et al., 1989); a situation which refers to an ionization probability of one when the saturation intensity of an atom is reached. The potential barrier maximum is at a distance of $x_0 = \sqrt{Z_{eff}/E}$ lowered to $V(x_0) = -2\sqrt{E} = -I_p$. Assuming that $Z_{eff} = 1$ one can now calculate the field strength and the saturation intensity. Table 3.1 shows ionization potentials and saturation intensities calculated form the BSI-model for the rare gases and are compared to some experimental values. The BSI-model clearly overestimates saturation intensity at a pulse duration of 50 ps. As laser pulses become shorter the saturation intensities of the BSI-model are reached.

$$E_{BS} = \frac{I_p^2}{4} \qquad I_{BS} = \frac{I_p^4}{16} \qquad I_{BS}\,[W/cm^2] = 4.02 \times 10^9 I_p^4\,[eV] \tag{1.7}$$

### 1.2.2. Second Step: Electron in the Continuum

Within the context of the strong field approximation (SFA) the Coulomb potential of the atom is neglected. Therefore, once the electron has overcome the barrier its motion in the continuum is driven by the linearly polarized laser field. The electron motion obeying the electric field is treated classically.
According to Newton's second law of motion the force acting on a free electron is simply: $F(t) = E_x \cos(\omega_0 t)$ leading to the equation of motion:

| Gas | $I_p(eV)$ | theo. $I_{SB}(10^{14}W/cm^2)$ | exp. $I_{SB}(10^{14}W/cm^2)$ |
|---|---|---|---|
| Helium | 24.59 | 14.67 | 6.2 |
| Neon | 21.56 | 8.69 | 4.1 |
| Argon | 15.76 | 2.48 | 0.3 |
| Krypton | 14.00 | 1.54 | 0.25 |
| Xenon | 12.13 | 0.87 | 0.12 |

**Table 1.1.:** Ionization potentials (Haynes, 2007) and saturation intensities of rare gases. The theoretical values are calculated from equation 1.7 assuming the BSI model. The experimental values were measured with a 50 ps laser pulse at a wavelength of 1.064 $\mu$m (L'Huillier et al., 1983).

$$\ddot{x}(t) = -E_x \cos(\omega_0 t) \tag{1.8}$$

This second order linear ordinary differential equation with its initial conditions $\dot{x}(t_i) = 0$ and $x(t_i) = 0$ can be easily solved analytically. $\dot{x}(t_i) = 0$ can be justified that after having tunnelled through the barrier, the electron has lost all its kinetic energy. The second condition simply neglects the distance of several Å between the nucleus and the location of birth in the continuum. The succesive integrations of equation 1.8 give:

$$\dot{x}(t) = -\frac{E_x}{\omega_0}[sin(\omega_0 t) - sin(\omega_0 t_i)] \tag{1.9}$$

$$x(t) = \frac{E_x}{\omega_0^2}[cos(\omega_0 t) - cos(\omega_0 t_i)] + \frac{E_x}{\omega_0} sin(\omega_0 t_i)(t - t_i) \tag{1.10}$$

Figure 1.6(a) shows the electron trajectories following equation 1.10 with respect to the ionization time. Electrons that are emitted before the field maximum (i.e. -0.67 fs $\leq$ $t_i \leq$ 0 fs) will not return to the parent ion: When the electric field inverses the electron can not be decelerated to zero velocity and will veer away from the point of birth in the continuum. Then again if the electron is born in the time interval 0 fs $\leq$ $t_i \leq$ 0.67 fs the electrons will be accelerated back towards the parent ion. At a laser intensity around I = $10^{14}$ W/cm$^2$ the longest trajectories are born at $t_i$=0 and will move 2 nm away from their origin before returning. Still the recollision energy is very low as shown in figure 1.6(b). The electron with the highest recollision energy is emitted at $t_i$=0.13 fs with a recollision energy of 3.17 $U_p$. Its trajectory refers to the cutoff trajectory.

The electron trajectories can be classified into two groups: long and short. Figure 1.7(a) shows that to each ionization time belongs a recombination time. Even though the time of flight can be very different for these trajectories, a pair of trajectories (short and long) can be found for recollision energies below 3.17 $U_p$. Short (long) electron trajectories refer to electrons that are emitted at 0.13 fs>$t_i$>0.67 fs (0 fs>$t_i$>0.13 fs). The earlier an electron is emitted during a laser cycle, the longer it will remain in the continuum till recombination (figure 1.7(b)). During the time of flight the hole left behind in the

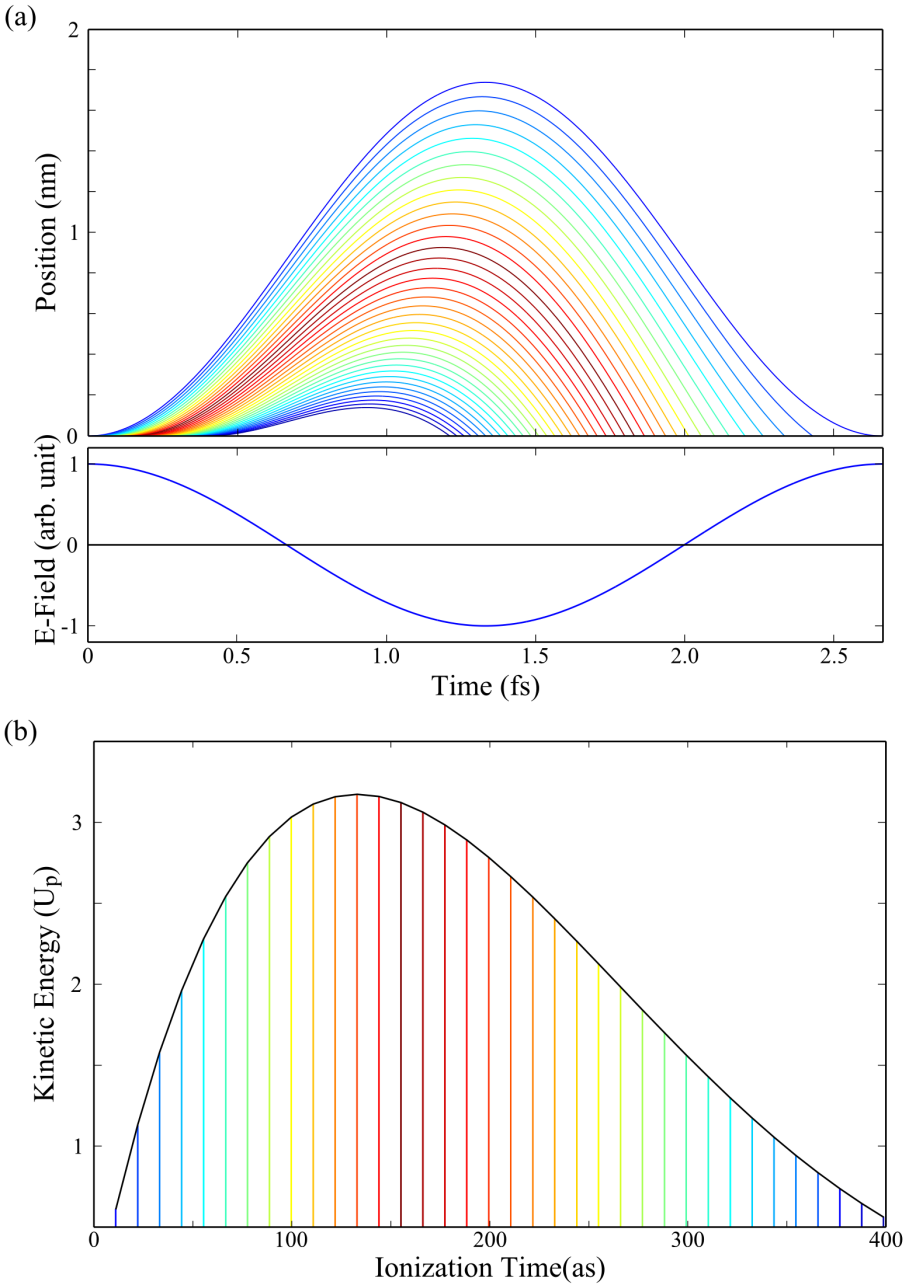


**Figure 1.6.:** (a) The electron trajectories are calculated for a laser intensity of $I = 10^{14}\,W/cm^2$ with a carrier wavelength centered at $\lambda = 800\,nm$. Trajectories are plotted for different ionization times. The oscillating laser field is displayed in bottom figure. The kinetic energy of electrons while recolliding with the parent ion is strongest for the red and weakest for the blue trajectories. (b) This kinetic energy is shown for each electron trajectory. The maximum kinetic energy is obtained at $3.17\,U_p$.

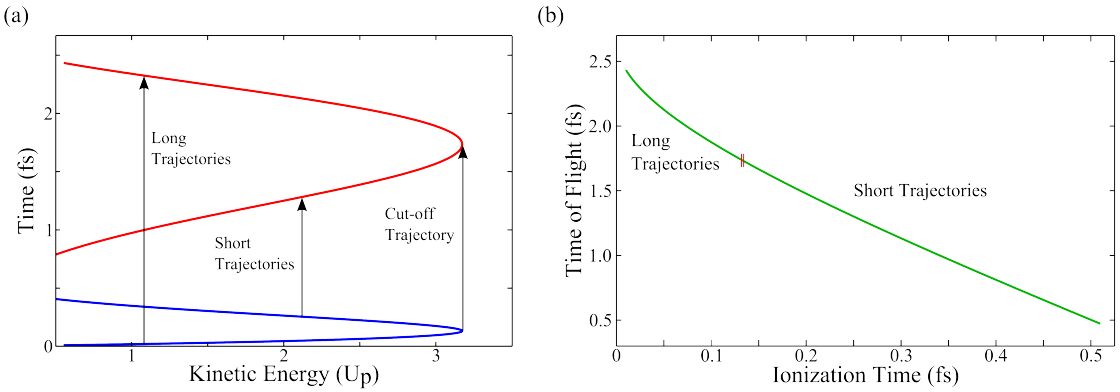


**Figure 1.7.:** (a) A different recombination time (red) is attributed to each ionization time (blue). For each energy recollision energy below 3.17 $U_p$ a couple of short and long trajectories can be identified. (b) The ionization time of an electron, determines its time of flight $\tau$.

ion acquires a phase shift which is proportional to the electron travel time $\tau_q$ and the ionization potential difference between the considered state and the ground state of the atom $\Delta I_p$ (Kanai et al., 2007):

$$\Delta\varphi_q = \Delta I_p \tau_q \tag{1.11}$$

where $\tau_q$ is the channel-average time delay between ionization and recombination also know as time of flight. This phase is imprinted on each harmonic order $q$ and permits to resolve different ionization channels at play in molecules (Smirnova et al., 2009b) or interferences of high harmonic emission in mixed atomic gases (Kanai et al., 2007).
Up to now only a linearly polarized laser field has been considered. What happens in the case of circularly or elliptically polarized fields? The electrons would clearly miss their parent ion, but not if they already had a certain transverse velocity at their birth what is indeed the case as stated in equation 1.6. When returning back to its origin the electron distribution is widespread due to their initial transverse velocities.
In terms of quantum mechanics this effect can also be described by the intrinsic dispersion of an electron wave packet. The dynamics of a free electron wave packet is governed by the Schrödinger equation. Such a wave packet can be written as a superposition of plane waves $e^{ikx}$ (Cohen-Tannoudji et al., 1998): The Schrödinger equation in SI-units for a free electron with mass $m_e$ is as follows:

$$i\hbar\frac{\partial}{\partial t}\psi(\vec{r},t) = \Big(-\frac{\hbar^2}{2m_e}\nabla^2\Big)\psi(\vec{r},t) \tag{1.12}$$

The waves have a dispersion relation of a free electron: $\omega(k) = \frac{\hbar k^2}{2m_e}$. The group and phase velocities are respectively given by:

$$v_p = \frac{\hbar k}{2m_e} \qquad v_g = \frac{\hbar k}{m_e} \tag{1.13}$$

This is an interesting result as it shows that these two velocities are fundamentally different. Indeed an electron with the classical momentum $p = \hbar k$ moves with the group velocity $v_g$. However the phase velocity is only half as fast as the group velocity this implicates an intrinsic spread for a free electron wave packet. Indeed an important transverse spread of the electron wave packet needs to be taken into account. The transverse width $(1/e^2)$ of the electron wave packet given in equation 1.6 will change during its time of flight $\tau$ as follows (Cohen-Tannoudji et al., 1998):

$$\Delta w(t) = \sqrt{2\tau(1 + t^2/\tau^2)} \tag{1.14}$$

Note that the smaller the width of the initial wave packet the stronger it will spread and vice versa. The probability density of the electron wave packet spreads proportionally. The right side of equation 1.14 has to be multiplied by a factor of $\sqrt{2}$ for obtaining the width.

### 1.2.3. Third Step: Recollision with its Parent Ion

As the electron recollides with the parent ion several processes can be realized (Corkum, 1993). In high order Above-threshold ionization [ATI] the electron can scatter elastically with the ion. Thereby it will be dephased and can gain energy from the laser field extending the ATI spectrum (Agostini et al., 1979; Paulus et al., 1994). Laser induced electron diffraction (LIED) measuring elastically scattered electrons has recently been used for the spatio-temporal imaging of molecules and their nucleii (Meckel et al., 2008; Blaga et al., 2012). Nonsequential double ionization (NSDI) may also occur when the electron scatters inelastically with the parent ion. The recolliding electron loses part of its kinetic energy. This energy serves to remove another electron from the parent ion which will be doubly ionized (Fittinghoff et al., 1992; Walker et al., 1994).
The electron may also recombine with the parent ion leading to the emission of photons in the VUV/XUV range with a maximal conversion efficiency of up to $10^{-5}$ (Hergott et al., 2002). The energy of the emitted photon corresponds to recollision energy of the photon plus the ionization energy released when recombining: $\dot{x}(t_r)^2/2 + I_p$. Thus the maxium energy of those photons is $3.17U_p + I_p$ as mentioned in the latter section. This cutoff law has also been verified empirically on the eve of HHG (Krause et al., 1992).
There are two important properties that can be deduced from the three step model: pulse duration and polarization of the emitted harmonics. The radiative recombination takes place on a time scale of less then 2.6 fs imposing a short duration of this emission. It occurs on a fs/sub-fs time scale namely in the range of attoseconds (as), a new limit that had never, with whichever technique, been obtained before (Paul et al., 2001; Hentschel et al., 2001; Mairesse et al., 2003; Tzallas et al., 2003). The second property that can also be extracted from the three step model is the state of polarization of the high

harmonic emission. As momentum needs to be conserved, the polarization between the absorbed and emitted photons are strongly correlated. High harmonics generated in a linear polarized laser field are themselves linearly polarized (Antoine et al., 1997).
An important aspect of HHG is the symmetry of the process. Recalling the nonlinear 2nd order polarizability $P^{(2)}(\omega_3)$ (Milonni and Eberly, 1988) in the pertubative regime one yields, using the Einstein summation convention:

$$P_i^{(2)}(\omega_3) = \epsilon_0 \chi_{ijk}^{(2)}(-\omega_3,\omega_1,\omega_2) E_j(\omega_1) E_k(\omega_2) \tag{1.15}$$

with $\chi^{(2)}$ the 2nd order susceptibility tensor, $\omega_1$ and $\omega_2$ the angular frequencies of the two input photons and $\omega_3$ the angular frequency of the photon which is generated. In the case of 2nd order harmonic generation the relationship between the frequencies is as follows $\omega_1 = \omega_2 = \omega_3/2$. It is easy to show that for materials with inversion symmetry the following statement holds: $P_i^{(2)}(\omega_3) = -P_i^{(2)}(\omega_3)$ what can only be fulfilled if $P^{(2)} \equiv 0$. This identity can be generalized for higher orders n: $P^{(2n)} \equiv 0$. In other words this means that one cannot observe nonlinearities of even order in gases, fluids and crystals with an inversion symmetric order. However consider that effects of $\chi^{(2n+1)}$ and $\chi^{(2n)}$ always play a role on boundary surfaces.
Randomly aligned gases are inversion symmetric. In a macroscopic generation medium one will always find an inversion symmetric pendant for HHG, such that harmonics of even order are suppressed in the spectrum in the pertubative regime. Also in non-pertubative regime only odd harmonics are present. This phenomenon can be understood in the following context: HHG takes place every half laser cycle. With the reciprocity of the Fourier transform, a harmonic spacing of twice the fundamental frequency is expected. As the process changes sign every half cycle the even Fourrier components of the frequency spectrum turn out to be zero.

## 1.3. Quantum Model of High Harmonic Generation

The semiclassic model explains the basic steps of HHG even delivering a cutoff law $3.17U_p + I_p$ which is in good agreement with experimental observations. Even phase information of the harmonic field can be deduced from this model as it explains well that electrons of different energy return at different times during the laser cycle. Figure 1.8 shows however that ionization times of the classical model do not agree with the measured ionization times (Shafir et al., 2012b). The experimental data rather strongly supports the quantum model. Thus the story needs to be wrapped up in the following way: "Part of an electron wavefunction in the ground state of an atom leaves it by means of tunnel ionization and propagates in the continuum. When returning the free electron wavefunction overlaps with the initial wavefunction inducing a dipole which emits high harmonic radiation." This kind of description does not only need a different theoretical framework but will also lead to new insights to HHG. A first analytical solution of this

problem was proposed by Lewenstein and coworkers and is today referred to the strong field approximation (SFA) (Lewenstein et al., 1994; Keldysh, 1965).

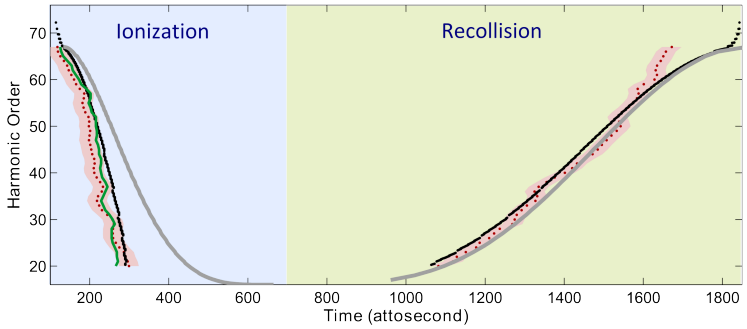


**Figure 1.8.:** Ionization and recollision times determined from the experimental measurement (red dots) with associated uncertainty (pink areas). Ionization and recollision times according to the classical (grey) and quantum model (black) are shown for matters of comparison (figure adopted from (Shafir et al., 2012b)).

### 1.3.1. The Strong Field Approximation

The starting point for describing a single electron bound to an atom in an oscillating electric field is the time dependent Schrödinger equation (TDSE) of this system:

$$i\frac{\partial\psi(\vec{r},t)}{\partial t} = \Big[-\frac{1}{2}\nabla^2 + V_0(\vec{r}) + \vec{r}\vec{E}(t)\Big]\psi(\vec{r},t) \tag{1.16}$$

with $V_0(\vec{r})$ the atomic potential and $\vec{E}(t)$ the electric field strength. Multielectron interactions shall be neglected. Only one electron interacting with the laser field and the atomic potential shall be considered. This refers to the single active electron approximation (SAE) (Keldysh, 1965). For systems such as alkali metal atoms this approximation is very intuitive. For rare gases the situation is different, the approximation is only valid when the photon energy of the fundamental laser field is much smaller than the ionization potential (Schafer, 2009; Kulander et al., 1992). A numerical solution of the TDSE is possible with today's processing power. However the analytical solution, which has been made feasible by the SFA, gives deeper insights in the physical process of HHG.
Within the scope of the SFA, the following assumptions are necessary:

**I)** In order to ensure the horizontal ionization channel (tunnel ionization) $\gamma \ll 1$ is sufficient. This assumes a low frequency of the laser field and a strong laser field. Only the ground state of the atomic/molecular system is considered.

**II)** The electron in the continuum is unaffected by the Coulomb potential and only the interaction with the laser field is taken into account. The electron is assumed to be free in the continuum.

**III)** Depletion of the ground state is neglected.

These assumption are partly conflicting. On the one hand the field has to be quite strong $U_p \gg I_p$, but on the other hand $I < I_{sat}$ has to be fulfilled. This results in a well defined intensity regime for HHG.
The first step of solving the Schrödinger equation 1.16 can now be done by making the following Ansatz:

$$\psi(\vec{r},t) = e^{iI_p t}\Big[a(t)\psi_0 + \int \frac{d^3\vec{k}}{2\pi} a(\vec{k},t)e^{i\vec{k}r}\Big] \tag{1.17}$$

with $a(t)\psi_0$ the ground state and the second term corresponding to small perturbation of the initial state. The expansion of this perturbation is written in a basis of plane waves what is a justified approximation if the Coulomb potential of the atom is neglected. The dipole moment $\vec{r}(t) = \langle\psi(\vec{r},t)|\,\vec{r}\,|\psi(\vec{r},t)\rangle$ can then be expressed as (Lewenstein et al., 1994; Chang, 2011):

$$\vec{r}(t) = -i\int_0^t \mathrm{d}t_i \int \mathrm{d}^3\vec{p}\;\; \underbrace{\vec{d}^*_{\vec{p}+\vec{A}(t_i)}}_{\text{recombination}}\;\underbrace{e^{iS(\vec{p},t,t_i)}}_{\text{propagation}}\;\underbrace{\vec{E}(t_i)\vec{d}_{\vec{p}+\vec{A}(t_i)}}_{\text{ionization}} \tag{1.18}$$

with $S$ the classical action, $\vec{A}$ the vector potential ($\vec{E} = -\partial\vec{A}/\partial t$) and $\vec{p}$ the canonical momentum. The beauty of this result is that it can be interpreted in terms of the three step model:

**I)** Ionization: The electron is transferred to the continuum state $|\vec{p}+\vec{A}(t_i)\rangle$ with canonical momentum $\vec{p}(t_i)$ at time $t_i$. The probability of this transition is $\vec{E}(t_i)\vec{d}_{\vec{p}+\vec{A}(t_i)}$ whereas the dipole matrix element is written as: $\vec{d}_{\vec{p}+\vec{A}(t_i)} = \langle\vec{p}+\vec{A}(t_i)|\,\vec{r}\,|\psi_0\rangle$.

**II)** Propagation in the continuum: Equivalent to Feynman's path integral formulation the electron acquires a phase proportional to the classical action $S$:

$$S(\vec{p},t,t_i) = -\int_{t_i}^{t}\Big[\frac{(\vec{p}+\vec{A}(t'))^2}{2} + I_p\Big]dt' \tag{1.19}$$

**III)** Recombination: At time $t = t_r$ the electron recombines with the accumulated momentum $(\vec{p}+\vec{A}(t_i))$ with a transition amplitude given by: $\vec{d}^*_{\vec{p}+\vec{A}(t_i)} = \langle\psi_0|\,\vec{r}\,|\vec{p}+\vec{A}(t_i)\rangle$.

Note that the form of the dipole operator is not irrelevant. Length, velocity and acceleration can give different results and remain to be debated. With the dipole moment in length gauge the harmonic spectrum can now be calculated by applying the Fourier transform to equation :

$$\vec{r}(\omega_q) = \int_{-\infty}^{+\infty} dt_r\,\vec{r}(t_r)e^{i\omega_q t_r} = \int_{-\infty}^{+\infty} dt_r \int_0^{t_r} dt_i \int d^3\vec{p}\,\vec{b}(t_r,t_i,\vec{p})\,e^{i\varphi_q(t_r,t_i,\vec{p})} \tag{1.20}$$

with the dipole phase

$$\varphi_q(t_r,t_i,\vec{p}) = \omega_q t_r + S(\vec{p},t_r,t_i) \tag{1.21}$$

and the amplitude of each contribution $\vec{b}(t_r,t_i,\vec{p}) = \vec{d}^*_{\vec{p}+\vec{A}(t)}\vec{E}(t_i)\vec{d}_{\vec{p}+\vec{A}(t_i)}$.

### 1.3.2. Saddle-point Approximation

The phase $S$ acquired by the electron in the continuum corresponds to the classical action and can be interpreted in terms of Feynman's path integral formulation (Salières et al., 2001). In contrast to classical mechanics this formalism allows all possible paths in the space-time plane, even if they are classically forbidden (Sakurai, 2005). It turns out however that only paths closest to the classical one survive in this formalism. The integrand $e^{iS}$ oscillates strongly such that trajectories from neighbouring paths cancel each other out. The path that satisfies $\delta S = 0$ provides the dominant contribution. According to Hamilton's principle the trajectory which fulfills this condition corresponds exactly to the classical path.
Also in the case of HHG the components of equation 1.20 which survive fulfill $\delta(S(\vec{p},t_r,t_i)+\omega_q t_r) = 0$. When applying Hamilton's principle in this context equation 1.21 has to be differentiated with respect to $\vec{p}$, $t_r$ and $t_i$ what then lead to the saddle point equations.

$$\frac{(\vec{p}+\vec{A}(t_i))^2}{2} + I_p = 0 \tag{1.22}$$

$$\int_{t_i}^{t_r} dt\,(\vec{p}+\vec{A}(t)) = 0 \tag{1.23}$$

$$\frac{(\vec{p}+\vec{A}(t_r))^2}{2} + I_p = \omega_q \tag{1.24}$$

These equations can be interpreted with respect to the three step model, each step can be identified by one of them:
Equation 1.22 states that the sum of kinetic energy and ionisation potential is zero at the time of ionisation $t_i$. This results in a negative kinetic energy of the electron which can be justified by tunnel ionization when allowing complex valued emission times $t_i$.
Equation 1.23 shows that the electron returns to its origin. In other words its trajectory is closed: $\int_{t_i}^{t_r} dt\vec{v} = 0$.
Equation 1.24 implies conservation of energy. The energy of the emitted photon is exactly equal to the energy released by the recolliding electron. The saddle point equations are also used for calulating the dipole phase which is an essential parameter depending on the action $S$ and the harmonic order $q$. A calculation performed by Varju and coworkers (Varju et al., 2005) shows that the dipole phase changes linearly with laser intensity (figure 1.9)(a). Moreover the slope depends on the type of trajectory and converges for

the cutoff as depicted in figure 1.9(b). This slope is characterized by the $\alpha$ parameter. First experimental measurements of the dipole phase (Mauritsson et al., 2004; Corsi et al., 2006) uncovered the same trend as predicted in the calculations:

$$\varphi_q = -\alpha_q I \tag{1.25}$$

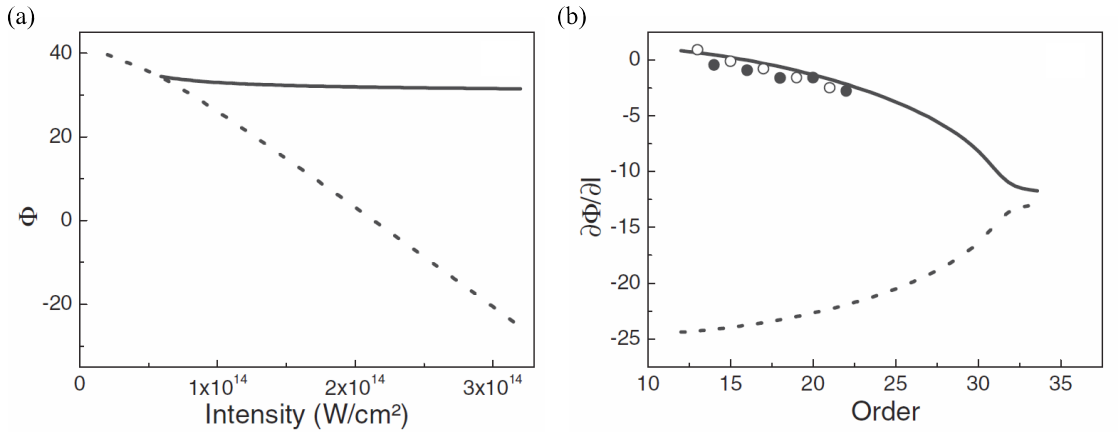


**Figure 1.9.:** (a) The dipole phase of harmonic 19 in argon calculated for short (solid line) and long trajectories (dashed line). (b) Variation of the dipole phase with harmonic order, for long (dashed line) and short trajectories (solid line) (figures adopted from (Varju et al., 2005)).

### 1.3.3. Quantum mechanical Cutoff Law

The exact cutoff law actually differs from the classical cutoff law $I_p + 3.17U_p$. This is mainly a consequence of two effects that are not considered in the classical picture. Firstly, due to the complex emission time, the electron is not born exactly at the position of the parent atom. The electron tunnels out of a non zero distance. As the electron recollides it acquires an additional kinetic energy as it covers an additional distance. Secondly due to the intrisic dispersion of an electron wave packet the kinetic energy averages and diminishes the latter effect. These two effects need to be considered as they lead to a higher kinetic energy of the electrons. The quantum mechanical cutoff is as follows (Lewenstein et al., 1994):

$$(h\nu)_{max} = F(I_p/U_p)I_p + 3.17U_p \tag{1.26}$$

where $F(I_p/U_p)$ is a corrective factor. Figure 1.10(a) shows the dependency of the corrective factor. Figure 1.10(b) compares the quantum mechanical cutoff law and the classical cut-law. The exact quantum mechanical law fulfills the criteria for the cutoff much better.

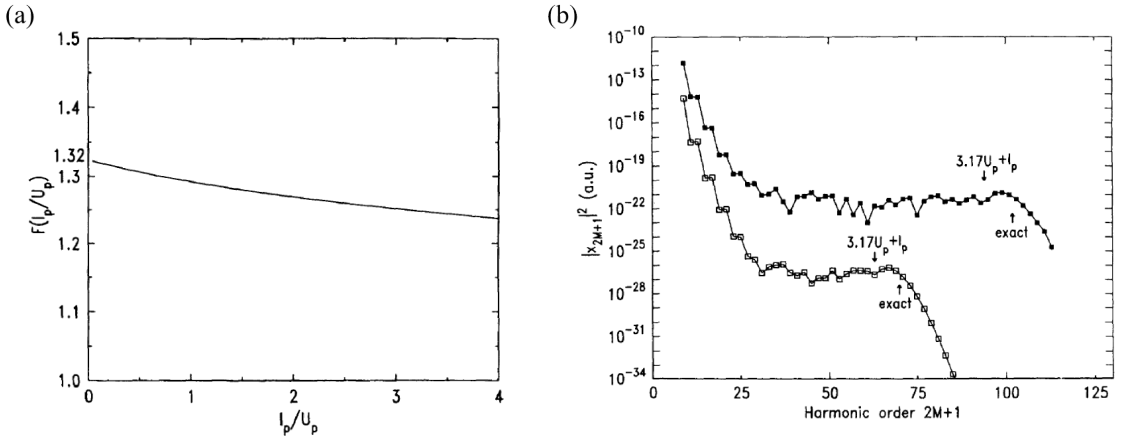


**Figure 1.10.:** (a) The corrective factor as a function of $I_p/U_p$. It reaches a value of 1.32 for $I_p/U_p = 0$. (b) Calculated spectra showing the harmonic strength of the Fourier component of the dipole moment. The quantum mechanical cutoff law is more acurate than its classical pendant (figures adopted from (Lewenstein et al., 1994)).

## 1.4. Classical Trajectory Monte Carlo Quantum Electron Scattering Theory

The three step and the Lewenstein model have two drawbacks. First of all both neglect the influence of the ionic potential during the time of flight of the free electron. Additionally they cannot reproduce spectral structures such as the minimum observed in figure 1.11. This Cooper minimum was first observed in the XUV photoionization of argon (Cooper, 1962). It originates from the zero dipole moment between the $p$ ground-state wave function and the $d$ wave function of the photoionized electron. It took almost 20 years since the first observation of this minimum in HHG (Wahlström et al., 1993) to its satisfying modelling (Wörner et al., 2009; Higuet et al., 2011). Existing theories had to be modified or even be recreated as presented in the following.

In a recent work a quantitative rescattering theory (QRS) for HHG partly considering the ionic potential in the recombination step has been proposed for atoms and molecules (Le et al., 2009). For this purpose a model system assuming an effective charge has been developped, showing coherent results both with SFA and TDSE calculations. Furthermore this theory states, that the high harmonic spectra can be expressed as a product of the electron flux recombining with its parent ion and the recombination probability.
In this context a semiclassical theoretical approach to HHG has been developped by Fabre and Pons (Higuet et al., 2011): Classical Trajectory Monte Carlo Quantum Electron Scattering Theory also referred to as CTMC-QUEST. It does not only take into account the influence of the Coulomb potential but is also the first theoretical tool which handles below threshold HHG appropriately (Botheron and Pons, 2009; Soifer et al., 2010). This

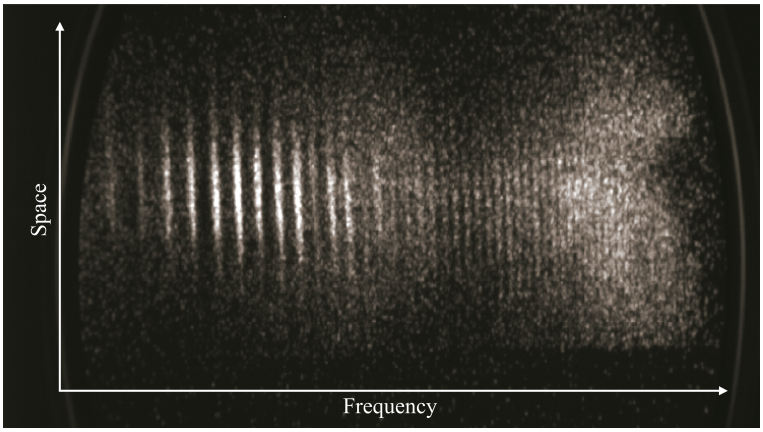


**Figure 1.11.:** High harmonic spectrum produced in argon gas at a fundamental laser wavelength of 1800 nm.

model is composed of the same three steps as the three step model and the Lewenstein model. Thus approximate calculations of the electron wave packet as performed in reference (Wörner et al., 2009) are avoided. Let's go step by step.
This method is based on the calculation of many electron trajectories and is thus treated in a theoretical framework. The initial phase space distribution needs to be established for ionization. The Wigner distribution proves to be a good choice for approximating the quantum radial electronic density. The ensemble of electron trajectories ejected from the ion core are propagated under the influence of the laser field and ionic potential of its parent ion. The electrons returning within the radius of a rescattering sphere are considered for recombination. This step is treated quantum mechanically however, decoding the structural information hidden by the irradiated sample.

### 1.4.1. CTMC and Initial Phase-Space Distribution

CTMC (Abrines and Percival, 1966) is a method for solving the Liouville equations. The electron density is described by a discrete representation of the phase space distribution $\rho(\vec{r},\vec{p},t)$:

$$\rho(\vec{r},\vec{p},t) = \frac{1}{\mathcal{N}} \sum_{j=1}^{\mathcal{N}} \delta(\vec{r} - \vec{r}_j(t))\delta(\vec{p} - \vec{p}_j(t)) \tag{1.27}$$

with $\vec{r}_j$ and $\vec{p}_j$ the generalized coordinates of a statistical ensemble. The temporal evolution of this phase space distribution is causally determined by the Liouville equation, the classical analog to the TDSE:

$$\frac{\partial \rho}{\partial t} + \{\rho,H\} = 0 \tag{1.28}$$

with $\{\}$ the Poisson bracket and $H = p^2/2 + V(r) + \vec{r}\vec{E}(t)$ the Hamiltonian. The equations of motion for the different electron trajectories are finally defined by a set of differential equations, the Hamilton equations:

$$\frac{\partial \vec{r}_j(t)}{\partial t} = \vec{p}_j(t) \tag{1.29}$$

$$\frac{\partial \vec{p}_j(t)}{\partial t} = -\nabla[V(\vec{r}_j) + \vec{r}_j\vec{E}(t)] \tag{1.30}$$

The statistical ensemble is described by microcanonical distributions in CTMC. The challenge of statistical mechanics is finding the initial phase space distribution $\rho(\vec{r},\vec{p},t)$ (Nolting, 2002). Knowing the potential of the physical system, the energy and the fundamental wavefunction can be calculated. Several bins are defined around the fundamental energy (Raković et al., 2001) of this model potential leading to a set of energies, with each energy associated to a microcanonical distribution $\rho(\vec{r},\vec{p},0)$. The known initial state can be approximated by a linear combination of microcanonical distributions, the so called improved initial phase-space distribution, resulting in a weight for each of these distributions. The number of initial trajectories is proportional to these weights.

### 1.4.2. Ionization for the CTMC Method

This method approximates quite well the quantum radial density $4\pi r^2 R^2_{3,1}(r)$ of the initial $3p$ ground state in argon as can be seen in figure 1.12. The nodal structure at small $r$ and the position of the large maximum do not fit well. However, it reproduces very well the tail of the density distribution at large r that dominantly contributes to tunnel ionization.

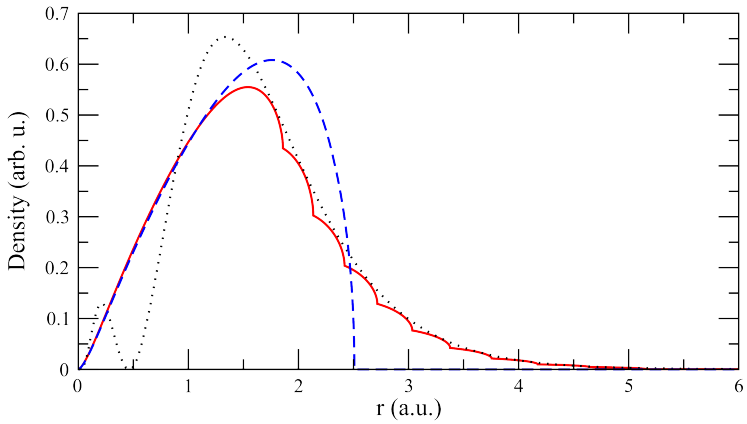


**Figure 1.12.:** Quantum radial electronic density (blackdotted line) of the fundamental argon 3p ground state compared to the initial density of one microcanonical distribution $\rho(-I_p,r,t=0)$ (blue dashed line) and the initial density $\rho(r,t=0)$ (red solid line) as a linear combination of ten microcanonical distributions.

An important question to raise is: How does tunnel ionization work in this approach? If only the phase space distribution belonging to $E_i = -I_p$ is allowed, almost no electrons escape the atom, what contradicts experiments and quantum calculations. A better description can be obtained by employing an improved initial phase space distribution, such as a Wigner distribution truncated according to the classical partition of the phase space. In that case CTMC provides a significant degree of ionization, which reasonably agrees with quantum estimates. This can be surprising since tunneling is classically forbidden. In fact, the improved initial phase space distribution includes trajectories with $E > -I_p$ such that ionization occurs in terms of above-barrier transitions (Balazs and Voros, 1990; Keshavamurthy and Miller, 1994). In the present non-stationary case, it can be similarly concluded that the usual quantum description of ionization through strong field-lowered Coulomb barriers has a classical counterpart that can be represented by improved CTMC calculations. The picture is simple: as observed in figure 1.13 electrons associated to the phase space distributions of the highest energy levels can classically leave the parent atom. Exactly these electrons correspond to the electrons in the tail of the radial density distribution (see figure 1.12).

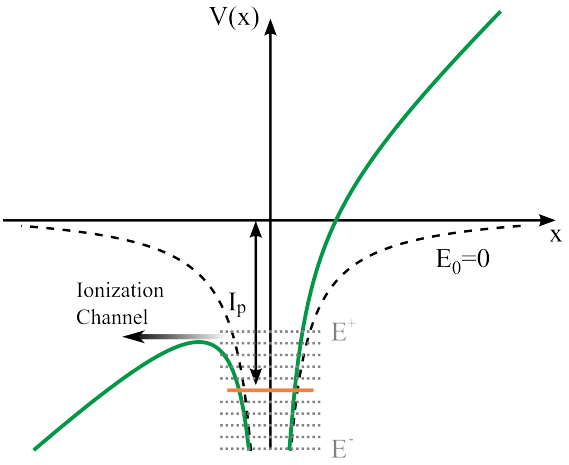


**Figure 1.13.:** Bins are defined for the improved initial phase space distribution around $-I_p$. The ionization channel is classically allowed for the highest energies.

### 1.4.3. Electron in the Continuum and Definition of the Recombining Wave Packet for CTMC

All possible electron configurations represented by the phase space distribution $\rho(\vec{r},\vec{p},t)$ obey the equations of motion 1.29 and 1.30. This enables to calculate the density distribution $\rho_{ret}(E_j,\vec{k}'',t)$ with $E_j$ the energy and $\vec{k}''$ the wave vector direction of the returning electrons when rescattering with the atom. An open question is, how is recombination defined in a classical model. A criterion of the recollision probability is set by defining

a rescattering sphere with the radius $R_{sec}$ as depicted in figure 1.14(a). The electrons returning within the radius of the sphere are considered for recombination. The radius of this rescattering sphere is on the order of the extension of the fundamental wavefunction. In order to determine the dependency of the sphere radius on the density of the returning electrons three different radii are considered as shown in figure 1.14(b). The returning electron density increases with bigger rescattering sphere, but the shape remains the same.

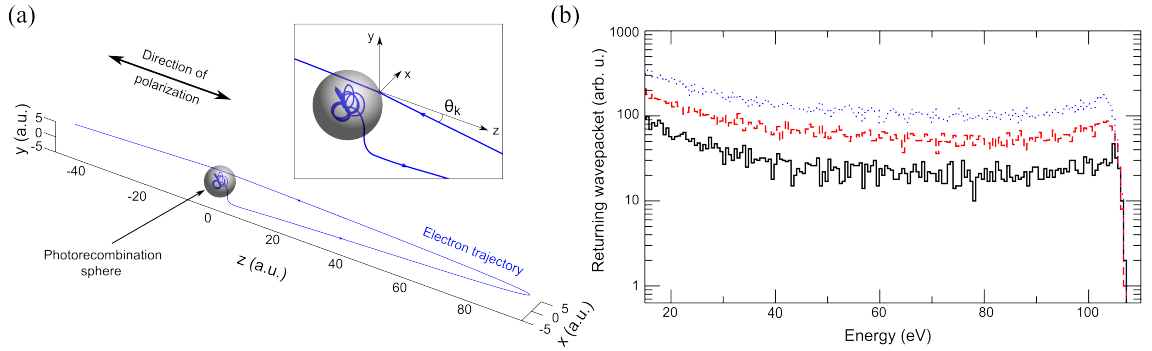


**Figure 1.14.:** (a) As in the three step model the electron rescatters with its parent ion. It only rescatters if it returns within the range of the rescattering sphere with a recombination angle $\theta_k$.(b) Density of returning electrons for three different radii of the rescattering sphere: $R_{rec} = 3\,a.u.$ (solid line) $R_{rec} = 5\,a.u.$ (dashed line) and $R_{rec} = 7\,a.u.$ (dotted line).

Another very important asset of CTMC is that short, cutoff and long trajectories can be identified. In figure 1.15(a) the cutoff trajectory corresponds to the highest electron energy. Electrons that return earlier (later) are attributed to short (long) trajectories. The density of returning electrons decreases with trajectory length as can be observed in figure 1.15(b). At first sight, this observation is contradictory to the fact that electrons following the longer trajectories are born earlier at a higher laser field intensity and experienced therefore a stronger ionization rate than the electrons of shorter trajectories. It is clear that another effect is dominating namely a stronger latteral spread of the long trajectories and consequently a higher chance of missing the rescattering sphere.

### 1.4.4. Recombination for CTMC

The harmonic spectrum could be calculated classically, but this would be very complex. As the probability of radiative recombination is quite low (on the order of $10^{-6}$ to $10^{-5}$) the number of trajectories that are needed to be calculated would be quite high and thus exceeding the limits of available computing power.
In a first quantum mechanical approach the recolliding wavefunction was approximated by plane waves. This approach has been successfully applied for the imaging of the nitrogen molecule (Itatani et al., 2004). It turned out that a plane wave is oversimplified

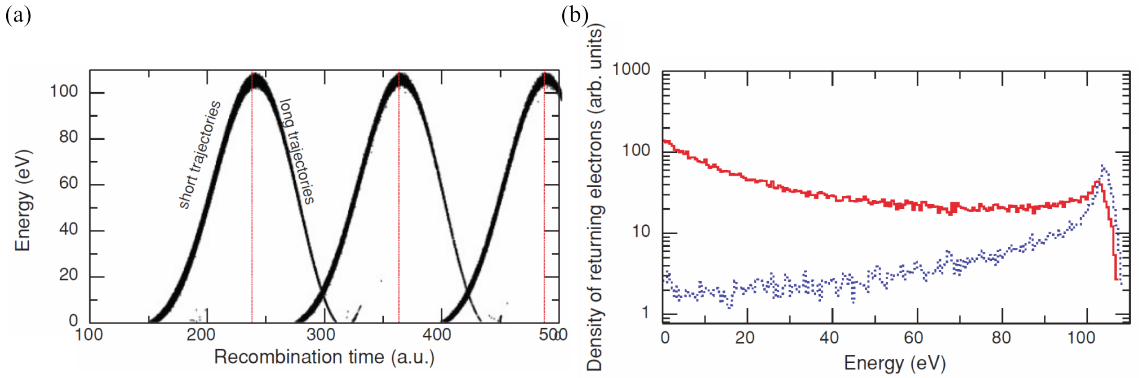


**Figure 1.15.:** (a) Total energy of the electrons returning at different recombination times. (b) Density of returning electrons for short (red solid line) and long trajectories (blue dotted line).

for recombination. Since it does not take into account the influence of the ionic potential which distorts the recolliding wave packet. Field-free continuum wave functions however approximate the influence of the core very well (Wörner et al., 2009). Therefore recombination is treated within the framework of the quantum rescattering theory. The probability of radiative recombination $\mathcal{P}_{PR}(E,\vec{k}'')$ can be established by applying the microreversibility principle on Fermi's golden rule (Cohen-Tannoudji et al., 1996). This establishes the transition induced by the electric dipole moment from the continuum of scattering states $\psi_{E,\vec{k}''}$ to the ground state $\psi_0$:

$$\mathcal{P}_{PR}(E,\vec{k}'') = \mathcal{P}_{PI}(\vec{k}') = \frac{\pi\sqrt{2E}}{2} |\langle\psi_{E,\vec{k}''}|\vec{n}\vec{r}|\psi_0\rangle|^2 \tag{1.31}$$

with $k''$ the wave vector and $E$ the total energy of the returning electron. Note however that the wavenumber of an electron at its birth is defined by $k' = \sqrt{2E}$ whereas the wavenumber of the recombining electron is influenced by the Coulomb potential of the parent ion: $k'' = \sqrt{2E - 2V(R_{rec})}$. Knowing the photorecombination probability and the density of returning electrons the harmonic spectrum can be expressed as:

$$\begin{aligned} S(\omega,\vec{n}',t) &= \int dE \rho_{ret}(E,\vec{k}'',t)\mathcal{P}_{PR}(E,\vec{k}'')\delta(E+I_p-\omega) \\ &= \frac{1}{\mathcal{N}} \sum_{i=1}^{\mathcal{N}_{ret}(t)} \mathcal{P}_{PR}(E_i(t),\vec{k}''))f(E_i(t),\omega) \end{aligned} \tag{1.32}$$

where $f(E_i(t),\omega) = 1$ for $E_i(t) = \omega - I_p$ and 0 if this condition is not fulfilled. The time integrated spectrum is finally obtained by summing over the pulse duration $\tau^*$: $S(\omega,\vec{n}',\tau^*) = \int_0^{\tau^*} S(\omega,\vec{n}',t)dt$. The challenge of quantum rescattering theory is finding the model potential describing a single active electron in a multi electron system. The

model potential crucially determines the expansion of the scattering wave. This approach has even been extended from atoms to simple molecules (Le et al., 2009).

## 1.5. HHG under experimental Conditions

Up to now HHG has only been treated considering a single atom in three different theoretical models. Under experimental conditions, high harmonic emission in a gas is generated in many atoms. All these atoms display dipoles which emit electromagnetic radiation that interfere with each other depending on their relative phase. As in second harmonic generation in crystals phase matching is an important issue and a long coherence length $L_{coh}$ must be established for efficient generation (Ashkin et al., 1963). Another issue in macroscopic samples is reabsorption: if the generation medium is longer than its absorption length $L_{abs}$, the emitted photons are reabsorbed by the medium itself.
The ring structures, as illustrated in figure 1.16, cannot be seized by these two macroscopic effects though. It turns out the the emission on axis/off axis can indeed be attributed to long or short electron trajectories.

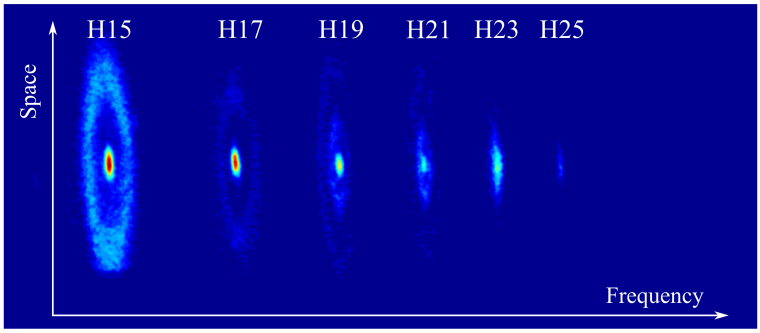


**Figure 1.16.:** High harmonic spectrum produced in argon gas at a fundamental laser wavelength of 800 nm. H19 shows a on axis emission and two different ring structures as an off axis emission.

Finally all theory stays redundant if it cannot put into practice. The Aurore Ti:Sa-Laser system at CELIA will be shortly presented together with the TOPAS, an optical parametric amplifier (OPA). The imaging of the HHG will be roughly presented as well as two different gas sources in which high harmonics are generated.

### 1.5.1. Phase matching Conditions for HHG

This section will consider the different contributions to phase matching in gases. A wave vector k for a light wave propagating through a gaseous medium exposed to a strong laser field has mainly two contributions: a dispersive one due to neutral atoms, ions and electrons in the gas (L'Huillier et al., 1992; Rundquist et al., 1998) and a geometrical one, the Gouy phase (Siegmann, 1986). In a first step the dispersive effects will be neglected

what can be justified by a low density of the emission medium. It comes out that phase matching conditions depend on the position of the laser focus with respect to the gas source (Salières et al., 1995; Antoine et al., 1996; Balcou et al., 1997; Gaarde et al., 1999).
Neglecting dispersive effects the phase matching conditions can be summarized as (Balcou et al., 1997):

$$\vec{k}_q = q\vec{k}_1 + \vec{K} \tag{1.33}$$

with the wave vector $\vec{k}_q$ of the emitted high harmonics. The wave vector $k_1$ is a sum of fundamental wave vector and a term related to the Gouy phase shift experienced by a Gaussian beam around the focus. This leads to a phase difference of wavefronts before and behind the focus which amounts to exactly $\pi$. The effective wave vector $\vec{K}$ is the gradient of the atomic dipole phase. Phase matching conditions can now be established when adding these two vectors (figure 1.17).

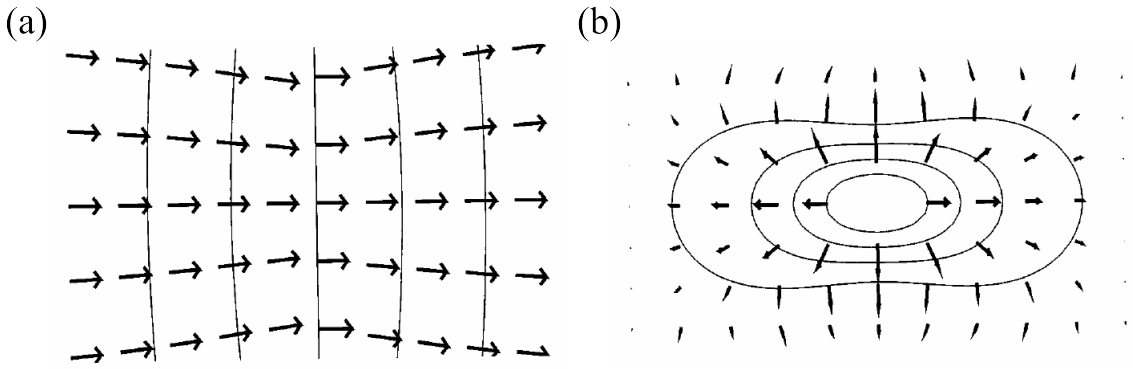


**Figure 1.17.:** (a) Wave vector $\vec{k}_1$ of the fundamental laser beam going through a focus including the effect of the Gouy phase shift. (b) The effective dipole phase wave vector $\vec{K}$ in the focal region (figures adopted from (Balcou et al., 1997)).

Figure 1.18 depicts four different conditions when overlapping the wave vector $\vec{k}_1$ of the fundamental beam and the effective dipole phase wave vector at different positions of the beam. It is clear that phase matching can not be fulfilled at focus as the effective wave vector is zero and cannot compensate the mismatch. However if the focus is moved on axis in front of the generating medium, the phase mismatch can be compensated and on axis emission will occur. When displacing the focus in the other direction after the generating medium, compensation will not be possible. Only at positions off axis in front of the focus, nonlinear phase matching conditions can be established with a $\vec{k}_q$ pointing off axis. In summary, depending on the position of the laser focus phase matching is favorized either in a on axis or off axis direction. These results already give a first notion why different trajectories are emitted in different directions as observed in figure 1.16. $\vec{K}$ is more pronounced for the long electron trajectories because their dipole atomic phase varies strongly with laser intensity (see equation 1.25).

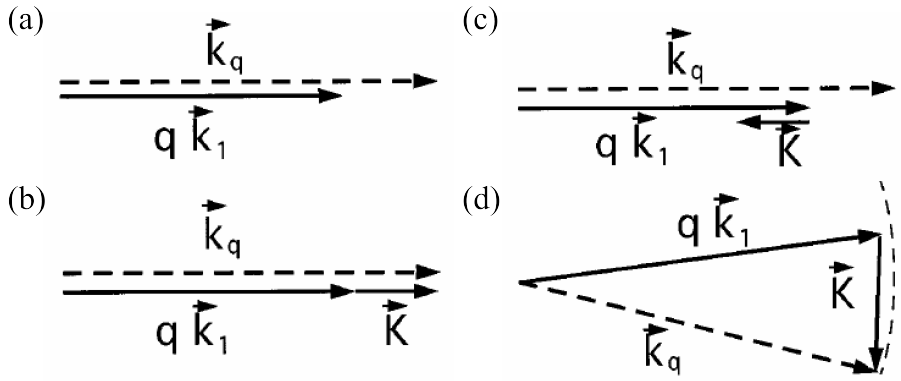


**Figure 1.18.:** Phase matching at different points of the focal region: (a) On axis at focus, (b) on axis after the focus, (c) on axis before the focus and (d) off-axis before the focus (figures adopted from (Balcou et al., 1997)).

Phase matching is never perfectly fulfilled along a medium with the length $L$, but only to a certain degree which is defined as the phase mismatch $|\Delta\vec{k}|L$. Balcou and coworkers have calculated this mismatch for different conditions (Balcou et al., 1997). The parameter characterizing this mismatch is the coherence length $L_{coh}$ defined as:

$$L_{coh} = |\pi/\Delta\vec{k}| \tag{1.34}$$

If the generation medium exceeds the coherence length, harmonic waves emitted at the edges of the medium emit out of phase and interfere destructively.

HHG requires a substantial gas density $\rho$ for efficient generation ($10^{17}\,\mathrm{cm}^{-3}$- $10^{18}\,\mathrm{cm}^{-3}$). In such a situation dispersive effects of the medium need to be taken into account. One has to distinguish between three contributions: atomic, electronic and ionic dispersion, whereas the latter is usually neglected (L'Huillier et al., 1992; Rundquist et al., 1998).
Atomic dispersion $\delta n_d(\lambda)$ is different for the fundamental wavelength $\lambda_0$ and the harmonic wavelength $\lambda_q$. The refractive index of the gas is $n(\lambda,\rho) = 1 + \delta n_d(\lambda)\rho$ (Mével et al., 2000). $\delta n_d(\lambda_0)$ is positive for photons with a lower energy than the ionization potential and $\delta n_d(\lambda_q)$ negative for photons with a larger energy. A one-dimensional model delivers the vector mismatch for the atomic and electronic case (Mével et al., 2000):

$$\Delta k_a(\rho,I) = k_a^q - qk_a^1 \approx -q\frac{2\pi}{\lambda_0}[\Delta n_a(\lambda_0) - \Delta n_a(\lambda_q)]\rho(1-\Gamma(I)) \tag{1.35}$$

where $\Gamma(I)$ is the ionization probability. The vector mismatch is oriented inversely to propagation direction.
Plasma dispersion is another substantial contribution to the vector mismatch, all free electrons contribute. The vector mismatch points in propagation direction (Mével et al., 2000):

$$\Delta k_e(\rho,I) = k_e^q - qk_e^1 \approx \frac{r_0\lambda_0}{q}[q^2-1]\rho\Gamma(I) \tag{1.36}$$

The wave vector mismatch is negative for atoms and positive for the plasma but always parallel to the fundamental wave vector. As long as the medium is not too strongly ionized phase matching on axis is well maintained.

### 1.5.2. Reabsorption in the Generation Medium

As in highly doped laser crystals, reabsorption in the generation medium plays an important role. A photon produced by HHG can be reabsorbed by the gas. The absorption length characterizes the critical length at which reabsorption begins to play an important role. It is defined as $L_{abs} = 1/(\sigma\rho)$, with $\rho$ the gas density and $\sigma$ the single photon ionization cross section. In a one-dimensional model the number of photons $N_{out}$ emitted by the $q^{th}$ harmonic on axis can be estimated with (Constant et al., 1999; Mével et al., 2000):

$$N_{out} \propto \rho^2 A_q^2 \frac{4L_{abs}^2}{1+4\pi^2(L_{abs}^2/L_{coh}^2)}\left[1+\exp\left(-\frac{L_{med}}{L_{abs}}\right)-2\cos\left(\frac{\pi L_{med}}{L_{coh}}\right)\exp\left(-\frac{L_{med}}{2L_{abs}}\right)\right] \tag{1.37}$$

where $L_{med}$ is the length of the generating medium. The evolution of equation 1.37 is illustrated in figure 1.19(a).

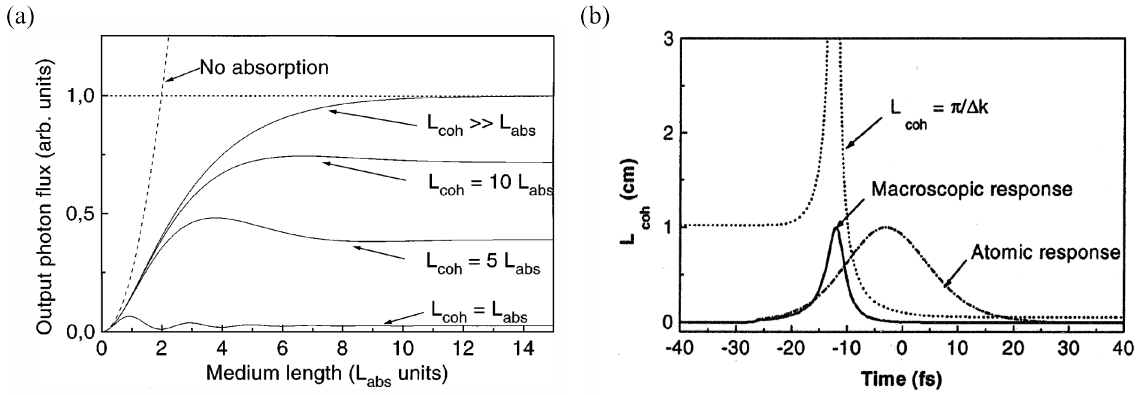


**Figure 1.19.:** (a) Number of on-axis emitted photons at different coherence length and absorption length ratios (figure adopted from (Constant et al., 1999)). (b) Photon yield of the atomic response (dotted dashed line) for a 40 fs laser pulse with a peak intensity of $10^{14}$W/cm$^2$ using a 4 cm long, 200 $\mu$m bore diameter capillary filled with 8 mbar of Xe. Phase matching reduces the HHG to a much shorter time interval leading to a macroscopic response (solid line) (figure adopted from (Mével et al., 2000)).

If no reabsorption was present, the number of emitted photons would grow exponentially in case of infinite coherence length. When absorption becomes significant the output photon flux saturates. The saturation level depends on the coherence length, and becomes very low if the coherence length becomes equal to the absorption length. The optimizing conditions for HHG can be summarized as:

$$\begin{aligned} L_{med} &> 3L_{abs} \\ L_{coh} &> 5L_{abs} \end{aligned} \tag{1.38}$$

As coherence length changes with laser intensity, it becomes a selective factor for HHG when taking into account dispersion. Figure 1.19(b) shows that the time window for a high coherence length can be much shorter than the laser pulse duration. This leads to a short time window of HHG in macroscopic media. The findings of this paragraph finally show, that several parameters have to be adjusted in experimental conditions for maximizing the XUV photon flux: Laser parameters[2], gas pressure and focussing conditions (optimization see paragraph 1.5.4).

### 1.5.3. Structure Interpretation of the Spectrum: Long and Short Trajectories

There is still one fundamental question which remains unanswered from a general point of view. How can the harmonic profile in figure 1.16 be explained. Harmonic 15 to 21 clearly show rings around the central signal. These structure can be explained beginning with the linear intensity dependence of the atomic dipole phase $\phi_q = -\alpha_q I$ (Varju et al., 2005) as already stated in equation 1.25. With the electric field:

$$E_q = A_q(t)e^{(i(\omega_q t - \varphi_q(t)))} = A_q(t)e^{(i\Phi(t))} \tag{1.39}$$

the instantaneous harmonic frequency can be written as (Gaarde et al., 1999; Salières et al., 1999):

$$\Omega_q(t) = \frac{\partial \Phi}{\partial t} = q\omega + \alpha_q \frac{\partial I(t)}{\partial t} \tag{1.40}$$

As $\alpha > 0$ this equation says that the XUV emission in the leading edge is blue-shifted and the XUV emission at the trailing edge is red-shifted. With $\alpha_q \approx 1\text{-}5 \times 10^{-14}\,\mathrm{cm}^2/\mathrm{W}$ for the short trajectory and $\alpha_q \approx 20\text{-}25 \times 10^{-14}\,\mathrm{cm}^2/\mathrm{W}$ for the long trajectory this shift is stronger for the latter and weaker for the former. Thus the frequency shift is stronger for long than for short trajectories. The spatial dependence can also be illustrated as shown in figure 1.20. The short trajectory signal remains closer on axis wheras the long trajectory signal is very divergent.

[2]These include laser intensity, pulse duration and the chirp of the laser pulse

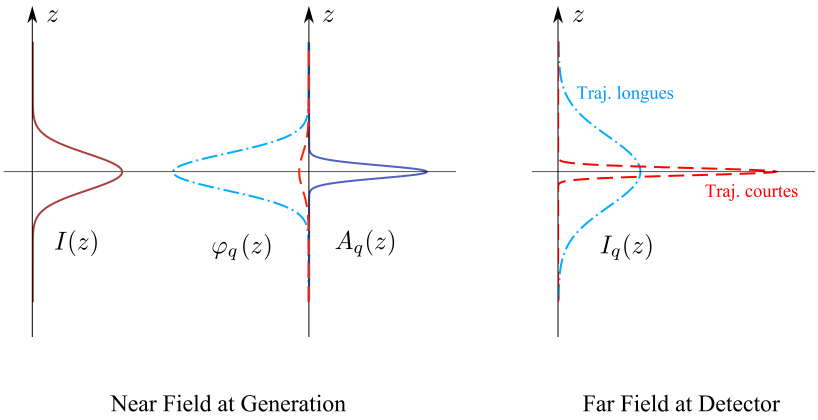


**Figure 1.20.:** The far field spatial profile is obtained by a Fourier transform of the near field profile at generation. The stronger the phase the stronger the divergence of the emitted harmonics (figure adopted from (Higuet, 2010)).

When increasing the intensity of the laser beam, another effect on the spectrum can be observed. With the phase $\varphi = \omega_0 t - \frac{2\pi}{\lambda} nz$ the intantaneous frequency can be written as:

$$\omega = \frac{\partial \varphi}{\partial t} = q\omega - \frac{q\omega}{c} z \frac{\partial n}{\partial t} \tag{1.41}$$

With increasing ionization the refractive index becomes negative. Consequently the presence of an electronic plasma contributes to a blue shift to the harmonic spectrum. The signal originating from the long electron trajectory is hollow and shows ring structures. A recent experimental and theoretical investigation for the long trajectories (Heyl et al., 2011) delivered very convincing results that the different rings can be interpreted in the context of Maker fringes (Maker et al., 1962). These fringes refer to an oscillating photon yield $S$ when changing the length $L_{med}$ of the generating medium. Neglecting the absorption, the following relation can be derived from equation 1.37:

$$S \propto L_{med}^2 \,\mathrm{sinc}^2\left(\frac{\pi L_{med}}{2L_{coh}}\right) = L_{med}^2 \,\mathrm{sinc}^2\left(\frac{\Delta k L_{med}}{2}\right) \tag{1.42}$$

with $\Delta k$ the sum of the wave vector mismatch contributions summarized in section 1.5.1. Dispersion terms are not considered. Maker fringes could for example be demonstrated in HHG in a gas cell when varying its length and thus the propagation phase (Kazamias et al., 2003). On the other hand theses fringes can also be observed if $L$ stays constant and $\Delta k$ is modulated. This is exactly the case for HHG: $\Delta k_q = -\alpha_q \partial I(t)/\partial z$. This consequently leads to an oscillating harmonic signal (Salières et al., 1999) what can be interpreted as Maker fringes as a function of time (see figure 1.21(a)).

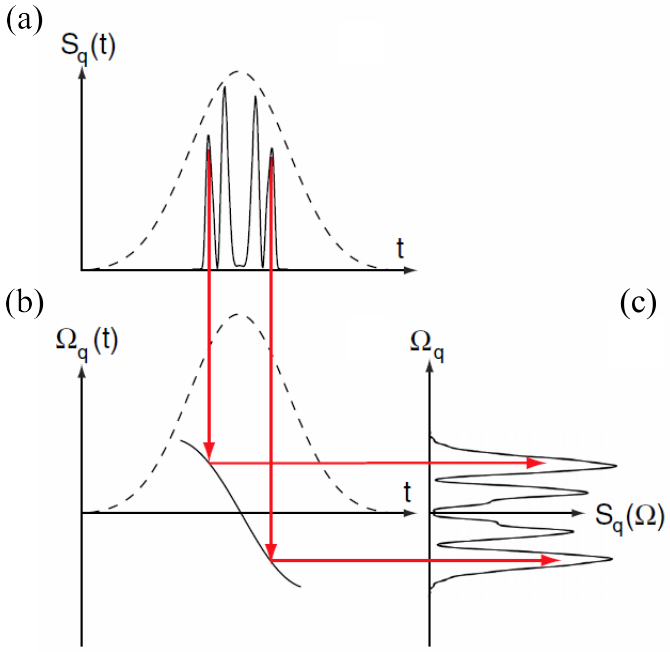


**Figure 1.21.:** (a) The photon yield $S$ is varying with intensity, what can be interpreted as Maker fringes. (b) Each intensity variation maps to an instantaneous frequency $\Omega_q$. (c) The oscillating photon yield can also be directly related to the instanteous frequency $\Omega_q$ (figure adopted from (Heyl et al., 2011)).

This explains how the different structures can be interpreted in the frequency domain. But the same can be observed as a function of divergence angle of the high harmonic radiation. Once again a low atomic dipole phase $\varphi_q$, as in the case of the low trajectory electrons, leads to an almost flat wavefront in the generating medium. In the far-field, onto the detector, this radiation will not have diverged much. On the contrary, for the long trajectory electrons, the wavefront is significantly curved (see figure 1.20). The signal from the short and long trajectories merges in the cutoff as $\alpha_q$ converges.
The same question arises as in the spatial domain: Why are structures visible for the long trajectory signal? The intensity dependence of phase matching leads to different preferential wave vector direction of the emitted high harmonic radiation along the intensity profile of the fundamental beam. In other words, the wave front of the emitted high harmonic generation will not be even but consist of wiggles. The far-field of such a signal is not smooth but gives rise to phase matching rings (Heyl et al., 2011).
Note that even though the recent work of (Heyl et al., 2011) nicely explains observed phenoma, their results do not exactly agree with previous results reported in literature. $\alpha_{17-19} \approx 40 \times 10^{-14}\,\mathrm{cm}^2/\mathrm{W}$ is found for example, whereas a maximum of $\alpha_q \approx 25$-$35 \times 10^{-14}\,\mathrm{cm}^2/\mathrm{W}$ was calculated before by Varju and coworkers (Varju et al., 2005). It has to be mentioned that structures in the high harmonic spectrum have also been interpreted in terms of intereference between the two shortest quantum paths of electrons contributing to HHG (Zaïr et al., 2008). Further studies should reveal which effect predominates under which conditions and when both need to be considered.

### 1.5.4. Experimental Setup and Techniques

This paragraph will shortly present the experimental setup at Bordeaux beginning with the laser. The main energy source, the homemade Aurore Ti:Sa-Laser system at CELIA delivers pulses with an energy of 7 mJ in the two arms, a duration of 25 fs and a central wavelength of 800 nm at a repetition rate of 1 kHz. As self-focusing limits the amplification of ultra-short laser pulses this laser system is based on chirped pulse amplification (CPA) (Strikland and Mourou, 1985). A scheme of the latest laser system is depicted in figure 1.22. The laser can be delivered in three different experimental rooms, two at the same time. During this PhD work the ocillator has been changed for delivering a broader M-shape spectrum in order to compensate for gain narrowing during further amplification steps and therewith support shorter amplified pulses. The pulses are stretched after the oscillator, still maintaining a broad spectrum. They are first amplified in a regenerative amplifier and in a final step in a four paths cryogenic amplifier. The recompression of the pulses is achieved as close as possible to the application inside each experimental room.

The grating compressor cannot compensate 2$^{\text{nd}}$ and 3$^{\text{rd}}$ order spectral phase independently (Fork et al., 1987). This would be necessary however when additional optical elements are introduced in the beam path. Table 1.2 shows the shortest possible pulses achieved with different windows after the output of the compressor. Also laser beam energy plays an important role as nonlinear propagation can induce high order phases and

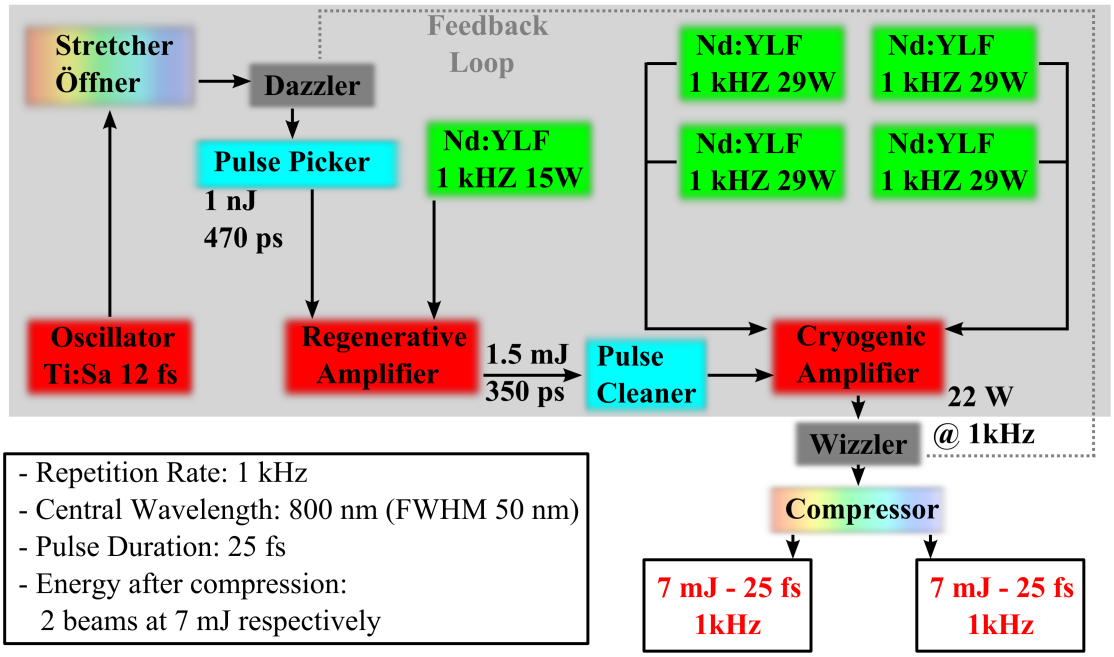


**Figure 1.22.:** Scheme of the laser system Aurore at CELIA.

cause self phase modulation (SPM).

The beam size becomes an issue at such high intensities. SPM in air leads to self-focusing and creates hot spots in the beam. This can be prevented by chosing a laser beam diameter which is large enough. The size is limited by mirror size, i.e. experimental feasability and cost, and one has to take care that no diffraction is created by laser beam. With a beam diameter ($1/e^2$) of $19.5 \pm 1$ mm a good compromise is found. Also other effects of third order nonlinearties play a role at such high intensities. Nonlinear elliptical polarization rotation (NER) is introduced in isotropic media (Jullien, 2006). The understanding of this nonlinear change in polarization state is crucial for experiments such as polarimetry (see paragraph 4.3.4). In an anisotropic medium even a cross-polarized wave (XPW) can be generated. It takes place in media with a third order nonlinearity and plays a role when optical elements are under mechanical stress.
HHG requires intensities of $10^{14}\,\mathrm{W/cm^2}$ which are achieved by focussing the laser beam into the generation medium. This requires a vacuum chamber if one wants to prevent self-focusing of the laser beam and reabsorption of the generated XUV photons by the ambient gas. In order to reach thus high intensities the beam needs to be temporally compressed with as less chirp as possible. By tuning the grating of the compressor pulse duration is minimized. This is either verified by a single-shot autocorrelator or by producing the strongest possible plasma in air with a lens. In order to reach optimal phase-matching conditions and prevent plasma dispersion, the intensity of the laser beam is adjusted by a diaphragm. The focussing is either implemented by a lens or a mirror. A lens introduces

| Input Energy (mJ) | no element | $MgF_2$ (3 mm) | + Fused Silica (2 mm) |
|---|---|---|---|
| 11 | 24.5 fs | 27.7 fs | 30 fs |
| 9 | | 25.2 fs | 29 fs |
| 7 | | 24.8 fs | 27 fs |
| 5 | | 24.4 fs | 26 fs |
| 3 | | 23.9 fs | 24.8 fs |
| Input Energy (mJ) | + $BK_7$ (10 mm) | + $BK_7$ (3 mm) | +$MgF_2$ (5 mm) |
| 11 | 41.5 fs | 31.5 fs | 35 fs |
| 8 | 37 fs | 29 fs | 33 fs |
| 7 | 36 fs | 28.6 fs | 32 fs |
| 5 | | 27 fs | 29.5 fs |
| 3 | 30 fs | 26 fs | 27 fs |

**Table 1.2.:** Laser pulse duration after the compressor at different laser pulse energies at the entrance of the compressor. The "+" sign indicates that the optical element is in combination with the compressor output window ($MgF_2$ (3 mm)). The pulses have been measured with a single shot autocorrelator.

dispersion, which cannot be completely compensated by the grating compressor and thus stretches the pulse temporally. A concave mirror overcomes this problem. However, if the angle of incidence (AOI) on this mirror is non-zero the beam focus is strongly astigmatic. The AOI is minimized on the concave mirror by minimizing the AOI on the last mirror before. Due to space issues the setup only allows the assembly of the two mirrors inside the vacuum chamber. In order to shift the focussing position they are on linear translation stage which is aligned parallel to the beam direction.

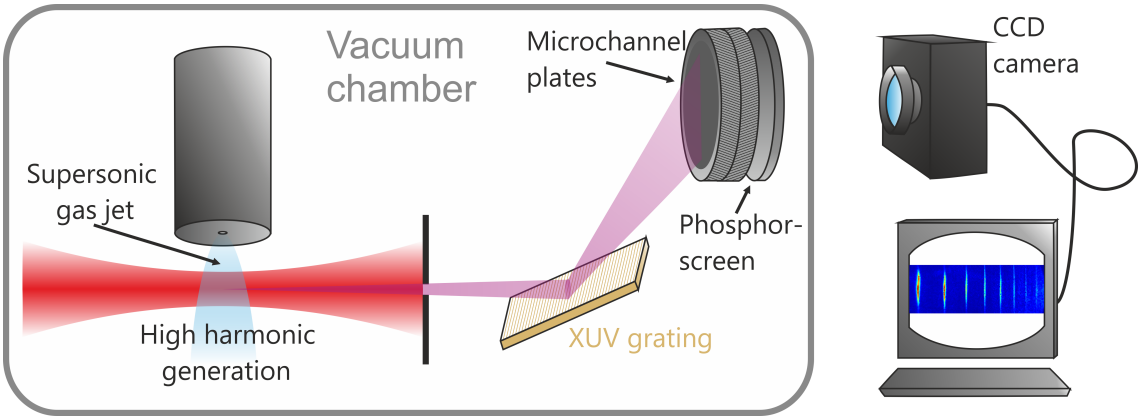


**Figure 1.23.:** Simple experimental setup for spectroscopically resolving a high harmonic spectrum.

Once the high harmonic generation is produced the spectrum is imaged by a an abberation-corrected concave grating for flat-field spectrographs (Hitachi). This setup

allows us to acquire a 2D spectro-spatial image on double microchannel plates (MCPs) (Hamamatsu) with a diameter of 40 mm. Combined with a phosphorscreen (Hamamatsu) the image is recorded onto a 12 bit CCD camera (PCO). The slit in figure 1.23 has been used to limit the infrared intensity onto the gold grating.

When working with target media of low ionization potential, the high harmonic cutoff energy is lowered and cannot be increased with intensities beyond saturation intensity. Another mean of enhancing the cutoff is a higher ponderomotive energy (see equation 1.26). By increasing the fundamental wavelength the cutoff is extended, scaling with $\lambda^2$. However the recombination efficiency is reduced, scaling with $\lambda^{-5}$ (Tate et al., 2007; Shiner et al., 2009), owing to a longer excursion time and consequently stronger spread of the electron wave packet (see equation 1.14). The experimental tool used for light conversion is the commercial high energy travelling-wave optical amplifier of white-light continuum (HE-TOPAS) (Light Conversion) used to generate pulses at wavelengths centered between 1100 nm and 2400 nm. The basic principle of this optical parametric amplifier (OPA) is as follows: Third order nonlinear response $\chi^{(3)}$ in a sapphire plate generates a white-light continuum. Even though the intensity of the new generated wavelengths is weak, these wavelengths are used as a signal beam to generate together with fundamental laser beam, called pump beam in this context, a new frequency, the idler beam (three wave mixing processes due to second order nonlinear response $\chi^{(2)}$). Three amplification stages in the HE-TOPAS ensure a sufficiently high laser intensity for the signal and idler beam. Either the idler or signal beam can be selected to work with by using a set of selective dichroic mirrors.
For the experiments during this work the HE-TOPAS was pumped with the Aurore Ti:Sa-Laser system in the old configuration, i.e. a pulse duration of 35 fs and an energy of 4.7 mJ at 800 nm. When working with the idler beam at 1900 nm, 800 $\mu$J could be extracted with an intensity stability of 6 % rms and a pulse duration of 50 fs. The signal beam delivered 1 mJ at a central wavelength of 1300 nm.

## 1.6. An Example: The Cooper Minimum in Argon

Now as the basics of HHG are established a first application will be presented: the Cooper minimum in argon. The first observations of the Cooper minimum are reported in the photoionization cross section (Cooper, 1962). It originates from the zero dipole moment between the $p$ ground-state wave function and the $d$ wave function of the photoionized electron. The minimum provides a simple test of the influence of the electronic structure of atoms on the shape of the harmonic spectrum. Its observation permits an insight in the structural signature of the atomic valence shell. When HHG was still in the egg it was reobserved in HHG by Wahlström and coworkers (Wahlström et al., 1993). The position of the Cooper minimum has not been tested until recently (Wörner et al., 2009). This minimum also proves as a an ideal sample to corroborate CTMC-QUEST. An excellent

agreement is found between CTMC-QUEST and experiment: 53.7 eV for the theoretical value and $53.8 \pm 0.7$ eV for the experimental minimum (Higuet et al., 2011).
First of all photoionization and radiative recombination are compared to each other as the Cooper minimum was observed in both processes. Also experimental setup for HHG is presented in detail. The position of the Cooper minimum is studied for different experimental conditions. Finally a comparison is addressed between experimental and theoretical results obtained by CTMC-QUEST.

### 1.6.1. Photoionization and Radiative Recombination

The position of the Cooper minimum measured in the high harmonic spectrum ($53 \pm 3$ eV (Wörner et al., 2009)) and the photoionization spectrum (48 eV - 49 eV (Marr and West, 1976; Chan et al., 1992; Samson and Stolte, 2002)) are different. As both processes can be connected by the microreversibility principle to each other this appears to be strange at first sight. In a first study the total photoionization cross section is compared to the recombination matrix element.
Similarly to Lewenstein model the SAE is applied, only considering one single valence electron playing a role during photon electron interaction. The effective model potential of argon is spherically symmetric (Muller, 1999):

$$V(r) = -\frac{1}{r} - \frac{Ae^{-Br} + (17 - A)e^{-Cr}}{r} \tag{1.43}$$

with $A = 5.4$, $B = 1$, and $C = 3.682$. Similarly to the hydrogen atom, the basis of the eigenstates $\psi_{n,l,m}(\vec{r})$ can be developped as the product of spherical harmonics $Y_l^m(\Omega)$ and a radial part $R_{n,l}(r)$. The knowledge of the wavefunctions in the argon atom is important for the calculation of the photoionization rate induced by absorption which is determined by Fermi's golden rule (Cohen-Tannoudji et al., 1996).

$$w(\vec{k},\vec{n}) = \frac{\pi}{2} k \left\langle \psi_{\vec{k}} \right| \mathcal{D} \left| \psi_{3,1,0} \right\rangle^2 \tag{1.44}$$

where $\mathcal{D} = -E\vec{n}\vec{r}$ is the electric dipole moment operator, $\psi_{3,1,0}$ refers to the ground state of the valence electron and $\psi_{\vec{k}}$ to the scattering continuum states of the electron. In the Lewenstein model the scattering states were approximated by plane waves (see equation 1.17). This Ansatz does not take into account the form of the scattering potential of the argon atom. A spherical model potential allows us to develop the scattering states in the spherical state basis of the eigenstates of the argon atom and therewith take this one into account.
Due to the selection rules of the electric dipole transition moment ($\Delta l = \pm 1$) only two scattering continuum states $\psi_{\vec{k}}$ contribute, with angular momenta $l = 0$ ($p \rightarrow s$) and $l = 2$ ($p \rightarrow d$). This leads to a simple analytical expression for the total photoionization cross section which is integrated over the full solid angle $4\pi$:

$$\sigma(k) = \frac{16\pi^3\omega}{9kc}(I_{k,0}^2 + 2I_{k,2}^2) \tag{1.45}$$

with c the speed of light and $I_{k,l}$ the radial integrals $I_{k,l} = \int R_{k,l}(r)R_{3,1}(r)r^3dr$. The two radial integrals are shown in figure 1.24(a). When $I_{k,2} = 0$ the total photoionization cross section adopts a minimum which is responsible for the Cooper minimum observed in photoionization (Cooper, 1962). The Cooper minimum of this calculation appears at 50.1 eV and agrees quite well with the minimum measured between 48 eV and 49 eV (Marr and West, 1976; Chan et al., 1992; Samson and Stolte, 2002).
In case of the recombination matrix element for HHG it has to be considered that tunnel ionization and recombination parallel to the field polarization are highly direction selective. The recombination matrix element can be written:

$$\begin{aligned} |d_{rec}|^2 &= |\langle\psi_{\vec{k}}|\,\vec{n}\vec{r}\,|\psi_{3,1,0}\rangle|^2 \\ &= \frac{1}{12\pi k^2}|I_{k,0}e^{i\delta_{k,0}} - 2I_{k,2}e^{i\delta_{k,2}}|^2 \end{aligned} \tag{1.46}$$

where $\delta_{k,l}$ is the rescattering phase. The results from photoionization and radiative recombination are compared in figure 1.24(b). The minimum from photoionization is clearly less pronounced at an energy of 50.1 eV than the minimum for the recombination dipole moment which is located at 51.6 eV. This difference can be justified by the selection of quantization axis through the polarization of direction of the electric field for the case of HHG. The calculated minimum from plane wave functions is situated at 21 eV (Wörner et al., 2009).

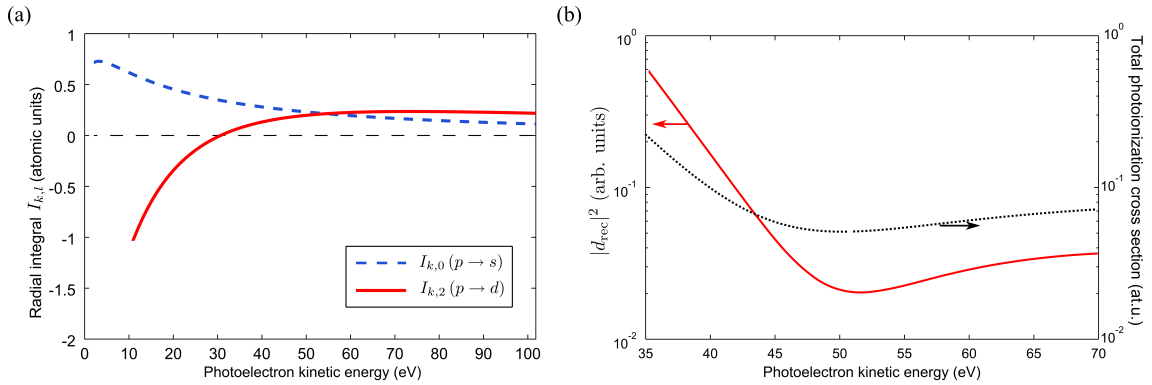


**Figure 1.24.:** (a) Radial integrals $I_{k,l}$. (b) Comparison of the recombination matrix element (red solid line) and the total ionization cross section (dotted black line).

### 1.6.2. Experimental Setup

Observing the Cooper minimum in HHG spectra around 50 eV would require high intensities ($\approx 2 \times 10^{14}\,\mathrm{W/cm^2}$) at a fundamental wavelength of 800 nm. At a pulse duration

of 40 fs the medium would be completely ionized before reaching the maximum intensity. Wörner and coworkers avoid saturation by using pulse durations of 8 fs at 780 nm (Wörner et al., 2009). Another possibility is the extension of the generation wavelength. According to the cutoff law ($h\nu_{max} \propto I\lambda^2$ see equation 1.26) higher energies can become accessible. This permits the generation of high harmonics at intensities below saturation. Extending the fundamental wavelength has another advantage: The resolution of the Cooper minimum is enhanced from 3.1 eV (800 nm) to 1.4 eV (1800 nm) as the separation between the harmonic orders is decreased ($\Delta\omega = 2\omega_{gen}$).

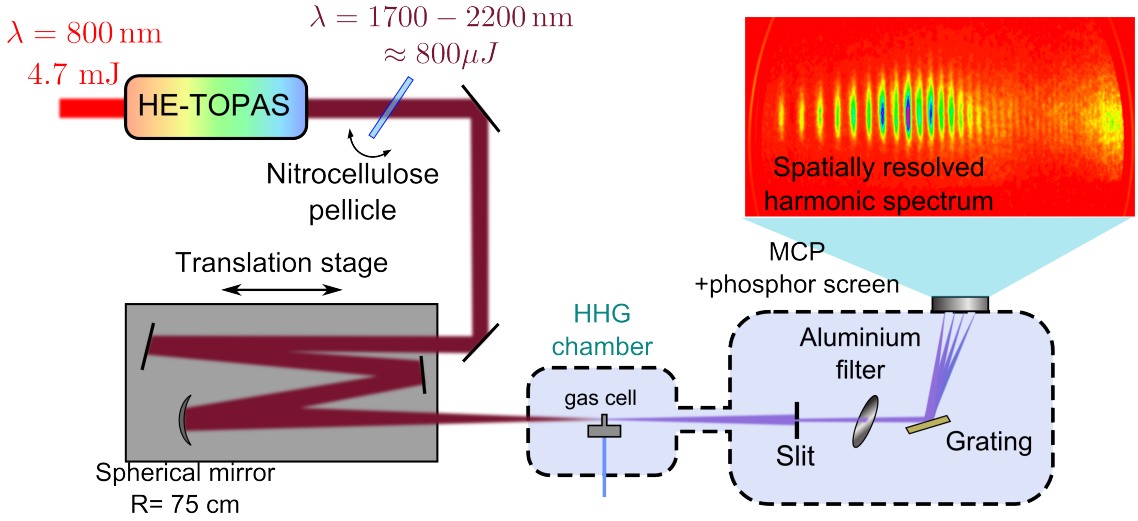


**Figure 1.25.:** Experimental setup used for detection of the Cooper minimum.

The experimental setup is shown in figure 1.25. The laser system and the HE-TOPAS which are used in the experiment are presented in section 1.5.4 (see also (Higuet, 2010) for more details). The energy of the long wavelength pulses delivered by the HE-TOPAS is adjusted by rotating a 30 $\mu$m thick nitrocellulose pellicle. By rotating the pellicle the transmission can be varied between 95 % at normal incidence and 50 % under 70° angle of incidence. The laser beam is focused by a silver mirror with a radius of curvature of 75 cm into a 2 mm continuous gas cell filled with argon. We use the spectrometer presented in section 1.5.4. An additional aluminium filter is inserted in this setup.
Also the second order of the gold grating is diffracted on the MCPs in such a way that the detected spectrum is a superposition of the 1$^{st}$ order and 2$^{nd}$ order diffraction. Photons at energies around 100 eV (2$^{nd}$ order) overlap at the position of the Cooper minimum at around 50 eV (1$^{st}$ order) and shift the position of the minimum to higher energies. An aluminium filter is therefore inserted in front of the spectrometer to block harmonics with energies beyond 73 eV (CXRO, 2012), thus suppressing the contribution of the 2$^{nd}$ order diffraction near the spectral position of the Cooper minimum. Indeed a superposition of the 1$^{st}$ order and 2$^{nd}$ order of the spectra may only occur below $73/2$ eV $= 36.5$ eV.
Finally an accurate calibration of the XUV spectrometer is an important point, allowing

us to assign absolute values to the scale of the frequency spectrum. The generation wavelength $\lambda_0$ is known, the spectral distance between each harmonic order $q$ follows a $\lambda_0/q$ law. Fitting the experimental data to this dependence can be ambiguous. Therefore the final verification of this calibration is a comparison to the abrupt cutoff of the aluminium filter observed in the spectrum at 73 eV.

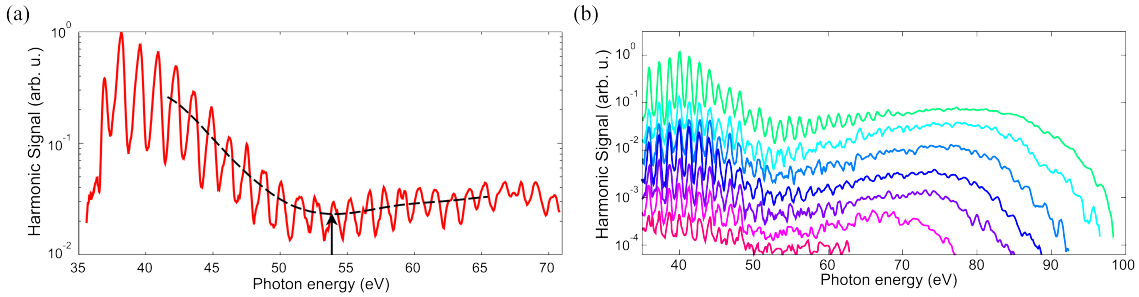


**Figure 1.26.:** (a) High harmonic spectrum in argon averaged over 25000 laser shots. The Cooper minimum is identified at 53.8 eV with the following laser parameters: $\lambda_{gen} = 1830$ nm, $I = 8 \times 10^{13}$ W/cm$^2$, $\tau^* = 50$ fs. (b) High harmonic spectra in the same conditions. The intensity is decreasing from $I = 8 \times 10^{13}$ W/cm$^2$ (top green line) to $I = 5 \times 10^{13}$ W/cm$^2$ (bottom violet line).

### 1.6.3. Experimental Results

The position of the Cooper minimum might depend on several parameters. Not only the sensitivity to the single atom response but also to macroscopic response has to be tested. Figure 1.26(a) shows typical spectrum and an envelope obtained by convoluting the spectrum with a Gaussian function. The width has more than twice the harmonic energy. The minimum corresponds to the Cooper minimum. Figure 1.26(b) depicts spectra at different intensities. The Cooper minimum is extracted and plotted in figure 1.27(a). The same procedure is carried out as a function of laser wavelength (see part (b)). Within the error bars the Cooper minimum remains at the same position: 53.8 eV. This is an indication that the strong laser field does not play an important role during the recombination process. This is important to note as a strong field might induce a Stark shift that can be neglected.

The macroscopic response of the medium is studied by varying phase matching conditions such as backing pressure, laser beam aperature and laser focus position. Figure 1.28 shows the position of Cooper minimum as a function of these three parameters. Within the error bars the minimum is observed around 53.8 eV and does not move. Consequently the minimum does not depend on macroscopic generation conditions over the ranges investigated. This means that the signature of the single atom response is accessible in the harmonic signal. Note furthermore that the harmonic signal remains nicely collimated which indicates that only the signal from short trajectories has been observed. The signal

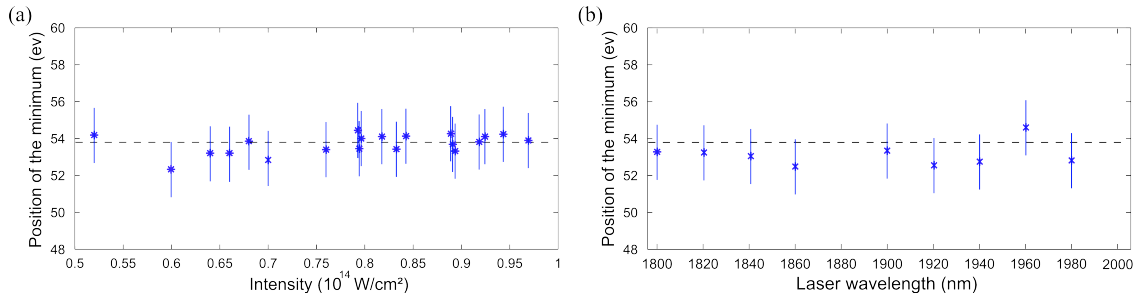


**Figure 1.27.:** Position of Cooper minimum as a function of (a) laser intensity and (b) laser wavelength.

from the long trajectories gets lost as the recombining electron wave packet spreads too much during its time of flight (Tempea and Brabec, 2000). However it has to be mentioned that Farrell and coworkers report contradictory results (Farrell et al., 2011). They also record the long trajectories at a generation wavelength of 800 nm and observed a variation of the shape of the Cooper minimum.

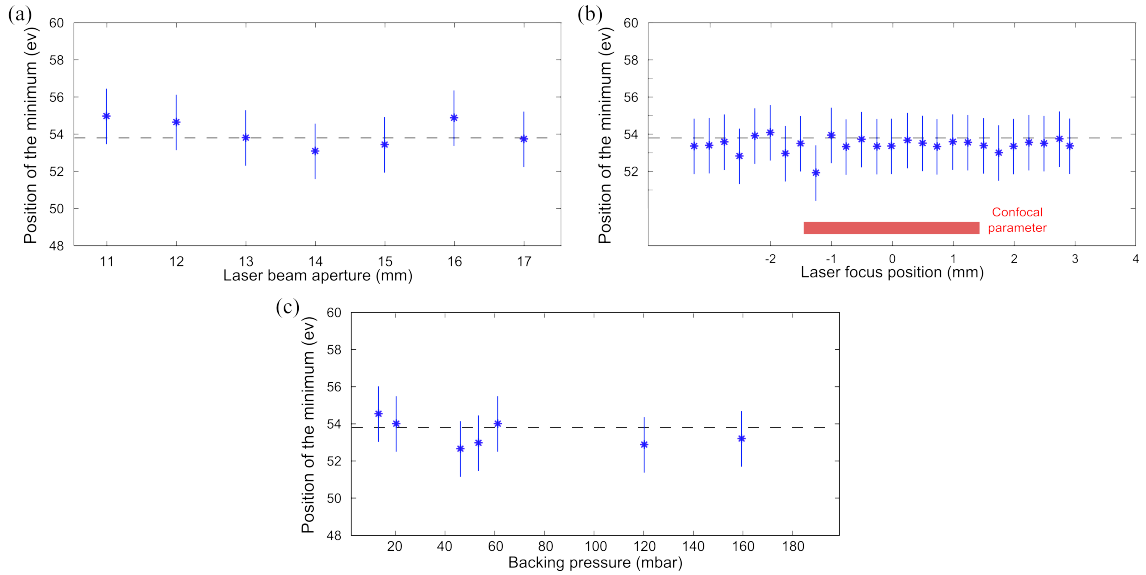


**Figure 1.28.:** Cooper minimum as a function of (a) laser beam aperature, laser focus position and (c) backing pressure.

In a final experimental study the importance of electron recollision angle is emphasized. By using an elliptically polarized laser field the recollision direction of the electron can be controlled. In a first simple approach the recollision angle is calculated within the framework of the three step model. By assuming nonzero perpendicular initial velocities of the electrons having escaped the core potential, the classical electron trajectories can be closed in an elliptical polarized laser field. The new recollision angle changes the

recombination matrix element defined in equation 1.46 which needs to be reevaluated with respect to a new quantization axis. The analysis of the theoretical outcome shows that the shape of the minimum changes with increasing laser ellipticty. As can be observed in figure 1.29(a) the Cooper minimum broadens towards high energies in reasonable agreement with the experimental measurements presented figure 1.29(b). Note however that there is a slight shift between the position of the experimental and theoretical Cooper minimum. This originates from the fact that not only the recombination matrix element needs to be taken into account, but also the density of returning electrons at a certain energy. These experimental outcomes can now be compared to calculations of CTMC-QUEST.

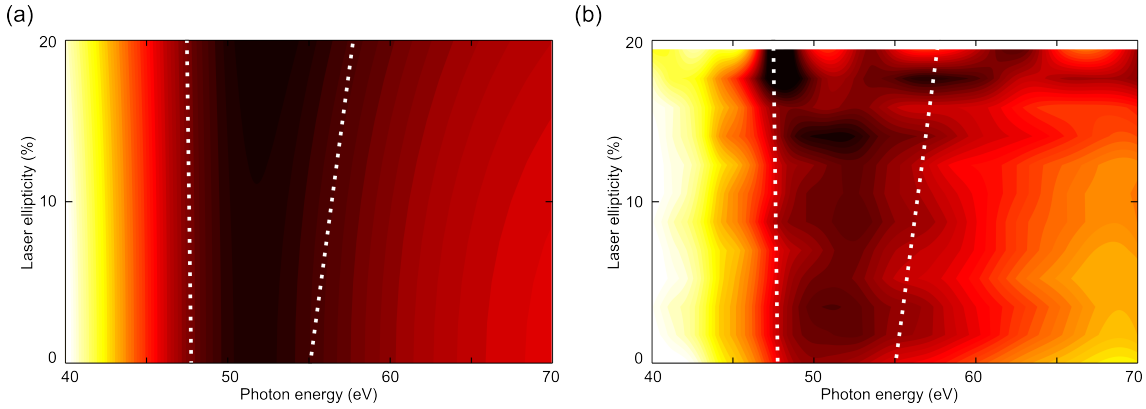


**Figure 1.29.:** (a) Calculation of $|d_{rec}|^2$ as a function of photon energy and ellipticity and (b) the measured harmonic spectra under same conditions ($\lambda = 1900$nm, $I = 10^{14}\,W/cm^2$).

### 1.6.4. Comparison with CTMC-QUEST

The theoretical anaylsis of the Cooper minimum in argon is implemented by CTMC-QUEST which includes the different contributions to the harmonic spectrum (see equation 1.32). CTMCT-QUEST does not only consider the photorecombination probability given by Fermi's golden rule (see equation 1.31) but also the density of returning electrons, i.e. the shape of the electron wave packet. Numerical calculations finally evaluate the harmonic spectrum determined by equation 1.32.
Figure 1.30(b) shows that the calculated position of the minimum depends on the trajectory family: long or short. As the density of returning electrons is different, the Cooper minimum is shifted for the two spectra. It is located at 51.7 eV for long and 53.7 eV for short trajectories. Neglecting the density of returning electrons (see figure 1.15(b)) results in a shift of the Cooper minimum. This is illustrated in figure 1.30(a) where the statistical distribution of the returning electron (thus neglecting their energy dependent density) shows a minimum at $51.7 \pm 0.5$ eV lower than the one observed for the CTMC-QUEST calculation ($53.5 \pm 0.5$ eV).

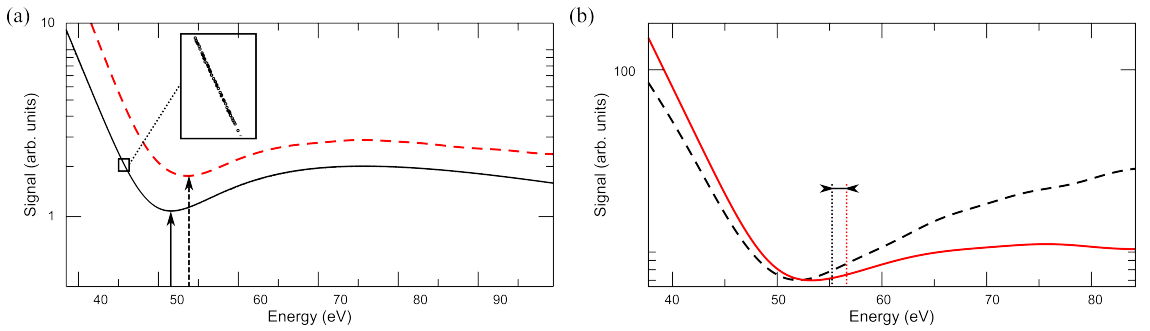


**Figure 1.30.:** (a) Comparision between the shape of the spectrum calculated with CTMC-QUEST (red dashed line) and statistical distribution of recombination probabilities (scattered points, that appear like a solid line). (b) Harmonic spectrum calculated with CTMC-QUEST taking into account only the long (dashed black line) or short (red solid line) electron trajectories.

Finally figure 1.31(a) compares experimental and theoretical spectra under same laser field conditions. It shows a very good agreement between the Cooper minimum obtained by CTMC-QUEST at 53.7 eV and the experimental spectrum at $53.8 \pm 0.8$ eV. Not only is the theoretical result consistent with the experimental measurement within the error bars, but also the shapes of the two spectra are similar. Furthermore the theoretical calculated spectrum does almost not shift when changing laser intensity what coincides with the measurements presented in figure 1.27. Only at the lowest intensity the minimum is slightly shifted what can be interpreted as a different energy distribution of the returning electron wave packet.
In summary one can say that CTMC-QUEST prooves to be a good tool for describing HHG in argon. The Cooper minimum, orginating from the electronic structure of atoms can be very well reproduced by the calculations, the agreement is almost perfect. Moreover this method is selective on the trajectory family allowing the discrimination of the experimental results.

## 1.7. Summary

The chapter begins with the theoretical introduction of HHG for the single atom response. The classical three step and the quantum model referred to the strong field approximation are presented. Both models neglect the influence of the ionic core during the time of flight of the free electron. A new model, CTMC-QUEST, based on a semiclassical theoretical approach has been developped taking into acount the core potential. Again it can be divided in three steps and thus avoids approximate calculations for the electron wave packet.
Under experimental conditions, high harmonic emission in a gas is generated in many atoms. Thus macroscopic effects such as phase matching and reabsorption need to be

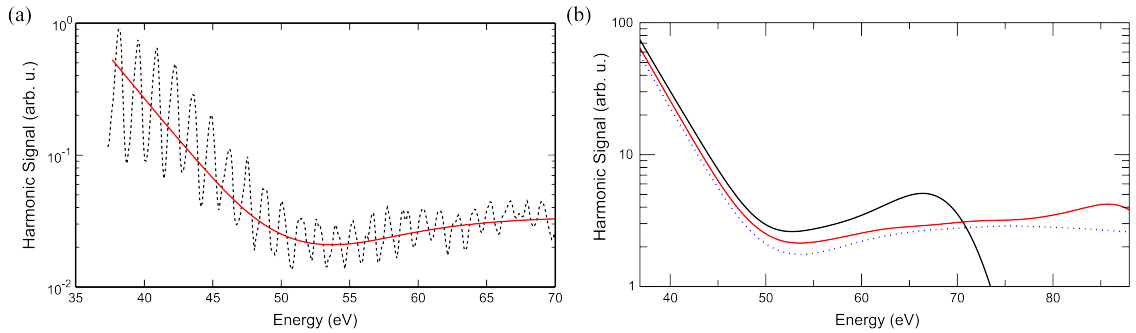


**Figure 1.31.:** (a) Cooper minimum calculated with CTMC-QUEST (solid red line) and experimental spectrum obtained at a wavelength of 1830 nm and intensity of $10^{14}\,\mathrm{W/cm^2}$ (dashed black line). (b) CTMC-QUEST calculation at 1830 nm at an intensity of $\mathrm{I} = 5 \times 10^{13}\,\mathrm{W/cm^2}$ (solid black line), $\mathrm{I} = 7.5 \times 10^{13}\,\mathrm{W/cm^2}$ (dashed red line) and $\mathrm{I} = 1 \times 10^{13}\,\mathrm{W/cm^2}$ (dotted blue line).

considered. Furthermore the high harmonic spectrum reveals an on axis signal and an off axis signal which is attributed to the short and long electron trajectories respectively. Phase matching rings in the spectrum might be interpreted in terms of Maker fringes.
Finally CTMC-QUEST is applied a first time in the Cooper minimum in argon. This minimum originates from the zero dipole moment between the $p$ ground-state wave function and the $d$ wave function of the photoionized electron. This minimum which has already been observed in photoionization is revealed by HHG. This is an important property, it proves that HHG is sensitive to orbital structure. We measured the minimum at $53.8 \pm 0.7$ eV wheras it occurs between 48 eV and 49 eV for the total photoionization cross sections. The experimental study was performed with the TOPAS, a parametric amplifier delivering pulses at 1800 nm. By using a high fundamental wavelength the precision of the Cooper minimum position is improved. With variation of the gas pressure, the focusing condition and the laser intensity the minimum did not move.
The different position of the Cooper minimum is owed to two effects. First the recombination process is the inverse to photoionization, however the recombination angle needs to be taken into account for the latter. Second the density of the returning electrons plays an important role for the recombining electrons. The shape of the experimental and theoretical spectra and the experimental position of the minimum ($53.8 \pm 0.7$ eV) the theoretical one (53.7 eV) match very well. Extending CTMC-QUEST to elliptically polarized pulses and molecules will prove if this method can be applied with the same success and overcome the difficulties encountered in quantum calculations.

## Résumé du Chapitre

*Depuis l'observation d'harmoniques d'ordre élevé dans des milieux gazeux (McPherson et al., 1987; Ferray et al., 1988), la génération d'harmoniques d'ordre élevé (GHOE) a démontré son importance, en permettant l'essort de la science attoseconde. La GHOE est réalisée en focalisant une impulsion laser femtoseconde à des éclairements intenses ($\approx 10^{14}$ W/cm$^2$) dans un gaz atomique ou moléculaire. Le spectre peut être très large, permettant des impulsions très courtes jusqu'à 67 as dans une impulsion isolée avec une largeur de bande de 75 eV (Zhao et al., 2012). L'émission est cohérente avec un angle de divergence limité de l'ordre du 2 mrad à 10 mrad et une polarisation bien définie. L'emission s'effectue sous forme d'un peigne de fréquences impaires de la fréquence fondamentale. Contrairement à la génération de seconde harmonique (Franken et al., 1961), la GHOE ne peut pas être décrite par la théorie de la perturbation. Seules les harmoniques les plus basses dépendent de l'ordre du processus multiphotonique alors que l'efficacité de conversion est presque constante dans la région du plateau (Ferray et al., 1988; Li et al., 1989). Le signal décroit finalement rapidement au delà d'une fréquence de coupure abrupte, le "cutoff".*

*Une autre application émergente qui fait l'objet de cette thèse est la spectroscopie optique extrêmement non linéaire (extreme non-linear optical spectroscopy: ENLOS). Dans ce contexte, la GHOE est utilisée comme sonde du système atomique ou moléculaire pour obtenir une information structurelle et dynamique. Le méchanisme caractéristique qui est exploité est la recollision du paquet d'onde électronique, la dernière étape de la GHOE. Cet auto-sondage est un concept fondamental dans ce travail: en se recombinant, le paquet d'onde électronique "interfère" avec la fonction d'onde de l'ion parent. Le dipole résultant émet des harmoniques d'ordre élevé qui encodent l'information de façon structurelle et dynamique sur l'orbitale.*

*Dans une première partie nous introduisons le modèle semi-classique à trois étapes qui décrit le processus de GHOE par un atome unique (Corkum, 1993; Schafer et al., 1993). Ce modèle présente néanmoins quelques défauts, comme, par exemple de mal prédire l'instant d'ionisation des électrons (Shafir et al., 2012b). Lewenstein a développé une théorie quantique qui présente un meilleur accord quantitatif avec les observations expérimentales (Lewenstein et al., 1994). Néanmois ce modèle ne prend pas en compte le potentiel ionique du noyau non plus. Pour prendre en compte les effets du potentiel ionique Fabre et Pons ont développé une nouvelle méthode basée sure une approche semiclassique: "Classical Trajectory Monte Carlo Quantum Electron Scattering Theory" (CTMC-QUEST) (Higuet et al., 2011). Contrairement aux deux modèles précédents, celui-ci reproduit bien un minimum structurel dans l'atome de l'argon: le minimum de Cooper. Ce minimum était prédit en théorie dans les sections efficaces de photoionisation des orbitales de valence (Cooper, 1962). Comme ces sections efficaces de photoionisation sont directement liées aux éléments de matrice de recombinaison ce minimum était effectivement observé dans les spectres harmoniques (Wahlström et al., 1993). Les*

*calculs de CTMC-QUEST montrent une position de minimum de Cooper à 53.7 eV qui est en bon accord de la position du minimum de Cooper observé experimentalement 53.8 ± 0.7 eV. CTMC-QUEST a été aussi appliqué pour calculer l'angle de la polarisation des harmoniques produites dans l'argon par un champ elliptique (Shafir et al., 2012a). Cette étude a montré que le calcul est seulement en bon accord avec l'observation experimentale si le potentiel ionique est pris en compte. CTMC-QUEST est par conséquent une méthode prometteuse moins exigeante en moyens de calculs et donc envisageable pour simuler des interactions avec des molécules plus grandes.*

# 2. High Harmonic Generation in strongly aligned Molecules

The previous chapter illustrated how the signature of the electronic structure of atoms can be decoded by HHG. How can this self-probing scheme be extended to molecules? In atoms a coherent signal is generated. Owing to the isotropy of the atoms, the emitted radiation is identical for each of them. In the case of molecules this is not necessarily the case, the amplitude and the phase of the signal emitted from each molecule can be different, depending on the orientation of each molecule. Indeed the ionization probability and the radiative recombination dipole moments vary as molecular orientation changes with respect to laser polarization. The following question arises consequently: How can this macroscopic isotropy be cracked for accessing anisotropic properties of single molecules? Different methods have been established for achieving molecular alignment: collisional processes, static electric fields or optical fields (Stapelfeldt and Seideman, 2003). The disadvantage of the first two techniques is however, that they can only be applied in very specific cases. The last method is rather unusual: a short strong laser field forces the molecules to align shortly after excitation (prompt alignment). A revival structure of aligned rotational wave packets has been predicted (Seideman, 1999) and been demonstrated shortly afterwards experimentally (Rosca-Pruna and Vrakking, 2001). The rotational wave packets revive at regular intervals which leads to a field-free alignment of the molecules. This field-free alignment permits the implementation of the self-probing scheme in molecules.

Yu and cowokers first predicted that high harmonic spectra in $H_2$ and $H_2^+$ encode the information of the molecular structure (Yu and Bandrauk, 1995). Several years later experiments were undertaken which proved a sensitivity of HHG towards orientation and the molecular axis (Velotta et al., 2001; de Nalda et al., 2004). Orbital reconstruction was pushed to its limits by the tomographic imaging of the highest occupied molecular orbital (HOMO) of nitrogen (Itatani et al., 2004). One year later minima have been observed in carbon dioxide molecules located at different positions (Kanai et al., 2005; Vozzi et al., 2005a). This minimum was identified as a dynamical minimum resulting from the interference between different channels. Smirnova and coworkers were able to retrieve structural and dynamical information in carbon dioxide in order to disentangle the multichannel contribution (Smirnova et al., 2009b,a). They disentangled the contribution of different channels to the high harmonic spectrum and were able to trace the hole left behind after ionization on a sub-femtosecond timescale. By controlling the molecular alignment angle a change of the hole dynamics is observed.

Two other groups have not observed this multichannel interference. Lock and coworkers

claim that lower lying orbitals of carbon dioxide and dinitrogen oxide do not contribute to HHG (Lock et al., 2009). Two-center interference is responsible for the observed high harmonic emission. Lower lying channels can apparently be neglected. Also Vozzi and coworkers have not observed a dynamical minimum in carbon dioxide at generation wavelengths of 1450 nm to 1700 nm. They therefore excluded contributions from different channels and were able to perform the tomographic reconstruction of the HOMO of carbon dioxide (Vozzi et al., 2011).
Wörner and coworkers also observed a dynamical minimum in carbon dioxide wheras the one from nitrogen is claimed to be structural (Wörner et al., 2010). Furthermore substantial subcycle transitions have been observed in nitrogen by Mairesse and coworkers, revealing a coupling between different channels (Mairesse et al., 2010). An analysis of the relative phases involved in HHG between the different channels strongly suggests an electron rearrangement during ionization.
The results obtained by HHG have one important constraint, they are dealing with an imperfect degree of alignment. Molecular alignment induced by a strong laser pulse is performed in a macroscopic ensemble of molecules, which can never be completely aligned. The molecules adopt a certain alignment distribution and thus the high harmonic signal only gives an average response of this distribution. Different approaches were developped for extracting the single atom response (Wagner et al., 2007; Akagi et al., 2009; Yoshii et al., 2011). Deconvolution of the angular distribution can be reached through an iterative procedure. This method is limited however, it only takes into account the variation of the field amplitude as the molecule is rotated and not the variation of the phase.
We chose a different method, directly attacking the root of the problem. To achieve a high degree of molecular alignment the molecules must be rotationally cold before excitation. This can be achieved by using a supersonic molecular gas jet. In order to obtain the coldest rotational distribution required for creating the best alignment of the molecular axis, we have used a strongly collimated supersonic expansion (Even-Lavie jet (Luria et al., 2011)) which enables us to generate high harmonics at a distance of 42 nozzle diameters from the nozzle. This results in an estimated rotational temperature of 5 K. A highly improved alignment distribution is obtained with this technique, setting a new standard for HHG in aligned molecules.
This chapter summarizes the theory of molecular alignment and rotational revivals. Alignment has been performed for two small linear molecules, carbon dioxide and nitrogen. Experimental results in carbon dioxide reveal features at low temperatures which have not yet been observed before. These should permit to draw new conclusions on the interplay between the different channels and therewith the hole dynamics. Owing to the higher degree of alignment a higher resolution is reached for the harmonic signal from nitrogen, measured as a function of molecular angle. This reveals a shape resonance predicted theoretically in molecular nitrogen (Jin et al., 2012).

## 2.1. Field-free Molecular Alignment by Laser Pulses

Molecules in a molecular gas jet are randomly oriented. They can be aligned by using strong laser pulses. Depending on the orientation of the molecule with respect to the polarization direction of the laser field the force induced on the molecule is different. Linear symmetric molecules experience the strongest torque if its principal axis is perpendicular to the field polarization. In contrast the molecule is unaffected if the principal axis is parallel to laser polarization. Thus the molecular axis are forced to similar orientations. This molecular ensemble could now directly be probed by a second pulse. Two different techniques were established, adiabatic alignment with picosecond pulses (Friedrich and Herschbach, 1995; Seideman, 1995) and nonadiabatic (impulsive) alignment with femtosecond pulses (Rosca-Pruna and Vrakking, 2001). The former method shows a higher degree of alignment than the latter method for the same laser intensities (Torres et al., 2005). Impulsive alignment has a great advantage however. Owing to the revival structure of the rotationally excited wavepacket, field-free alignment is accomplished. This is important as the two fields disrupt each other if they overlap: HHG and the creation of a rotationally excited wavepacket are perturbed.
The electric field $\vec{E}$ of the laser induces a dipole moment $\vec{\mu} = \alpha \cdot \vec{E}$. The polarizability $\alpha$ is orientation dependent and is therefore represented by a tensor. The value along the most polarizable axis is labelled $\alpha_\parallel$ and $\alpha_\perp$ along the second most polarizable axis, which is perpendicular to the former axis. In case of a linear molecule the least polarizable axis coincides with the second most polarizable one $\alpha_\perp$ and $\alpha_\parallel > \alpha_\perp$. Each molecule acquires an additional potential energy $U = -(\vec{\alpha} \cdot \vec{E}) \cdot \vec{E}$ which only depends on the angle $\theta$ between the field and the molecule's principal axis. At nonresonant frequencies, well below the electronic transition energies, the field-matter interaction is governed by the potential U only taking into account the angle-dependent term[1] (Stapelfeldt and Seideman, 2003; Rouzée, 2007):

$$U = -\frac{1}{4} E_0^2 f^2(t)(\alpha_\parallel - \alpha_\perp)\cos^2(\theta) = -U_0(t)\cos^2\theta \tag{2.1}$$

where $f(t)$ is the envelope of the laser pulse with a maximum field strength $E_0$. The torque exerted by this potential is $-dU/d\theta$. It will force the molecules to align with their principal axis along the polarization direction. In other words the angular dependent potential well adopts a minimum for parallel alignment.

### 2.1.1. Rotational Wave Packets

In quantum mechanics classical particles are represented by wavepackets formed by the coherent superposition of quantum states. The idea of a wavepacket is found for many other applications in physics and chemistry (Stolow, 1998). The notion of a rotational wave packet can be understood by describing the molecules in terms of rigid rotors. The

[1] Atomic units are used in this chapter.

rotational eigenenergies are calculated applying the rotational energy operator $B\mathbf{J}^2$ on the angular part of the nuclear wavefunction $\psi(\theta,\phi,t)$. The eigenenergies of this operator are spaced as $B\mathbf{J}^2 = B_0 J(J+1)$ with $J$ the angular quantum number (classical equivalent: angular momentum) being a positive integer and $B_0$ being the rotational constant. The eigenfunctions of the rotational operator are the spherical harmonics $Y_J^M(\theta,\varphi)$, with the magnetic quantum number $M$. $M$ is the projection of $J$ with respect to the electric field and adopts the following values: $M = -J, -J+1, ..., J-1, J$. The evolution of $\psi(\theta,\phi,t)$ taking into account the nonresonant interaction with the laser field is finally governed by (Dooley et al., 2003):

$$i\frac{\partial}{\partial t}\psi(\theta,\phi,t) = [B\mathbf{J}^2 - U_0(t)\cos^2\theta]\psi(\theta,\phi,t) \tag{2.2}$$

As the molecules rotate their bonds stretch, i.e. the rigid rotor is only an idealization. This leads to an increase of angular momentum which is corrected as $E_J = B\mathbf{J}^2 = B_0 J(J+1) - D_0[J(J+1)]^2$ with $D_0/B_0 \approx 10^{-6}-10^{-4}$. The equation is solved numerically by a program written by Weber (Weber, 2007). The coupled linear differential equations are solved for the different angular quantum numbers using a fourth-order Runge Kutta algorithm. The interaction term $-U_0(t)\cos^2(\theta)$ couples the eigenstates $J \rightarrow J+2$ and $J \rightarrow J-2$. In other words, Raman transitions lead to the population of higher states with an equal distance of $J = 2$ leading to the creation of a rotational wave packet. Different $M$-states remain uncoupled.

In a molecular gas jet the rotational temperature distribution is quite broad. The weights of the original rotational state population is governed by the Boltzmann distribution:

$$P_J \propto g_J(2J+1)e^{-E_J/k_B T_{rot}} \tag{2.3}$$

where $g_J$ is a parameter which is different for even or odd $J$-states and $T_{rot}$ the rotational temperature of the molecules. The cooler the initial rotational temperature, the lower the number of original populated states (see equation 2.5). Thus revivals are more pronounced at low than at high temperatures. Figure 2.1 depicts the Boltzmann distributions for the different rotational temperatures in nitrogen and carbon dioxide.

If the pulse envelope $f(t)$ has a pulse duration on the order of the rotational period of the molecules, these will be trapped by the potential $U = -U_0(t)\cos^2\theta$. When the pulse has passed by, the alignment gets lost. In contrast to adiabatic alignment, short laser pulses ($\approx$ 100 fs) are used in case of impulsive alignment. Such a laser pulse gives the molecules a short kick, with a force proportional to the induced dipole moment. The molecules are therewith aligned shortly after the laser pulse. Prompt alignment cannot be used for HHG as probe and pumb-beams still overlap temporarily. High harmonics are therefore generated at the rotational revival of the wave packet. The full revival occurs at a time delay $\Delta t = T_{rot} = \pi/B_0$, the wave packet revives exactly to its original one. As the revival times are (see table 2.1) much higher than the duration of the pump pulse, HHG can be accomplished without disruption of the pump beam (field free).

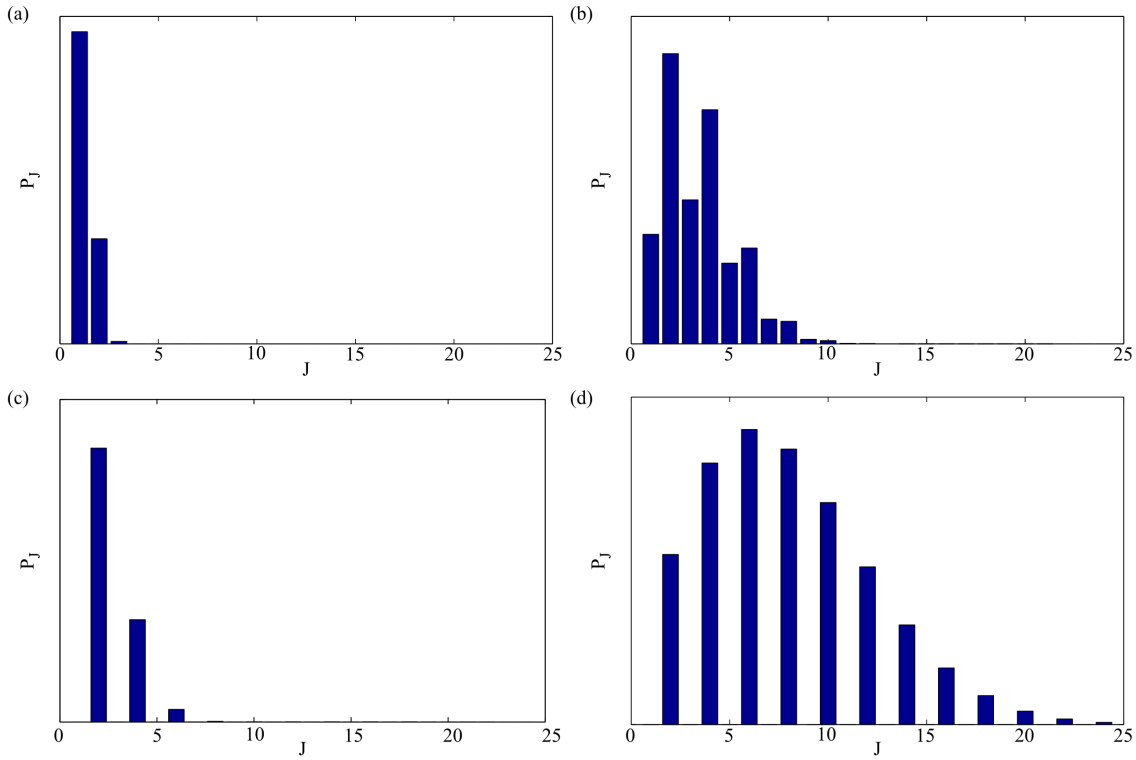


**Figure 2.1.:** Boltzmann distributions of rotational states J, at different rotational temperatures for nitrogen at (a) 5 K and (b) 50 K and carbon dioxide at (c) 5 K and (d) 50 K.

| Molecule | $B_0$ ($\mathrm{cm}^{-1}$) | $D_0$ ($\mathrm{cm}^{-1}$) | $\alpha_\parallel - \alpha_\perp$ ($\mathrm{Å}^3$) | $g_e$ | $g_o$ | $T_{rot}$ (ps) |
|---|---|---|---|---|---|---|
| $N_2$ | 1.99 | $5.7 \times 10^{-6}$ | 1.0 | 2 | 1 | 8.38 |
| $CO_2$ | 0.39 | $1.3 \times 10^{-7}$ | 2.0 | 1 | 0 | 42.7 |

**Table 2.1.:** Rotational constants for nitrogen and carbon dioxide (NIST, 2012).

The degree of alignment is given conventionally by the statistical average over the following expectation value (Rouzée, 2007):

$$\begin{aligned}\langle\langle\cos^2\theta\rangle\rangle_{stat}(t) &= \langle\langle\Psi_{J_0,M_0}|\cos^2\theta\,|\Psi_{J_0,M_0}\rangle\rangle_{stat}(t)\\ &= \frac{\sum_{J_0,M_0} g_{J_0} e^{-\frac{E_{J_0}}{k_B T}}\,\langle\Psi_{J_0,M_0}|\cos^2\theta|\Psi_{J_0,M_0}\rangle\,(t)}{\sum_{J_0} P_{J_0}}\end{aligned} \tag{2.4}$$

where $J_0$ and $M_0$ correspond to the intially occupied states before the interaction with the alignment pulse. $\langle\langle\cos^2\theta\rangle\rangle_{stat}(t)$ is 0 if the axes of all molecules are perpendicular to the polarization axis of the electric field. It adopts the value of $1/3$ if the distribution becomes isotropic and unity if all molecules are perfectly aligned along the polarization axis.
After interaction with the alignment pulse different J are populated. Neglecting the centrifugal distortion and the Stark shift term which induces a permanent alignment the quantity characterizing the alignment $\langle\langle\cos^2\theta\rangle\rangle_{stat}(t)$ is proportional to (Renard et al., 2004):

$$\langle\langle\cos^2\theta\rangle\rangle_{stat}(t) \propto \cos(\omega_J t + \Delta\theta_J^{J_0,M_0}) \tag{2.5}$$

$$\Delta\theta_J^{J_0,M_0} = \theta_J^{J_0,M_0} - \theta_{J+2}^{J_0,M_0} \tag{2.6}$$

$$\omega_J = 2B_0(2J+3)$$

This equation shows that each $J$-component oscillates with a period of $\pi\hbar/[B(2J+3)]$. Renard and coworkers showed that owing to the property of the spherical harmonics $\langle\langle\cos^2\theta\rangle\rangle_{stat}(t)$ is strongest for low $J_0 = 0$ and therewith for low $M_0 = 0$. Also the quantum beat phase $\Delta\theta_J^{J_0,M_0}$ plays an important role for the position of the revivals.
Figure 2.2 depicts an alignment scan performed in nitrogen with pump-probe polarizations that are parallel to each other. Revival structures are not only visible at the full revival of 8.38 ps. At the time $T_{rot}/2$ and $T_{rot}/4$ more revival structures are revealed. The contrast between the aligned and anti-aligned molecules is strongest at the half revival.

The degree of alignment can however not be determined precisely by HHG. The response of high harmonic emission in differently aligned molecular gases is not known and is certainly not linear. The exact value can be measured by Coulomb exlosion (Dooley et al., 2003; Kumarappan et al., 2006; Lee, 2006). As this technique is not used in Bordeaux we try to estimate the value[2]. The temporal structures of the calculated signal and measured harmonic signal are compared. Note that the high harmonic response is not linearly dependent to $\langle\langle\cos^2\theta\rangle\rangle_{stat}(t)$. Therefore a comparison of the absolute signal is neglected. The initial parameters (number of rotational states, pulse duration, laser intensity) of the calculation are determined in a manner that the temporal features and

[2]This estimation is commonly used for HHG by the scientific community.

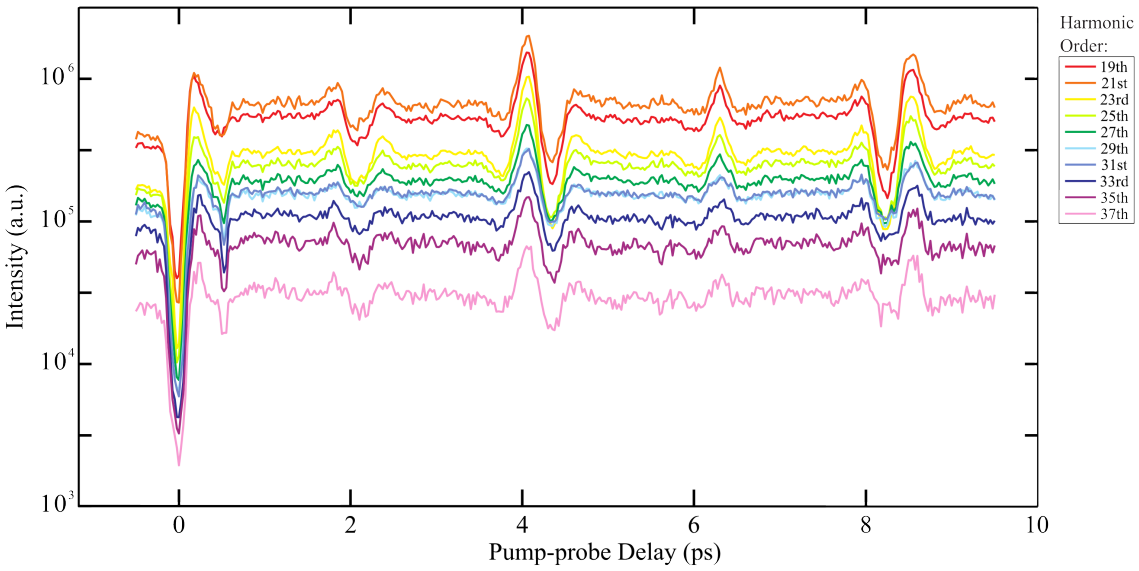


**Figure 2.2.:** Harmonic signal in nitrogen as a function of pump-probe delay with parallel pump-probe polarizations.

the periodicity of the extremal values adopt best the measured signal. When changing one of these parameters the calculated signal disagrees to a higher degree from the measured signal.
At the half revival the alignment is followed by an anti-alignment and inversely at the full revival. The angular distribution follows the same pattern, at half revival it first exhibits a prolate shape and then an oblate shape and repeats the same vice versa at full revival. The signal from harmonic 19 is two times stronger at the half revival than at the full revival. This reflects a more distinct alignment distribution as can be observed from the calculated polar diagrams in figure 2.3(a) and figure 2.3(b). Not also that the distribution never points exactly in the polarization direction of the laser. The shape of the distribution always adopts the form of a butterfly.

We find a maximum of the molecular alignment at a pump-probe delay of 4.1 ps in the experiment. Figure 2.3 delivers a $\langle\langle\cos^2\theta\rangle\rangle_{stat}(t) = 0.85$ that is very high, if compared to iodobenzene that achieved a record with $\langle\langle\cos^2\theta\rangle\rangle_{stat}(t) = 0.92$ (Kumarappan et al., 2006). A rotational temperature of 5 K is expected within the gas jet which is much lower to the rotational temperature observed with the former General valve. Figure 2.4 shows a comparison for the rotational temperature reached with the Even-Lavie valve and the former valve. The shape of the distributions are significantly different: this results from different gas expansion characteristics from the gas jet nozzle. The alignment distribution is peaked at an alignment angle of 27° at a rotational temperature of 50 K. At a temperature of 5 K the alignment distribution is narrower and peaked at an angle of 9°. The attenuation of the rotational temperature to probe an aligned macroscopic ensemble is thus necessary for measuring a signal which is much closer to the single

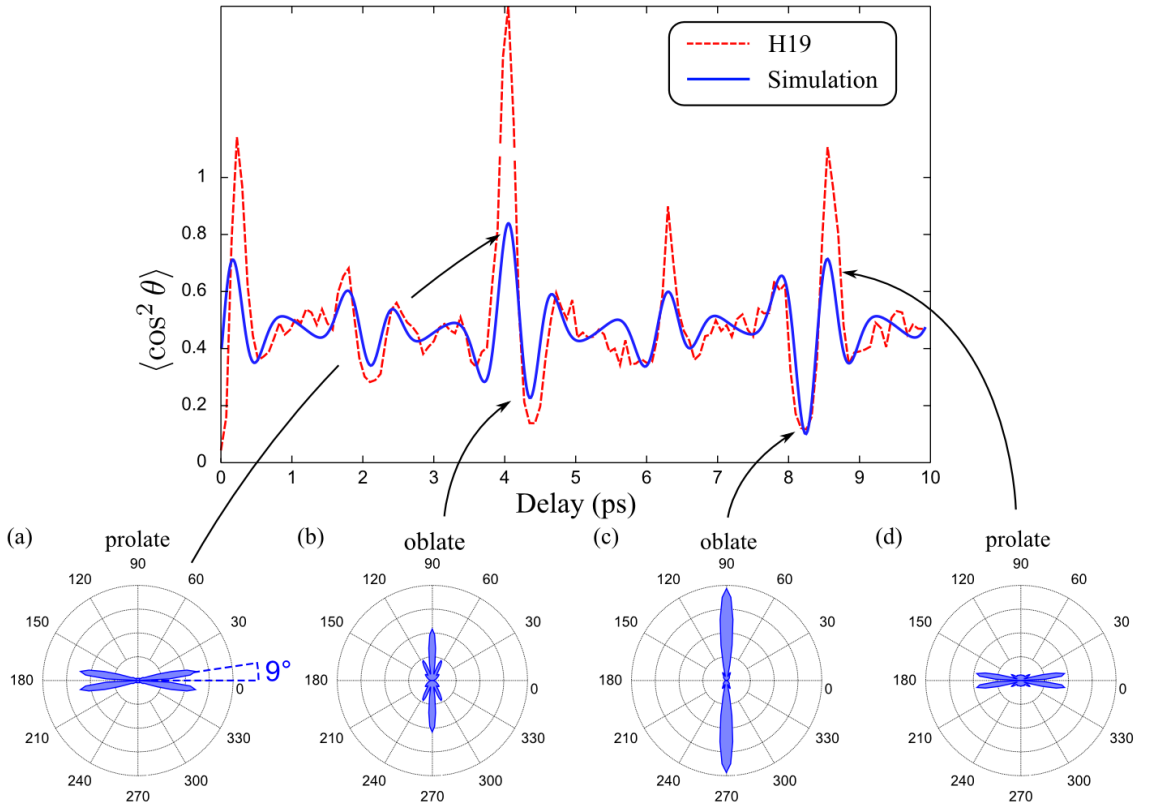


**Figure 2.3.:** Comparison between the signal from harmonic 19 and the calculation of $\langle\langle cos^2\theta\rangle\rangle_{stat}(t)$. The pulse duration of the alignment pulse is 70 fs with an intensity of $6 \times 10^{13}$ W/cm$^2$. The polar diagrams depict the alignment distribution of the molecular ensemble. The polarization direction of the alignment pulse is in horizontal direction. A rotational temperature of 5 K was taken for the simulation, leading to $\langle\langle \cos^2 \theta\rangle\rangle_{stat}(t) = 0.85$ (figure adopted from (Higuet, 2010)).

molecule response.
When expanding into the vacuum the molecules experience collisions, which transfer the rotational internal kinetic energy to translational energy (Scoles et al., 1988). The higher the distance from the nozzle, the more collisions the molecules have undergone and thus the lower the rotational temperature. The gas density is however significantly reduced far from the nozzle which is a great disadvantage for optimizing HHG, remember the macroscopic signal highly depends on the number of emitters and therewith on the pressure. Thus HHG has to be performed close to the nozzle, with the disadvantage of poor alignment. The achieved rotational temperature crucially depends on the expansion characteristics of the nozzle. Low rotational temperatures are especially obtained in supersonic gas expansions. The nozzle of the Even-Lavie valve exhibits this characteristic with a jet expansion half angle of 10°. This low divergent jet allows us to generate high harmonics at a distance of 40 nozzle diameters (150 $\mu$m). The Even-Lavie jet is thus the key technology for reaching cold rotational temperature. These are varied by heating up the nozzle.

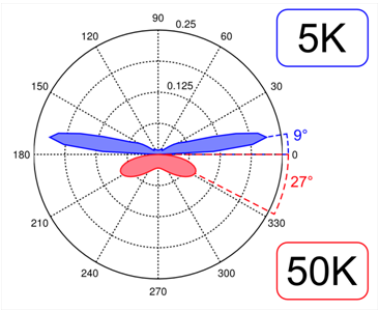


**Figure 2.4.:** Alignment distribution at a rotational temperature of 5 K and 50 K at the half revival.

At colder rotational temperatures the alignment distribution is strongly peaked and the average alignment angle of the molecules is closer to the direction of laser polarization than in the case of warmer rotational temperatures. The weak alignment at warmer rotational temperatures originates from the high number of $J_0$ and $M_0$ contributing to $\langle\langle\cos^2\theta\rangle\rangle_{stat}(t)$ (see equation 2.2). Figure 2.1 clearly illustrates that only 3 states contribute significantly to this initial distribution at a temperature of 5 K, wheras 10 need to be taken into account at 50 K. This coldest rotational distribution is required for creating the best alignment of the molecular axis.

## 2.2. High Harmonic Generation in aligned Nitrogen Molecules

First results are presented in the smaller of the two molecules, namely $N_2$. Since the tomographic reconstruction of the HOMO, the nitrogen molecule has taken a very prominent role for HHG (Itatani et al., 2004). As a matter of fact, the visionary work from

Itatani and coworkers triggered a lot of questions. Very soon afterwards multielectron effects were considered (Patchkovskii et al., 2006). The experimental reconstruction of the first excited electronic state (HOMO-1) followed four years later (Haessler et al., 2010). Also substantial subcycle transitions between the X- and A-channel (see figure 2.5) are expected from experimental observations (Mairesse et al., 2010). The B-channel is considered to play only a minor role due to its high ionization potential. The harmonic phase, which is fundamental for orbital reconstruction, has been found to be intensity dependent, indicating a transition from the single- to the multi-channel regime (Diveki et al., 2012).
First the symmetry sensitivity of HHG to the molecular orbital is demonstrated. Then the experimental setup of a non-collinear pump-probe scheme is presented. Finally the results from experiments performed in a cold molecular gas jet are displayed. These are obtained at different nozzle temperature and generation intensities.

### 2.2.1. High Harmonic Spectra decoding the Structure of Molecular Orbitals

As already mentioned in chapter 1 the tunnel ionization rate strongly depends on the orientation of the molecule with respect to the electric field (see figure 1.5). The molecular geometry responsible for direction dependent tunnel ionization rate is visualized in terms of the Dyson orbital $\psi_{Dj}$. It is defined as the projection of the ionic wavefunction $\psi_j^{(N-1)}$ of the ion in state $j$ after removal of an electron from the N-electron wavefunction of the neutral molecule $\psi_{NT}^{(N)}$ (Smirnova et al., 2009b):

$$\psi_{Dj} = \sqrt{N}\,\langle \psi_j^{(N-1)} |\, \psi_{NT}^{(N)} \rangle \tag{2.7}$$

As tunnel ionization is exponentially sensitive to the ionization potential $I_p$ (see equation 1.4), the process is expected to be most efficient for the ground state. One has to consider the geometry of the Dyson orbitals (see figure 2.5). Due to nodal structures of the Dyson orbital in the ground state, ionization is suppressed for molecules which are aligned perpendicular to laser polarization. In other words, the opposite sign of the Dyson orbitals' lobes lead to destructive interference and ionization suppression (Muth-Böhm et al., 2000; Tong et al., 2002).
The harmonic signal is not only determined by the tunnel ionization probability but also by recombination. The recombination dipole moment is governed by the same geometry. Different phases are acquired for different ionization channels, the phase of each channel can be split in four different contributions (Smirnova et al., 2009a):

**I)** Phase acquired during ionization.

**II)** Phase accumulated by the electronic states $j$ of the parent ion during the electron propagation $\phi_j \propto e^{-iE_j\tau}$.

**III)** The Volkov phase accumulated by the continuum electron which is different for two ionization channels $j = 1,2$: $\Delta\varphi \approx (E_2 - E_1)\Delta\tau$, with $\Delta\tau$ the difference in travel time for the two channels.

**IV)** The phase of the recombination matrix element.

Smirnova and coworkers demonstrated that at a certain time of flight $\tau$ of the continuum electron destructive interference from two different channels can be associated (Smirnova et al., 2009a).

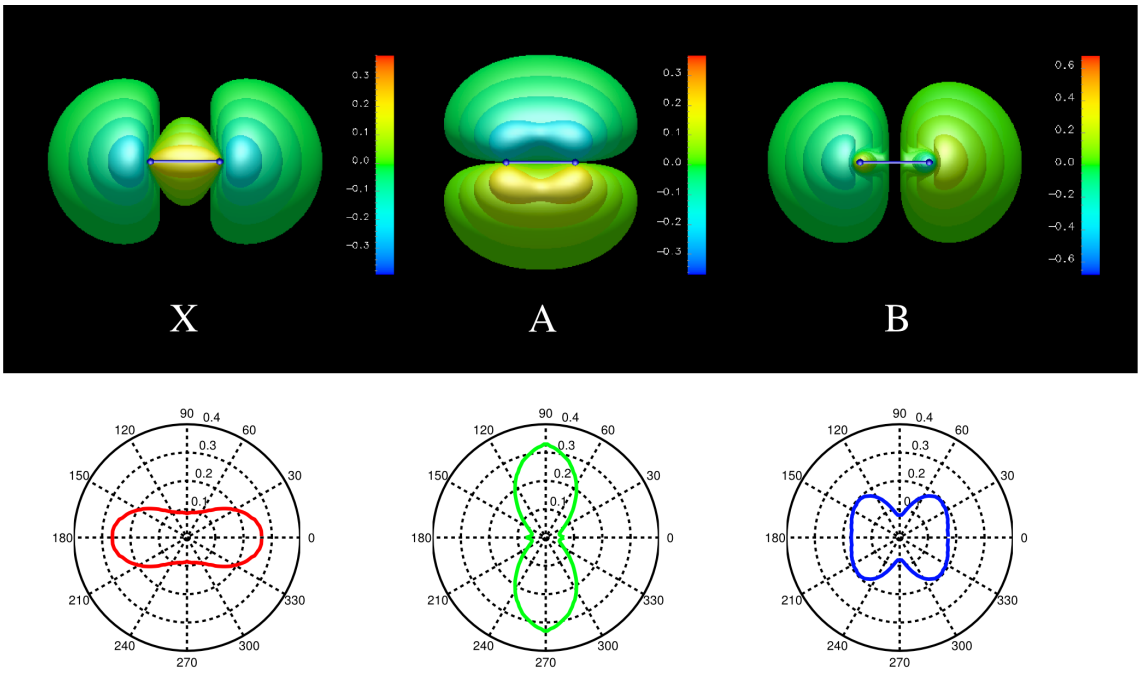


**Figure 2.5.:** Dyson orbitals corresponding to different ionization channels in nitrogen: X-channel, ground state: $E_X$ =15.6 eV, A-channel, first excited electronic state: $E_A$ = 16.9 eV and B-channel, second excited electronic state: $E_B$ = 19.1 eV. The polar diagrams illustrate for each orbital the normalized tunnel ionization probability (figure adapted from (Higuet, 2010)).

### 2.2.2. Experimental Setup for Optical Alignment

At the time when the experiment was performed the Aurore Ti:Sa-Laser system was delivering 7 mJ, 35 fs, 800 nm pulses at 1 kHz. The experimental setup is presented in chapter 1 (see figure 1.23). Figure 2.6 displays the setup which is used for optical alignment. The laser beam is separated by using a 50/50 beam splitter. The pump beam is delayed by $\Delta$t using a motorized translation stage. The degree of alignment also

depends on the laser parameters such as intensity and alignment pulse duration (Haessler, 2009). A good alignment was found when stretching the alignment pulse from 35 fs to 70 fs, by propagation through a 10 mm thick SF10-plate. The $\lambda/2$-plate rotates the molecular alignment with respect to the generating beam polarization axis by an angle $\theta$. HHG from the pump beam is not recorded as pump and probe beams are non-collinear. This has the strong advantage that the pump intensity can be increased. Both beams are focussed by a spherical mirror with a focal distance of f = 37.5 cm into the gas jet. The beams are reflected by two mirrors at an angle of incidence (AOI) of 7.5°. This causes a slightly astigmatic focus. The pump intensity is around $6 \times 10^{13}$W/cm$^2$, the probe intensity is varied by a diaphragm.

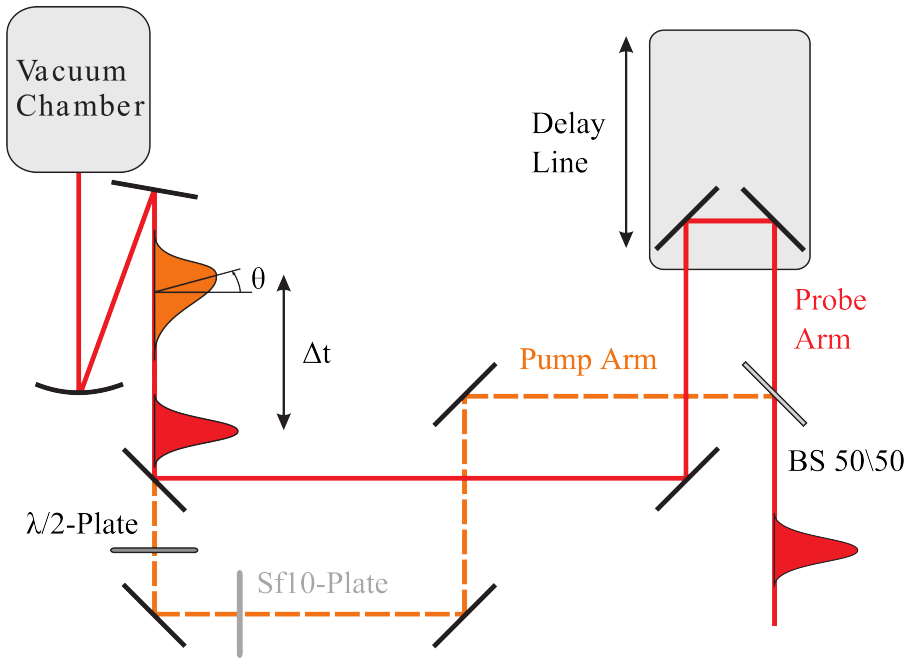


**Figure 2.6.:** Experimental Setup for HHG in aligned molecules.

### 2.2.3. HHG in strongly aligned Nitrogen from multiple Orbitals

The alignment scan in nitrogen presented in figure 2.2 fits the features of the calculation in figure 2.3. At low gas temperatures ($T_{rot} = 5$ K), clusters can be formed in the gas jet. These might contribute to HHG and interfere with the radiation emitted from aligned molecules. Their formation should be negligible for nitrogen however, its adhesion is very low. The tendency to stick together is characterized by the condensation parameter which is very low for nitrogen (see table 4.1 chapter 4). Significantly higher backing pressures than what we use for molecular alignment (9 bar and 11 bar) are needed for efficient cluster generation in nitrogen.
An intriguing feature is revealed in figure 2.2. In the cutoff i.e. harmonic 33, 35 and

37 a local maximum appears at strongest anti-alignment ($\Delta t = 8.52\,ps$). The rotational wavepacket adopts an oblate shape at this position. The axes of the molecules are in a plane which is perpendicular to laser polarization. What is the reason?
In 2008 McFarland and coworkers first observed the influence of the HOMO-1 in aligned nitrogen molecules (McFarland et al., 2008). Paragraph 2.2.1 explains the suppression of ionization due to destructive interference from to neighbouring orbital lobes with opposite phase. The mechanism is also valid for the recombination dipole moment. This leads to suppression of HHG from the X-channel if the polarization direction is perpendicular to the molecular axis. The contrary is the case for the A-channel (see figure 2.5) ionization is enhanced and thus leads to a significant HHG from this channel.
McFarland and coworkers also observed an inverted behaviour at the half revival. In a cross-polarized pump-probe scheme the signal usually adopts a minimum at 4.1 ps due to ionization suppression from the X-channel. The cutoff harmonics show however a maximum, which is interpreted as the contribution from the A-channel (McFarland et al., 2008). The appearance of a stronger signal from the A-channel makes sense, owing to a superior ionization potential it dominates over the emission from the X-channel. We also looked for this feature, but were not able to reproduce it, even though we tried different generation intensities. The pulses used in their experiment were shorter (30 fs vs. 35 fs), the alignment pulse was longer (90 fs vs. 70 fs), the gas jet warmer ($T_{rot} = 40\,K$ vs. $T_{rot} = 5\,K$) and the alignment intensity lower ($2.5 \times 10^{13}\,W/cm^2$ vs. $6 \times 10^{13}\,W/cm^2$).
Let's come back to the local maximum observed in figure 2.2 in the parallel pump-probe configuration at the anti-alignment. This feature has not yet been reported before. For the same reason as above the A-channel might be revealed at the full revival anti-alignment. At the half revival anti-alignment the minimum for harmonic 37 is slightly cut, probably for the same reason. The anti-alignment is weaker at half than the full revival. This shows that a high degree of alignment is crucially important. If it was weaker, this feature would not have been measured.

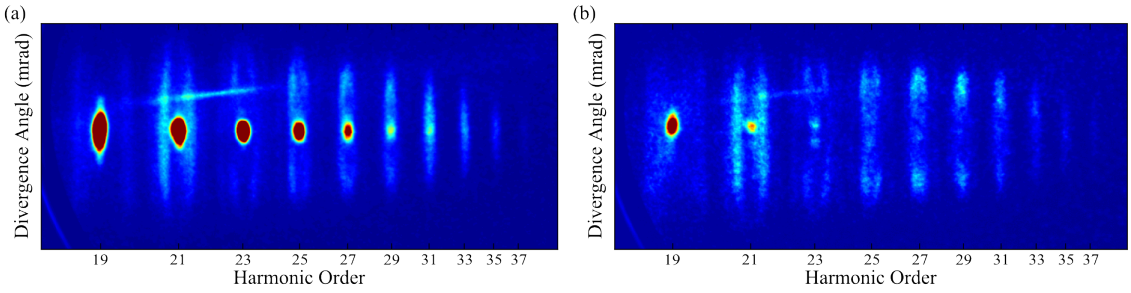


**Figure 2.7.:** Spectra in nitrogen at (a) parallel and (b) perpendicular laser polarization for the pump and probe beam. The nozzle temperature is at 80 °C with a backing pressure of 11 bar.

Figure 2.7 illustrates the high harmonic spectra in aligned nitrogen molecules. The signal from short and long trajectories can be clearly distinguished, and is merging in the

cutoff. As we increase the laser intensity, the ring structure from the long trajectories expands. These two effects are expected from phase matching conditions as explained in chapter 1. It is noticeable that the signal from the short trajectories almost disappears at perpendicular alignment. Where does this strong contrast between perpendicular and parallel alignment originate from?

### 2.2.4. Shape Resonance in strongly aligned Nitrogen Molecules

Figure 2.8 illustrates the harmonic signal as a function of alignment angle at different intensities. The spectra on the figure illustrate how the cutoff is decreasing with intensity. A distinct feature appears for the lowest harmonics at parallel alignment. It is stronger for the intermediate generation intensity but still clearly visible at lower and higher intensities. This strong enhancement of the signal has not been observed yet at a generation wavelength of 800 nm (see for example figure 3(b) from (Mairesse et al., 2008a)). We study it for two reasons. First an enhancement of the high harmonic emission is always of interest if it is used in pump-probe experiments (see chapter 5). Second the origin of this characteristic might give further insights in the molecular structure of nitrogen.
Figure 2.9(a) displays the same signal for the long trajectories. The selection of the long trajectory signal was done by subtracting the central spot (short trajectories) from the total signal. The signal for harmonic 19 is weak and experiences a sudden drop with respect to harmonic 21. One observes however that the signal of harmonic 19 is not fully recorded by the detector (see figure 2.8). Due to the strong divergence the lower and upper parts of the signal are cut[3]. Thus it is not possible to measure the signal from harmonic 19. If harmonic 19 is neglected, the same strong increase can be observed for the long as has been observed for the short trajectories for low harmonic orders at parallel alignment. The enhancement of the signal from harmonic 23 to harmonic 21 is more dramatic at higher intensities than at lower intensities. It shows the same tendency however. The contrast of the signal from harmonic 21 at parallel and perpendicular alignment is 30.3 for the short and 5.6 the long trajectories.

At a certain time of flight $\tau$ of the continuum electron constructive interference from two different channels could cause such a maximum (see paragraph 2.2.1). If this was the case for the strong signal observed here, one would expect different tendencies for the long and short trajectories as they acquire different phases. The similar behaviour from short and long trajectories indicates however that different ionization channels should not play an important role. This hypothesis is confirmed by the intensity dependence. When varying the intensity, trajectories with a different time of flight contribute to the same harmonic order and $\tau$ varies. Thus a change of signal is expected with intensity. Figure 2.11(a) shows however that harmonic 19 is almost constant within an intensity range of $1.0 \times 10^{14}\,\mathrm{W/cm^2}$ to $1.5 \times 10^{14}\,\mathrm{W/cm^2}$. As interference between the different channels (dynamical effects) can be excluded this feature can be attributed to a structural origin.

[3]The signal is cut either due to the differential pumping hole or the limited height of the grating.

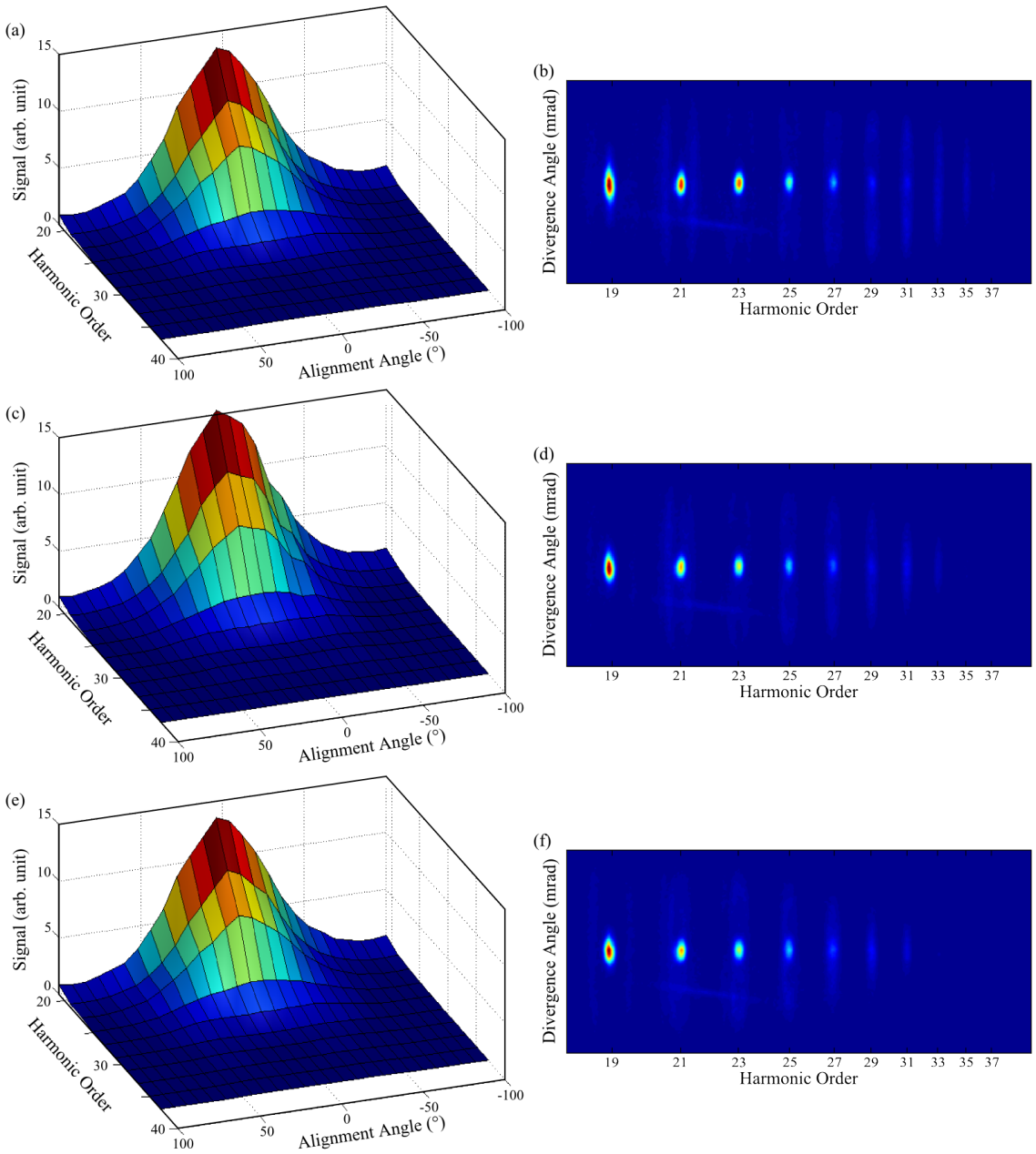


**Figure 2.8.:** High harmonic signal in nitrogen as a function of alignment angle and harmonic order for the short trajectories in parallel configuration. The generation intensity, determined by the harmonic cutoff decreases from (a) $1.5 \times 10^{14}\,\mathrm{W/cm^2}$ to (c) $1.4 \times 10^{14}\,\mathrm{W/cm^2}$ to (e) $1.2 \times 10^{14}\,\mathrm{W/cm^2}$. The backing pressure is 10 bar at a nozzle temperatures of 80 °C.

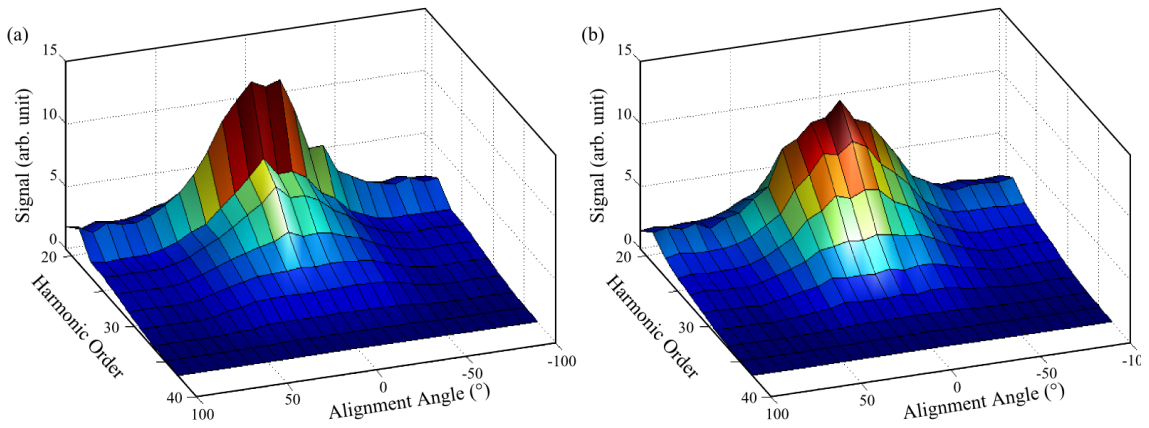


**Figure 2.9.:** High harmonic signal in nitrogen as a function of alignment angle and harmonic order for the long trajectories in parallel configuration. The generation intensity, determined by the harmonic cutoff decreases from (a) $1.5 \times 10^{14}\,\mathrm{W/cm^2}$ to (b) $1.2 \times 10^{14}\,\mathrm{W/cm^2}$. The backing pressure is 10 bar at a nozzle temperatures of 80 °C.

Jin and coworkers calculations revealed a strong high harmonic signal at the same wavelengths at parallel alignment (Jin et al., 2012). They attributed this observation to a shape resonance in nitrogen, but could not confirm it experimentally. Figure 2.10 displays their calculation for the differential ionization cross section. As discussed in the case of the Cooper minimum in chapter 1, the photorecombination probability is proportional to this cross section. Thus harmonic 15 to 25 are expected to be strongly enhanced at a generation wavelength of 800 nm for the HOMO. Their calculations agree well with our observations. In order to record the decline of the harmonic signal at lower harmonic orders the harmonic detector needs to be moved by four to six orders. Figure 2.10(b) shows that the contribution from HOMO-1 is negligible at parallel alignment. The photorecombination probability from HOMO-1 is relatively high however at perpendicular alignment. This is in good agreement with the discussion in chapter in paragraph 2.2.3. The A-channel is dominating the X-channel at perpendicular alignment in the cutoff. Still the full calculation including ionization, propagation and recombination is required for drawing a conclusion on this. Another important point to include are subcycle transitions between the HOMO and HOMO-1 as the photon energy of 1.55 eV is close to the energy gap between the two states (Mairesse et al., 2010).

Harvey and coworkers currently perform calculations on this phenomenon taking our experimental results as a comparison. They attribute this shape resonance to an autoionizing state (Strelkov, 2010) which causes a resonant enhancement of HHG. An autoionizing can be formed when the centrifugal barrier is taken into account in addition to the Coulomb potential. In multielectron systems the attraction close to the nucleus changes its scaling from $-1/r$ to $-Z/r$, where $Z$ is the charge of the nucleus. In reasonable heavy systems this creates a significant well in addition to the centrifugal barrier. However the inter-

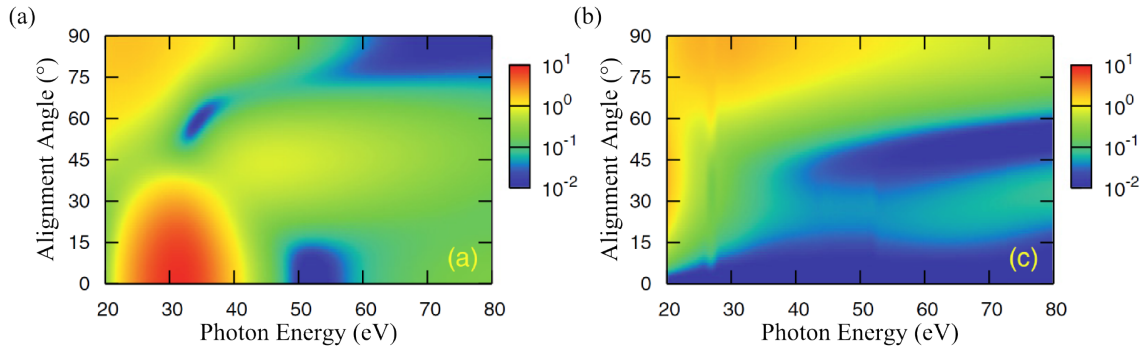


**Figure 2.10.:** Calculated differential photoionization cross section as a function of polarization direction of the (a) HOMO and (b) HOMO-1 for nitrogen (figure adopted from (Jin et al., 2012)).

action range of this well is only short-ranged. At very small distances to the molecular center the centrifugal barrier ($\propto J(J+1)/r^2$) dominates over $-Z/r$.

Figure 2.11 displays harmonic 19 to 35 as a function of alignment angle at different laser intensities. The structure of the shape resonance is apparent for harmonic 19, 21 and 23. Other details appear in the signal, which have never been observed before. Harmonic 29 to 33 reveal a clear minimum at parallel alignment and signal maxima at an alignment angle around $\pm 40°$. These structures do not seem to vary with intensity. Another observation is represented in figure 2.11(b) for harmonic 33. The minimum detected at an angle of $\pm 80°$ at a laser intensity of $1.5 \times 10^{14}\,\mathrm{W/cm^2}$ moves to $\pm 70°$ for lower intensities. This tendency can also be clearly observed for other harmonic orders: a minimum moving to lower absolute alignment angles at higher intensities (see figure 2.11(c)-(f)). This intensity dependence indicates a dynamical effect.
Remember the local maximum at the anti-alignment of the full revival in figure 2.2. This feature might be attributed to a contribution from the A-channel which is dominant when laser polarization is perpendicular to the molecular axis. Exactly this is the case for the maximum which is observed at an alignment angle of $\pm 90°$ for the cutoff harmonics. The minimum which is moving with decreasing intensities to lower absolute angles could therewith be identified as a destructive interference between the X-channel and the A-channel. Note, this is consistent with the calculed differential photoionization cross section in figure 2.10, the A-channel is dominating over the X-channel in the cutoff. Now, only the different phase contributions are missing for the reproduction of this minimum. Once again, we would like to emphasize that the resolution of the dynamical minimum had not been possible if the strong degree of molecular alignment had not been reached by the Even-Lavie jet.

The calculation of the shape resonance by Jin and coworkers has been done in a relatively warm gas jet. With $\langle\langle\cos^2\theta\rangle\rangle_{stat}(t) = 0.6$ a degree of alignment has been reached, which is significantly lower than the one achieved by the Even-Lavie valve ($\langle\langle\cos^2\theta\rangle\rangle_{stat}(t) = 0.85$). We therefore changed the nozzle temperature in order to study

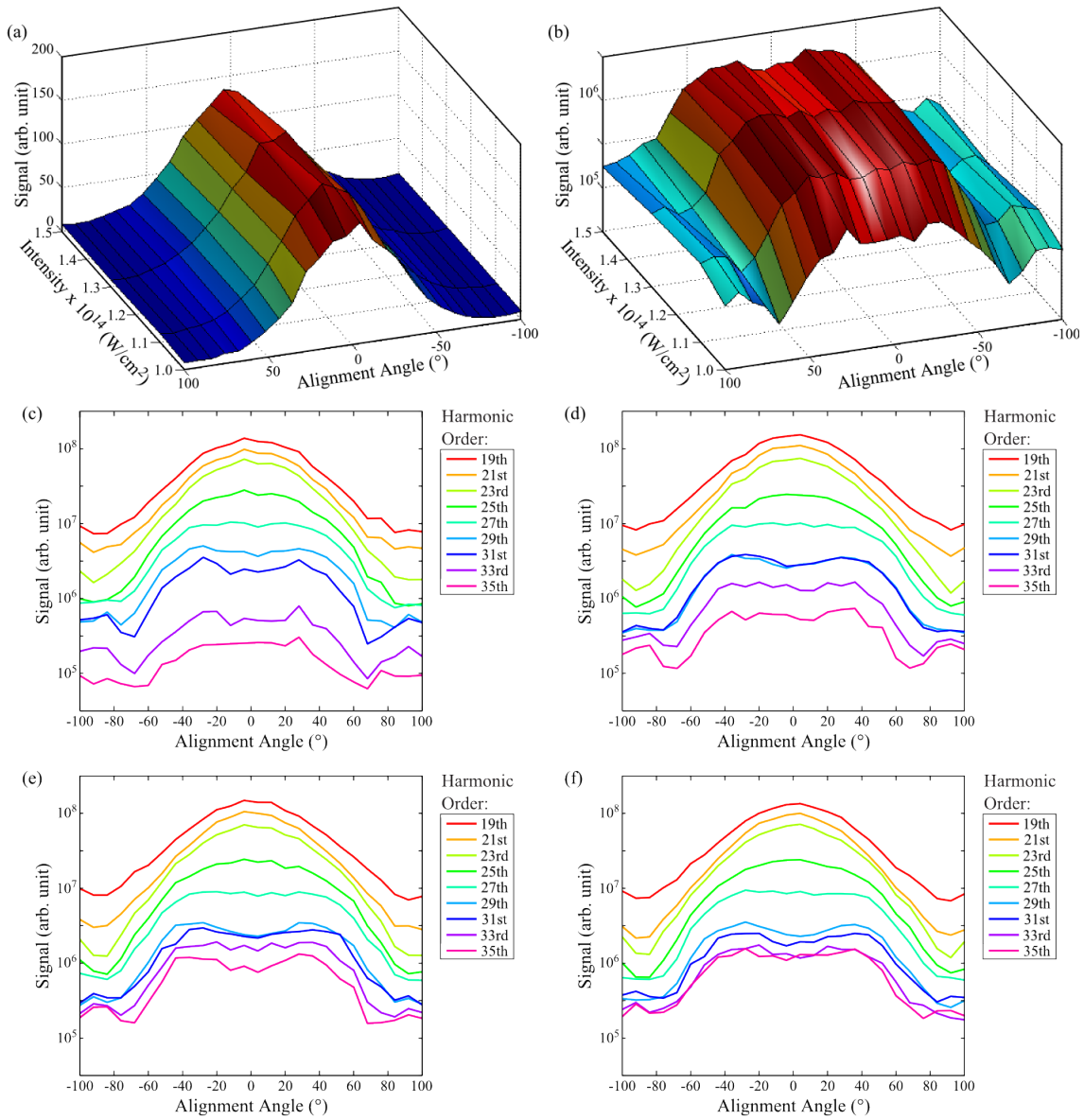


**Figure 2.11.:** (a) Harmonic 19 and (b) harmonic 33 as a function of generation intensity and alignment angle. The backing pressure is 10 bar at a nozzle temperatures of 80 °C. Harmonic signal in nitrogen as a function of alignment angle at an intensity of (c) $1.0 \times 10^{14}\,\mathrm{W/cm^2}$, (d) $1.2 \times 10^{14}\,\mathrm{W/cm^2}$, (e) $1.4 \times 10^{14}\,\mathrm{W/cm^2}$ and (f) $1.5 \times 10^{14}\,\mathrm{W/cm^2}$.

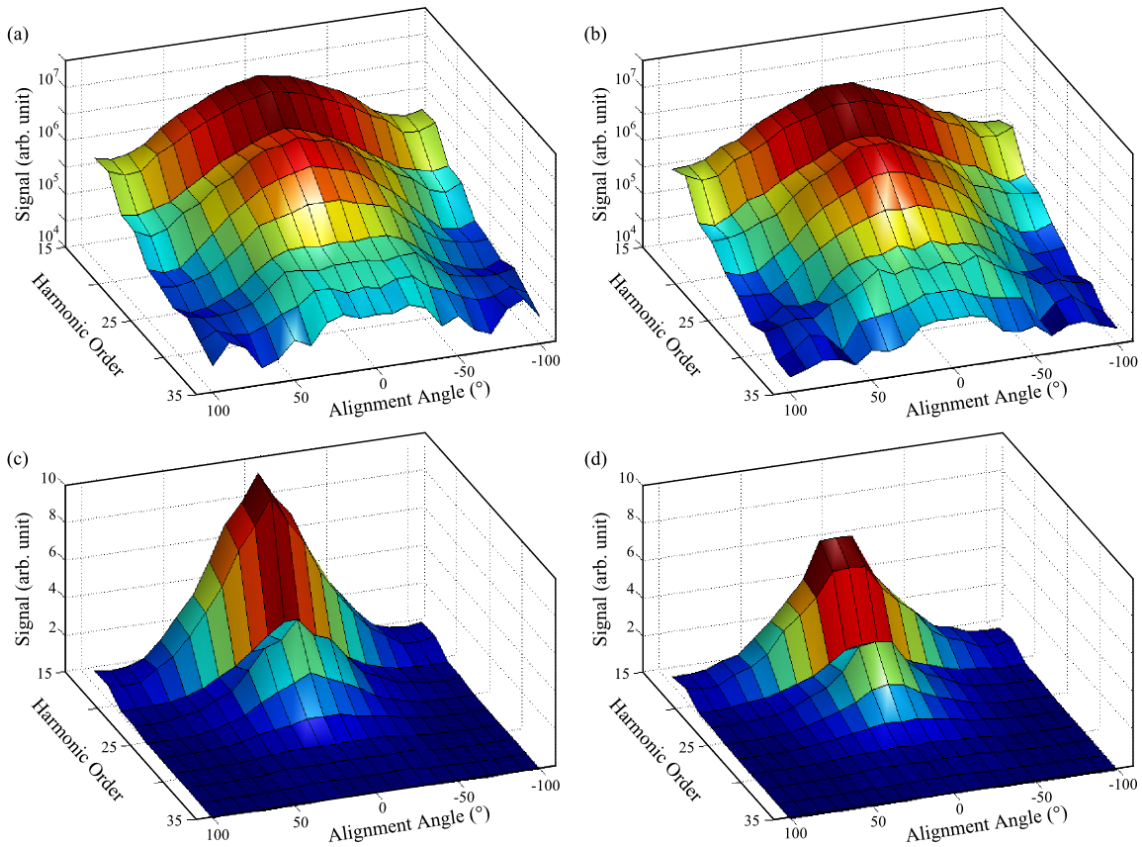


**Figure 2.12.:** High harmonic signal in nitrogen as a function of alignment angle from harmonic 17 to harmonic 35 in (a), (b) logarithmic and (c), (d) linear scale at a generation intensity of $1.2 \times 10^{14}\,\mathrm{W/cm^2}$. The signals are symmetrized at parallel alignment. The backing pressure is 11 bar at nozzle temperatures of (a), (c) 80 °C and (b), (d) 160 °C.

the dependence on the rotational temperature. Figure 2.12(a) and figure 2.12(b) illustrate scans at different nozzle temperatures. Figure 2.12 displays the harmonic signal from the short trajectories as a function of alignment angle at different nozzle temperatures. The shape resonance is clearly observed at a nozzle temperature of 80 °C. It decreases however significantly at the higher nozzle temperature, i.e. a lower degree of molecular alignment. Again the additional two features which are described above are observed. The signal adopts a maximum at $\pm 30°$ and a minimum in between. Also the dynamical minimum at an alignment angle of $\pm 80°$ becomes visible. At 160 °C, these features clearly disappear. Figure 2.13 depicts the corresponding alignment scans which reveal a similar behaviour. Only the quarter revival of the two scans seems to be shifted. The contrast between alignment and anti-alignment are similar. Another scan at even higher nozzle temperatures might have been useful for reaching even higher rotational temperatures.

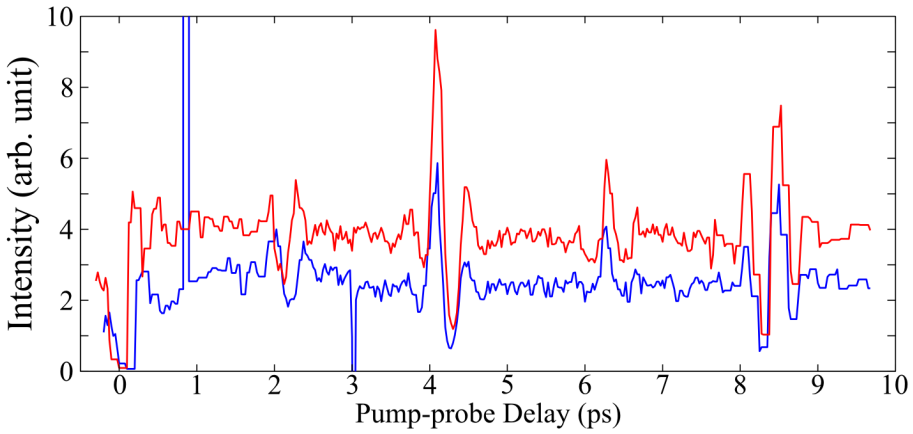


**Figure 2.13.:** Alignment scan in nitrogen for harmonic 19 at a nozzle temperature of 80 °C (red) and 160 °C (blue).

## 2.3. High-Order Harmonic Generation in strongly aligned Carbon Dioxide Molecules

Carbon dioxide is another linear molecule with a different orbital structure which has been widely studied by HHG. First experiments of HHG in aligned carbon dioxide molecules have been performed by Kanai and Vozzi together with coworkers (Kanai et al., 2005; Vozzi et al., 2005a). In the two experiments a minimum was observed in the high harmonic spectra, however at different positions. These type of minima were already predicted theoretically in aligned $H_2$ and $H_2^+$ (Lein et al., 2002). The explanation was structure-related interference from the different contributions emitted from different atomic centers. If the distance between such two centers corresponds to half the de Broglie wavelength of the recolliding electron wavepacket destructive interference is expected. The minimum

structures were attributed to such a structural minimum (Kanai et al., 2005; Vozzi et al., 2005a), with the opening question: Why should this type of minimum show up at different positions in the spectrum? The experiments at Tokyo and Milano were conducted at different intensities. Smirnova and coworkers confirmed this intensity dependence theoretically and experimentally (Smirnova et al., 2009a). The new interpretation of the minimum, dubbed dynamical minimum, was completely different. More than one molecular channel plays a role for HHG, namely the highest occupied molecular orbital (HOMO) and the two orbitals beyond: HOMO-1 and HOMO-2. Furthermore the position of the minimum was found to depend also on the laser wavelength (Wörner et al., 2010).
A typical alignment scan is depicted in figure 2.14. The prolate shape of the rotational electron wave packet is reached at a delay of 21.2 ps. In contrast to nitrogen (see figure 2.2), the harmonic signal shows a minimum at this delay.

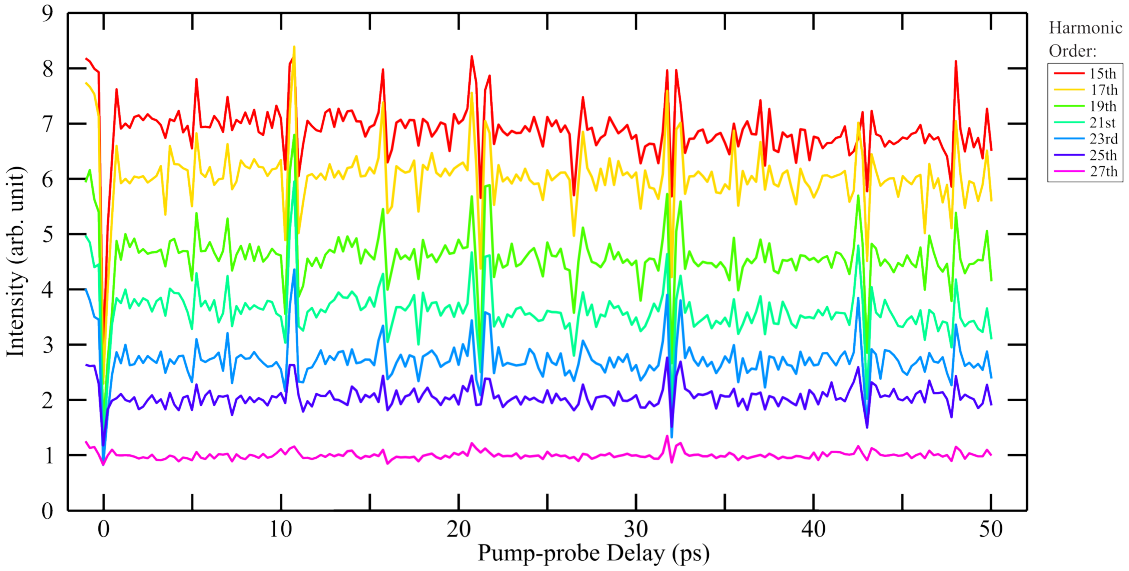


**Figure 2.14.:** Alignment scan in carbon dioxide with parallel pump-probe polarizations.

### 2.3.1. HHG in a cold Carbon Dioxide Gas Jet

Before going into detail with the new features observed in aligned carbon dioxide, one has to evaluate the medium of generation. Supersonic gas jets are also used for the formation of clusters as elaborated in chapter 4. Paragraph 4.5 elucidates the contribution of clusters to the high harmonic signal in cold gas jets. It concludes that cluster formation cannot be excluded in such a jet. The alignment pulse at an intensity of $6 \times 10^{13}\,\mathrm{W/cm^2}$ probably destroys the largest clusters. The cluster participation to HHG from aligned carbon dioxide molecules is expected to be negligible.

In order to study a possible effect from clusters on the alignment scan, a second analysis has been performed. At the half revival of the alignment scan an oscillation is observed

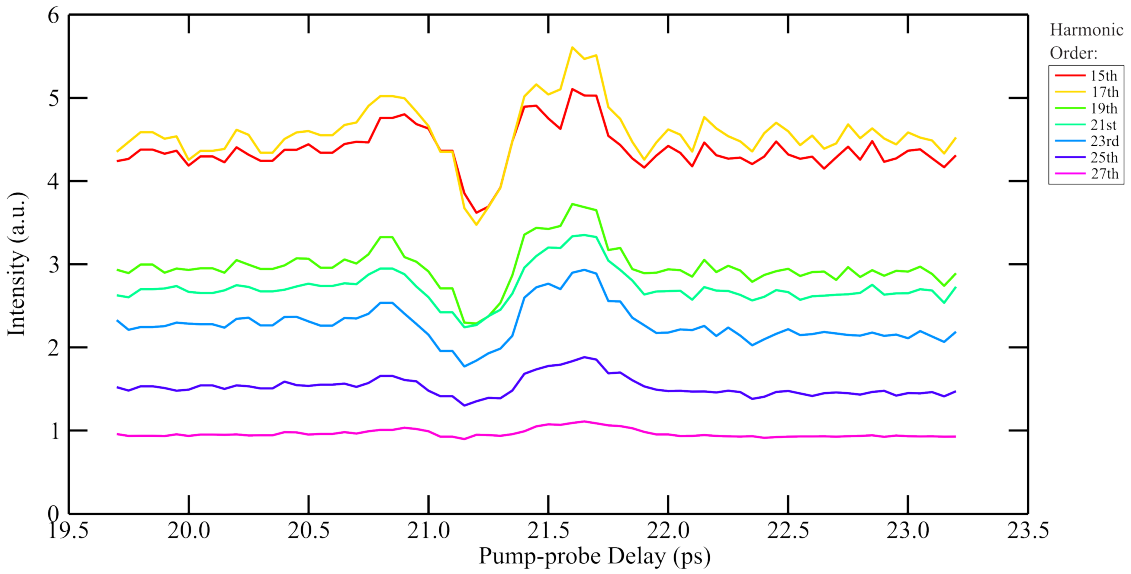


**Figure 2.15.:** Alignment scan in carbon dioxide with parallel pump-probe polarizations at the half revival of the rotational wave packet.

(see figure 2.15). The degree of revival is now extracted in the following way: After subtracting the background from the signal, a Fourier transform is performed to extract the amplitude of the oscillatory component. The amplitude is then normalized to the sum of the Fourier transform. The degree of revival, i.e. the normalized component of the Fourier spectrum is plotted for each pixel. It is illustrated in figure 2.16(b) in a revival map. A strong signal also shows a high degree of revival. Even the cutoff harmonics, long trajectories down to harmonic 19 reveal a significant degree of revival. Only the harmonic signal from the long trajectories from harmonic 15 and 17 seems not to be affected by the alignment pulse. This might be attributed to a low signal. As clusters are insensitive to alignment the degree of revival is expected to be zero. If clusters contributed significantly to the high harmonic signal, these regions would be identified in the 2D spatio-spectral signal. The degree of revival would be expected to decrease significantly for the off axis cutoff harmonics[4]. This is not observed however. We therefore conclude that clusters do not play a role in the signal from the alignment scan.

### 2.3.2. The Minimum in aligned Carbon Dioxide

One question from paragraph 2.3 is still pending: Why does the harmonic signal show a minimum at the maximal degree of revival at a pump-probe delay of 21.2 ps? As already discussed in paragraph 2.2.1 the tunnel ionization rate strongly depends on the orientation of the molecule with respect to the electric field (see figure 1.5). The Dyson orbital of the ground state exhibits a nodal structure (see figure 2.17). Due to the nodal structure

[4]HHG from large clusters has been identified in these regions in chapter 4.

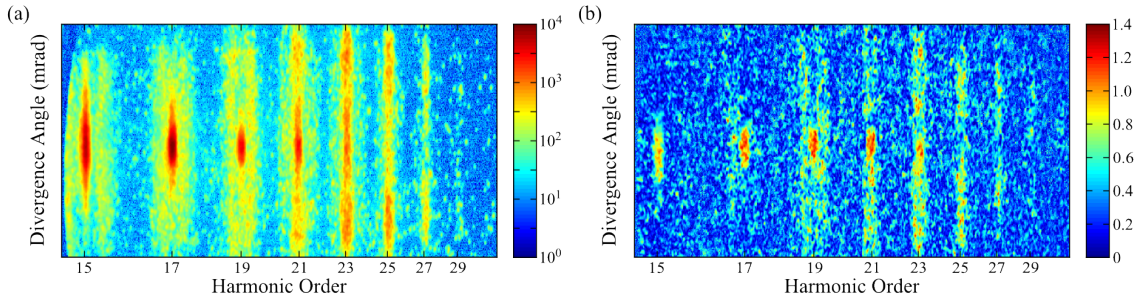


**Figure 2.16.:** (a) High harmonic spectrum and (b) revival map in carbon dioxide at 9 bar at 80 °C.

of the Dyson orbital for the ground state, ionization is suppressed for molecules which are aligned parallel or perpendicular to the laser polarization. Figure 2.17 also illustrates the relative strong-field ionization amplitudes between the first three channels in carbon dioxide. The B-channel contributes significantly to ionization when the molecular axis is parallel to the laser polarization even though the ionization potential is 4.3 eV higher than that for the X-channel. If the molecular axis is perpendicular to the laser polarization, the B-channel becomes negligible and the A-channel gains in importance.

Figure 2.18 shows harmonic spectra with a clearly distinguishable signal from short and long trajectories. As we increase the laser intensity, the ring structure from the long trajectories expands. These two effects are expected from phase matching conditions as explained in chapter 1. In part (a) of the figure a minimum is observed for the short trajectories at harmonic 19. If the nature of the minimum was structural, it should affect the signal from short and long trajectories similarly. As in nitrogen, this minimum might be the result of destructive interference between the different ionization channels. Smirnova and coworkers demonstrated that at a certain time of flight $\tau$ of the continuum electron, destructive interference between two different channels leads to such a minimum (Smirnova et al., 2009a). The main phase difference contribution originates from $(E_B - E_X)\tau$, with $E_B$ and $E_X$ the ionization potentials of the respective channels. They observed that the minimum in the harmonic spectra from aligned carbon dioxide molecules shifts linearly with laser intensity in agreement with their calculations. We believe that this is also the case for the minimum observed in the short trajectories. It has to be noted that the central part of harmonic 17 in figure 2.18(a) is split in two. When moving the alignment beam slightly upward or downward, by tweaking a mirror, the depletion of this central part is moving respectively. The following paragraph demonstrates that a higher degree of alignment shifts the dynamical minimum to lower harmonic orders. We suspect that this effect is also responsible for the minimum observed for harmonic 17. The alignment is stronger at the center of the pump-beam and thus creates a destructive interference for the lower harmonics. Thus the minimum of harmonic 17 is an indicator for the stronger alignment on axis.

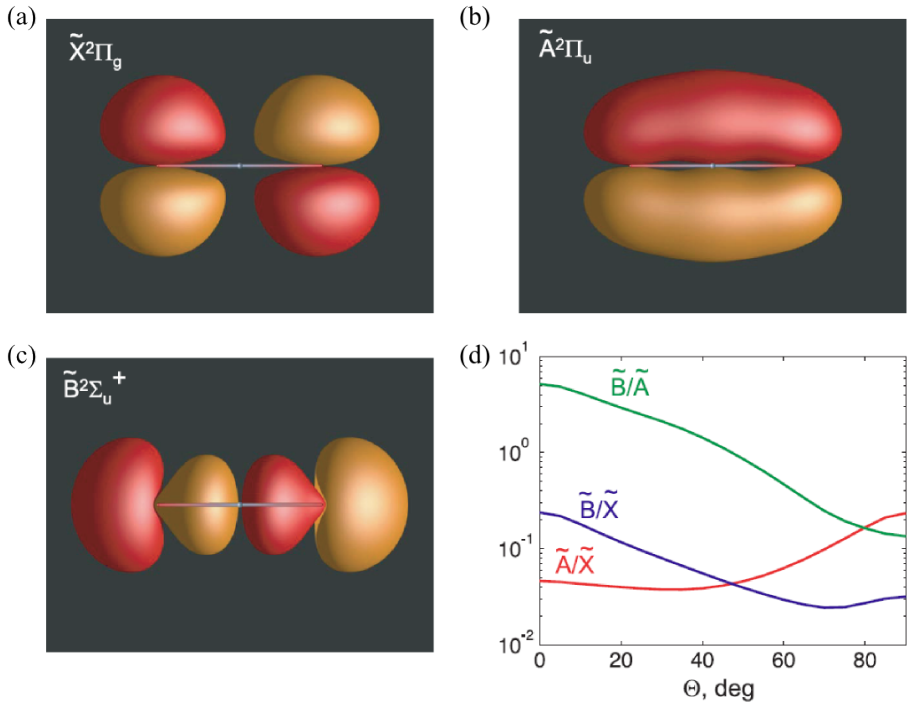


**Figure 2.17.:** Dyson orbitals corresponding different ionization channels in carbon dioxide: (a) X-channel, ground state: $E_X = 13.8\,\text{eV}$, (b) A-channel, first excited electronic state: $E_A = 17.3\,\text{eV}$ and (c) B-channel, second excited electronic state: $E_B = 18.1\,\text{eV}$. The red and orange lobes correspond to different signs of the Dyson orbitals at a level of 90 % of electron density. (d) Relative strong-field ionization amplitudes between different channels (figure adapted from (Smirnova et al., 2009b)).

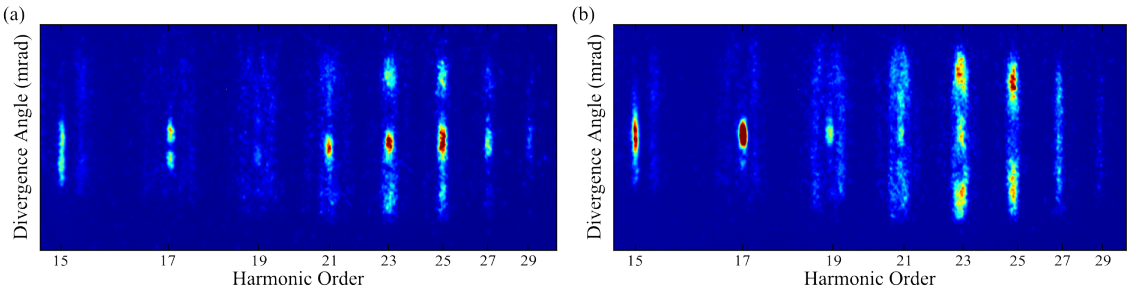


**Figure 2.18.:** Spectra in carbon dioxide at (a) parallel and (b) perpendicular laser polarization for the pump and probe beam. The nozzle temperature is at 80 °C with a backing pressure of 9 bar.

### 2.3.3. High-order harmonic generation in strongly aligned Carbon Dioxide Molecules

The setup used in the previous experiment (Smirnova et al., 2009a) has room for improvement. By using the Even-Lavie valve which delivers a rotationally cold gas jet, and higher alignment pulse intensities, the degree of alignment is enhanced. The degree of alignment is decreased by an increase of the nozzle temperature. The evolution of the harmonic signal corresponding to the short trajectories is illustrated in figure 2.19 and figure 2.20 as a function of alignment angle and nozzle temperature. The selection of the short trajectory signal is realized by selecting the central spot. The signal of the long trajectories is obtained by subtracting the signal of the central spot from the total harmonic signal. At a nozzle temperature of 80 °C harmonic 15, 17 and 19 reach a clear minimum at a parallel or perpendicular alignment angle[5]. The maximum is at an alignment angle between 60° and 70°, where the dominating X-channel is strongly contributing to the high harmonic signal.

The higher harmonic orders (see figure 2.20) reveal a maximum at a parallel alignment angle at low nozzle temperatures, i.e. at a narrow alignment distribution peaked at an alignment angle of 9°. This results from the strong contribution of the B-channel. The maximum vanishes at higher temperatures. The representation of the experimental results in 3D temperature dependent maps emphasizes the importance of a low rotational temperature for the gas sample. Otherwise important features cannot be resolved and experimental results cannot be interpreted correctly.

Figure 2.21 displays the high harmonic signal corresponding to the short trajectories as a function of alignment angle and harmonic order. In parallel alignment the minimum is located at harmonic 19. It moves to harmonic 23 as the alignment distribution deteriorates. The maximum is always located at harmonic 25. This switch from a local minimum to a maximum reflects the switching from one ionization channel to another one. The ionization potential and ionization probability is higher for the B-channel in this molecular orientation. This leads to a dominating signal from this channel for the cutoff harmonics.

A minimum is observed for harmonic 19 at parallel alignment at a temperature of 80 °C. It corresponds to the dynamical minimum, reflecting the destructive interference between the X- and B-channel. As the degree of alignment is decreased this local minimum moves towards harmonic 23 at a nozzle temperature of 180 °C. At 80 °C the local minimum moves to higher alignment angles for higher harmonic orders. This is displayed as a U-shaped minimum in figure 2.21(b). Remember now, that the average angle to polarization direction is 9° at parallel alignment. As the nozzle is heated up, the average angle increases. At a temperature of 80 °C the average angle to polarization direction becomes significant. At an indicated alignment angle of zero in figure 2.21(f) the average alignment angle is 27° with respect to laser polarization. Thus the same effect, which is responsible for the motion of the local minimum to higher alignment angles at 80 °C,

[5]The terms parallel and perpendicular are used with respect to the laser polarization direction.

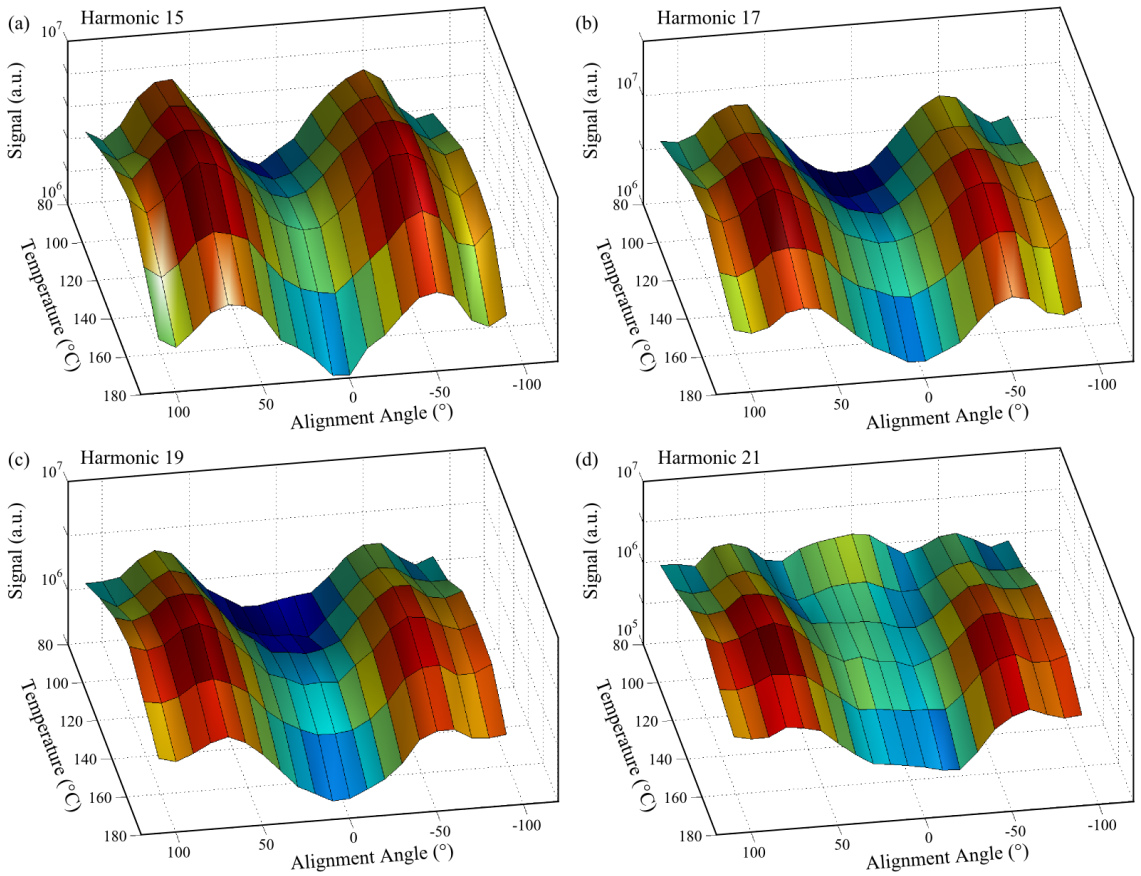


**Figure 2.19.:** High harmonic signal in carbon dioxide as a function of alignment angle and temperature for the short trajectories at a backing pressure of 9 bar. Harmonic 15 (subfigure (a)) to harmonic 21 (d) is illustrated.

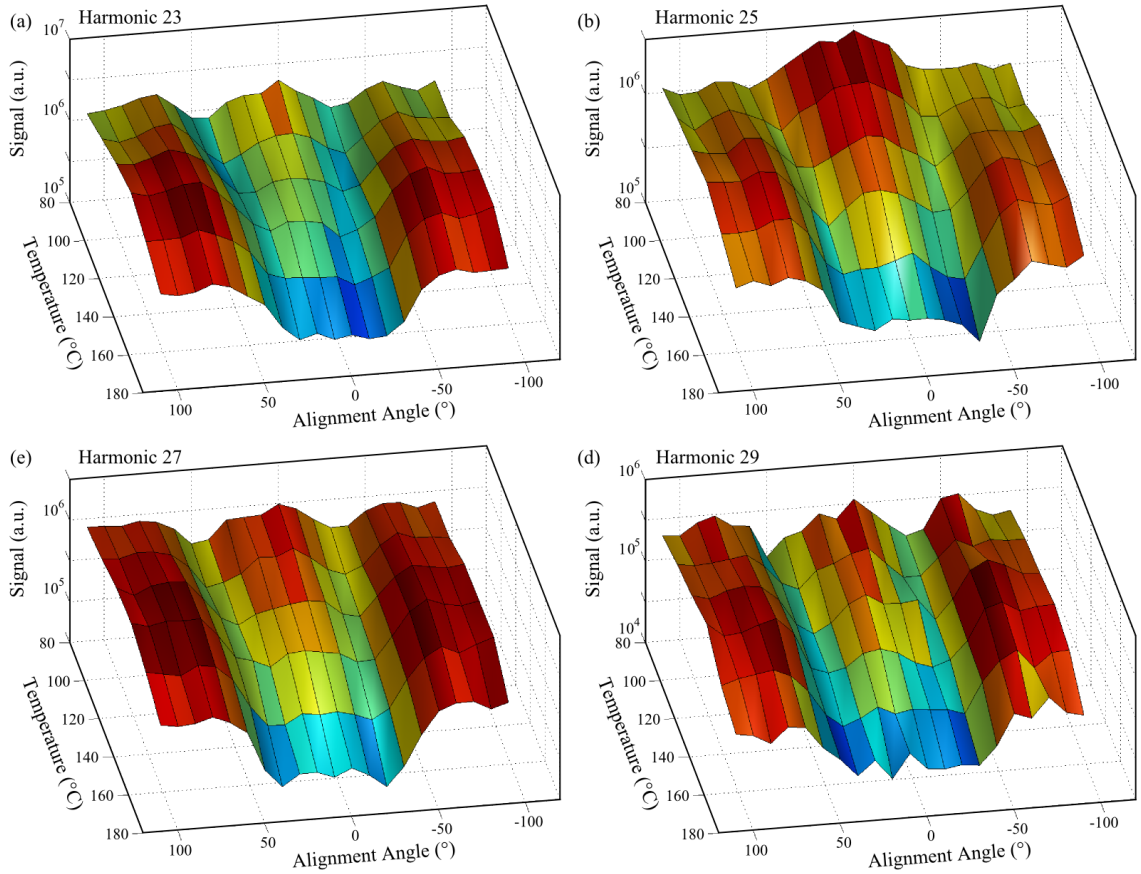


**Figure 2.20.:** High harmonic signal in carbon dioxide as a function of alignment angle and temperature for the short trajectories at a backing pressure of 9 bar. Harmonic 23 (subfigure (a)) to harmonic 29 (d) is illustrated.

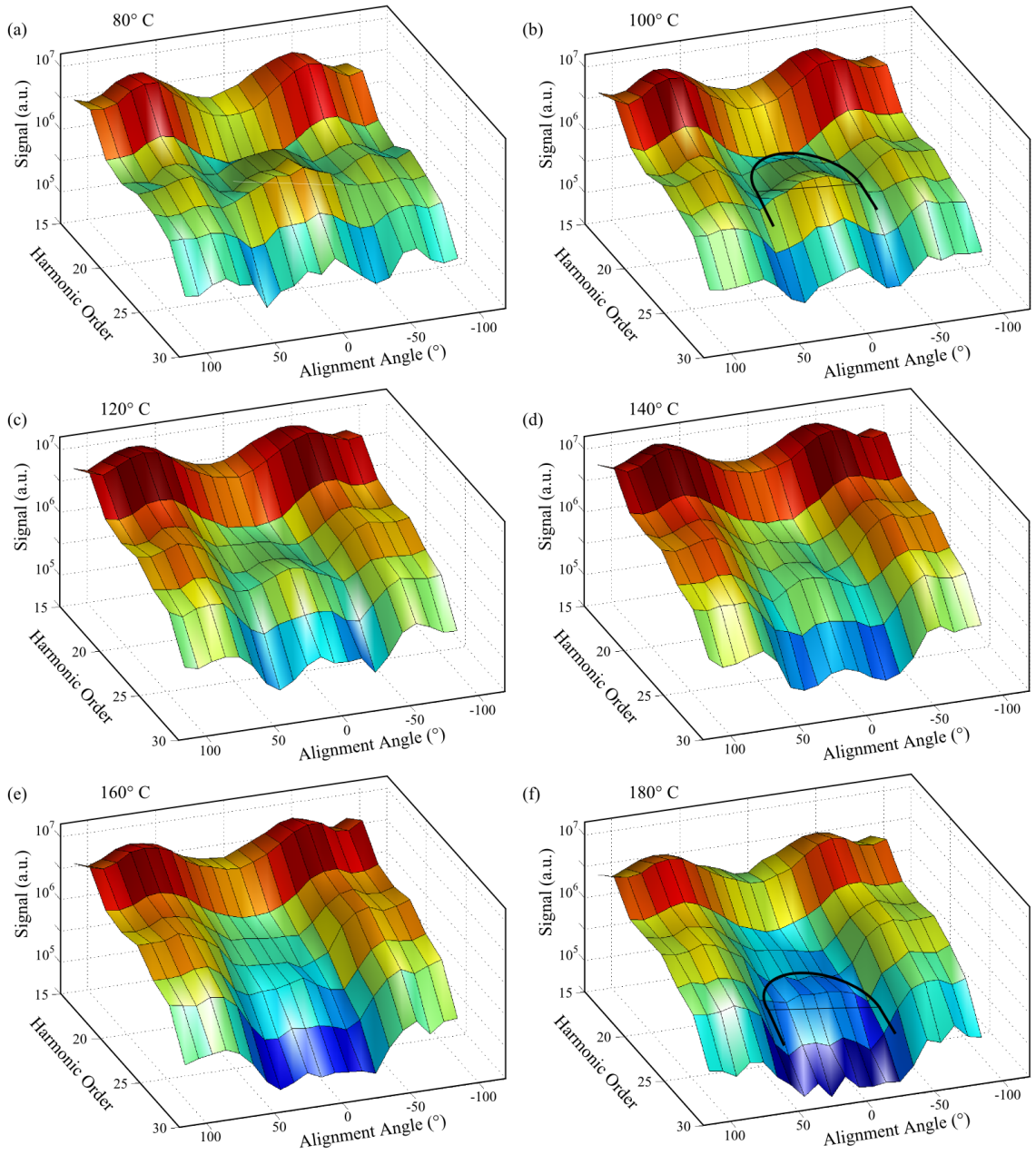


**Figure 2.21.:** High harmonic signal in carbon dioxide as a function of alignment angle and harmonic order for the short trajectories. The backing pressure is 9 bar at increasing nozzle temperatures from (a) 80 °C to (f) 180 °C.

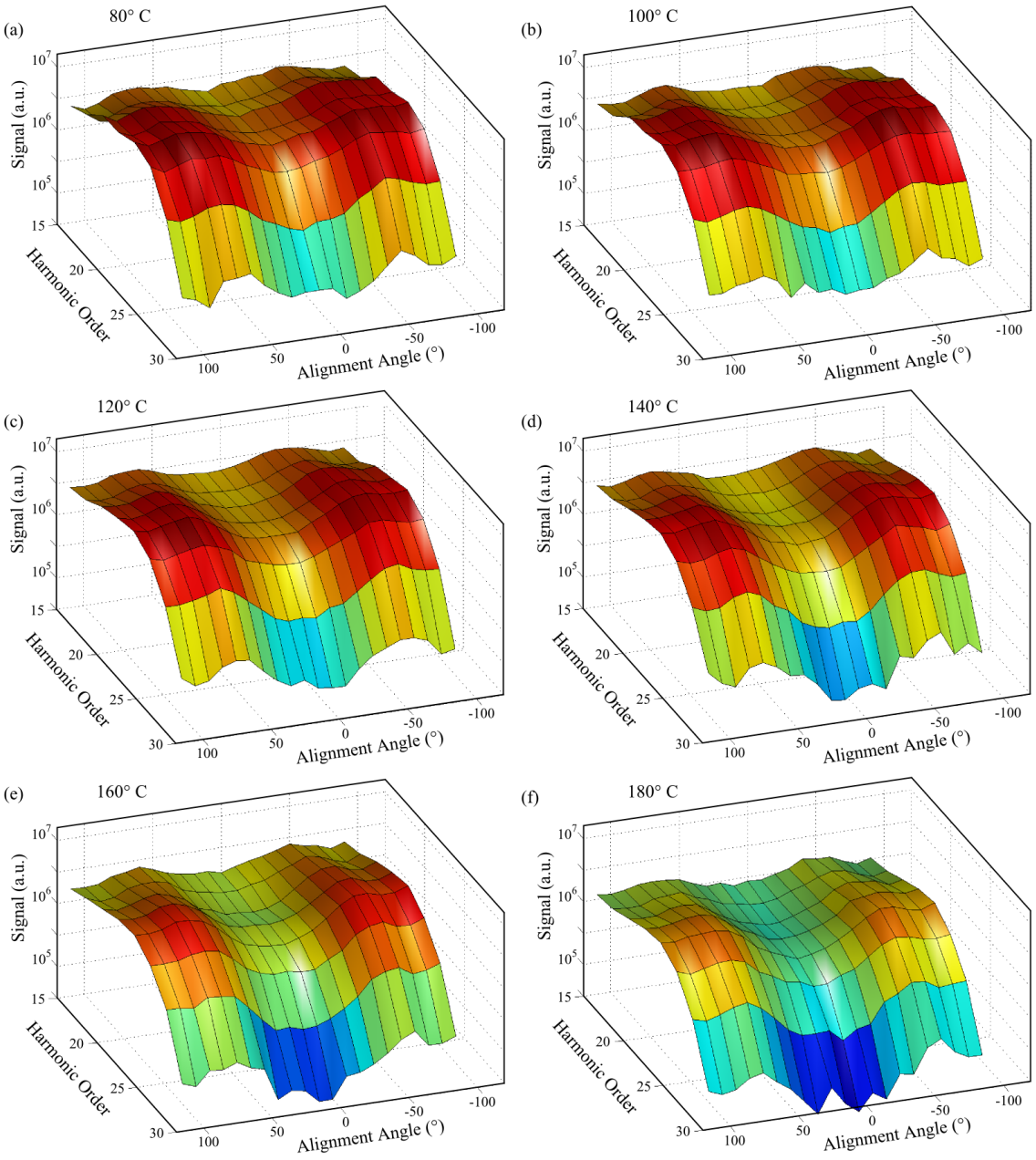


**Figure 2.22.:** High harmonic signal in carbon dioxide as a function of alignment angle and harmonic order for the long trajectories. The backing pressure is 9 bar at nozzle temperatures of (a) 80 °C to (f) 180 °C.

pushes the minimum from harmonic 19 to harmonic 23 when increasing the temperature. The location of the minimum at parallel alignment can thus be used as a relative measure of the alignment distribution at same generation conditions. The lower degree of alignment strongly influences the interference between the X- and B-channel. The weight of the B-channel to the harmonic signal is decreased with a deteriorated alignment distribution. Another effect is also observed when heating up the jet nozzle. The contrast of the minima at parallel and perpendicular alignment is less pronounced at higher temperatures for harmonic 15, 17 and 19.
Figure 2.22 illustrates the same 3D-maps for the signal from the long trajectories. The overall signal decreases due to lower pressures at high nozzle temperatures. Harmonic 17 also seems to show a local maximum at all alignment angles for nozzle temperatures of 80 °C and 100 °C. Apart from these features the maps show identical structures for all harmonic signals, a minimum at parallel and perpendicular alignment angle and a maximum at an alignment angle between 60° and 70°. A minimum cannot be detected in this condition. The influence from the B-channel at parallel alignment is not clear. This emphasizes, that origin of the minimum is dynamical.
The experimental results in strongly aligned molecules show a dynamical minimum at lower harmonic orders than in reference (Smirnova et al., 2009a). We attribute this observation to the higher degree of alignment. Latest calculation predict an involvement of the C-channel ($I_p$ =13.8 eV+5.6 eV = 19.4 eV) which couples with the other channels. The simulation implies that the X- and A-channels dominate for the lower harmonics the wheras the B- and C-channel take over for the higher harmonics.

## 2.4. Conclusion and Outlook

We examined the rotational excitation of nitrogen and carbon dioxide molecules by a femtosecond laser pulse with pump probe spectroscopy using HHG as a probe signal. To achieve a high degree of molecular alignment the molecules must be rotationally cold before. This goal is achieved by employing a strongly collimated supersonic molecular jet (Even-Lavie) which enabled us to generate high harmonics at a distance of 42 nozzle diameters from the nozzle. Furthermore a non-collinear pump probe setup was used which did not limit pump intensities. These two improvements allowed us to reach very low estimated rotational temperatures of 5 K. We measured the high harmonic signal of short and long trajectories as a function of pump-probe delay and alignment angle.
The harmonic signal in nitrogen is recorded as a function of pump-probe and delay reveals a new feature at low rotational temperatures. A local maximum at the anti-alignment of the full revival for the cutoff harmonics is interpreted as a strong contribution from the A-channel to the signal. When recording the signal as a function of alignment angle, a minimum is observed for the higher harmonic orders. The minimum moves when the intensity is changed. This might be attributed to the interference between the X- and the A-channel. We thus recorded for the first time a minimum with a dynamical behaviour

in nitrogen. The second new characteristic at a generation wavelength of 800 nm is the strong enhancement of harmonic 17 and 19 at parallel alignment revealing a recently predicted structure: the shape resonance in nitrogen (Jin et al., 2012).
The low rotational temperatures also allowed the measurement of a signal with a higher resolution in carbon dioxide. The signal from the higher order harmonics is clearly stronger at lower nozzle temperature at parallel alignment. The dependence of the dynamical minimum is studied as a function of nozzle temperature, i.e. alignment distribution. We observe a minimum that moves to lower harmonic orders at the improved distribution. These results are currently theoretically reproduced, predicting a fourth channel being involved.
As the interaction between different channels can be better resolved these results will also change the current picture electron-hole dynamics for carbon dioxide (Smirnova et al., 2009b,a) and nitrogen (Haessler et al., 2010). Alignment suffices for these two symmetric molecules but in case of asymmetric molecules, alignment is not adequate any more, control of orientation is necessary. Frumker and coworkers recently achieved orientation in combination with HHG in carbon monoxide by breaking the symmetry of the aligning pulse (Frumker et al., 2012). Orientation techniques together with the utilization of the Even-Lavie valve will set new standards for future experiments. Also orbital tomography benefits from the enhanced alignment distribution. Amplitudes and phases which are crucial for orbital reconstruction are expected to be measured with higher accuracies.

## Résumé du Chapitre

*Nous avons montré que la GHOE pouvait être utilisée pour étudier la structure orbitale d'un atome: l'argon. Nous avons ici étendu les études à des petites molécules linéaires comme l'azote ou le dioxyde de carbone. L'alignement des molécules est arbitraire dans un jet de gaz. Pour observer la signature de la structure moléculaires dans un signal harmonique il convient de réaliser un alignement macroscopique préalable des molécules. L'alignement moléculaire est cependant possible à l'aide d'une impulsion laser focalisée qui brise l'isotropie de la cible macroscopique (Rosca-Pruna and Vrakking, 2001). Pourtant la distribution de l'alignement dépend crucialement de la température rotationelle des molécules du jet de gaz. Une vanne Even-Lavie permet d'atteindre des températures basses avec une excellente distribution d'alignement qui satisfait une condition importante pour la GHOE: des impulsions de gaz très brèves avec une densité élevée. Une expansion de gaz supersonique avec un angle d'expansion fortement collimaté permet de générer des harmoniques d'ordre élevé à une distance de 42 diamètres du col de tuyère. On estime une température rotationnelle de 5 K. C'est une température qui n'était pas encore obtenue dans le contexte de la GHOE, établissant une nouvelle norme pour les futures expériences de l'imagerie des dynamiques moleculaires (Smirnova et al., 2009b; Haessler et al., 2010), mais aussi pour la tomographie orbitale (Itatani et al., 2004).*

*Avec ce degré élevé d'alignement nous sommes capables de résoudre une résonance de forme dans l'azote qui a été récemment prédite dans la section efficace différentielle de photoionisation (Jin et al., 2012). Cette résonance de forme est attribuée à un état auto-ionisant qui entraîne une amélioration de la résonance. Grâce aux basses températures rotationelles nous avons observé un minimum avec les caractéristiques d'un minimum dynamique. Ce minimum dynamique se révèle quand on change l'intensité de l'impulsion de génération. Un comportement dynamique provient de l'interférence entre les différentes orbitales. Ce type de minimum est bien établi dans le dioxyde de carbone (Smirnova et al., 2009a) et montre une dépendance sur la distribution de l'alignement dans nos mesures. Nous avons aussi été capable de mesurer le signal avec une résolution plus haute dans le dioxyde de carbone. Les résutats sont actuellement reproduits par des simulation théoriques qui montrent la contribution d'une orbitale supplémentaire. Grâce à un alignement fort nous avons été capable de mieux résoudre des caractèristiques structurelles et dynamiques. Cet alignement fort est nécessaire pour comprendre les dynamiques attosecondes qui jouent un rôle dans l'ion moléculaire pendant le temps de vol de l'électron.*

# 3. High Harmonic Transient Grating Spectroscopy probing electronic Relaxation of $NO_2$

Rotational wave packet revival in linear molecules have been studied in the last chapter. This trivial dynamical behaviour becomes more complex if chemical reactions of nonlinear molecules are studied. A deep understanding of these reactions requires the ability to observe dynamics on an atomic time scale namely femtoseconds. Comprehension of these reactions is of fundamental interest and is the first step towards their control. Ahmed H. Zewail was awarded the Nobel price of chemistry for his breakthroughs in the field of Femtochemistry (Zewail, 2000) which has undergone a rapid development since then. The dynamics of a chemical reaction are determined by the electrons occupying the highest occupied molecular orbitals (HOMOs) or in other words the valence electrons. Several techniques have been applied for tracing valence electron dynamics. Electron diffraction with a ps-resolution was employed for direct imaging of transient molecular structures (Ihee et al., 2001) and was later extended to a self-probing scheme (Meckel et al., 2008). With photoelectron spectroscopy (Nugent-Glandorf et al., 2001; Blanchet et al., 1999) the resolution of these dynamics was pushed to the fs-time scale. A very recent method, time-resolved holography with photoelectrons, might be extended from atoms to molecules to time resolve electron dynamics (Huismans et al., 2011).
The previous chapter emphasized the sensitivity of HHG to the symmetry of molecular orbitals in a self-probing scheme. HHG was used in this context as a very sensitive probe as demonstrated in the vibrational dynamics of $SF_6$ (Wagner et al., 2006; Walters et al., 2007). This approach has been extended to the case of $N_2O_4$ resolving the Raman-active vibrational modes (Li et al., 2008). A more sophisticated method has been is used in the context of this thesis: HHG combined with transient grating spectroscopy, first demonstrated by Mairesse and coworkers (Mairesse et al., 2008c). The transient grating setup utilizes two pump pulses in a crossed geometry creating an excitation grating. Compared to the common pump-probe setup it allows the extraction of phase information and a very high sensitivity as the background is omitted for diffracted orders. This technique was used successfully shortly after its first demonstration, for tracing the dissociation of $Br_2$ (Wörner et al., 2010).
In this chapter the dissociation and electronic relaxation of $NO_2$ are studied. $NO_2$ is interesting from two different point of views: an atomospheric one and a fundamental scientific one. First $NO_2$, a reddish brown toxic gas, plays a crucial role in the ozone cycle of the troposphere. A considerable source of $NO_2$ are combustion engines and biomass burning. These processes contribute directly to the production of summer smog and do not only reduce the local air quality but also increase tropospheric ozone globally and thus effect

the ozone cycle (Richter et al., 2005). Tropospheric ozone is not only a greenhouse gas but also reacts oxidizing with other chemical compounds in the atmosphere. It therewith changes the gas concentration of the atmosphere but also creates toxic oxides. Studying the photodissociation, a process which is induced by UV light in the atmosphere, will allow us to get a better understanding of these fundamental processes in the atmosphere. Second the first electronic excited state of $NO_2$ is strongly coupled to its ground state through a conical intersection. Nuclear motion is determined by the potential energy surfaces (PES) corresponding to the different electronic states (Yarkony, 1996). A conical intersection permits a coupling between the two PES at certain molecular coordinates. They play an important role in photochemistry because they convert electronic energy into nuclear kinetic energy (Whitaker, 2011). Until now the conical intersection of $NO_2$ has been mainly studied theoretically (Santoro and Petrongolo, 1999; Santoro et al., 2000; Sanrey and Joyeux, 2007; Arasaki and Takatsuka, 2007; Arasaki et al., 2010). $NO_2$ is however compact molecule with a conical intersection that is experimentally seizable. HHG transient grating spectroscopy is employed for studying $NO_2$ around its conical intersection.
Before introducing the experimental setup the molecular system $NO_2$ is presented. An experimental study of the photodissociation of $NO_2$ on a picosecond timescale follows. Then a simulation of HHG of the excited $NO_2$ is demonstrated which reveals interesting dynamical features. The simulation is compared to the experimental results. The chapter summarizes the result of two experimental campaigns, one conducted at the NRC Steacie Institue at Ottawa, Canada and the other at CELIA, Bordeaux, France. The two studies agree in general but lead to slightly different experimental results which are interpreted controversially (Wörner et al., 2011; Ruf et al., 2012).

## 3.1. Potential Energy Surfaces of $NO_2$

The potential energy in the $NO_2$ molecule depends on its bond angle and the distances between the respective nitrogen and oxygen atoms $R_1$ and $R_2$. In the ground state the point group of $NO_2$ is $C_{2v}$ with the two oxygen atoms having the same distances to the center nitrogen atom ($R_1 = R_2$). After excitation the symmetry reduces to $C_s$ with $R_1 \neq R_2$.
Different models of potential energy surfaces (PES) have been developped (Leonardi et al., 1996; Kurkal et al., 2003; Arasaki and Takatsuka, 2007). The second one turns out to be the most reliable for studying $NO_2$ at dissociation. Kurkal and coworkers use sophisticated ab initio calculations based on a multireference configuration interaction (MRCI) level taking a large basis set. They provide the potential surfaces for the ground state and first excited electronic state of the molecule in two different representations. Treating the coupling at the avoided crossing (conical intersection) in the adiabatic representation is technically very demanding (Kurkal et al., 2003). This imposes diabatization of the surfaces by a unitary transformation (rotation) of the adiabatic states and thus smoothes

out the strong variation. Both representations are depicted in figure 3.1. The conical intersection is only visible in the adiabatic representation illustrating the strong electronic coupling between the excited and ground state. In diabatic representation the energy minimum of the electron ground state and excited state are shifted with respect to the nuclear coordinates. This implies that after excitation of the $NO_2$ molecule to the first excited state, the electron wave packet relaxes towards this minimum as the pendulum of a clock. But unlike this pendulum two different dynamics happen on different timescales. The faster dynamic takes place on a femtosecond timescale as the electron wave packet moves along the bending coordinate, passing the crossing seam[1] and possibly changing the energy surfaces to the ground state. Excitation is most efficient along the O-O axis of $NO_2$. Therefore the polarization of the pump pulses acts as an alignment selection of the molecules. If the $NO_2$ molecule is excited by a photon with an energy of 3.22 eV ($\lambda = 400$ nm) (Ionov et al., 1993) or higher it dissociates on a picosecond timescale what is visualized in figure 3.1(a) as the distance between oxygen and nitrogen increases.

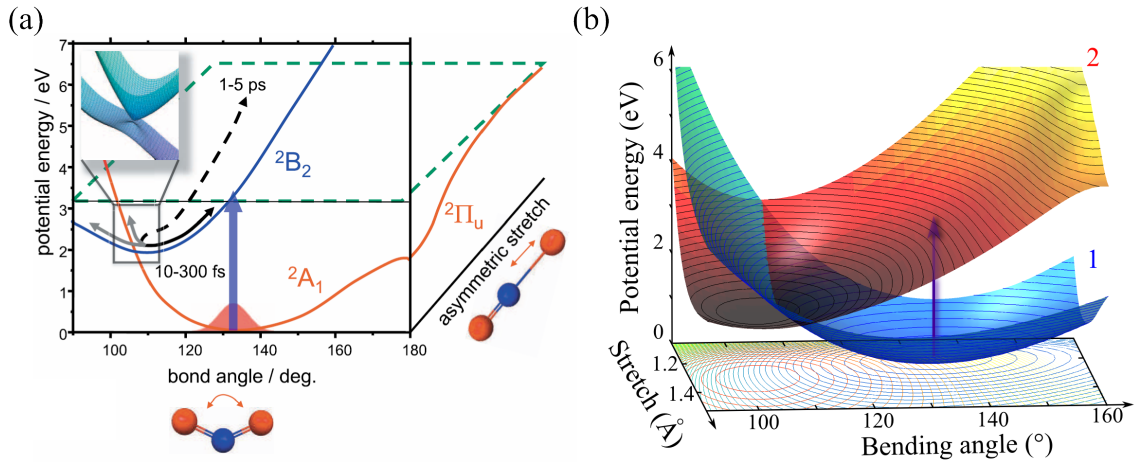


**Figure 3.1.:** (a) Potential energy surface in diabatic representation depicting the ground and excited electronic state of $NO_2$ as a function of bond angle and NO distance. The inset shows the adiabatic represention with its conical. (b) Potential energy surface in diabatic representation with the $1^2A'$ ground and the $2^2A'$ excited electronic state of $NO_2$ as a function of bond angle and NO distance $R_1$. In both images the asymmetric stretch $R_2$ is fixed.

The diabatic representation (see figure 3.1(b)) is needed for further trajectory surface hopping (TSH) simulations. The PES in the diabatic representation calculated by Kurkal and coworkers (Kurkal et al., 2003) neglects the electronic coupling between the ground and excited state. The electronic coupling $V_{12}$ remains after diabatization. It can be expressed by the diabatic energies[2] $E_1$ and $E_2$ and adiabatic energies $E_X$ and $E_A$ of the

[1] Diabatization imposes a minimization of the coupling for the three molecular coordinates (Kurkal et al., 2003). The conical intersection thus disappears and turns into a crossing seam (see figure 3.23).

[2] 1 and 2 correspond to the ground and excited state respectively in the text.

ground and first excited state respectively:

$$V_{12}^2 = \frac{1}{4}[(E_A - E_X)^2 - (E_2 - E_1)^2] \tag{3.1}$$

The electronic coupling can be different from zero when the distances between the oxygens and nitrogen atom $R_1$ and $R_2$ are not equal. In regions with strong coupling the sign of $V_{12}$ is not clear from equation 3.1 but is in a first approximation proportional $Q_- = R_1 - R_2$.

## 3.2. Transient Grating

Electron dynamics take place on a femto- to attosecond time scale. Femtosecond time scales can be seized with a simple pump probe setup: A pump pulse excites the sample of interest and a second pulse probes it at different time delays after excitation. The time delay between the pump and probe pulse is controlled spatially with a translation stage (see figure 3.3). The relative time delay between two pulses is tuned by changing the propagation length between the two pulses: $\Delta t = \Delta s/c$. For example 10 fs of time delay corresponds to 3 $\mu$m of propagation length difference. The time resolution of such a setup is limited by the pulse duration of both pulses and the smallest step size of the translation stage.
The signal change after such an excitation can be very weak leading to an unfavourable S/N ratio. In case of electrical signal a Lock-In Amplifier can be used for improving the S/N ratio. This electric filtering method cannot be applied for optical signals. Therefore another elegant approach is chosen, namely transient grating spectroscopy. This technique is based on four-wave mixing with a perturbative behaviour (Boyd, 1992; Bertrand et al., 2011). This approach has been used within the context of conventional nonlinear spectroscopy (Rouzée et al., 2007) and shortly afterwards in combination with HHG (Mairesse et al., 2008c).

In the following, we describe only the setup employed at Bordeaux. Where necessary comparisons are drawn with the setup built at Ottawa. As illustrated in figure 3.2, two non-collinear beams are overlapped in time and space creating an optical interference grating in the $NO_2$ gas jet. This is achieved by using two parallel beams, vertical one above the other, separated by a distance between the beams of $d = 16$ mm. They are focussed by a concave silver mirror with a focal distance of $f = 0.375$ m into the gas jet. The fringe spacing of the grating $a$ is calculated by the following formula:

$$\theta = 2 \arctan\left(\frac{d}{2f}\right) \tag{3.2}$$

$$a = \lambda_{pump}\frac{\cos(\theta/2)}{\tan(\theta)} \tag{3.3}$$

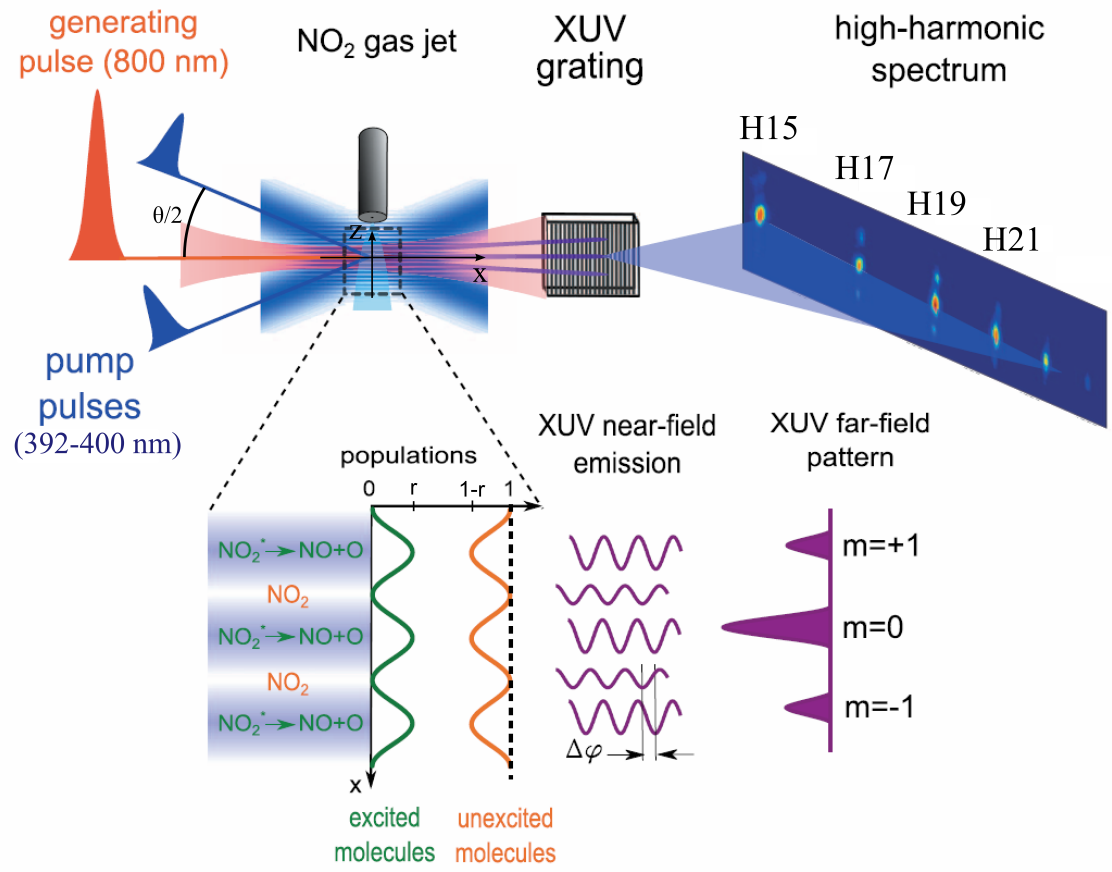


**Figure 3.2.:** Principle of the transient grating. Two non-collinear synchronized pump beams are crossed with an angle $\theta$ and create an optical grating which itself induces a spatial modulation of molecular excitation. The diffracted light, induced by the optical grating, is spatially clearly separated from the undiffracted light.

where $\lambda_{pump} = 400\,\text{nm}$ is the pump wavelength. If $\sin(\theta) \approx \theta \approx \tan(\theta)$ holds equation 3.3 can be simplified to:

$$a = \frac{\lambda_{pump} f}{d} \tag{3.4}$$

This provides a sinusoidal intensity modulation with a fringe spacing of 9.4 $\mu$m. At positions of low intensities, molecules remain as they are, at high intensities they are excited however. This leads to a grating with a spatial modulation of excited and unexcited molecules (see figure 3.2), or in other words a grating of molecular excitation with a fringe spacing of 9.4 $\mu$m. As amplitude and phase of the generated high harmonics are different for excited and unexcited molecules in the near field the grating thus leads to a diffraction pattern in the far field. The diffracted signal, which carries the signature of the excited molecules, is spatially well separated from undiffracted light and therewith significantly improves the signal. In the case of only one pump beam this signal is overlapped by the harmonic signal which contributes only as a time-independent background.
The lower part of figure 3.2 illustrates the spatially modulated fraction of excited molecules which has its maximum value $r$ at constructive interference of the optical grating. With $k = 2\pi/a$ defined by the fringe spacing $a$, the fraction of excited molecules is expressed as $r(z) = r(cos(kz) + 1)$ in case of a single photon excitation process. The dipole moment with amplitude $d$ and phase $\phi$ of the XUV emission for a certain photon energy $\Omega$ is $E_g(\Omega) = d_g e^{i\phi_g}$ for the molecules in the ground state and $E_e(\Omega) = d_e e^{i\phi_e}$ for the molecules in the excited state. The coherent superposition of these two fields leads to the high harmonic emission across the transient grating in the near field:

$$\begin{aligned} E(\Omega,z) &= E_g(\Omega,z) + E_e(\Omega,z) \\ &= (1 - r(z))d_g e^{i\phi_g} + r(z) d_e e^{i\phi_e} \end{aligned} \tag{3.5}$$

Fraunhofer diffraction delivers the far field pattern of the emitted high harmonics, it is obtained by applying the Fourrier transform on the near field profile (Hecht, 2002):

$$\begin{aligned} \mathcal{FT}(E(z)) =& \Big((1-r)d_g e^{i\phi_g} + r d_e e^{i\phi_e}\Big)\delta(\xi) \\ &+ \frac{r}{2}\Big(d_e e^{i\phi_e} - d_g e^{i\phi_g}\Big)\Big(\delta(\xi + \frac{k}{2\pi}) + \delta(\xi - \frac{k}{2\pi})\Big) \end{aligned} \tag{3.6}$$

This equation gives the signal of the undiffracted ($m = 0$) and the diffracted light ($m = \pm 1$):

$$I_{m=0} = |r d_e e^{i\phi_e} + (1-r) d_g e^{i\phi_g}|^2 \tag{3.7}$$

$$I_{m=\pm 1} = \frac{r^2}{4} |d_e e^{i\phi_e} - d_g e^{i\phi_g}|^2 \tag{3.8}$$

As the signal from the molecules in the ground state is the dominating contribution in the undiffracted light the signal from the excited molecules has only a much lower relative contribution. The first order diffracted light always delivers a difference signal independent from the fraction of excited molecules. This fraction is usually low, on the order of several percent. $d_g e^{i\phi_g}$ can be understood as a reference signal in a homodyne detection scheme.

### 3.2.1. Experimental Setup and Alignment Procedure

Figure 3.3 illustrates the experimental setup for high harmonic transient grating spectroscopy of $NO_2$. For this experiment the Aurore Ti:Sa-Laser system at CELIA is employed delivering pulses with an energy of 7 mJ, and a pulse duration of 25 fs (see chapter 1, section 1.5.4). A beam splitter reflects 20% of the laser energy which is used as the pump beam. 80% are transmitted and used as the probe beam. The relative delay between these two beams is controlled by a computer controlled translation stage (Newport). The polarization of the probe beam is controlled by a $\lambda/2$-plate. The pump beam diameter is reduced by a factor of 2.5 using a convex and a concave mirror as a telescope. The frequency is doubled by a type 1 SH-BBO crystal (Eksma) with a thickness of 200 $\mu$m. In order to make sure that the chirp is the same for HHG and second harmonic generation (SHG), the dispersion induced by the beamsplitter and the entrance window of the vacuum chamber is compensated. A BK7 window (d = 5 mm) and a $SiO_2$ (d = 3 mm) window are installed between the beam splitter and the SH-BBO crystal. The thickness of the crystal still permits a considerable tunability of the spectrum without temporarily broadening the frequency doubled pulses too much. With a spectral FWHM of 7 nm the expected Fourier limited pulse duration assuming a Gaussian pulse profile is 33.6 fs. The pump beam is split further by a 50/50 beamsplitter. Dichroic and dielectric mirrors with a low reflectivity for a wavelength of 800 nm and a high reflectivity at 400 nm are used for filtering out the fundamental beam. The relative delay between the two pump beams is controlled by a manual translation stage in one of the two pump arms. An adjustable aperature inserted between the BBO crystal and the 50/50 beamsplitter allows us to tune the pump energy in each arm between 10 and 35 $\mu$J per pulse. The two pump beams are recombined on a silver mirror with a diameter of two inches. The center of the mirror is drilled at 45° with a diameter of 10 mm. The probe beam passes through the hole whereas the two pump beams are reflected at a vertical distance of 8 mm above and below the center of the mirror. The three parallel beams are in a plane vertical to the experimental table and focussed by a silver mirror with a focal length of 37.5 cm into the $NO_2$ gas jet. A small angle of incidence (AOI) of 2.8° on the silver mirror ensures a negligible astigmatism at focus.
The pump energy is controlled with an iris in front of the BBO crystal. Depending on the iris diameter the waist radius of the blue beams varies between 60 $mu$m and 170 $\mu$m (following the calculations of appendix B). With a fringe spacing of 9.4 $\mu$m, the optical grating consists of 10 to 20 periods. With a waist radius of approximately 60 $\mu$m (see

appendix B) for the region of HHG, the transient grating always overlaps with it and consequently provides diffraction. The probe intensitiy deduced from the the harmonic cutoff is about $1.2 \times 10^{14}\,\mathrm{W/cm^2}$. The detection scheme of the XUV emission is commented in chapter 1, section 1.5.4. The created ions are dectected by means of a mesh connected to high voltage. Therefore the nozzle has to be grounded. The signal is detected after filtering out the low frequencies with a high-pass-filter.
Two different valves provided the generation medium. In the first case a General valve with a nozzle diameter of 100 $\mu$m, was employed at a repetition rate of 100 Hz with a backing pressure of pure $NO_2$ at $\approx$ 780 mbar. High harmonic emisssion was produced at a distance of a few 100 $\mu$m from the nozzle. Dimer formation is reduced by heating the nozzle to 80°C leading to only 10 % $N_2O_4$ in the gas. Additionally owing to its low excitation probability of 4 % (Roscoe and Hind, 1993) at 400 nm $N_2O_4$ is not expected to influence the harmonic yield. The second valve is an Even-Lavie valve that can be operated at a repetition rate of 1 kHz. In contrast to the General valve it is also corrosion proof. The great disadvantage of this valve is however a required minimum backing pressure of 12 bar for operation. A gas mixture of helium and $NO_2$ is prepared for reaching pressures around 16 bar. A conical nozzle with a diameter of 250 $\mu$m is employed with a focus distance of approximately 1.6 mm from the throat of the nozzle. As lower rotational temperatures (see chapter 2) are expected for this kind of valve, different dynamical behaviour might possibly be observed.

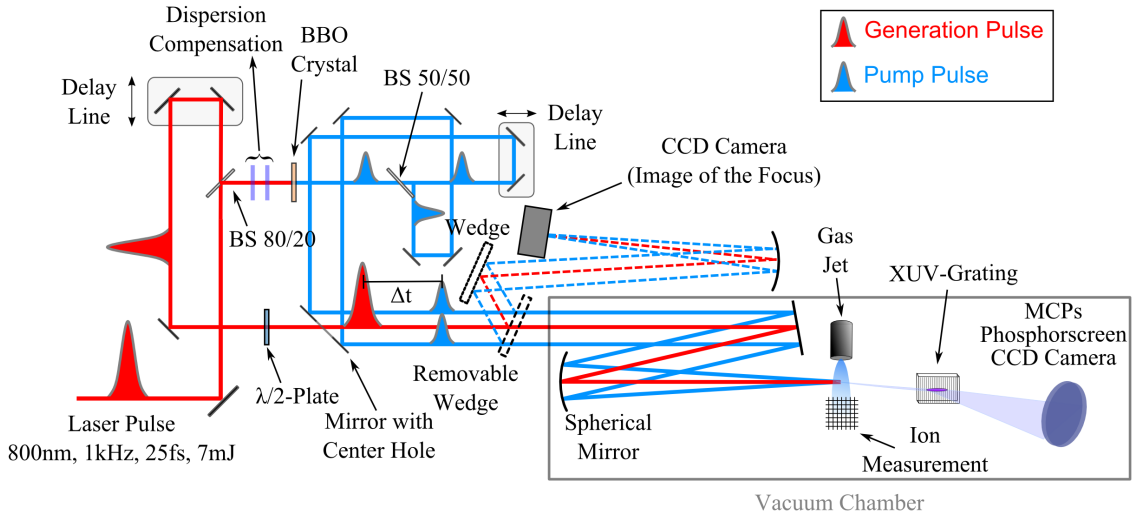


**Figure 3.3.:** Transient grating setup for $NO_2$.

The alignment procedure is tricky as three independent parameters (time delay, z- and y-direction) need to be well adjusted for a spatial and temporal overlap between the pump and probe beam. To begin with it starts with finding the spatial overlap before finding the temporal one.
The spatial overlap is checked by imaging the overlap of the focii of the three beams on a

CCD camera. In order to prevent damage of the CCD chip two wedges and neutral density filters are employed. A removable wedge is installed just in front of the vacuum chamber. It is mounted on a rail and can reliably be moved back in exact the same position as it was in before being removed. The image of the beam is done by a silver mirror with exactly the same focal length as the concave mirror used for focussing the beam into the gas jet. Note that the distance between the wedge and the two focussing mirrors has to be the same respectively because the two pump beams are not exactly parallel to each other. This would change focussing conditions if the distances were different and therewith create a different overlap in the generating chamber than observed by the camera. Also the aperature diameter should be maintained as in generation conditions for the image on the CCD camera.
Once the spatial overlap is obtained two different methods can be applied for finding the zero delay btween pump and probe pulse. In the first case, the third harmonic order is generated in a BBO crystal by one pump and the generation beam. The generated 266 nm light is observed as fluorescence on a white paper after spatial separation from the 400 nm and 800 nm light by a prism. Shadowgraphy is the second method: a plasma is generated in air by the fundamental laser beam employing a concave mirror with short focal length ($f \approx 10$ cm). The plasma creates a shadow in the blue pump beam what can be observed on a screen well behind the focus. One major advantage of this method is, that the plasma has a lifetime on the order of nanoseconds and therefore influences the pump beam even if the distance between pump and probe beam is still several millimeters. When decreasing the distance difference between the two beams the shadow of the pump beam on the screen becomes stronger up to a point when it suddenly disappears. This happens when the pump beam is in advance of the red probe beam and is therewith unaffected by the plasma. Both methods do also require a good spatial overlap of the two beams. In case of the second method the pattern might be difficult to observe at the beginning, what is often a question of spatial overlap. By tweaking the last mirror of the pump beam the shadow is enhanced. Once the temporal overlap is established for the fixed pump beams by tuning the automatic translation stage of the probe beam the temporal overlap has to be found for the other beam, this time by moving the manual translation stage. A perfect temporal and spatial overlap can be verified on the CCD camera. The image of the interference pattern of the two pump beams should form a nice grating which is overlapped by the probe beam.

Further optimization (spatial and temporal) is done directly in the harmonic signal when generating in argon, again beginning with the fixed pump and the probe beam. The goal is to create a strong wave mixing pattern (Bertrand et al., 2011) as illustrated in figure 3.4. This is done iteratively and repeated for the second beam. Once the perfect overlap is achieved for the three beams, the experiment is ready for high harmonic transient grating spectroscopy in $NO_2$. Depending on the stability of the laser, the fine alignment has to be repeated once or twice a day.

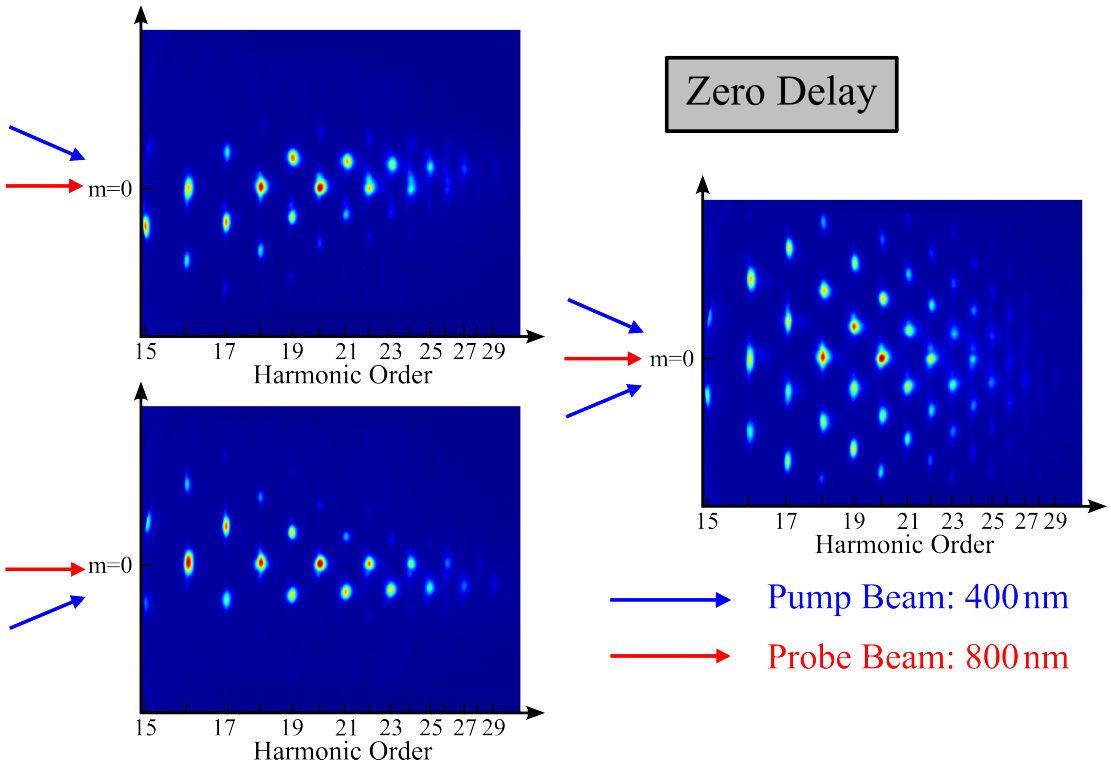


**Figure 3.4.:** Wave mixing between the red and blue beams at zero delay when generating in argon.

## 3.3. Photodissociation of $NO_2$ on a Picosecond Timescale

Photodissociation of $NO_2$ has been investigated in the past, studying the laser induced fluorescence signal in NO. The group around Curt Wittig worked intensively on photodissociation of $NO_2$ at different molecular temperatures and different photoexcitation wavelengths. In a first study (Ionov et al., 1993), the dissociation time of $NO_2$ was determined between 0.4 ps and 6.25 ps. At room temperature (rotationally warm molecules) the dissociation time increases from 0.4 ps to 5.88 ps when increasing the excitation wavelength from 375.2 nm to 401.7 nm. In rotationally cold molecules ($T = 6$ K) the dissociation time increases from 0.36 ps to 6.25 ps when increasing the excitation wavelength 382.0 nm to 397.8 nm. Dissociation is even suppressed at higher wavelengths. The dissociation time was also found to be higher for cold molecules than for warm molecules. In a second study (Stolyarov et al., 2002) molecules that were rotationally colder ($T = 1.3$ K) have been investigated. The dissociation time increased dramatically and was determined between 8 ps and 51 ps for wavelengths between 397.5 nm and 397.9 nm.
Here the pump-probe signal of the first order diffracted light $I_1$ and undiffracted light is traced. Figure 3.5(a) depicts the evolution of the two signals when pumping at 395 nm with pump and probe polarization orthogonal to each other. The figure combines two different scans, one with a stepsize of 10 fs in a time window between -100 fs and 500 fs and the other with steps of 250 fs between 0.5 ps and 5.5 ps. Each measuring point was averaged over 1250 laser shots. The next section will treat femtosecond dynamics, for now we stick to the picosecond timescale.

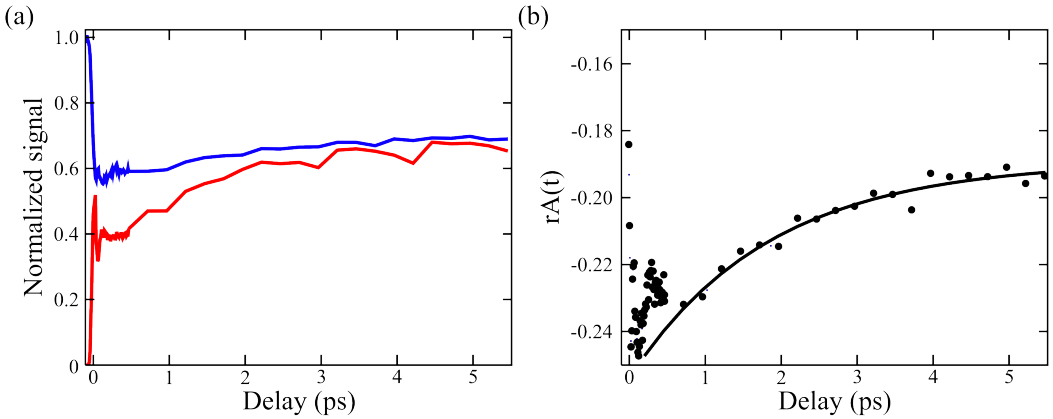


**Figure 3.5.:** (a) Probe signal of the diffracted signal $I_1$ (red) and undiffracted signal (blue) from harmonic 15 using a pump pulse centered at 395 nm. Both pump pulses had an energy of 20 $\mu$J respectively and were polarized perpendicularly to the probe pulse. The diffracted signal is multiplied by 35. (b) Evolution of $rA(t)$ with the associated fit providing a dissociation time $\tau = 1.8 \pm 0.3$ ps.

After excitation the signal of the undiffracted light drops immediately to 56 % of the value before excitation. Then both the diffracted and undiffracted signals increase steadily

to a certain saturation value. When the pump wavelength is changed beyond the dissociation limit, the picosecond dynamics vanish (see figure 3.6(a)). The diffraction efficiency is defined by:

$$\eta = \frac{I_1}{I_0 + I_{+1} + I_{-1}} \tag{3.9}$$

where $I_0$ is the undiffracted and $I_{+1}/I_{-1}$ ($I_1 = 1/2(I_{+1}+I_{-1})$) the first order diffracted signals. The diffraction efficiency is quite small and only reaches $\approx 2\,\%$. $NO_2$ is dissociated using pulses centered at 395 nm what corresponds to $\approx 90\,\%$ of the spectrum being above the dissociation threshold of 398 nm. After dissociation of $NO_2$ also its fragments NO and O contribute to HHG. However the tunnel ionization probability is different for NO and O as it depends exponentially on the ionization potential (see equation 1.4). At an intensity of $1.2 \times 10^{14}\,\mathrm{W/cm^2}$ (electric field strength: $3 \times 10^{10}\,\mathrm{V/m}$) and an ionization potential of $I_p = 9.26\,\mathrm{eV}$ for NO and $I_p = 13.61\,\mathrm{eV}$ for O, the tunnel ionization rate is 133 times stronger for NO than for O. Thus the contribution of O atoms can be neglected and in a first approximation the harmonic dipole moment taking into account dissociation can be written as:

$$E_e = E_{NO_2^*} e^{-t/\tau} + E_{NO}(1 - e^{-t/\tau}) \tag{3.10}$$

where $\tau$ is the dissociation time of $NO_2$, $E_{NO_2*}$ and $E_{NO}$ the complex harmonic dipole moments of excited $NO_2$ and NO fragments respectively. As these dipole moments cannot be measured directly a relationship to the measured intensities is established. Thus the dissociation time can be determined from the data of figure 3.5(a). The normalized difference between the undiffracted and diffracted signal is given by:

$$rA(t) = \frac{1}{2}\left[\frac{I_0(t) - 4I_1(t)}{I_0(t<0)} - 1\right] \tag{3.11}$$

$$= r\left[\mathcal{R}e\left(\frac{E_{NO_2^*}}{E_g}\right) \times e^{-t/\tau} + \mathcal{R}e\left(\frac{E_{NO}}{E_g}\right) \times (1 - e^{-t/\tau}) - 1\right] \tag{3.12}$$

This equation directly allows us to access the dissociation time. Figure 3.5(b) depicts the evolution of $rA(t)$. Note that equation 3.12 is only valid once the population transfer between the $1^1A'$ to the $2^2A'$ state is completed. The extracted dissociation time is $1.8 \pm 0.3\,\mathrm{ps}$. At a dissociation wavelength of 395 nm a dissociation time of 1.54 ps and 2.44 ps have been measured for molecules at room temperature and cold ($T = 6\,K$) molecules respectively (Ionov et al., 1993). This suggests that the rotational temperature of the molecules probed here is in between the two. Figure 3.6 depicts the dynamics measured at Ottawa at pump wavelength of 397.2 nm. Under these conditions a dissociation time of 2.4 ps and 5.0 ps was measured at room temperature and cold temperatures respectively (Ionov et al., 1993). With a dissociation time of $\tau = 2.71\,\mathrm{ps}$ this indicates that the gas jet employed at Ottawa might have been warmer than the jet at Bordeaux.

This is consistent with the fact that the nozzle diameter was 100 $\mu$m in Bordeaux and 250 $\mu$m in Ottawa.

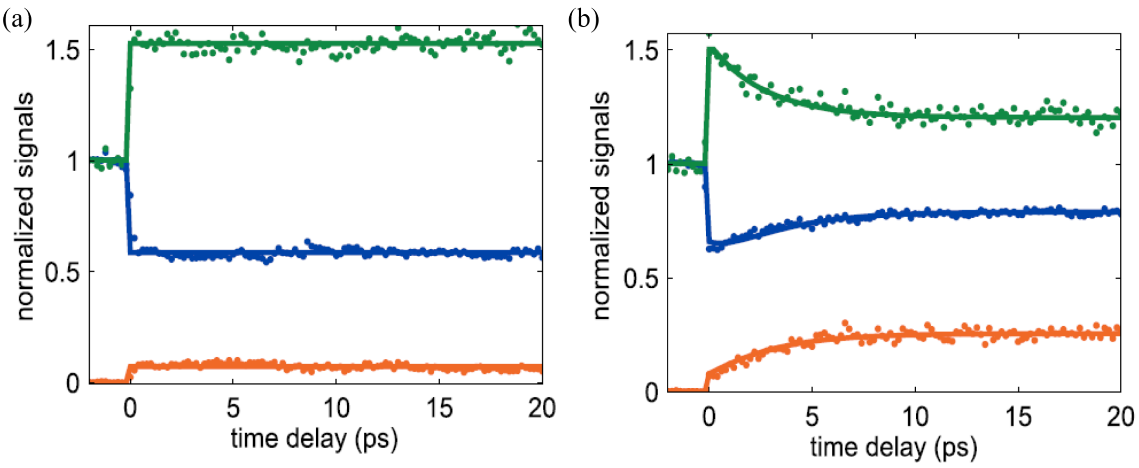


**Figure 3.6.:** Transients recorded in Ottawa.(a) Ion signal (green) and probe signal of the diffracted signal $I_1$ (orange) and undiffracted signal $I_0$ (blue) from harmonic 13 using a pump pulse centered at 407 nm. Both pump pulses had an energy of 10 $\mu$J respectively and were polarized perpendicularly to the probe pulse. (b) Same transients at a pump wavelength of 397.2 nm.

The dynamics of this excitation were attributed to a single photon process (Ionov et al., 1993). Multiphoton excitations would populate higher lying electronic states which would not contribute to HHG due to their low binding energies. Thus the strong modulation (see figure 3.5(a)) of the signal after excitation implies that only single photon excitation needs to be considered.

## 3.4. Femtosecond Dynamics in $NO_2$

The $NO_2$ molecule is excited at different wavelengths for triggering dynamics on a femtosecond timescale. The vibrational dynamics induced by pump pulses at a wavelength of 400 nm are decoded and almost completely understood. The experimental results of femtosecond dynamics triggered by a pump at 266 nm and 800 nm are also presented subsequently. Their analysis and interpretation is currently under progress.
Paragraph 3.5 shows that $NO_2$ is a molecule featuring a highly chaotic behaviour. This property and the fast dynamical behaviour of the population require a time resolution within the first few hundred femtoseconds after excitation. However a short duration also requires a thin BBO crystal with a lower SHG efficiency. Thus a compromise has to be made for the pulse duration.

### 3.4.1. Femtosecond Dynamics measured in Ottawa

According to the chronological order of the measurements, the results from Ottawa are presented first. Figure 3.7 depicts the data presented in reference (Wörner et al., 2011). Molecular excitation is triggered by a pump pulse centered at 401 nm, with an energy of 10 $\mu$J and a pulse duration of 40 fs in the cross-polarized[3] configuration. The diffracted signal reveals a transient with an oscillatory evolution. The first oscillation maximum is at 35 fs, the minimum at 70 fs and the second maximum at 130 fs. Even a second minimum and a third maximum with a lower contrast are observed at larger time delays.

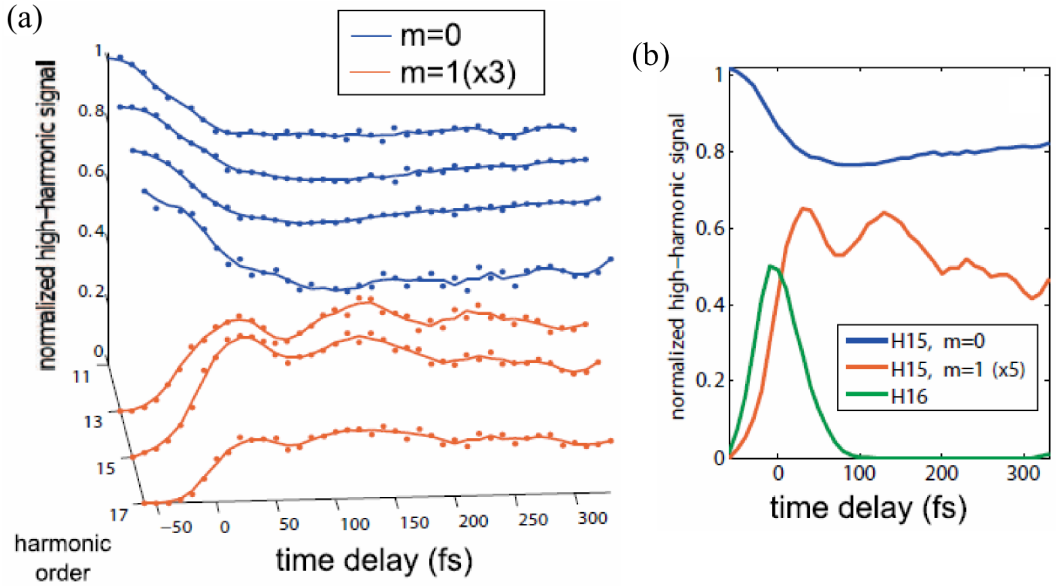


**Figure 3.7.:** (a) Evolution of the undiffracted signal (blue) and the diffracted signal (orange, multiplied by three). (b) Undiffracted (blue) and diffracted signal (orange) from harmonic 15 and cross-correlation obtained from harmonic 16 (green). The excitation was triggered by pump pulses of 10 $\mu$J centered at 401 nm orthogonally polarized to the probe beam.

Another transient illustrated in figure 3.8 also reveals dynamics in the total signal which is not observed in the undiffracted signal from figure 3.7. The FWHM of the cross-correlation is 62 fs. Only two oscillations are observed and not three as in the data above. For sake of comparison the net diffracted signal is shown in figure 3.8(b). It appears that the third oscillation is present only, when the signal is not normalized by the total harmonic signal. This indicates that the third oscillation in figure 3.8(b) is also caused by HHG fluctuations in this particular data set. At a higher sampling rate this third oscillation peak seemed however to be reliably reproduced as depicted in figure 3.7. In general one can clearly see that the data presented in figure 3.8 seem to be different

[3]The polarization of the pump and probe pulse are perpendicular to each other.

from the data depicted in figure 3.7. This might be due to too low statistics but also due to a different treatment of the signal: Therefore the data depicted beyond only shows the diffraction efficiency which is supposed to be more reliable than the raw diffracted signal as it corrects the HHG fluctuations.

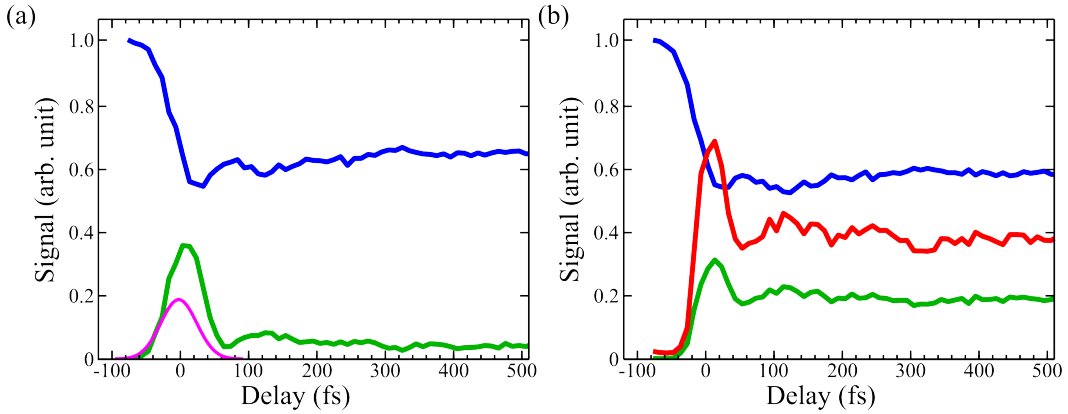


**Figure 3.8.:** Evolution of the total signal (blue), the raw diffracted signal (red, divided by two) and the first order diffraction efficiency (green, multiplied by 2) for harmonic 11 (a) and harmonic 15 (b) triggered by pump pulses of 15 $\mu$J centered at 400 nm orthogonally polarized to the probe beam.

One has to rule out the contribution of the $N_2O_4$ to the observed femtosecond dynamics. The signal, a homodyne interference, shall only be attributed to one molecular species. Otherwise the analysis of the data becomes very complicated. At a temperature of 80 °C the partial pressure of $N_2O_4$ is still $\approx$ 10 % and might such still contribute to the signal. Pumping at 400 nm leads to excitation of the Raman active modes of $N_2O_4$ with a period of 130 fs (Li et al., 2008). When cooling down the nozzle to room temperature the partial pressure of $N_2O_4$ increases to $\approx$ 70 %. Transients are shown in figure 3.9 for parallel and perpendicular pump-probe polarization. Clear oscillation with a period of 130 fs can be observed. The temporal position of the first and second oscillation maxima almost coincide with those observed at 80 °C (see figure 3.11), however the dynamics are fundamentally different. Further oscillations are not observable in the case of $NO_2$ at delays larger than 200 fs. Also the maximum of first order diffraction efficiency is shifted in the case of $NO_2$ with respect to $N_2O_4$. We can also confirm that the contrast of the oscillations is stronger in the parallel polarization than in perpendicular polarization, as claimed in the supplementary information of reference (Wörner et al., 2011). As in $NO_2$ this polarization dependence resembles the orientation dependence of the molecules. The pump polarization determines a preferential alignment direction for the excited molecules. As HHG is very sensitive to the orientation of the molecular axis, the signals are different. The data illustrated in figure 3.12 agrees with measurements performed in $N_2O_4$ at Bordeaux. This excludes $N_2O_4$ as a culprit responsible for the detected dynamics which can only be attributed to dynamics occuring in $NO_2$.

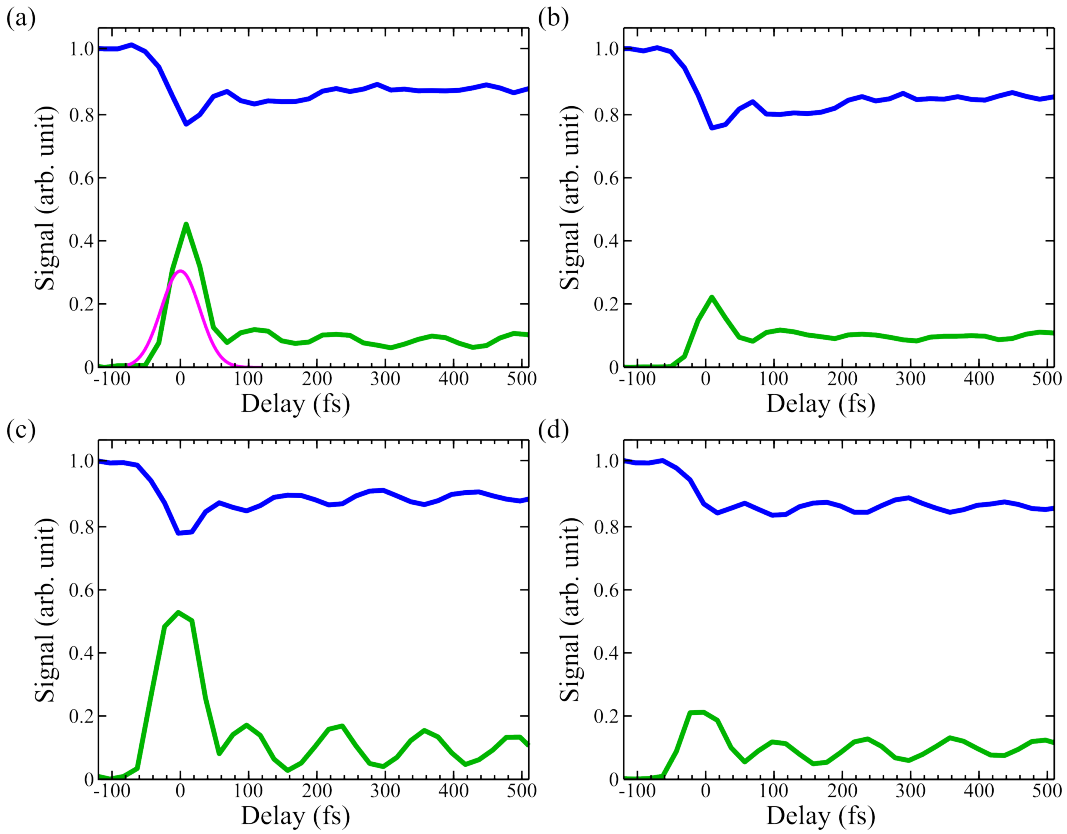


**Figure 3.9.:** Total harmonic signal (blue), first order diffraction efficiency (green) and the cross-correlation (FWHM = 67 fs) for (a) harmonic 11 and (b) harmonic 13 for a perpendicular polarization angle between pump and probe beams. Subfigures (c) and (d) show the same scans in the parallel configuration.

### 3.4.2. Femtosecond Dynamics measured in Bordeaux

Femtosecond dynamics were triggered by pumping at wavelengths between 392 nm and 400 nm employing two different molecular gas jets with different rotational temperatures. The observed dynamics are weak at parallel polarization between pump and probe beam. The observable feature increases monotonously with increasing polarization angle between the pump and probe beam (see figure 3.10). Excitation is direction selective along the O-O axis of the $NO_2$ molecule. In parallel configuration the excited molecules are probed parallel to the O-O axis. In case of the cross-polarized beams the excited molecules are probed parallel to the axis of rotational symmetry. This orientation also dominates the emission from the unexcited molecules. Owing to this direction dependence a higher sensitivity is observed for the cross-polarized experiment as displayed in figure 3.10. Therefore further measurements were conducted at a perpendicular polarization angle between the pump and probe beam.

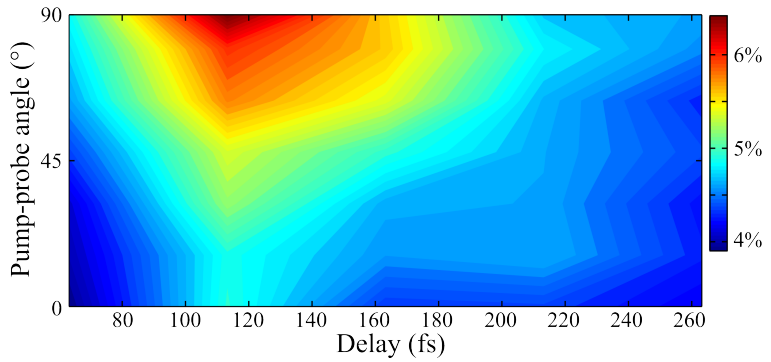


**Figure 3.10.:** First order diffraction efficiency as a function of the polarization angle between pump and probe beam and delay. The first order diffraction efficiency is normalized to its value at t = 260 fs. At this time delay the dynamics have faded.

In a first measurement the femtosecond dynamics were recorded using a pump energy of 20 $\mu$J for each of the pump pulses centered at 400 nm. Figure 3.11 depicts the time dependence of the overall signal and the first order diffraction efficiency (see equation 3.9) for harmonic 15 to harmonic 21 using a finer sampling each 10 fs. This result is obtained by averaging over 6250 laser shots per delay, averaging over 5 consecutive scans. The even harmonics are a result of wave mixing (Bertrand et al., 2011) and are only present if pump and probe beams overlap. Thus this signal corresponds directly to a cross-correlation between pump and probe beam. The pump also initiates molecular dynamics which can affect the even harmonic signal. This effect is taken into account when determining the zero delay: The cross-correlation signal is defined by $I_{even}/I_{odd}$ where $I_{even}$ is the signal of a even harmonic and $I_{odd}$ the average of the two adjacent odd harmonics. This procedure assumes that even and odd harmonics are affected similarly by the change of molecular geometry. The maximum of the cross-correlation signal occurs 10 fs before the maximum of diffracted harmonic signal. The cross-correlation in figure 3.11(a) delivers a FWHM

of $54 \pm 1$ fs. Three different contributions must be taken into account for calculating the FWHM: first the FWHM of the pump pulse (35 fs), second the FWHM of the probe pulse (25 fs) and third the additional delay induced by the diffraction of the optical grating (20 periods: 26 fs). The calculated convolution of the delay induced by the grating and the pump pulse under an angle of 1.2° is 44 fs. A second convolution of this result with the probe pulse gives a FWHM of 50 fs. This is very close to the measured value. The difference might arise from the influence of several dispersive elements (windows and beam splitters) in the beamline that cannot be compensated by the compressor. Additionally the overlap between the two pump beams is possibly not perfect.

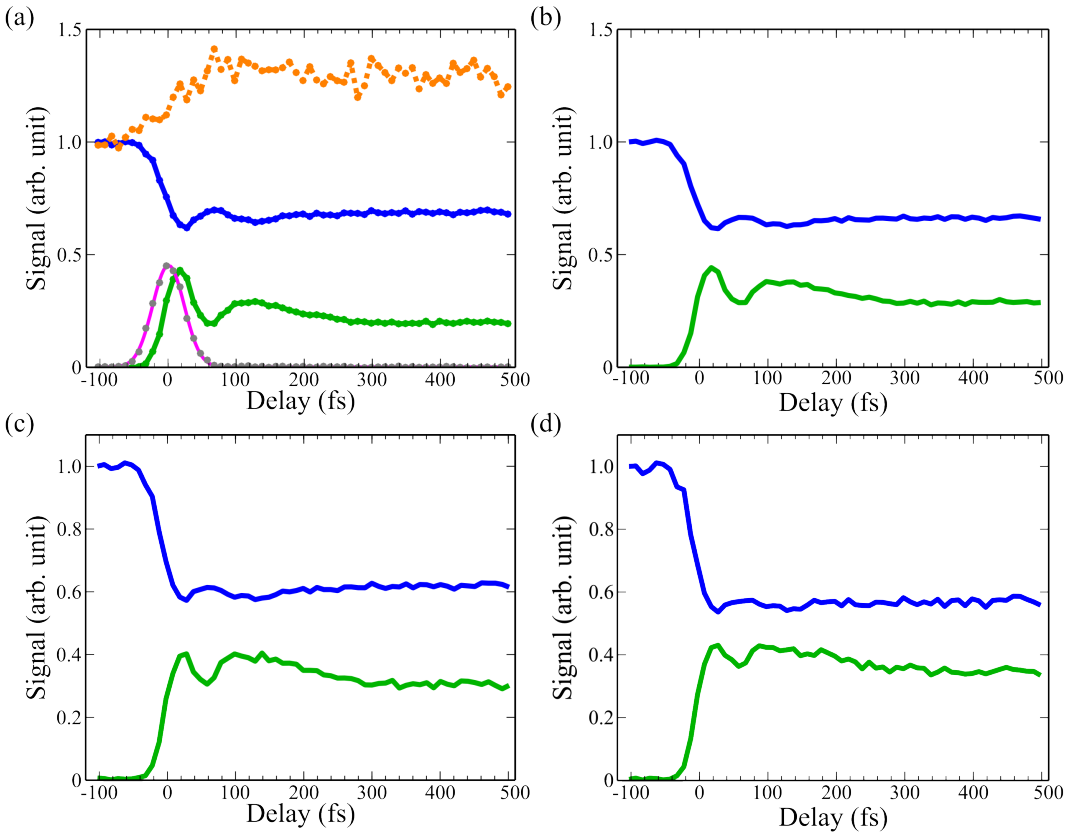


**Figure 3.11.:** Evolution of the ion yield (orange) the first order diffraction efficiency (green, multiplied by 20) and the total signal (blue) for harmonic 15 (a) to harmonic 21 (d) triggered by pump pulses of 20 $\mu$J, centered at 400 nm orthogonally polarized to the probe beam. Gaussian fit (pink) of the normalized cross-correlation (signal harmonic 16 divided by signal from harmonic 13 and 15).

As the total harmonic signal decays after pumping, the first order diffraction efficiency becomes significant. The total harmonic signal shows a minimum at 15 fs , a maximum at 65 fs and then again a minimum at 130 fs. Then it increases slowly what can be attributed to the dissociation of $NO_2$ which is very visible in the picosecond dynamics. At a pump

wavelength of 400 nm and a bandwidth of 7 nm 25 % of the excited molecules are above the dissociation limit. The first order diffraction efficiency shows an inverted behaviour, a maximum at 15 fs, a minimum at 58 fs and another maximum at 120 fs. The observed contrast is better for the first order diffraction efficiency than for the total signal. The ion signal increases with the first order diffraction efficiency but does not reveal any oscillatory dynamics.

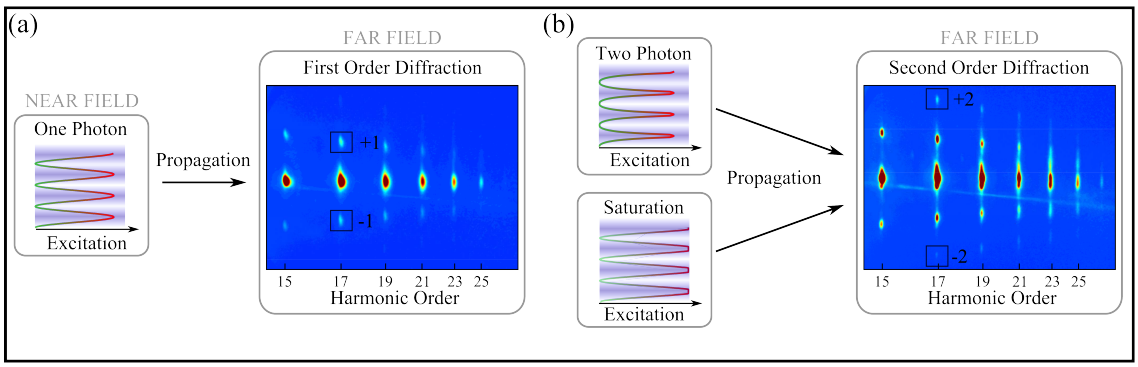


**Figure 3.12.:** (a) In case of sinusoidal modulation of the transient grating only first order diffraction is expected in the far field. (b) If the origin of excitation is a two-photon process or if saturation of the one-photon absorption is reached second order diffraction is observed in the far field.

Interestingly second order diffraction is observed in the far field if the pump energy is increased to 35 $\mu$J for each arm. Figure 3.12 depicts the two possible origins of the second order diffraction. Two-photon excitation modifies the near field transient grating so that it follows the square of a sinusoidal modulation of the pump intensity. In a second scenario the saturation of the molecular excitation induces an anharmonicity in the grating modulation. Both effects can lead to second order diffraction.
Figure 3.13 depicts the time dependence of the first order diffraction and second order diffraction for harmonic 15 to harmonic 21. The temporal evolutions of the first order diffraction efficiency and second order diffraction efficiency are similar. The first order diffraction efficiency is principally identical with the one depicted in figure 3.11, only the relative heights of the two oscillation peaks differ. When changing the pump energy between 10 $\mu$J and 35 $\mu$J per pump pulse in each arm the detected dynamics are not affected. The weak value of the first oscillation peak for the second order diffraction might be owing to a weaker contribution from wave mixing. Wave mixing is weaker for the higher orders (Bertrand et al., 2011). Thus second order diffraction would be suited to even better reveal the true dynamics around zero delay. Also the second order diffraction efficiency for harmonic 15 is very weak. The similarity in time dependence suggests that higher order excitation processes can be excluded as different dynamics would be expected. Indeed appearance of second order diffraction is more compatible with saturation of the one photon process. To check this the pump energy required for saturation is estimated.

The $^2A_1 \longrightarrow {}^2B_2$ absorption cross section (Vandaele et al., 2003) is $\approx 6 \times 10^{-19}\,\mathrm{cm}^2$. The calculation from appendix B delivers a pump waist size of 60 $\mu$m (the diaphragm for tuning pump intensity has a diameter of 4 mm). With these parameters saturation should occur at $\approx 25\,\mu$J per pump pulse and agrees well with what has been observed in the experiment.

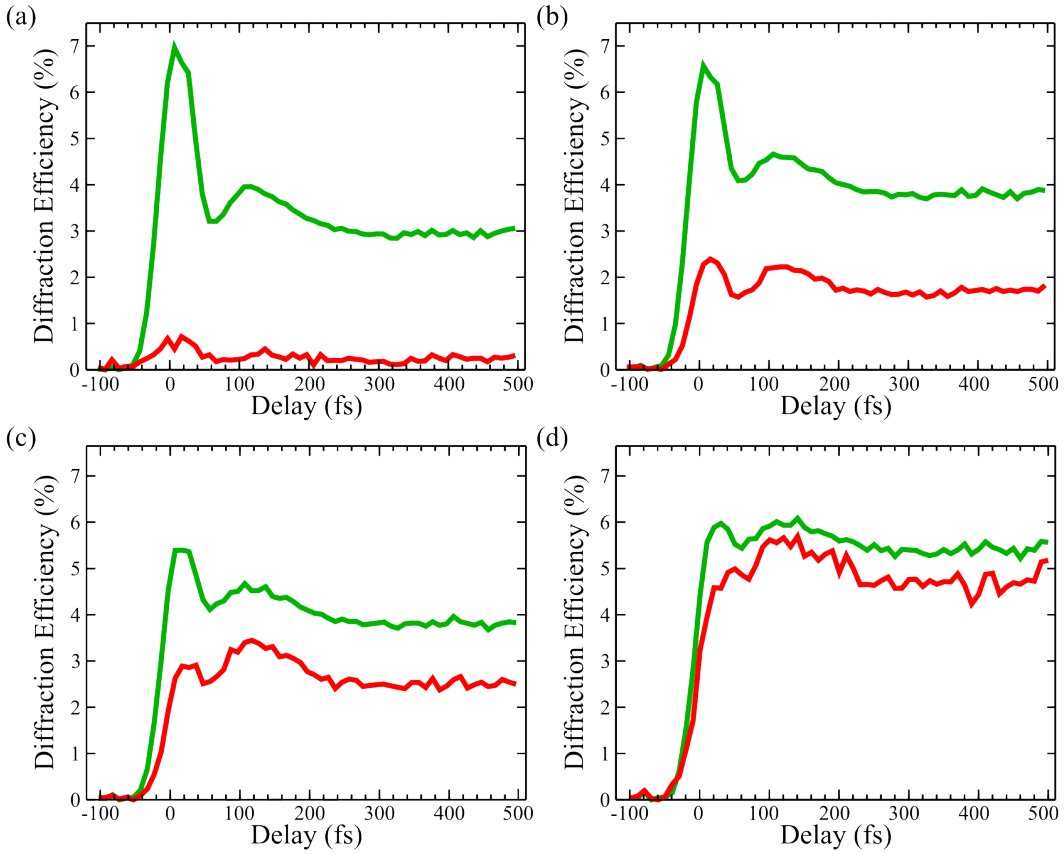


**Figure 3.13.:** Evolution of the first order (green) and second order diffraction efficiency (red, multiplied by 20) for harmonic 15 (a) to harmonic 21 (d) triggered by pump pulses of 35 $\mu$J centered at 400 nm orthogonally polarized to the probe beam.

Furthermore the dependence of the dynamics have been studied not only as a function of pump energy but also as a function of rotational temperature and pump wavelength. Next to the General valve an Even-Lavie valve (conical nozzle diameter: 250 $\mu$m), pulsing at a repetition rate of 1 kHz has been employed. This valve can only be operated at backing pressures higher than 10 bar which is not compatible with a pure $NO_2$ gas load since the vapour pressure is only $\approx 780$ mbar at room temperature. Therefore $NO_2$ must be mixed in a different bottle with helium, a buffer gas that will not contribute to the harmonic spectra at the intensities used in the experiment. First the bottle has been filled up with $NO_2$ and then by 16 bar of Helium. The Even-Lavie valve was then operated with such a mixture at a nozzle temperature of 120 °C. The focus distance from the nozzle is

approximately 2 mm in this configuration. When using the General valve this distance is lower with a few 100 $\mu$m. The rotational temperature is expected to be lower with the Even-Lavie valve. Figure 3.14 compares the first order diffraction efficiency for harmonic 17 from the General valve and the Even-Lavie valve. Due to the strong dilution of $NO_2$ in the gas mixture the signal has a higher noise for the latter case. Only the ratio between the first and second oscillation bump is different which might be due to the fact that the two measurements were performed on two consecutive days at slightly different pumping conditions.
Finally the femtosecond dynamics were also studied at different pump wavelengths (392 nm to 400 nm). Again no dynamical variations could be observed, only higher noise for the first order diffraction efficiency is noticeable. In conclusion the observed femtosecond dynamics do not depend on pump energy, rotational temperature of the $NO_2$ molecules and pump wavelength within the variation range.

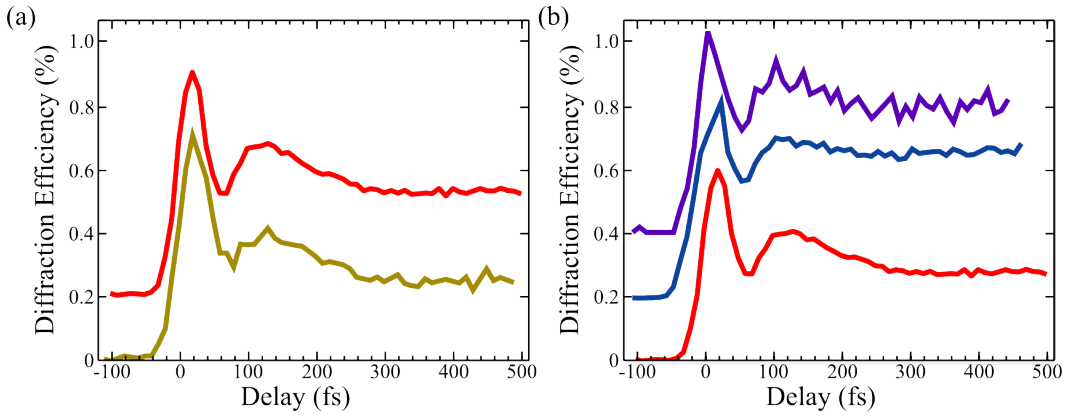


**Figure 3.14.:** (a) Evolution of the first order diffraction efficiency generating in a warm (red) and cold (yellow) molecular beam. (b) Time Dependence of first order diffraction efficiency at different pump wavelengths: 400 nm (red), 395 nm(blue) and 392 nm (purple).

### 3.4.3. Discussion

The two transients measured at Bordeaux and Ottawa (see figure 3.7) are directly compared in figure 3.15. On first sight the two different results agree well, however several differences can be noticed. First the diffraction efficiency measured in Bordeaux is four times lower than in the Ottawa experiment. Second the dynamics appear as well in the undiffracted harmonic signal and not only in the diffracted one. Third, only two oscillations are observed and not three. Also the timing of the oscillations seems to be different in the Bordeaux and Ottawa experiments. The Ottawa data reveal a first oscillation maximum at 35 fs, the minimum at 70 fs and the second maxium at 130 fs (Wörner et al., 2011) what is similar to the data taken at Bordeaux: 15 fs, 58 fs and 120 fs.

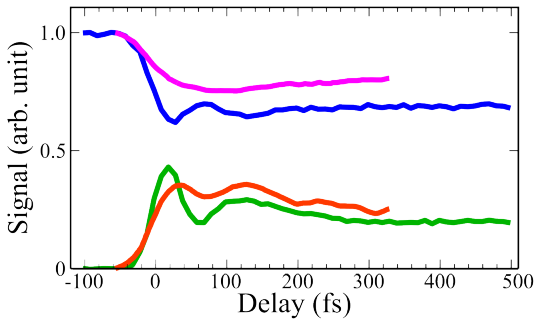


**Figure 3.15.:** Normalized undiffracted signal to the undiffracted signal at negative pump-probe delays measured at Bordeaux (blue) and Ottawa (pink). First order diffraction efficiency from harmonic 15 measured in Bordeaux (green, multiplied by 10) compared to first order diffraction efficiency observed in Ottawa (orange, multiplied by 5).

The differences between the two experiments are hard to determine, as shown above they do not depend on wavelength, pump energy, rotational temperature and cross-correlation between. As the molecular dynamics are induced by a one photon transition they do not depend on the chirp of the pump pulse (Brumer and Shapiro, 1989; Joffre, 2007). The procedures for the cross-correlation calibration are different at Bordeaux and Ottawa. We normalized the cross-correlations by the overall signal, as this is different at negative and positive delays. The two cross-correlations might differ by up to 10 fs. Experimental artefacts like prepulses or strange pulse shapes might play a role for the different observations, and cannot be excluded in the two cases. The difference in diffraction efficiency might originate from two different possibilities: Either the one in Bordeaux is too low or the one in Ottawa is too high. The lower diffraction efficiency in Bordeaux might be an indication that the experimental parameters are not optimized. The transient grating might not be optimized due to a different fringe spacing (Bordeaux: 9.4 $\mu$m vs. Ottawa: 13.3 $\mu$m) or pump beam quality. An equal beam intensity is important for a good contrast of the grating. One of the two pump beams is reflected from a beam splitter and the other one is transmitted. It is difficult to compensate this effect and therewith pump duration and intensity might be slightly different, what deteriorates the contrast. However the calculated theoretical diffraction from reference (Kraus and Wörner, 2012; Kraus et al., 2012) and figure 3.25 agree well with the experimental data from Bordeaux. This suggests that the diffraction efficiency measured in Ottawa is too strong. One possible reason for the high diffraction efficiency in Ottawa might be a lower detector response at the position of the zero order diffraction. This leads to a spectro-spatial dependent response from the detector emphasizing the first order diffraction compared to the zero order diffraction. This might distort the diffraction efficiency to higher values.

### 3.4.4. Femtosecond Dynamics triggered at a Pump Wavelength of 266 nm or 800 nm

In a further experiment dynamics were incuded by pump pulses centered at 800 nm. The initial rotational dephasing of $NO_2$ has been observed from non-resonant four-wave mixing (Pastirk et al., 2001) when pumping at 800 nm. The same setup as described for excitation at pulses centered 400 nm was used. The pump energy was 230 $\mu$J for each pump pulse which corresponds to a diaphragm diameter of 5.6 mm. Due to the higher fringe spacing of the transient grating the first diffracted order is much closer to the zero order signal and was thus afflicted with a higher background from zero order. Also the cross-correlation cannot be extracted because the wave mixing signal always overlaps. It has to be pointed out, that the results of these scans have not been reproduced yet. Figure 3.16(a) shows a signal oscillating with a period of about 500 fs. The delays were sampled each 50 fs and were averaged over five consecutive scans, leading to an accumulation of 50000 laser shots per delay. The five scans contributed equally to the oscillation of the signal, all of them exhibit an oscillation, but with a stronger noise. This oscillation resembles a transient which has been observed by Hamard and coworkers (Hamard et al., 2010).

| | $1^{st}$ extremum | $2^{nd}$ extremum | $3^{rd}$ extremum |
|---|---|---|---|
| Photoionization Signal | 0.70 ps | 0.95 ps | 1.46 ps |
| HHG | 0.70 ps | 0.90 ps | 1.20 ps |

**Table 3.1.:** Comparison between the ocillation peaks and dips of the photoionization signal from reference (Hamard et al., 2010) to the extrema of the high harmonic transients.

Table 3.1 draws a comparison to their photoionization signal, i.e. $NO^+$, from this work. This signal has been measured when pumping at 404 nm and probing at 270 nm with the polarization perpendicular to each other. The first order diffraction efficiency does not really confirm the observed oscillations which are visible in the total harmonic signal. The noise level is too high. It has to be noted however that the two peaks at 0.5 ps and 0.9 ps coincide with the minima of the total harmonic signal. A transient grating with a smaller fringe spacing might be helpful for enhancing the contrast. When changing pump polarization to parallel (see figure 3.17), the oscillations are not as pronounced for the total harmonic signal. The first order diffraction efficiency of harmonic 19 reveals however the same oscillations that have been observed in perpendicular configuration. The oscillation has been assigned (most likely) to the absorption of two pump and two probe photons, triggering quantum beat signal. This would imply that the dynamics observed from the high harmonic signal originates from the absorption of four pump and six probe photons. Further studies need to be carried out in order to check this hypothesis.

Another feature that is revealed is a slow decay up to 0.5 fs which is also visible in perpendicular configuration (see figure 3.17). This decay is especially visible for first order diffraction efficiency. A decay with the same timescale has been observed by Pastirk and

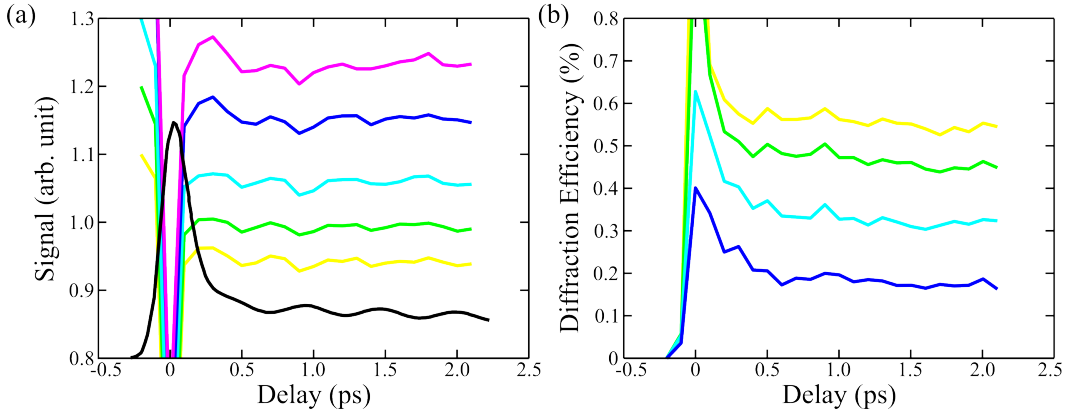


**Figure 3.16.:** (a) Time dependence of the total harmonic signal for harmonic 17 (yellow) to harmonic 25 (pink) with a pump centered at 800 nm with a polarization perpendicular to the probe polarization. The transients are shifted with respect to each other for better visibility. In comparison the time-resolved signal (solid black line) of $NO^+$ for a pump centered at 403.7 nm and a probe centered at 269.7 nm is depicted (extracted from reference (Hamard et al., 2010), figure 2(b)). (b) Same scan illustrating the first order diffraction efficiency multiplied by 20 for harmonic 17 (yellow) to harmonic 23 (blue).

coworkes (Pastirk et al., 2001) employing the transient grating techique in a convential setup. It was attributed to an initial rotational dephasing in the sample.

Figure 3.18 and figure 3.19 illustrate the time dependence of the harmonic signal and higher order diffraction efficiencies at two different energies: 260 $\mu$J and 360 $\mu$J for each pump pulse. At high energies even third order diffraction is visible. This feature might originate from a strong saturation of the transient grating but might also have another origin. Mairesse and coworkers have studied high-order harmonic transient grating spectroscopy in rotationally excited molecules (Mairesse et al., 2008c). A grating of rotational wave is created leading to diffraction. They found that the structure of this grating depends stongly on the pump-probe delay and intensity. The change of symmetry of the grating can thus very well lead to higher order diffraction.

Figure 3.18 depicts the zero order harmonic signal and first order diffraction efficiency at two different pump energies. A decay of up to 0.5 ps is clearly visible for zero order harmonic signal at low pump energies whereas this decay seems to be faster when increasing the pump energy. The first order diffraction efficiency does not reveal such a decay, however harmonic 15 shows local minimum at 0.2 ps and a local maximum at 0.3 ps for both pump energies. The higher contrast for diffraction efficiency of harmonic 15 might be attributed to the higher spatial separation of the diffracted orders for the lower order harmonics. The minimum that is resolved does not fit the time delay of the minimum that is observed in reference (Pastirk et al., 2001). The long temporal overlap of the four-wave mixing signal might shift this minimum to higher time delays.

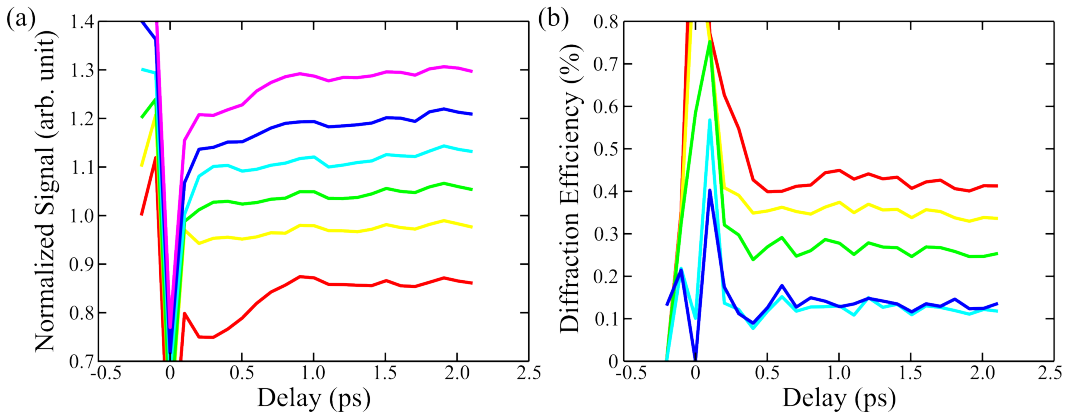


**Figure 3.17.:** (a) Time dependence of the total harmonic signal for harmonic 15 (yellow) to harmonic 25 (pink) with a pump centered at 800 nm with a polarization perpendicular to the probe polarization. The transients are shifted with respect to each other for matters of clear arrangement. (b) Same scan illustrating the first order diffraction efficiency for harmonic 15 (red) to harmonic 23 (blue) multiplied by 20.

Figure 3.19 illustrates the second order and third order diffraction efficiencies at two different pump energies. Second order diffraction reveals a clear local minimum at 0.1 ps which is close to the one observed by Pastirk and coworkers. Four-wave mixing becomes weaker for the higher orders (Bertrand et al., 2011). Thus the minimum is pushed more to higher delays for the low order harmonics than the high order harmonics. The transients are however different at the two pump energies, the decay has a lower contrast and is faster at higher pump energies. Third order diffraction is not observed at 260 $\mu$J. Even though the contrast is not very high for third order diffraction a decay is still clearly observable at 360 $\mu$J with a minimum, depending on the harmonic order, located between 0.1 ps and 0.2 ps.

If the observed signal corresponds to a rotational excited wave packet at prompt alignment a stronger alignment would be expected at higher pump pulse energies. As the structure of the transient grating for rotational excited wave packets depends on pump intensity (Mairesse et al., 2008c), diffraction efficiceny of the grating might be higher at low intensities. The observation of prompt alignment has important implications for future experiments in $NO_2$. Pump-probe spectroscopy signals from aligned $NO_2$ at the half-revival would have a strongly enhanced contrast allowing us to reveal new features in femtosecond transients.

Final pump-probe measurements were performed in Ottawa with a pump beam centered at 266 fs. Cireasa and coworkers detected a couple of sharp long-lived photoion-photoelectron peaks triggered by the excitation at 269 nm (Cireasa et al., 2009). They were attributed to excitation of an $NO_2$ Rydberg state around 9.2 eV by two pump photons. The energy of each pump pulse was 21 $\mu$J in each arm. The first order diffraction

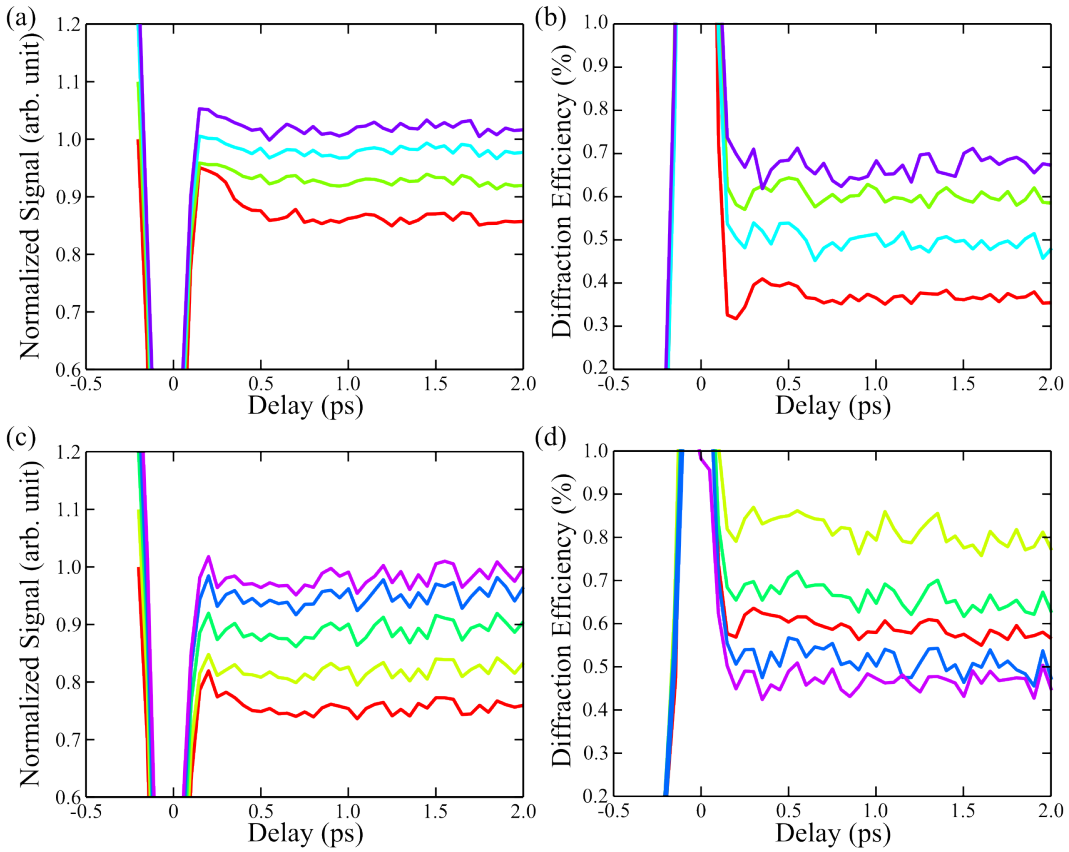


**Figure 3.18.:** Transients taken in perpendicular pump-probe configuration at low pump energies (260 $\mu$J, upper panels) and high pump energies (360 $\mu$J, lower panels). (a), (c) Time dependence of the zero order harmonic signal for harmonic 15 (red) to harmonic 21 (violet). (b), (d) Same scans illustrating the first order diffraction efficiency for harmonic 15 (red) to harmonic 21 (violet) multiplied by 20. The transients are shifted with respect to each other for matters of clear arrangement.

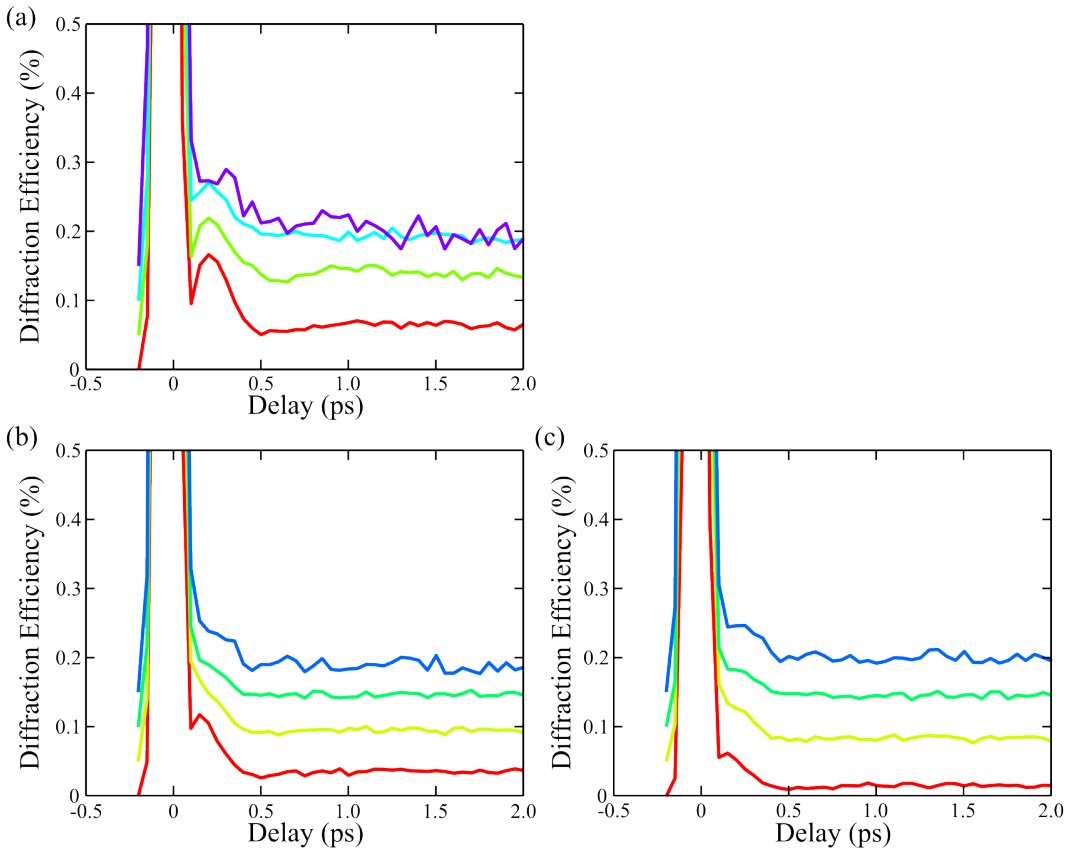


**Figure 3.19.:** Transients taken in perpendicular pump-probe configuration at low pump energies (260 $\mu$J, upper panel) and high pump energies (360 $\mu$J, lower panels). (a), (b) Time dependence of second order diffraction efficiency for harmonic 15 (red) to harmonic 23 (violet). (c) Same scans illustrating the third order diffraction efficiency for harmonic 15 (red) to harmonic 23 (violet) multiplied by 20. The transients are shifted with respect to each other for matters of clear arrangement.

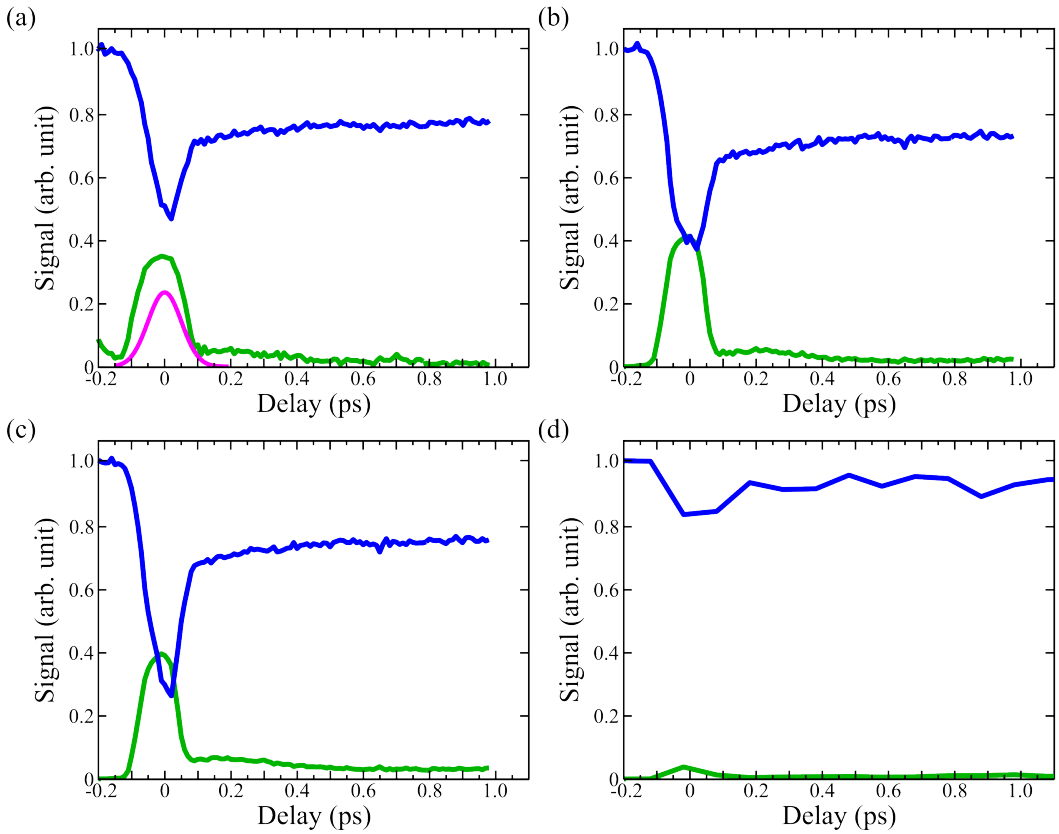


**Figure 3.20.:** Evolution of the total harmonic signal (blue) and the first order diffraction efficiency (green) for harmonic 11 (a) to 17 (d). The pump pulse is centered at 266 nm and cross-polarized with respect to the probe pulse.

is well separated from wave-mixing signals or the zero order and has therefore a good signal to noise ratio. Each transient illustrated in figure 3.20 was averaged over 5 scans and sampled every 10 fs. The total harmonic signal drops after excitation and is followed by a slight increase. The first order diffraction efficiency shows the similar decays up to 0.5 ps as in figure 3.17 and 3.16 and then almost approaches zero.

## 3.5. Simulating the electronic fs-Relaxation induced at 400 nm

Halvick and coworkers from the ISM, Bordeaux performed the simulations initiated by Pons in order to reproduce the experimental results. Generally nonadiabatic dynamics of small molecules (such as $NO_2$) can be calculted in a quantum-time dependent (QTD) approach. However as the molecule size increases this method is not feasible any more, owing to a lack of required computing power. While the dynamics of $NO_2$ have been simulated by QTD methods (Santoro et al., 2000; Sanrey and Joyeux, 2007; Arasaki and Takatsuka, 2007) we apply here a method also applicable for bigger molecules: trajectory surface hopping (TSH). These studies were based on a diabatic representation of the electronic Hamiltonian. The initial distribution quantum wave packet or surface hopping trajectories are calculated and then propagated over a 3D space (bond angle and N-O stretch). Here the high harmonic signal is calculated from the trajectory distribution. The ionic potential curves and dipole moments necessary for calculating the high harmonic signal are only available as a function of bond angle. Thus the distribution over bond angle cannot be taken into account and is averaged out. The contributions to the high harmonic signal is summed up coherently over the bond angles for each molecular state. This 1D model is finally compared to the experimental transients featuring the molecular vibration of the $NO_2$ molecule.

### 3.5.1. Trajectory Surface Hopping Calculations

The TSH used in this context was already implemented by Halvick and coworkers (Halvick et al., 2002). It is based on Tully's fewest switches algorithm (Tully, 1990). This algorithm calculates the transition probability of switching the PES at each integration time. Conservation of energy sets the condition for the velocity component on the coupling vector if a switch occurs. First the initial phase space distribution has to be determined in the excited state when $NO_2$ interacts with an ultrashort laser pulse. This is done classically in a two step procedure (Meier and Engel, 2002). The distribution for the vibrational ground state of the electronic ground state is represented by the Wigner function $\rho_W^{(X)}$ and filtered by the resonant one-photon transition:

$$\rho(\vec{q},\vec{p}) = \rho_W^{(X)}(\vec{q},\vec{p}) e^{-(D_{12}-\hbar\omega)^2/2\alpha\hbar^2} \tag{3.13}$$

where $D_{12}$ is the difference of the potential energy of the transition, $\omega = 400$ nm the central frequency of the pulse and $\alpha$ the parameter of the pulse envelope defined by $e^{-\alpha t^2}$.

The pulse envelope (FWHM: 30 fs) defines the starting time of each trajectory during the passage of the excitation pulse. Figure 3.21 shows the evolution of the diabatic state population, either by taking the same start time for all the trajectories or starting the trajectories at a random starting time given by the distribution function $e^{-2\alpha t^2}$. In the following $1 \times 10^4$ trajectories were taken. Also smaller batches ($2 \times 10^3$ and $5 \times 10^3$) were used for which no difference in the evolution of the dynamics were observed. Also different pump wavelengths at 392 nm and 395 nm have been tested. When comparing the dynamics at the three wavelengths (392 nm, 395 nm and 400 nm) no significant differences can be observed until t = 100 fs.

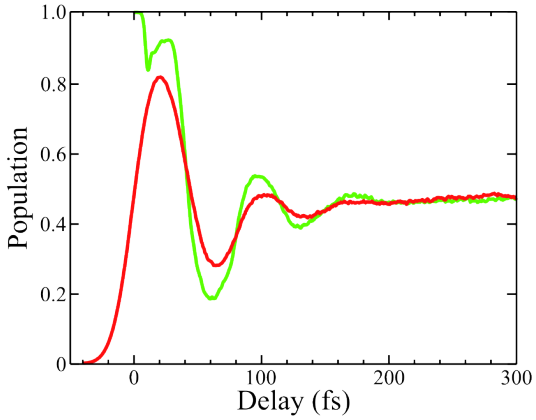


**Figure 3.21.:** Population of the excited PES assuming the same start time for all the trajectories (green) and a start time determined by the envelope of the pump pulse (red).

Figure 3.22 illustrates the normalized populations for the diabatic PES of the excited and ground state. Snapshots are taken at different instants of time, they are displayed in figure 3.23. At t = 0 fs only trajectories on the excited PES are present. These move towards the potential minimum and reach the crossing seam at t = 10 fs. Only few trajectories cross to the respectively other PES at the seam because the electronic coupling is still inefficient as the trajectories are still well located around $Q_- = R_1 - R_2 = 0$. From now on the swarm spreads considerably with respect to the bond angle and already has a considerable width when reaching the turning point at 20 fs. As it oscillates back (30 fs to 60 fs) the coupling which is proportional to $Q_-$ is substantial and a significant amount of the excited state population is transferred to the diabatic ground state. The diabatic excited state is repopulated at 100 fs during the following oscillation cycle and two oscillations cycles later at 170 fs. These recurrences are visible in figure 3.22(b), but no further can be observed, the trajectories are completely scattered in the whole phase space.

When comparing these results to QTD calculations from (Arasaki and Takatsuka, 2007) a good quantitative agreement can be ascertained, but recurrences are much stronger for the QTD calculations. A strong trajectory swarm dispersion has already been predicted

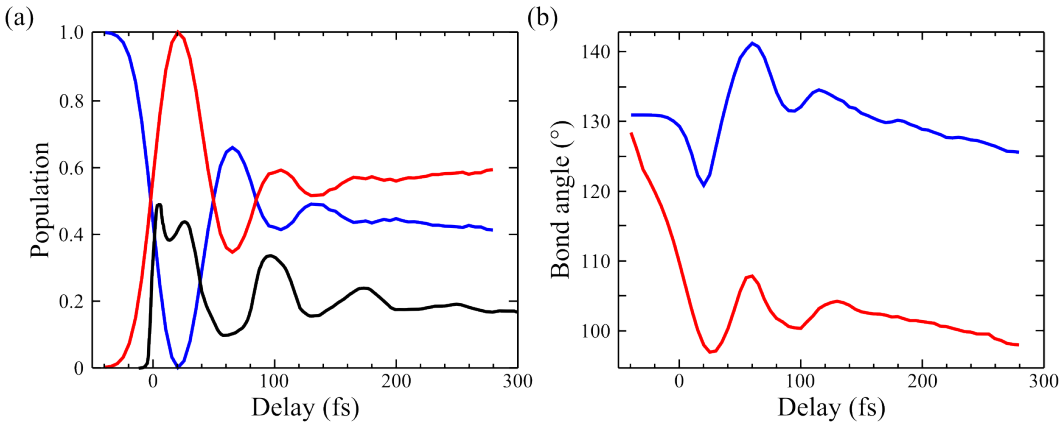


**Figure 3.22.:** (a) Population of the first excited (red), the ground diabatic state (blue) from TSH calculations and the first excited diabatic state (black) from QTD calculations. (b) The average bond angle of the molecule in the ground state (blue) and the excited molecule (red) from TSH calculations. A 100 % excitation probability was assumed for the results from TSH calculations.

before (Georges et al., 1995), leading to a chaotic[4] behaviour for trajectories starting at energies close to dissociation threshold. Classical chaos is probably the reason for the quantitatively different results from QTD and TSH calculations.

### 3.5.2. Calculation of High Harmonic Emission

HHG can be taken into account following the three step model in chapter 1: tunnel ionization, propagation in the continuum and finally radiative recombination. Ionization rates and complex recombination dipole moments were taken from the first of the articles (supplementary information) published in the course of this study (Wörner et al., 2010). They were only calculated for three different bond angles (85°, 102° and 134°) with $NO_2$ in the $C_{2v}$ symmetry. As the ionization rates and complex recombination dipole moments are not available along the asymmetric stretch coordinates, the calculation of HHG can only be implemented within the scope of a 1D model. The dipole amplitudes and recombination phases were interpolated for intermediate bond angles. Different ionization channels were taken into account for the calculation, each with a possibly different phase (Smirnova et al., 2009a): first the recombination phase, second the continuum evolution phase, third the evolution of the electronic states of the ion during the electron propagation in the continuum and fourth the ionization phase. Three of these phases are taken into account, the ionization phase is expected to be close to zero. The third phase evolution is discussed in section 1.2.2, chapter 1. It is determined by the time of flight $\tau$ and the ionization potential difference between the excited and the ground state molecules: $\Delta\varphi_q \approx \Delta I_p \tau_q$. The time of flight and the recombination phase stays constant for a

[4]The distance between trajectories starting close to each other in phase space grows exponentially.

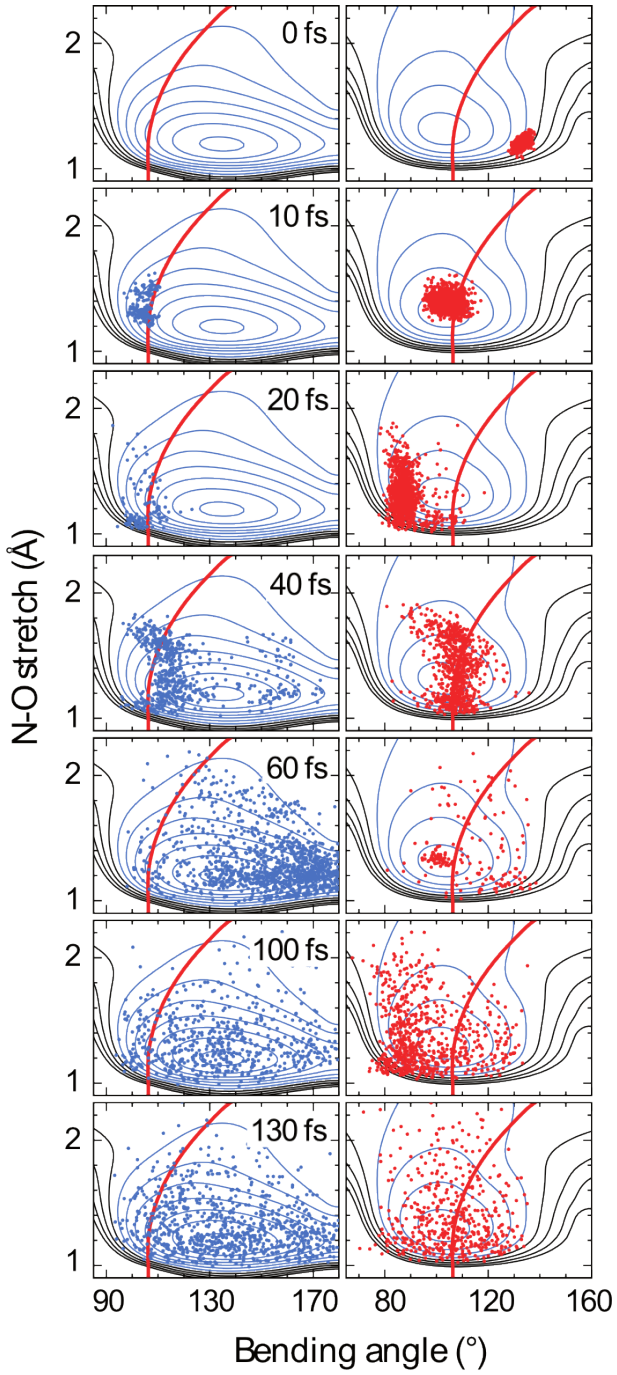


**Figure 3.23.:** Snapshots of the trajectory swarm and contour lines (every 0.5 eV) of the ground (blue) and excited diabatic PES (red). The blue and red dots represent respectively the coordinates of the trajectories on the ground and excited diabatic PES. The crossing seam of the two PES is represented by the thick red line.

certain harmonic order[5] at a specific intensity. But the phase of the high harmonic emission changes because $\Delta I_p$ varies during the vibrational motion of the molecule, i.e. the electron wave packet movement on the two different PES. The potential difference $\Delta I_p$ was extracted from the ionic potential curves which were calculated by Arasaki and coworkers (Arasaki et al., 2010). Figure 3.24 shows the harmonic phase shift $\Delta I_p \tau$ as a function of bond angle for the two potential surfaces PES 1 and PES 2. The main part of the PES 1 trajectories stay between 120° and 142° whereas the trajectory swarm of PES 2 stays essentially between 95° and 110°. The phase dependence as a function of bond angle is linear around the respective potential minima. The phase shift ranges from -0.4 $\pi$ to 0.4 $\pi$ for PES 1 and from 0.2 $\pi$ to 0.8 $\pi$ for PES 2.

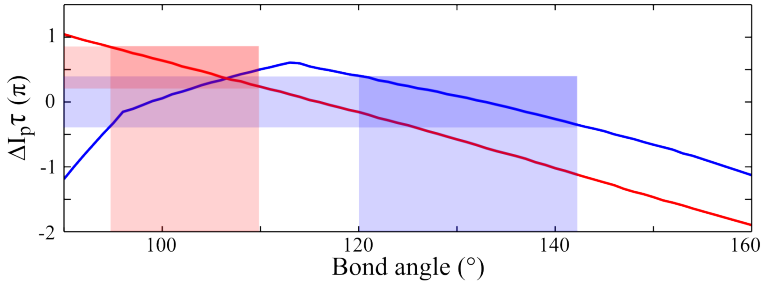


**Figure 3.24.:** Harmonic phase shift $\Delta I_p \tau$ in units of $\pi$, as a function of bending angle for emission from PES 1 (blue) and PES 2 (red). The shaded areas correspond to the bending angles explored by the main part of the trajectory swarm.

In order to calculate the diffracted and undiffracted signal given in equation 3.8 , the harmonic signal is summed coherently over the different bending angles $\theta$ for the ground and excited states (Wörner et al., 2010):

$$I_0(t) \propto \left| \int (1-r) d_g e^{i\phi_g} + r W_1(\theta,t) d_1(\theta) e^{i\phi_1(\theta)} + r W_2(\theta,t) d_2(\theta) e^{i\phi_2(\theta)} d\theta \right|^2 \tag{3.14}$$

$$I_1(t) \propto \frac{1}{4} \left| \int r W_1(\theta,t)(d_1(\theta) e^{i\phi_1(\theta)} - d_g e^{i\phi_g}) + r W_2(\theta,t)(d_2(\theta) e^{i\phi_2(\theta)} - d_g e^{i\phi_g}) d(\theta) \right|^2 \tag{3.15}$$

with $d_j$ the amplitude and $\phi_j(\theta)$ the amplitude and phase of the dipole moment for emission from PES j and $W_j(\theta,t)$ the time-dependent bending wave packet on PES j (see figure 3.25(a) and figure 3.25(b)) and r the fraction of excited molecules at maximal intensity of the transient grating. The bending wave packet $W_j(\theta,t)$ is calculated from the trajectory swarms in figure 3.23 and averaging over the stretching coordinates.

Figure 3.25(c) displays the calculated and experimental total signal $I_{tot} = I_0 + 2I_1$ normalized to one at negative delays and the diffraction efficiency $\eta_1 = I_1/I_{tot}$ convoluted

[5] As in the experiment only short trajectories are considered.

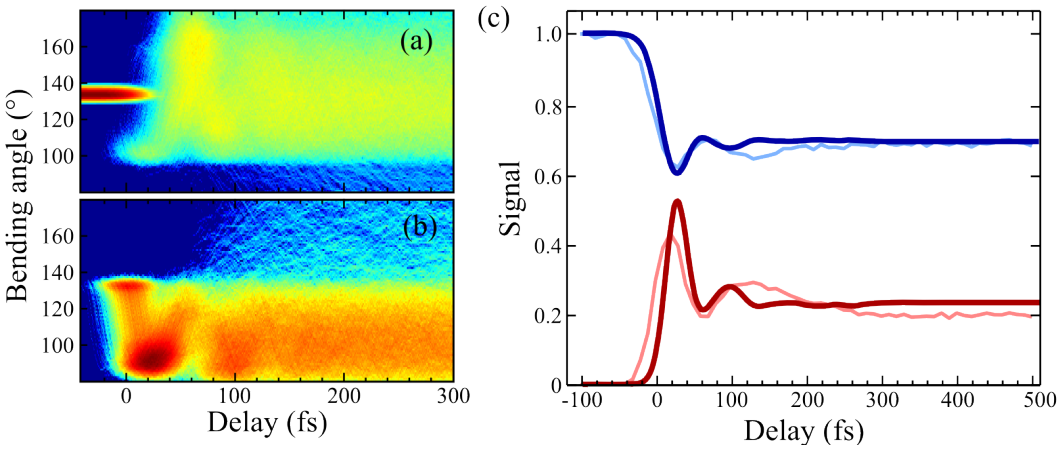


**Figure 3.25.:** Evolution of the bending wave packets $W_1(\theta,t)$ (a) and $W_2(\theta,t)$ (b) in logarithmic scale. (c) Comparison between the calculated (dark) and measured (light) high harmonic signal total signal (blue) and first order diffraction efficiency (red, multiplied by 20).

by a gaussian function of 15 fs FWHM taking into account the duration of the harmonic generation process. The fraction of excited molecules r is assumed to be 20 %. The simple 1D model shows a remarkably good agreement with the experimental results: It reproduce very well the signal amplitudes and the main dynamical features. A closer look at the first order diffraction efficiency and the total signal reveals however some differences between the theory and experiment. The first peak is shifted to slightly lower delays for the experimental result what might be due to a significant signal from the cross-correlation between pump and probe close to zero delay. Furthermore the second peak is narrower in the calculated results. It lies at 100 fs while the broader maximum of the experimental results lies at 120 fs. Additional maxima which are predicted by the calculation at 170 fs and 240 fs are not observed experimentally. This is probably owed to the spreading of the wave packet along the stretching coordinate.

One issue that needs to be addressed is the origin of the femtosecond dynamics. Do they originate from the population transfer between PES 1 and PES 2 or the oscillation of the bending wave packets? The role of the population transfer between PES 1 and PES 2 is studied by keeping the populations on the two diabatic surfaces constant: $\int W_1(\theta,t)d\theta = \int W_2(\theta,t)d\theta = 1/2$ at each delay. This suppresses transfers between the populations of the two states and allows us to isolate only the effect from the vibrational wave packet motion with respect to the bond angle. On figure 3.26 calculations surprisingly show that the dynamics are very similar with and without population transfer, only the amplitude of the first oscillation peaks is lower. This is a very important result. It claims, that the oscillations from the experimental transients can originate from the pure vibrational motion of the wave packets.
In a next step the contribution from PES 1 or PES 2 to the oscillation of the signal is

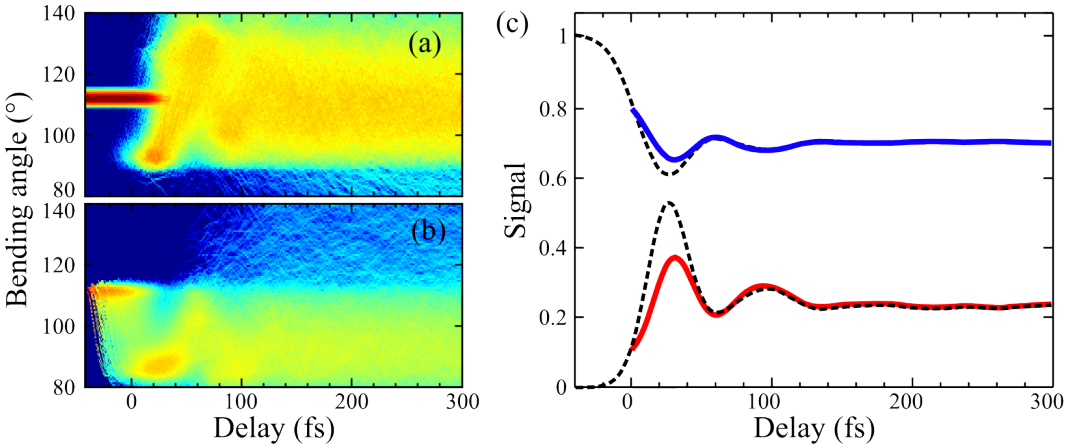


**Figure 3.26.:** Evolution of the bending wave packets $W_1(\theta,t)$ (a) and $W_2(\theta,t)$ (b) in logarithmic scale imposing constant equal populations for the two diabatic states. (c) Total harmonic signal (blue) and first order diffraction efficiency (red, multiplied by 20) obtained by imposing constant equal populations for the two diabatic states. The black dashed line displays the calculation from figure 3.25(c).

further disentangled. Figure 3.27 illustrates how PES 1 and PES 2 contribute separately to the diffraction efficiency. The contribution from PES 1 is negligible whereas it is substantial for PES 2. This can be interpreted by the phase shift range $\Delta I_p \tau$ (see figure 3.24). For PES 1 and PES 2, it ranges from -0.4 $\pi$ to 0.4 $\pi$, for PES 1 and from 0.2 $\pi$ to 0.8 $\pi$ respectively during the wave packet motion. Figure 3.27(b) shows the effect on the diffraction efficiency, its variation is significantly stronger for PES 2 than for PES 1. This behaviour is very peculiar for $NO_2$, and might be inverted for other molecules that experience a stronger recombination phase. If the pump and probe beams are aligned parallel the recombination phase is shifted by almost $\pi$ (see supplemetary information (Wörner et al., 2011)) and leads to a different change for diffraction efficiency. This implies that high harmonic transient grating spectroscopy cannot be used as a general tool for detection of electronic dynamics without caution. Indeed this application rather depends on the respective molecular system. However, it can be stated that similar phase shifts can lead to very different diffraction efficiencies, because the absolute value of the phase plays an important role!

The coupling between PES 1 and PES 2 or in other words the effect of the conical intersection (adiabatic representation) is crucial for the transient behaviour of the diffraction efficiency. If the coupling is switched off (see figure 3.28(b)) PES 2 is not depopulated at 60 fs and not repopulated at 100 fs. This leads to an second oscillation peak which is much weaker at 100 fs as illustrated in figure 3.28(c). The dynamical population transfer through the conical interesection at 100 fs is consequently important for observing the second oscillation peak at 100 fs. The coupling between PES 1 and PES 2, and molecular vibration of the first excited state are identified as the origins of the wave packet dynamics

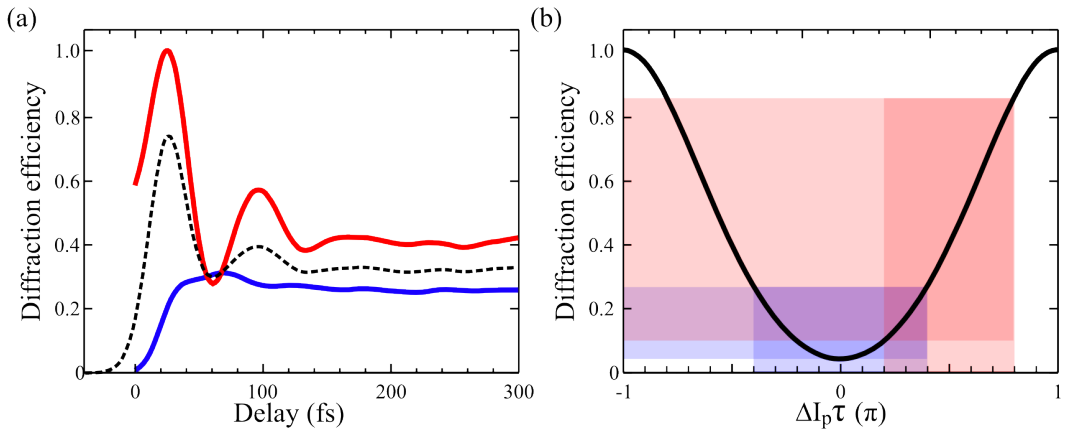


**Figure 3.27.:** (a) Contributions from the PES 1 (blue) and PES 2 (red) to the first order diffraction efficiency. The black dashed line displays the calculation from figure 3.25(c). (b) Normalized first order diffraction efficiency as a function of the phase modulation $\Delta I_p \tau$. The shaded areas correspond to the bending angles which are explored by the main part of the trajectory swarm on PES 1 (blue) and PES 2 (red).

observed in section 3.4. The population transfer through the conical intersection in itself has only little influence. The bending motion of the wave packet plays the major role, but still coupling between the ground and excited state is essential. Generally the transient grating signal is sensitive to different kind of dynamics. This depends on the absolute recombination phase of the molecular system of interest once resolving ground state vibrations, first excited state vibrations or even transitions through a conical intersection. High harmonic transient grating spectroscopy can thus be a very useless or useful tool, it all depends on the absolute phases and their differences.

### 3.5.3. Discussion

The above results are compared to two recent publications. In the first case (Kraus et al., 2012) a 1D quantum calculation for the bending wave packet was applied. The wave packet was modelled by Gaussian functions centered at the angular position expected from the 3D calculation. The harmonic emission was calculated taking into account the same parameters as in the calculations presented above. Their calculation leads to a strongly modulated signal featuring at least four oscillation peaks. Figure 3.29 depicts their and our calculation in direct comparison. In the second case (Kraus and Wörner, 2012) the wave packet motion was neglected and only the influence of the populations on the two PES was considered. In the 3D calculation a constant harmonic dipole moment and phase was assumed only taking account variations of $\Delta I_p \tau$. The signal revealed almost no modulations at all. This is attributed to a fast blurring of the initial wave packet, averaging out the phase modulations $\Delta I_p \tau$. Note however that it has been

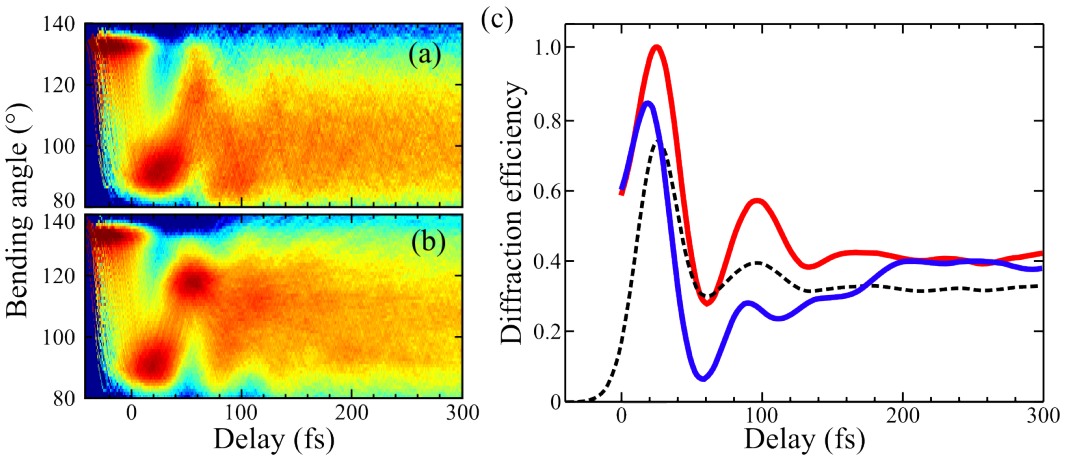


**Figure 3.28.:** Evolution of the bending wave packets $W_2(\theta,t)$ with coupling between PES 1 and PES 2 (a) and without coupling (b). (c) First order diffraction efficiency induced by the trajectories on PES 2, with (red) and without (blue) the coupling to the ground state. The black dashed line displays the calculation from figure 3.25(c).

pointed out that the absolute phase is crucial (e.g. figure 3.27). This makes it difficult to justify the neglect of the dipole phase.

It should be emphasized that the experimental and theoretical results compared in section 3.5.2 are consistent. This lack of agreement in references (Kraus et al., 2012; Kraus and Wörner, 2012) raises doubts about the theoretical approach. If it was true that only the population on the two different surfaces are responsible for the dynamics, one would expect the same contrast of the transients for cross-polarized or parallel polarization. This is however not the case (see figure 3.10) what shows very well that the different dipole phase and ionization channels play an important role for the two orientations (see (Wörner et al., 2011)). It might be true that the blurring of $\Delta I_p$ has a significant effect if the stretch coordinates are taken into account thus smoothing out the two oscillation peaks. This can only be tested by performing the full 3D calculation. The complex radiative recombination dipole moments need to be calculated for different stretch coordinates and the 3D ionic potential curves.

## 3.6. Perspectives

This study, intiated by first results of high harmonic transient grating spectroscopy in $NO_2$ (Wörner et al., 2011), lead to different experimental results with a different interpretation. One major open question remains concerning this new interpretation: Is the 1D calculation really oversimplified? Further calculations require the 3D ionic potential curves and the dipole moments at different stretch coordinates. This calculation would show if phase variations of $I_p\tau$ are quickly washed out by the wave packet spreading in

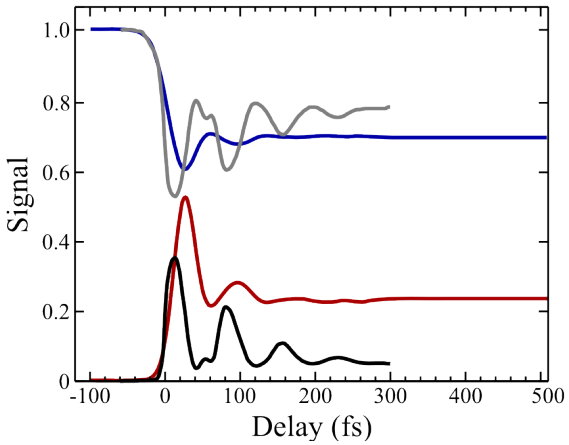


**Figure 3.29.:** Comparison between the calculated high harmonic signal total signal (blue) and first order diffraction efficiency (red, multiplied by 20) depicted in figure 3.25 and the zero order harmonic signal (grey) and first order diffraction efficiency (black, multiplied by 20) from reference (Kraus et al., 2012).

the three dimensions.
On the experimental side an increase of the probe wavelength might be interesting, allowing us to check the dependence of oscillatory transients on $I_p\tau$. At the same generation intensities electron trajectories with a higher time of flight are generated, also leading to a broader spectrum. Another experimental challenge still remains in the field free alignment of $NO_2$. The excitation of the rotational wave packet at 800 nm should allow the observation of rotational revivals. Working with aligned $NO_2$ molecules should increase contrast for future femtosecond pump-probe experiments.
This work has many perspectives for other possible molecular systems to be studied. Ozone might be a suitable candidate, it has the same geometry as the $NO_2$. Furthermore it plays a central role in atmospheric chemistry, the ozone layer in the stratophere filters out the hard UV radiation from sunlight. The absorption maximum in the UV range is around 250 nm in the Hartley band (Qu et al., 2005). This band could be accessed by photoexcitation of the third harmonic (266 nm). We started a collaboration with Janssen from the LPMAA, Paris on the realization of such an experiment. However, the production of ozone with a reasonable concentration proves to be technically challenging however.

## Résumé du Chapitre

*Le troisième chapitre est consacré à l'étude de la dynamique vibronique au voisinage d'une intersection conique et de la photodissociation du dioxyde d'azote, une molécule non linéaire. Cette molécule ne joue pas seulement un rôle important dans la chimie de l'atmosphère, mais présente également beaucoup d'intérêts fondamentaux. Il montre un couplage vibronique substantiel au voisinage d'une interaction conique. Nous explorons sa photodissociation et sa dynamique vibrationelle avec une méthode expérimentale sophistiquée: la GHOE combinée est réalisée dans un milieu spatialement structuré par un réseau transitoire d'excitation (Mairesse et al., 2008c). Dans cette configuration, deux faisceaux pompes sont utilisés dans une géométrie croisée créant un réseau d'excitation. Ce réseau induit une modulation spatiale de l'amplitude et de la phase harmonique dans le milieu générateur ce qui ce traduit en champ lointain par l'apparition d'ordres de diffraction du faisceau harmonique. Par rapport à la configuration pompe-sonde classique elle permet l'extraction des informations de phase et une très grande sensibilité accrue à la fraction des molécules excitées puisque les ordres diffractés n'apparaissent qu'en présque d'une excitation moléculaire.*

*Deux campagnes avec des conditions expérimentales légèrement différentes ont été réalisées, une à Ottawa et l'autre à Bordeaux. Leur interprétation a aussi évolué au cours de ce travail. Initialement, suite aux résultats obtenus en collaboration à Ottawa, les dynamiques observées on été interprétées par le transfer de population intervenant à l'intersection conique entre deux surfaces d'énergie potentielle (Wörner et al., 2011).*

*En complément des expériences menées à Bordeaux qui ont testé la robustnesse des résultats en fonction des paramètres expérimentaux, Halvick et ses collègues ont effectué des calculs en trois dimensions basés sur la méthode du "trajectory surface hopping" (TSH). La GHOE a ensuite été calculée à partir des paquets d'ondes d'électrons fournis par TSH. La simulation de la GHOE pouvait seulement être mise en oeuvre dans un modèle en une dimension comme le potentiel ionique et les moments dipolaires étaient seulement disponibles en fonction de l'angle de liaison mais pour la seule distance NO d'équilibre. Pourtant notre calcul en une dimension est en bon accord avec nos résultats expérimentaux, conduisant à une interprétation différente des transitoires observés sur une échelle femtoseconde. Les simulations montrent que les oscillations du paquet d'onde et un couplage entre les deux surfaces d'énergie potentielle sont responsables de la dynamique femtoseconde (Ruf et al., 2012). Une extension vers un modèle en trois dimensions permettrait d'écarter les dernières ambiguités de cette interprétation.*

# 4. High Harmonic Generation in Clusters

Up to now in this manuscript HHG was treated in atoms, diatomic molecules and triatomic molecules. In this chapter we venture another medium for HHG, namely clusters. In physics a cluster can be defined as a particle which consists of two up to one million atoms, with a radius on the order of magnitude of several nanometers. In fact one has to understand clusters as the bridging between single atoms/molecules and bulk solids. Clusters can have quite different properties than their solid state equivalent: e.g. nanoparticles from metals can have semiconducting or insulating properties (Cha et al., 1993; Busani et al., 1998). Moreover electrical, magnetic and chemical properties are cluster size-dependent. Gold which is chemically inert[1] can definitely adopt catalytic properties for certain cluster sizes (Haruta, 1997; Grunwaldt and Baiker, 1999; Sanchez et al., 1999). Deuterated methane clusters are used to study nuclear fusion and might lead to tabletop experiments in this field of research (Grillon et al., 2002). Nanoparticles might be an efficient and secure hydrogen storage (Zhao et al., 2005; Dillon et al., 1997) and thus cut the Gordian knot for small scale energy storage as needed for electric fuel cells, making hydrogen-powered cars a reality. Clusters have many other applications in medicine, military technology, atom computers and in science in general.
In this context clusters won't directly lead to the solution of profane problems, but will be rather an object of study for the specific scientific subject of HHG. Experiments of HHG from clusters revealed spectra with an extended cutoff (Donnelly et al., 1996; Vozzi et al., 2005b), suggesting clusters as a promising generation medium. The exact mechanism of HHG still remains debated however. The basic mechanism of HHG from single atoms is well understood in terms of the three step model (see chapter 1). This model is too simple for the explanation of experimental observations of HHG from clusters.
Various extensions of the three step model have been proposed (Hu and Xu, 1997; Moreno et al., 1994; Véniard et al., 2001; Zaretsky et al., 2010). The dominant channel generally considered is ionization and recombination to the same atom (atom-to-itself). Since clusters are dense media, there is also a possibility of recombination to neighbouring ions (Moreno et al., 1994; Véniard et al., 2001). This atom-to-neighbour emission can produce incoherent radiation due to a lack of phase-locking between the two atomic wavefunctions (Zaretsky et al., 2010). Another contribution to harmonic emission may come from a wavefunction partially delocalized over the whole cluster, from which electrons tunnel out of and to which they recombine coherently (cluster-to-itself). In addition to these recollisional mechanisms, very different mechanisms could also co-exist as is the case in overdense plasmas (Quéré et al., 2006) or bulk crystals (Ghimire et al., 2011). From an experimental point of view a particular difficulty consists in disentangling the harmonics

[1] There is one exception, it can be dissolved in aqua regia or nitro-hydrochloric acid.

produced by different species (monomers and different size clusters) and possibly different mechanisms.
In this chapter a detailed experimental study of HHG from clusters is presented which aims at disentangling the harmonic signal from clusters and identifying the mechanisms at play. We perform an advanced experimental characterization of the high harmonic emission from clusters for an elucidation of the phenomenon. Varying the cluster size separates the spatially resolved spectrum in two regions showing opposite behaviours. These regions show different responses to laser ellipticity and different polarization states. They correspond to two different classes of emitters and generating mechanisms. The fast decay of the harmonic signal with laser ellipticity indicates that these harmonics are produced by a recollision mechanism which strongly depends on the cluster size, as expected in a cluster-to-itself picture. This last measurement finally allows an estimation of the electron coherence length in krypton clusters.

## 4.1. Clusters in Gas Jets

As in atoms and molecules, HHG in clusters is performed in a gas jet. This paragraph introduces the cluster formation in a gas jet and discusses relevant properties. How do monomers arrange themselves in such a cluster? If we talk about HHG the electronic structure in clusters is very important, it is fundamentally different than that of its monomers. Also quantitative values need be addressed: how large is the average cluster size in a gas jet, what is the cluster size distribution and what monomer ratio contributes to clusterization?

### 4.1.1. Cluster Formation

Rare gas atoms have fully occupied valence shells and can therefore only form covalent bonds. The van-der-Waals force or more precisely the London dispersion force describes the attraction between two instantaneously induced dipoles due to fluctuation of the electron cloud surrounding the rare gas atoms. The counteracting force is the Pauli repulsion force originating from the Pauli exclusion principle: Two fermions must not exhibit the same set of quantum numbers, what leads to spatial separation of electrons having the same spin. These two counteracting forces can be described by the Lennard-Jones potential:

$$V(r) = \epsilon\left[\left(\frac{r_m}{r}\right)^{12} - 2\left(\frac{r_m}{r}\right)^{6}\right] \tag{4.1}$$

where V describes the potential energy, $\epsilon$ the well depth and $r_m$ the interatomic separation at which the energy passes through a minimum. Figure 4.1 shows the potential curve for different rare gas dimers. The values for well depth and interatomic separation can be extracted from (Tang and Toennies, 1986). The binding energy of a krypton

dimer is 17.4 meV and thus below the thermal energy at room temperature (25 meV). Consequently dimerization requires an efficient cooling mechanism of the gas.

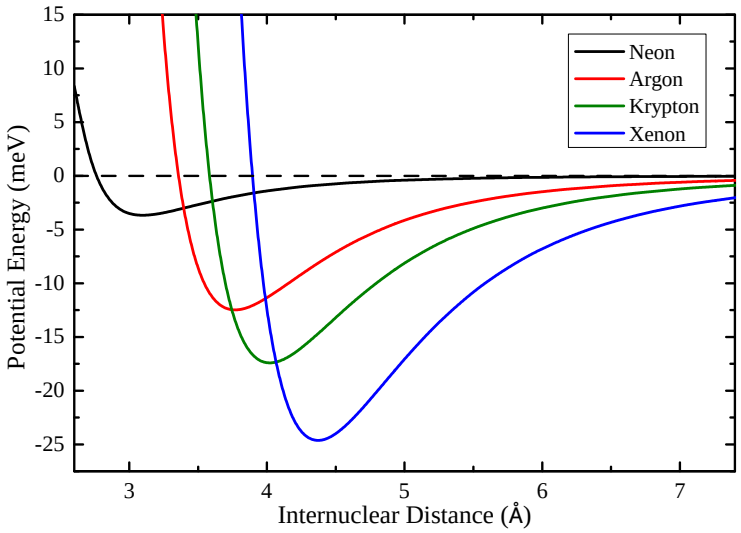


**Figure 4.1.:** Lennard-Jones potential for different rare-gas dimers.

Such a cooling is typically achieved by adiabatic gas expansion through a nozzle. These conditions are fulfilled by a gas expansion through a nozzle into vacuum. Applying the Van der Waals equation for real gases one can show that the adiabatic expansion leads to a temperature change of the system (Lundwall, 2007):

$$T_2 = T_1 - \frac{a}{C_V V_m} \tag{4.2}$$

where $T_{1,2}$ is the temperature before and after the expansion, $a$ the intermolecular attraction in the gas, $C_V$ the heat capacity of the gas at a constant volume and $V_m$ the molar volume before the expansion. Three-atom collisions during the expansion lead to dimerization whereas the third collisional partner dissipates thermal excess energy as kinetic energy. Similar collisions between atoms and clusters will occur subsequently, resulting in bigger clusters. This process also leads to a momentum transfer in the direction of the gas jet with a narrow velocity distribution and therewith a decrease of the gas temperature. The gas supersaturates and forms solid density droplets, which are held together by Van der Waals forces (Hagena and Obert, 1972).

### 4.1.2. Supersonic Gas Beams

Shaping a gas jet has become a science of its own but is certainly crucial for obtaining low jet temperatures. A high gas jet density along the propagation direction of the gas beam leads to a high collision rate and consequently cold beams. The beam spread and exit velocity results in completely different density distribution of the gas jet as shown

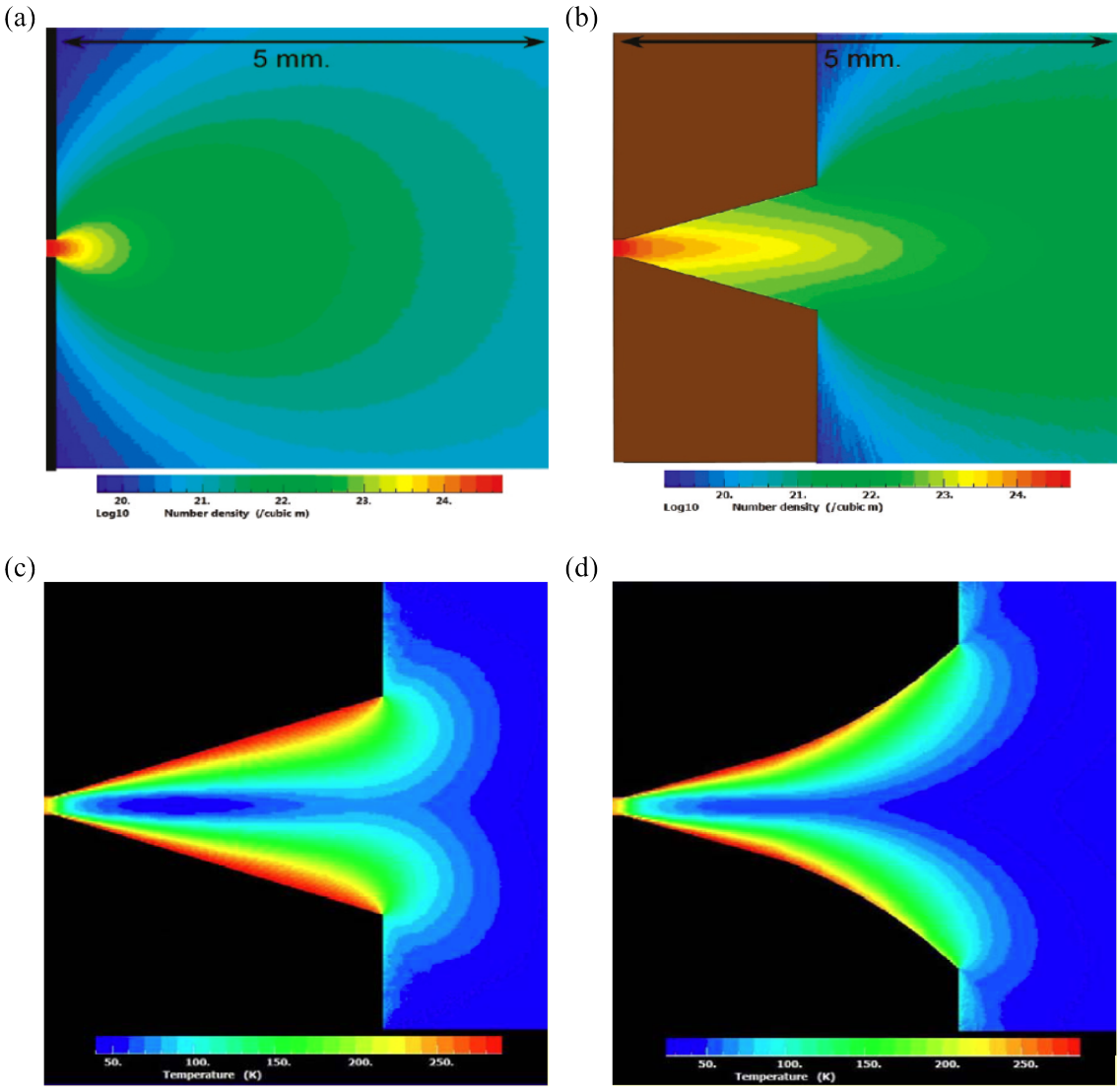


**Figure 4.2.:** (a) Calculated density contours of helium expanding from a 0.2 mm sonic nozzle. The beam spread is wide (FWHM: 1 Steradian) with a high density decrease of the beam (dropping by a factor of 4000 at a distance 25 nozzle diameters on axis). (b) Density map for a conical 0.2 mm supersonic nozzle. The full opening of the nozzle is 50°. The beam spread corresponds to 0.43 Steradian, leading to a gas density which is dropping by a factor of 700 over a distance of 25 nozzle diameters on axis (figures adopted from (Luria et al., 2011)). Simulation of the translational temperature of a conical (c) and a trumpet nozzle (d) (adopted from a report).

in figure 4.2. The sonic jet reaches lower temperatures close to the nozzle exit, but cannot compete with those of the supersonic jet at higher distances. Higher collimated beams can be reached with conical or trumpet nozzles. Figure 4.2(c) and figure 4.2(d) compare the nozzle geometries. A minimum translational temperature is reached on axis inside the conical nozzle. However the temperature increases again in the orifice along the gas expansion direction. This simulation identifies the trumpet geometry as more advantageous, as the temperature decreases monotoneously during gas expansion to the same absolute minimal temperature as in the conical case. At laser focus, i.e. in front of the nozzle the temperature is lower for the trompet than for the conical nozzle.

### 4.1.3. Cluster Structure

A striking difference between bulk material and clusters is their surface fraction. The percentage of surface atoms is decreasing with increasing cluster size. This ratio determines many properties of clusters such as chemical reactivity, band structure and structure of clusters in general. For instance the surface energy of icosahedral clusters consisting of 13 atoms is much higher than that of 14 atoms. As a matter of fact clusters will preferentally form full shells, with a face-centered-cubic (fcc) or icosahedral structure consisting of a number of atoms referred to "magic numbers" (Echt et al., 1981). Thus cluster structure strongly depends on the clustersize. Farges *et al.* showed that small clusters containing 20 monomers up to 50 monomers present the same noncrystalline structure: it is composed of icosahedral of 13 atoms (Farges et al., 1983). In a following paper the same group showed that clusters ranging from 50 to 750 atoms form a multilayer icosahedral structure and further transforming to the fcc crystalline bulk structure (Farges et al., 1986). Another experimental study claims that the transition to a fcc structure already at cluster sizes of 200 atoms (Kakar et al., 1997). These observations disagree with theory which predicts a transition only between 2000 and 3000 atoms (Xie et al., 1989). Doyle *et al.* suggest, that vibrational entropy might play an important role in determining the equilibrium structure of a cluster (Doyle and Calvo, 2002). The transition occuring at different favored structures indicates that the cluster structure is determined by an optimum between surface energy and bulk strain. On the one hand surface energy is higher for icosahedral geometries but on the other hand the interlayer distance is energetically preferable for the fcc geometry. Figure 4.3 depicts these two different geometries for clusters of different size.

### 4.1.4. Electronic Structure

Photoelectron spectroscopy sheds light on the electronic occupied states in clusters. It is based on the firstly from Einstein predicted photoelectric effect (Nobel Prize 1921). This effect describes how the energy of a photon $h\nu$ (if the photon energy is higher than the electron's binding $E_{bind}$ energy) is absorbed by some material, whereupon the material emits an electron with the following kinetic energy $E_{kin}$:

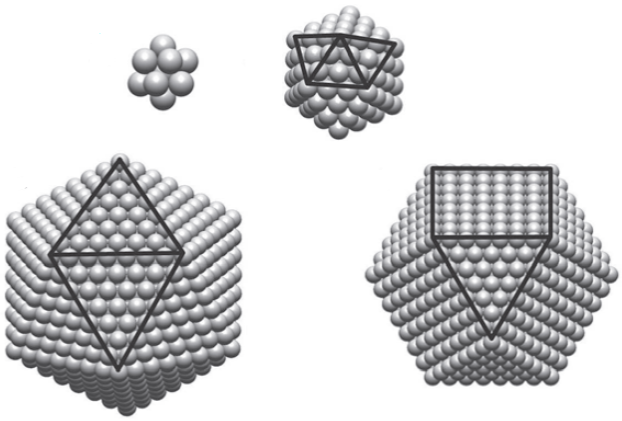

**Figure 4.3.:** Examples of magic clusters: 13 atom icosahedral cluster, 147 icosahedral cluster, 1415 atom icosahedral cluster and 1415 fcc cluster (figure adopted from (Lundwall, 2007)).

$$E_{kin} = h\nu - E_{bind} \tag{4.3}$$

Measuring the kinetic energy of the electron thus gives information about the binding energy of the electrons. The resolution of photoelectron spectroscopy was pushed to new limits by Kai Siegbahn (Nobel Price 1981), opening the field of *Electron Spectroscopy for Chemical Analysis* (ESCA). This spectroscopic method can be divided in *Ultraviolet Photoelectron Spectroscopy* (UPS), reading out the valence electron structure, and *X-ray Photoelectron Spectroscopy* (XPS), which is used to measure the structure of strongly bound core electrons.

An example of UPS spectra in argon, krypton and xenon clusters is shown in figure 4.4(a) (Feifel et al., 2004). Two sharp peaks can be identified which correspond to atomic lines split by spin-orbit coupling. One can very well observe that this coupling is stronger for heavier atoms as they have more protons. More interesting are the broad spectral features at lower ionization energies. They cannot be observed in a sample of pure monomers. They grow with cluster size and can therefore be attributed to electronic bands (Carnovale et al., 1991). XPS spectra from core electrons show that these electrons are highly localized and depend on the environment in the cluster. As depicted in figure 4.4(b) the broad feature from clusters splits up in two parts for the electronic core levels. This is due to polarization screening which induces a polarization of the charge distribution of the surrounding atoms, leading to a lower potential energy of the final state and therefore to a lower binding energy (Björneholm et al., 1995; Tchaplyguine et al., 2004). Polarization screening increases with the polarizability, which itself increases with atom size from argon to xenon. Polarization screening is strongly distance dependent, in case of an infinite solid nearest neighbour atoms contribute to approximately two third of the total screening effect (Björneholm et al., 1996). The remaining third is attributed to the remaining solid. From

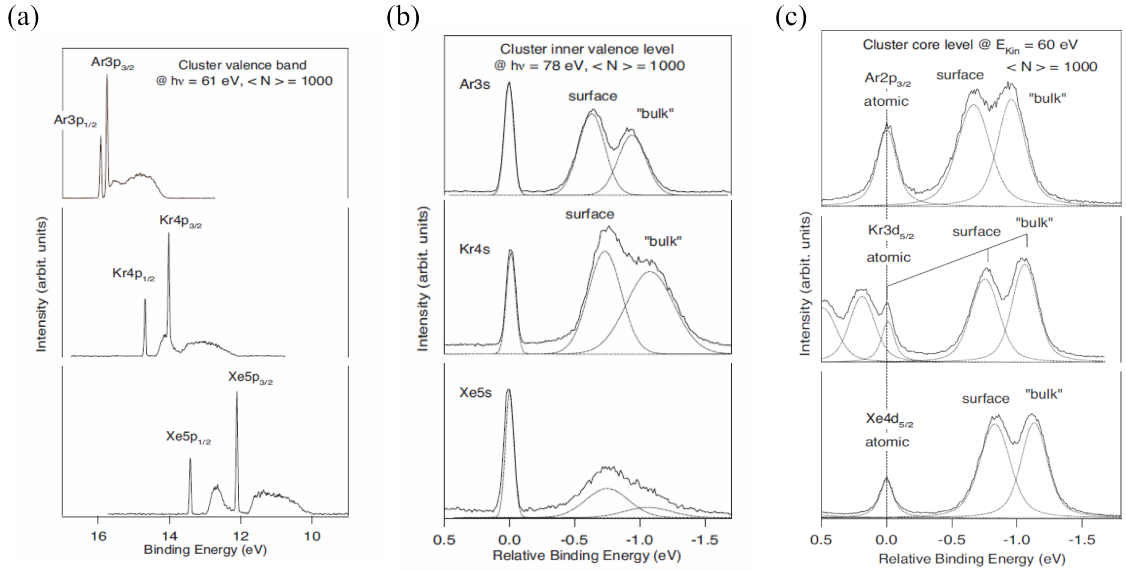


**Figure 4.4.:** (a) Photoelectron spectra of the outer valence orbitals for argon, krypton and xenon clusters for a mean size of 1000 atoms. (b) Photoelectron spectra of inner valence shells for different rare gas clusters. They show a gradual change from a localized behaviour for argon, over a intermediate case of krypton to a delocalized behaviour in xenon. (c) Photoelectron spectra from the outermost core level (figures adopted from (Feifel et al., 2004)).

this it follows that it affects bulk atoms stronger than surface atoms. Valence levels are only partially influenced by this effect confirming a substantial degree of delocalization of valence electrons from their parent atom. As illustrated in figure 4.4(c) the polarization screening is important for the core levels, implying a strong localization of the electrons.

### 4.1.5. Cluster Dynamics

Clusters exposed to strong field are ionized in two different ways (Saalmann, 2006). Inner ionization refers to the excitation of electrons from atomic bound states to the continuum state of the whole cluster. The cluster atoms will be multiply ionized leading to a hydrodynamic expansion of the hot nanoplasma surrounding the cluster (Krainov and Smirnov, 2002). Further heating leads to outer ionization: quasi-free electrons are completely expelled from the cluster leaving a positively charged cluster behind. Atomic ions will be repelled from each other by the Coulomb field what results in so called Coulomb explosion.
In addition to field ionization, impact ionization might play an important role in the ionization process of the cluster. This is especially true for clusters with a low interatomic separation (Hu and Xu, 1997). Especially the higher charged ions are produced by electron impact ionization (Fukuda et al., 2006).

### 4.1.6. Cluster Size and its Distribution

Cluster formation has been thoroughly studied (Hagena and Obert, 1972; Hagena, 1987) using optical diagnostics such as Rayleigh scattering. The mean cluster size in a gas jet is described by an empirical scaling parameter, the Hagena parameter $\Gamma^*$ (Smith et al., 1998), named after his creator:

$$\Gamma^* = k\frac{(d/\tan\alpha)^{0.85}}{T_0^{2.29}}p_0 \tag{4.4}$$

with d ($\mu m$) the nozzle diameter of the jet, $\alpha$ the jet expansion half angle, $p_0$ (mbar) the backing pressure of the jet, $T_0$ (K) the pre-expansion temperature and k the condensation parameter. k is a constant depending on the bond formation of each individual gas and is given in table 4.1:

| Gas | $H_2$ | $D_2$ | $N_2$ | $O_2$ | $CO_2$ | $CH_4$ | He | Ne | Ar | Kr | Xe |
|---|---|---|---|---|---|---|---|---|---|---|---|
| k | 184 | 181 | 528 | 1400 | 3660 | 2360 | 3.85 | 185 | 1650 | 2890 | 5500 |

**Table 4.1.:** Condensation parameter k for different gases (Smith et al., 1998).

The average cluster size $\bar{N}$ can thus be estimated with (Dorchies et al., 2003):

$$\bar{N} = 33\left(\frac{\Gamma^*}{1000}\right)^{2.35} \tag{4.5}$$

This scaling law was determined under specific experimental conditions and is not valid for other conditions. Buck *et al.* found different laws for the mean cluster size $\bar{N}$ in different ranges of $\Gamma^*$ (Buck and Krohne, 1996). One can find many other different empirical expressions in literature for the mean cluster size, however one can state that they usually do not differ by more than a factor of 2. The cluster size distribution in the gas jet can be approximated by lognormal distributions. These have been observed in ammonia, water, carbon, sulphur and aluminium clusters. Dorchies and coworkers give the standard deviation $\delta\bar{N}/\bar{N}$ of the clustersize distribution (Dorchies et al., 2003). It can be estimated to 42 % at a backing pressure of 20 bar and decreases to 36 % for 40 bar and to 33 % for 60 bar.
Another important parameter is the ratio of atoms $r_c$, which clusterize. In first case a ratio of 15 % has been found in a $CO_2$ gas jet, when using a cylindrical nozzle at a backing pressure of 5 bar (Ramos et al., 2005). The result is quite different when a Campargue type (Campargue, 1983) gas source is used. When applying a backing pressure of 5 bar argon gas only 3 % of the atoms cluterize (Fort et al., 1997). This difference can probably not only be justified by the different condensation parameters. The different nozzle geometries play certainly an important role. In another experiment the cluster mass fraction has been determined in pump-probe experiment, taking advantage of the time-dependent refractive index of the expanding cluster (Arefiev et al., 2010). A cluster mass fraction of 14 % is estimated when using a conical nozzle backed by 41 bar of argon gas.
A formula which determines the ratio of atoms, contributing to clusterization is established based on thermodynamic assumptions (Krainov and Smirnov, 2002) and has been verified experimentally (Danil'chenko et al., 2009):

$$r_c = \frac{T_c}{\epsilon_0} \ln \bar{N} \tag{4.6}$$

where $T_c$ is the condensation temperature in the jet and $\epsilon_0$ the binding energy per atom in a cluster. However very different values are found for the ratio $T_c/\epsilon_0$ in the two publications. The former claims typical values of $T_c/\epsilon_0 = 0.1$ whereas values $T_c/\epsilon_0 = 0.03$ to $T_c/\epsilon_0 = 0.07$ have been found experimentally for clusters from pure carbon dioxide and a gas mixture of carbon dioxide and krypton (Danil'chenko et al., 2009). With a condensation temperature of $T_c = 53$ K (Farges et al., 1981) and a binding energy of $\epsilon_0 = 116$ meV per atom (Kittel, 2005) for krypton one receives a ratio of $T_c/\epsilon_0 = 0.59$ what is clearly different from the two former ratios. It is however crucial to know this ratio exactly as already small differences can lead to substantial differences for the monomer cluster ratios. Furthermore $T_c$ depends strongly on cluster size and on the gas entropy per atom (Ratner, 1999). As no reliable values could be established for $T_c/\epsilon_0$, it is not possible to determine the ratio of atoms which contributes to clusterization.
Measurements for studying the average cluster size are complex. Rayleigh-scattering, which has frequently been used to analyze cluster jets is not sufficient for obtaining information on cluster number and mean size (Dorchies et al., 2003). Ramos and coworkers

employed Rayleigh- together with linear Raman-scattering for measuring these quantities (Ramos et al., 2005). A similar measurement would need to be established for answering the question on the cluster to monomer ratio.

## 4.2. Motivation for High Harmonic Generation in Clusters

Clusters are formed in a cold gas jet. In chapter 2 experiments with such a gas jet are presented. Thus it is important to establish the contribution of HHG from clusters to the high harmonic signal in order to separate the two different signals: HHG from strongly aligned molecules and HHG from clusters. In paragraph 4.5 of this chapter the role of clusters is elaborated. There is however another interest in studying HHG from clusters. First experiments were carried out in the mid-nineties. They demonstrated that HHG from clusters showed higher emission frequencies than from the corresponding monomers (Donnelly et al., 1996; Vozzi et al., 2005b). These results are presented and compared to our studies.

### 4.2.1. Results from early Experiments

Figure 4.5 summarizes three former results obtained in clusters. In a first study (Donnelly et al., 1996) HHG was performed in argon using three different sources: a static-gas cell, a sonic and a supersonic gas jet. Only monomers are present in the cell whereas average cluster size increases with a colder translational temperature in the sonic and supersonic gas jet (see also section 4.1.2). The high harmonic cutoff increases by two harmonics when using a supersonic jet as compared to a gas cell. This extended cutoff was eventually attributed to shielding of the laser field within the cluster which leads finally to higher appearance intensity for cluster harmonics.
A second work on HHG in clusters followed shortly afterwards (Tisch et al., 1997). This time harmonics were generated in xenon, a gas that has a three times higher condensation parameter than argon. The harmonic yield and the Rayleigh scattering signal from the gas source is measured as a function of the backing pressure (see figure 4.5(b)). With the onset of clustering the Rayleigh scattering signal increases and the pressure scaling law changes from the power square to the power cube. An up to a five-fold yield enhancement of HHG in clusters is deduced from the anomalous backing pressure dependence.
A third study only performed a decade later was conducted by Vozzi and coworkers in argon gas. As illustrated in figure 4.5(c) an extended cutoff has been measured when larger clusters were present in the generation medium. Moreover an optimal photon yield was observed for harmonic 25 at a nozzle temperature of 180 K and a Hagena parameter of $\approx$7000 (see figure 4.5(d)). This result lead to the conclusion that high harmonics generated at low temperature are emitted from the surface of large clusters scaling with $T^{1.7}$. At higher temperatures, i.e. in the case of smaller clusters the signal is dominated by the emitting source density and scales with $T^{-2}$.

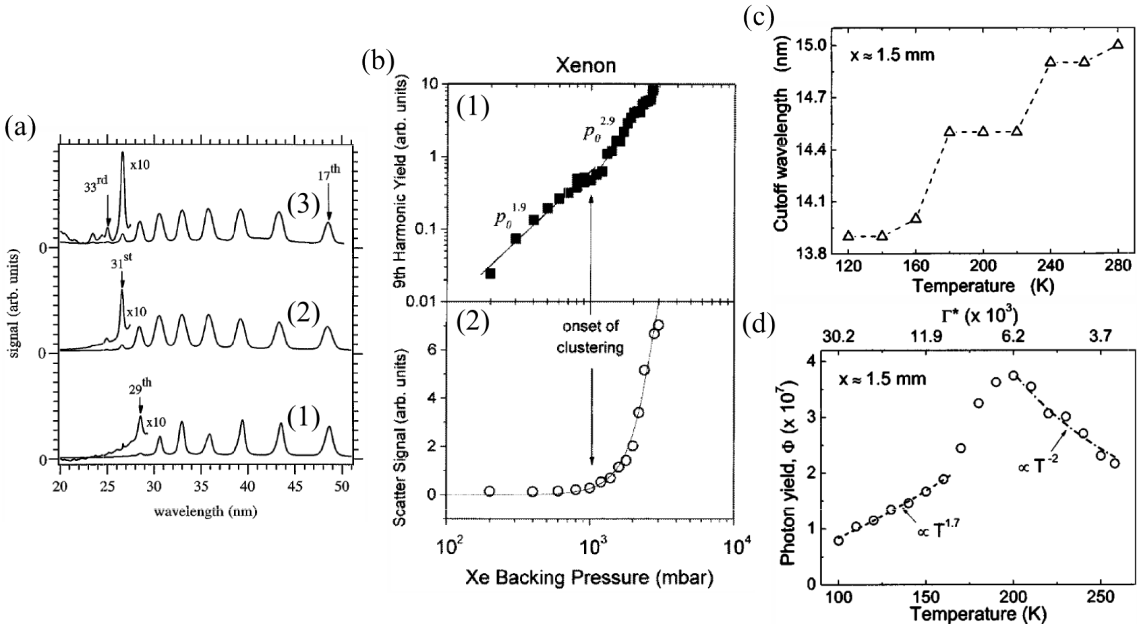


**Figure 4.5.:** (a) High harmonic spectra from argon in (1) a static-gas cell, (2) a sonic jet and (3) a supersonic jet (figure adopted from (Donnelly et al., 1996)). (b) Comparison of the (1) ninth harmonic yield generated in xenon to (2) the Rayeigh scattering signal (figure adopted from (Tisch et al., 1997)). (c) Harmonic cutoff wavelength as a function of temperature. (d) Photon yield for harmonic 25 as a function of temperature and Hagena parameter (figures(c) and (d) adopted from (Vozzi et al., 2005b)).

### 4.2.2. Different Interpretations of HHG from Clusters

The exact mechanism of HHG from clusters is still debated, various extensions of the three step model have been suggested. Shortly after the introduction of this model another principally different idea of recombination has been proposed for two-electron molecular ions: recombination with a neighbouring ion which can lead to an excess energy of $I_p + 8U_p$ (Moreno et al., 1994, 1997; Bandrauk and Yu, 1999). The model was extended later to a linear chain of ions and could be confirmed (Numico et al., 2000; Véniard et al., 2001). However one has to consider that the initial phase of the parent ion and the phase of the neighbouring ion play an important role. The phase of the electron wave packet and the bound electronic wavefunction cancel out in the case of monomers leading to coherent recombination (Smirnova et al., 2009a). There is no reason why phases of electronic wavefunction of neighbouring atoms are correlated in Van der Waals clusters. The coupling in Van der Waals clusters is only weak.
Zaretsky and coworkers (Zaretsky et al., 2010) are even going a step further and do not impose this condition for HHG. He proposes an incoherent recombination of the electron wave packet with an ion different from its parent ion, still resulting in high harmonic emission. This point of view can be regarded as very controversial as high harmonics are a priori supposed to be coherent. Another contribution to harmonic emission to consider is a wavefunction partially delocalized over the cluster, from which electrons tunnel out and to which they recombine coherently (cluster-to-cluster). In addition to these recollisional mechanisms, very different mechanisms could co-exist as in the case of overdense plasmas (Quéré et al., 2006) or bulk crystals (Ghimire et al., 2011).
A variety of efforts have been made in order to gain further understanding of HHG in clusters: Light absorption by the periphery atoms might undertake the role of field shielding whereby the atoms in the cluster experience a different laser pulse profile and consequently a reduced saturation (Donnelly et al., 1996). In addition, one should also consider the possible role of intermediate states' resonance effect in the process of avalanche multiphoton ionization in a multiwell system (Hu and Xu, 1997).

### 4.2.3. Comparison: Temperature Dependence

The results from Vozzi and coworkers are compared to three different temperature scans performed in clusters. We generate high harmonics in a supersonic gas jet, using a valve (Even-Lavie) pulsed at 1 kHz. Different nozzles can be mounted on this valve. Here we use a d =150 $\mu$m diameter trumpet nozzle with jet expansion half angle of $\alpha \approx 10°$. The laser was focused using a 37.5 cm focal spherical mirror at 4.8 mm from the nozzle exit, which ensures proper jet thermalization. The angle of incidence on the spherical mirror was $\approx 7.5°$, what already causes a slightly astigmatic beam profile at the laser focus. Figure 4.6 depicts the different scans that were taken, two in carbon dioxide at a backing pressure of 10 bar and 20 bar and one scan in krypton at a backing pressure of 20 bar. The signal shown is normalized to the signal at 80 °C for each harmonic order.

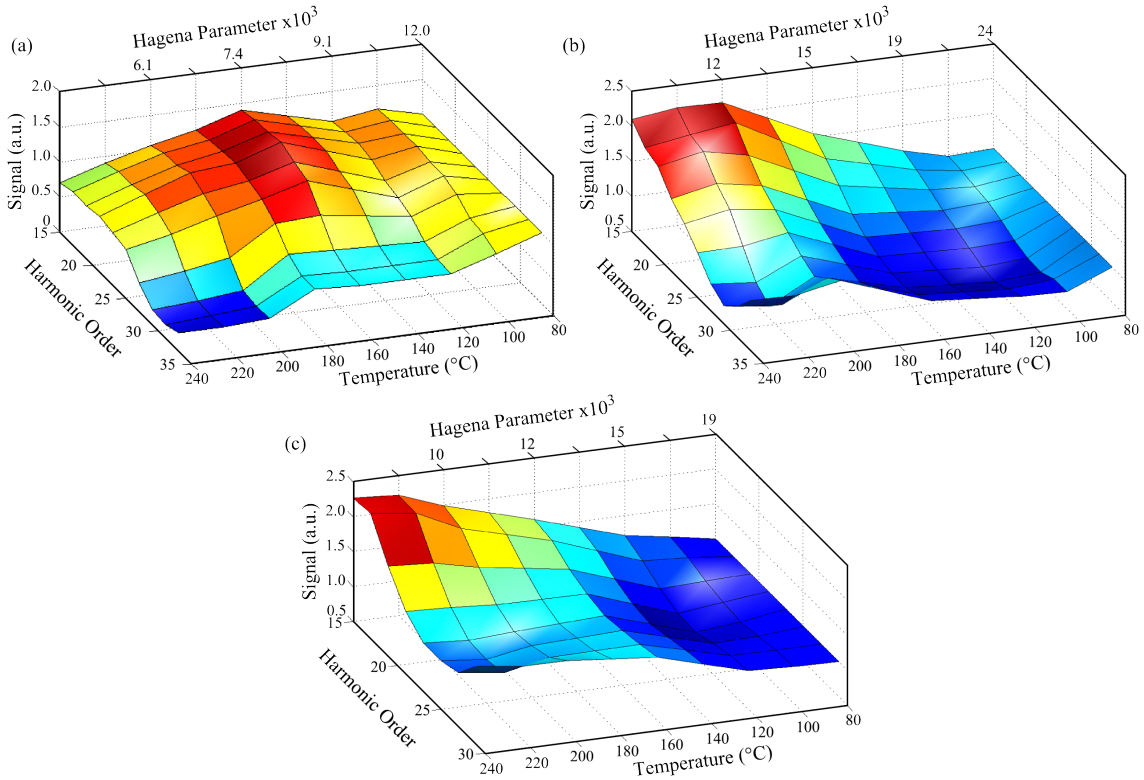


**Figure 4.6.:** Total signal of different harmonics as a function of temperature normalized to its value at 80 °C. HHG are generated in carbon dioxide at a backing pressure of (a) 10 bar, (b) 20 bar and (c) in krypton at a backing pressure of 20 bar.

Based on the assumption that the signal is optimized at a Hagena parameter of 7000, the signal illustrated in figure 4.6 is interpreted. In order to set the Hagena parameter in relation to the temperature figure 4.7 shows its progress in the three different clustering conditions. The critical Hagena parameter is only reached when setting the nozzle temperature at $\approx 170°\mathrm{C}$ and the backing pressure of carbon dioxyde at 10 bar. In the two other cases the Hagena parameter is always above these values. When comparing the plateau harmonic signal to the observations from Vozzi and coworkers (see figure 4.5(d)) a good qualitative agreement can be established: the signal decreases on both sides of an optimum reached at a Hagena parameter 7000. As we will see the cutoff harmonics reveal a different behaviour.

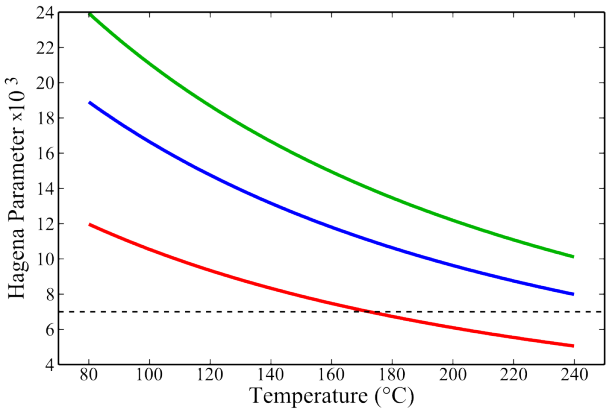


**Figure 4.7.:** Hagena parameter as a function of temperature for carbon dioxide at a backing pressure of 10 bar (red), 20 bar (green) and krypton at a backing pressure of 20 bar (blue).

Up to now only the spatio-spectrally integrated signal was recorded as was done in the case of the former studies. As the recombination mechanism in clusters might be different it is important to differentiate between the signal from short and long trajectories. As it is difficult to distinguish these in the spectrum, a difference signal in form of a 2D spatio-spectrally resolved representation is more illustrative. Figure 4.8 depicts the difference spectra from carbon dioxide in the 2D representation for two temperature intervals. The first temperature interval is chosen between 80 °C and 160 °C and the second between 160 °C and 240 °C. The first differential measurement (see figure 4.8(b)) clearly reveals two regions, the off axis cutoff region and the on axis plateau region. The signal from the on axis plateau region increases up to 160 °C in agreement with the behaviour of the total signal from the plateau region illustrated in figure 4.6(a). The off axis cutoff signal decreases for this temperature range. Above 160 °C the overall signal decreases (see figure 4.8(c)). Below 160 °C the 2D differential measurement reveals what the integration over one harmonic signal does not, namely different temperature behaviour for one and the same harmonic. Above 160 °C this distinction is much less pronounced and the integration over the entire harmonic represents well its trend.

Note that as the temperature varies, not only the cluster size is affected, but also the gas density in the expanding gas jet, it scales with $1/\sqrt{T}$ (Scoles et al., 1988; Beijerinck and Verster, 1981). One could argue that the signal drop is due to the decrease of monomers. Assuming that the signal scales with the square number of emitters a temperature scaling of $1/\mathrm{T}$ is expected and thus a drop of only 16 % of the signal between 160 °C and 240 °C. This is however not observed. For example the signal increases by 30 % and more for cutoff harmonics in krypton at a backing pressure of 20 bar. One can therefore conclude that another effect than the drop of the monomer density plays an important role.

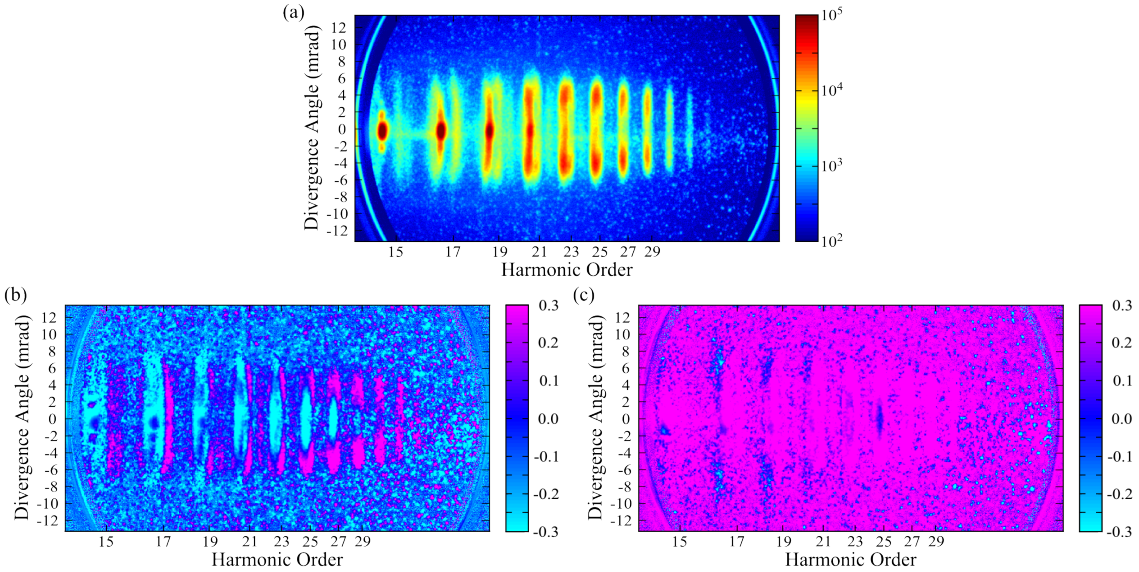


**Figure 4.8.:** (a) Spectrum generated in carbon dioxide at a backing pressure of 10 bar. (b) Difference signal of spectra generated in carbon dioxide at a backing pressure of 10 bar. A spectrum $S_{160}$ taken at 160 °C is subtracted from a spectrum $S_{80}$ taken at 80 °C and then normalized by the sum of the two spectra $((S_{80} - S_{160})/(S_{80} + S_{160}))$. (c) A spectrum $S_{240}$ taken at 240 °C is subtracted from a spectrum $S_{160}$ taken at 160 °C and then normalized by the sum of the two spectra $((S_{160} - S_{240})/(S_{160} + S_{240}))$.

Figure 4.9 depicts the same 2D spatio-spectrally resolved presentions for krypton and carbon dioxide at a backing pressure of 20 bar. Again the same tendency is observed for the off axis cutoff and on axis plateau signal. Differential signals at temperature steps of 20 °C show the same tendency. In addition to the harmonic spectrum isotropic radiation is observed as vertical lines corresponding to plasma lines (Fort et al., 1997; McPherson et al., 1987). They originate from electronic transitions in excited ions in the cluster. Impact ionization within the cluster leads to inner shell ionization, leaving the freed electrons in a quasy bound cloud behind (Krainov and Smirnov, 2002; Saalmann, 2006). Impact ionization is thus less important in small than in large clusters. This effect is very well demonstrated as the signal of the plasma lines decreases with smaller average cluster size

(see figure 4.9).
How do these results compare to the findings from Vozzi and coworkers (see figure 4.5)? For the plateau harmonics the qualitative trend can be reproduced but the cutoff harmonics do not follow this tendency. It seems however that this agrees with the study depicted in figure 4.5(d), a maximum signal is observed at a Hagena parameter around 7000. The temperature dependency of the cutoff harmonics remains a mistery however. One even has to differentiate the signal originating from one harmonic, it shows regions of different temperature behaviour and might therefore indicate HHG from different type of emitters.

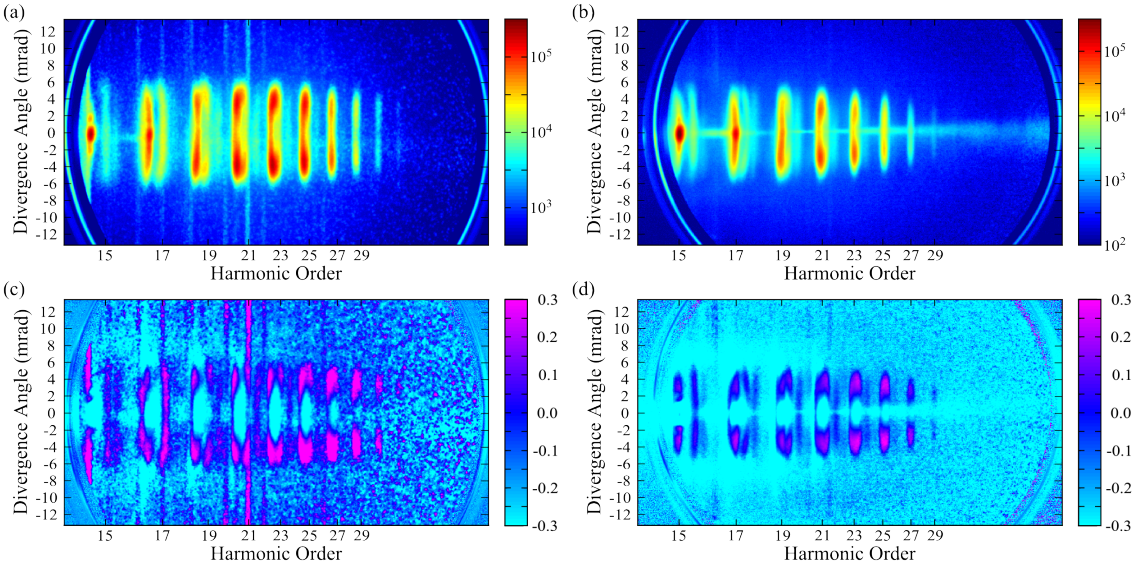


**Figure 4.9.:** Spectra generated in carbon dioxide (a) and krypton (b) at a backing pressure of 20 bar. Difference signal of spectra generated in (c) carbon dioxide and (d) krypton at a backing pressure of 20 bar. A spectrum $S_{240}$ taken at 240 °C is subtracted from a spectrum $S_{80}$ taken at 80 °C and then normalized by the sum of the two spectra $(S_{80} - S_{240})/(S_{80} + S_{240})$.

### 4.2.4. Comparison: Pressure Dependence

Just like a temperature scaling law has been deduced by Vozzi and coworkers (Vozzi et al., 2005b) a pressure scaling law is derived in this context. Two assumptions were made in their work which are questionable. The first one is that the density scaling in a gas jet is governed by the ideal gas law leading to a monomer density dependence of $n \propto p/T$. At least the temperature dependence has found to be different for an ideal free-jet (Scoles et al., 1988; Beijerinck and Verster, 1981) namely with $n \propto 1/\sqrt{T}$. Another parameter which is unknown is the number of monomers contributing to clusterization (see section 4.1.6), they assumed that all monomers contribute to clusterization. According to their model (at a Hagena parameter larger than 7000) that only atoms located at the cluster

surface emit high harmonics the following relation can be established between the density of emitting sources $n_X$, the cluster radius $R$ and the cluster density $n_C$: $n_X \propto n_C R^2$. With $R \propto N^{1/3}$ and $N \propto (\Gamma^*)^{2.44} \propto p^{2.442}$ it follows $n_X \propto n_C p^{2.44 \cdot 2/3}$. The cluster density is scaling with $n_C \propto \rho/N \propto p \cdot p^{-2.44}$ where $\rho$ is the initial monomer density in the gas jet. This leads to a photon yield $\Phi$ dependency of $\Phi \propto n_X^2 \propto p^{0.37}$. This formula therewith predicts a trend which is tested in the following study: the average cluster size is varied by changing the pressure and while keeping the same temperature.

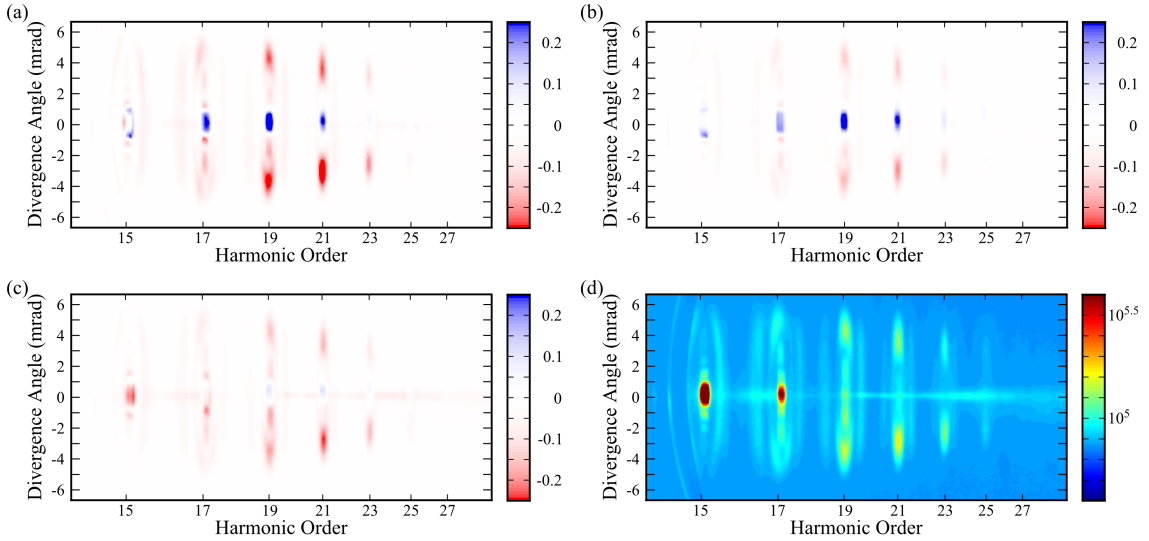


**Figure 4.10.:** Difference signals of spectra generated in krypton. A spectrum $S_{20}$ taken at 20 bar is subtracted from a spectrum $S_{10}$ taken at 10 bar and normalized by the sum of the two spectra $(S_{10} - S_{20})/(S_{10} + S_{20})$. The difference spectra are taken at different temperatures, namely at (a) 110 °C, (b) 140 °C and (c) 170 °C. (d) Spectrum taken at 110 °C.

Figure 4.10 displays pressure difference spectra at distinct temperatures. A value of 0.13 is expected from the calculated scaling law from above. The same nozzle is used as described in section 4.2.3. The first and second spectrum are taken at 110 °C and 140 °C in krypton and once again allow us to distinguish two regions behaving fundamentally different. The off axis cutoff region signal is decreasing whereas the on axis signal is increasing when changing the backing pressure from 20 bar to 10 bar. Only at a nozzle temperature of 170 °C the signal behaviour is changing, the signal increase on axis is almost negligible when decreasing the pressure. The different regions resolved in the 2D differential measurements demonstrate that considering the total signal of one harmonic order is too simplified. Already the trend of the power scaling law for the total harmonic signal $\Phi \propto p^{0.37}$ cannot be verified for all the harmonics. Note also that this power scaling law disagrees with the one observed in figure 4.5(b) by Tisch and coworkers (Tisch et al.,

[2]The Hagena scaling law given in their article is used for this calculation.

1997). Gas jet and clustering conditions are certainly different in the three experiments. In the case of small clusters it seems that the signal from one harmonic signal shows a monotonous trend. However when clustering becomes more important and large clusters are formed in the supersonic gas jet, the signal of the respective harmonic orders needs to be distinguished. This can only be done in a 2D spectro-spatial analysis.

## 4.3. Inhomogeneous High Harmonic Generation in Krypton Clusters

The real mechanism of HHG in clusters is not clear yet and is still discussed controversally. From an experimental point of view a particular difficulty consists in disentangling the harmonics produced by different species (monomers and different size clusters) and possibly different mechanisms. In this paragraph a detailed experimental study of HHG from clusters is presented which aims at disentangling the harmonic signal from clusters and identifying the mechanisms at play. By studying the spectral and spatial profile of the harmonics as a function of pre-expansion gas temperature, a region corresponding to pure cluster emission is identified. The signal from this region shows a strong decay of harmonic signal with increasing laser ellipticity. Moreover the sensitivity to laser ellipticity increases when reducing the average cluster size. This measurement finally leads to a simple model of HHG in clusters: Cluster-to-Itself Model. Finally polarization measurements are presented revealing an unexpected result: depolarized HHG in the cutoff.

### 4.3.1. Temperature Dependence

In this experiment the average cluster size $\bar{N}$ is varied by changing the nozzle temperature between 140 °C and 240 °C. The same nozzle is used as described in section 4.1.6. The average clustersize was thus varied between $\bar{N} \approx 14000$ and $\bar{N} \approx 4000$. With a Wigner-Seitz radius of 2.57 Å (Krainov and Smirnov, 2002) in krypton clusters this corresponds to respective average cluster diameters of 124 Å and 84 Å. The standard deviation $\delta N$, of the cluster size distribution is broad and leads to a significant contribution of small clusters. It is estimated by $\delta N/\bar{N} \approx 48\,\%$ (Dorchies et al., 2003). At a time when the experiment was performed the Aurore TiSa-Laser system was not upgraded yet and delivered 7 mJ, 35 fs, 800 nm pulses at 1 kHz. The experimental setup is depicted in chapter 1, including the slit which is depicted in figure 1.23. Each recorded image was averaged over 15000 laser shots including a subtraction of the electronic background of the CCD camera.

Figure 4.11(a) shows a harmonic spectrum obtained at a laser intensity of $1 \times 10^{14}\,\mathrm{W/cm^2}$. The horizontal line around zero divergence angle is due to scattered light from lower harmonics. As already mentioned in section 4.2.3, isotropic radiation is observed as vertical lines, corresponding to plasma lines. A strong line observed around 49.4 nm can be attributed to an electronic transition in $Kr^{3+}$ (NIST, 2012). Other spectral lines are identified as lines corresponding to electronic transitions from $Kr^{2+}$ (46.1 nm), $Kr^{3+}$ (37.3 nm,

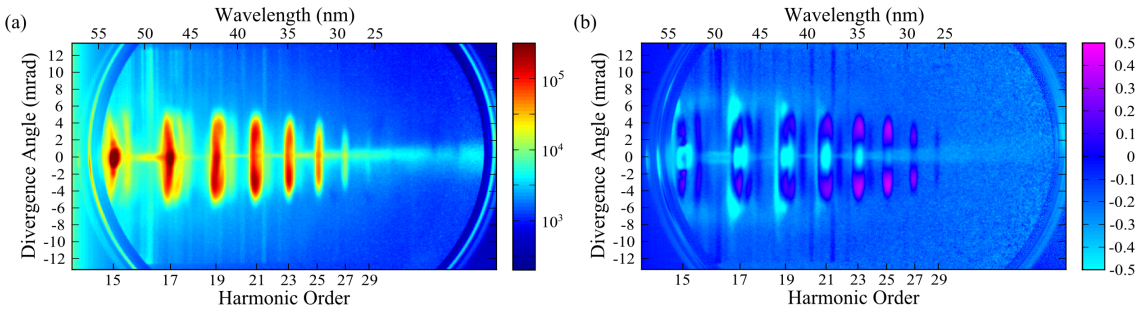


**Figure 4.11.:** (a) Spectrum integrated over 735000 laser shots at laser ellipticties from -0.45 to 0.45 at a temperature of 80 °C. We integrated also over lower laser ellipticities for enhancing the plasma lines. At higher laser ellipticities HHG is suppressed but the plasma emission remains the same. (b) Difference signal of a spectrum taken at 240 °C subtracted from a spectrum taken at 80 °C and then normalized by the sum of the two spectra.

46.5 nm) and $Kr^{4+}$ (41.8 nm) (NIST, 2012). Second order diffraction from the gold grating cannot be excluded. A good match with spectral lines from literature indicate however a good correlation between the ionic states and the spectral line positions. The laser intensity employed is not high enough to field ionize krypton atoms up to three ($I_p = 52.5$ eV) or up to four times ($I_p = 64.7$ eV) (Haynes, 2007). Equation 1.7 gives the saturation intensities from Barrier Suppression Ionization model. Intensities of $3.1 \times 10^{16}$ W/cm$^2$ and $7.0 \times 10^{16}$ W/cm$^2$ would be required for reaching saturation of three or four times ionized krypton atoms, what is two orders of magnitude higher than available in this experiment. Only impact ionization within the clusters leading to inner shell ionization can be responsible for the formation of such highly ionized krypton (Krainov and Smirnov, 2002; Saalmann, 2006).
Apart from plasma lines the spectrum from figure 4.11(a) does not show specific features that could be a signature of the presence of clusters in the medium. As in the previous paragraph we monitor the spatially and spectrally resolved evolution of the signal as the nozzle temperature increases from 80 °C to 240 °C. The same two regions as recorded above are revealed as illustrated figure 4.11(b): a low energy component (up to harmonic 23) which increases with temperature, and an off axis component (dominant from harmonic 21 to 29) which presents a higher cutoff and decreases monotonously with temperature similar to the plasma lines.

Figure 4.12 depicts the spatio-spectrally integrated signal for two different harmonic orders and the plasma line. When heating up the nozzle, the average clustersize decreases as well as the signal from the plasma lines. What happens to the large clusters though? They certainly disintegrate into monomers or smaller clusters even if the quantitative change of distribution is not know (see section 4.1.6). Thus it strongly suggests that the signal from the pink regions in figure 4.11(b) can be attributed to HHG from large clusters. As they dissociate the fractions contribute stronger to the on axis signal in the

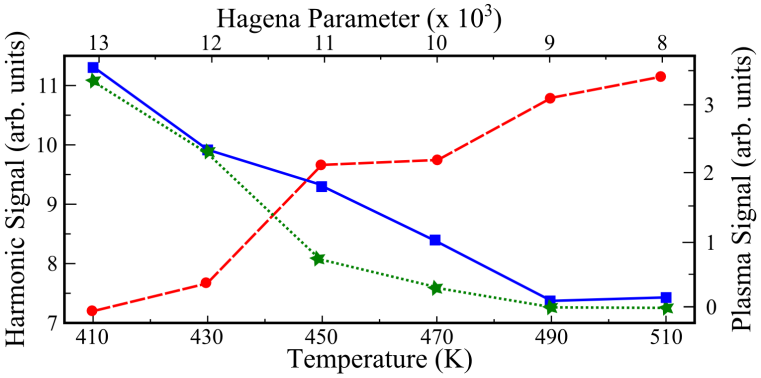


**Figure 4.12.:** Integrated signal of harmonic 15 (red), 25 (blue) and the plasma line (green) centered at 49.4 nm as a function of temperature of the gas nozzle. The intensities of the three signals has been shifted in order to fit the frame.

plateau region. In the following the focus is set on the signal from large clusters, whose behaviour is correlated to that of plasma lines.

### 4.3.2. Ellipticity Dependence

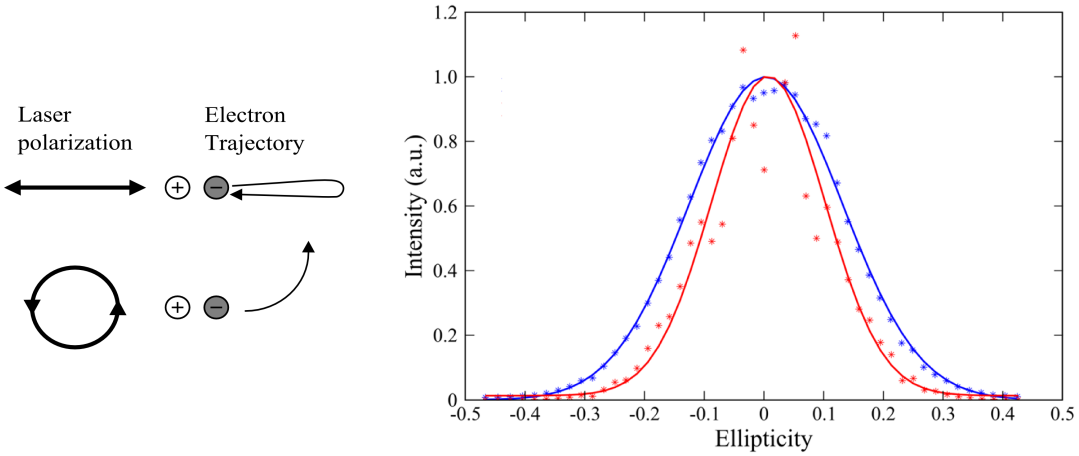


**Figure 4.13.:** Dependence of the harmonic signal as a function of driving laser ellipticity. The sensitivity is higher for the off axis signal of harmonic 25 (red, $\beta = 56 \pm 4$) than for the on axis signal from harmonic 15 (blue, $\beta = 31 \pm 3$).

In order to characterize the different mechanisms that may be at play in the harmonic emission, we studied the sensitivity of the high harmonic signal to the ellipticity $\epsilon$ of the generating laser field. The main polarization axis was kept vertical by employing a fixed zero-order quarter waveplate behind an adjustable zero-order half waveplate. The ellipticity was varied from -0.45 to 0.45 recording 49 points. The decay rate $\beta$ of the

harmonic intensity $I$ with ellipticity is deduced by a Gaussian fit: $I \propto \exp(-\beta\epsilon^2)$. Figure 4.13 illustrates this dependence for harmonic 15 (signal integrated on axis) and harmonic 25 (signal integrated off axis). It is evident that the sensitivity to ellipticity is higher for cutoff harmonic than for the plateau harmonic.
The decay rate $\beta$ is extracted for each single pixel owing to the 2D spatio-spectrally recorded signal. A four parametric Gaussian function (amplitude, width, background, center) is fitted for each pixel. The width is converted to $\beta$ and a betamap is constructed piece by piece. Figure 4.14 shows betamaps recorded at different temperatures. An decay can be observed for the whole harmonic spectrum, which is consistent with a recollision picture of HHG. As in figure 4.11(b) the same areas can be identified, the off axis cutoff with $\beta > 45$ and the on axis plateau with $\beta < 45$. Remarkably the decay rate increases with the nozzle temperature in the former case, while it hardly affect $\beta$ in the latter case.

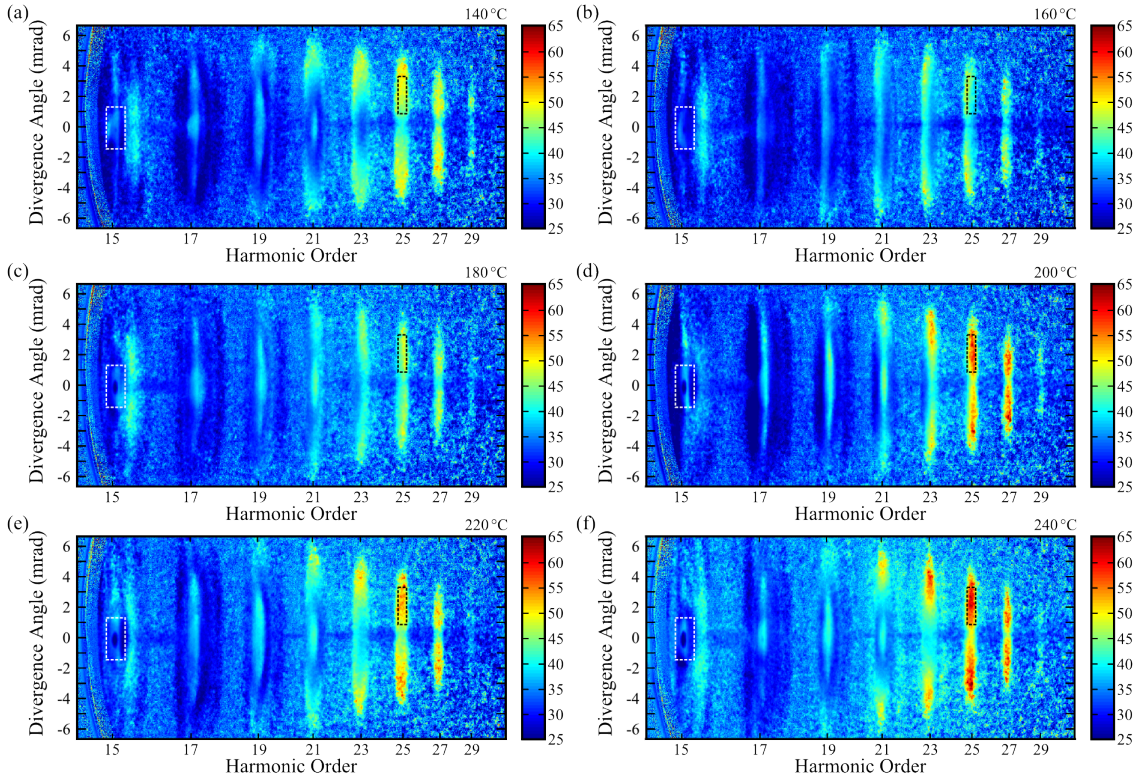


**Figure 4.14.:** Harmonic decay rate $\beta$ for each recorded pixel fitted by a four parametric Gaussian. The temperature changes in ascending order by 20 °C from subfigure (a) beginning with 140 °C to the spectrum of subfigure (f) taken at 240 °C.

In a last step the beta dependence with temperature is quantified by applying the simplest possible fit: a two parametric linear fit. Figure 4.15(a) depicts the beta dependence for harmonic 15 and harmonic 25 with a signal integrated over the two regions displayed in figure 4.14. The evidence from the fit is clear, beta does not vary for the on axis signal from harmonic 15 but shows a strong dependence with temperature and thus average

cluster size for the off axis signal from harmonic 25. Again the slope of the linear fit is extracted for each pixel. Figure 4.15(b) and figure 4.15(c) illustrate the slopemaps for positive and negative slopes.

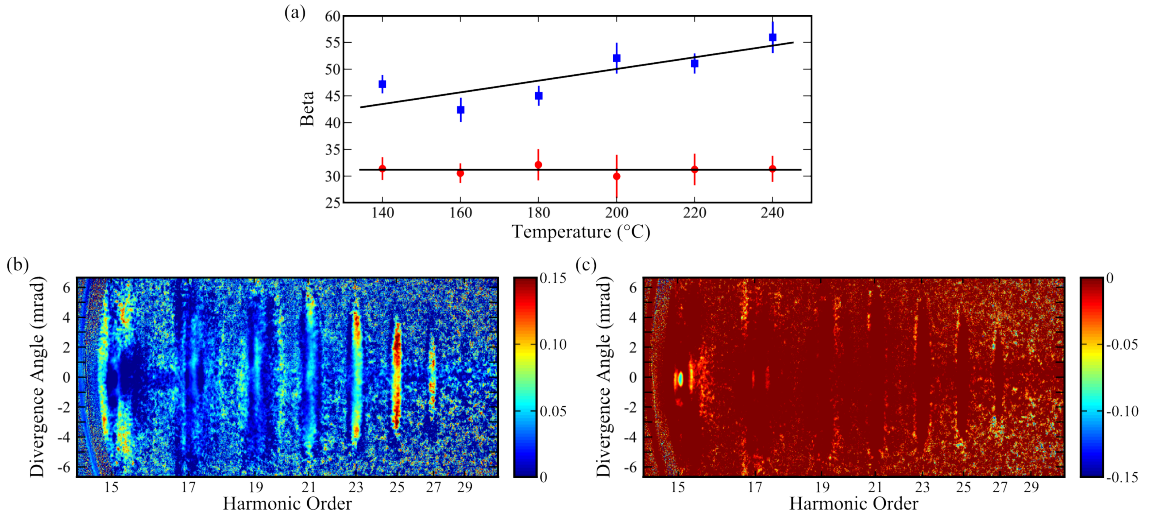


**Figure 4.15.:** (a) Evolution of $\beta$ with temperature for harmonic 15 (red) and harmonic 25 (blue). The values are an average over the areas depicted in figure 4.14. The error results from standard deviation when summing over all pixels. The temperature dependence is fitted by a two parametric linear model. The slope is extracted for each pixel and displayed for (b) positive slopes and (c) negative slopes. The slope is given in $\beta/T$ $(1/^{\circ}\mathrm{C})$.

These two maps are the proof showing the contribution of cluster signal. At zero slope no temperature dependence can be measured. This suggests that emission from cluster only play a minor role in these regions. As the slope adopts a non zero value the emission from clusters becomes substantial however. Figure 4.15(b) clearly attests that the usual supects (compare to figure 4.14 and 4.11(b)), namely the off axis cutoff harmonics, feature a strong dependence on average cluster size. Also the long trajectory of harmonic 15 reveals a temperature dependence. This one is not as strong and is probably overlapped by a signal originating from monomers. Another interesting feature appears in figure 4.15(c) for harmonic 15 on axis. This is the only spot of the whole spectrum revealing a negative slope.

### 4.3.3. Interpretation and the Cluster-to-Itself Model

First we will focus on the regions showing a positive slope (see figure 4.15(b)). The exact mechanism of high harmonic generation in clusters responsible for the emission of the cutoff harmonics, has yet to be determined. First, let us mention that the laser intensity and electron density are too low to produce significant coherent wake emission from the plasma (Quéré et al., 2006). Second, the fast decay of the harmonic signal with

ellipticity indicates that the process is recollisional and is thus different from what was recently reported in the case of bulk crystals (Ghimire et al., 2011), which still shows a significant signal at $\epsilon = 0.5$. Third, recombination to neighbouring ions (Moreno et al., 1994; de Aldana and Roso, 2001; Véniard et al., 2001; Zaretsky et al., 2010) can also be excluded as it would lead to lower $\beta$-values. Recombination to the neighbouring ions suggested to provide an extended cutoff in clusters. The last scenario can be ruled out by new experimental results.
We therefore suggest another mechanism of HHG in clusters. Figure 4.16 illustrates this mechanism, namely tunnel ionization from a partly delocalized electron wavefunction and recombination to this wavefunction (cluster-to-itself). As presented in paragraph 4.1.4 localized electronic states in Van der Waals clusters (Feifel et al., 2004), could be driven by the strong laser field from one site to another, ending up in a partially delocalized wavefunction after a few optical cycles (Lein, 2005). This process is accompanied by a significant amount of ionization of the cluster (as observed from the plasma lines) which will increase its ionization potential and explains the higher cutoff that is observed for the cluster emission. Recording the harmonic signal versus $\epsilon$, one obtains the cross-correlation between the recolliding wavefunction and the ground wavefunction.

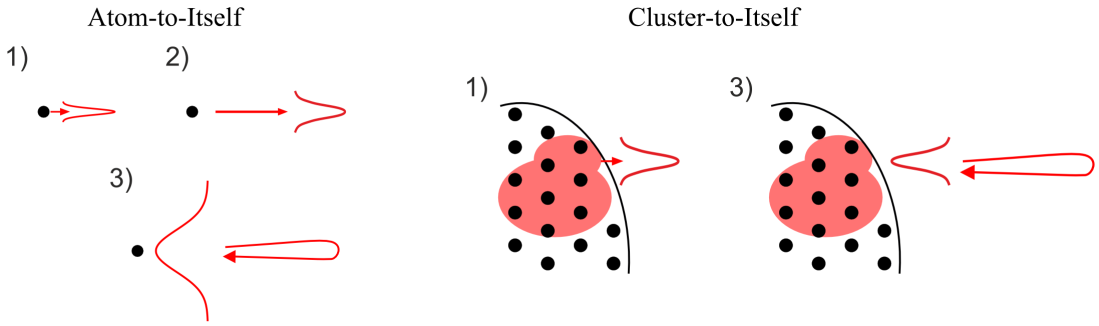


**Figure 4.16.:** Transversal spread of the electron wavefunction when recolliding to parent ion. In case of clusters an electron can tunnel out from a partly delocalized wavefunction in the cluster and recombine coherently with it. The initial spread of the electron wavefunction is determined by the size of the delocalized electron cloud.

In the Cluster-to-Itself model, depicted in figure 4.16, the initial transversal spread of the freed electron wavefunction is proportional to the size of the delocalized electron cloud it is originating from. Therewith the initial size (wave packet width: $1/e^2$) of the electron wave packet can reach 10 Å (delocalization over 1.5 sites in the cluster). This is much larger than for an electron wave packet tunneling out of a single atom (3.3 Å, for the cutoff trajectory at zero ellipticity). The wave packet spreads laterally during acceleration - the narrower the initial wave packet, the stronger the spread (see section 1.2.2). The decay rate, $\beta$, is determined by the width of the recolliding wave packet and the extension of the initial wavefunction, i.e. the cluster size. In other words it reflects the spatial cross-correlation between the recolliding electron wavefunction and

the wavefunction of the atomic ground state. A more accurate result would be expected by calculating the dipole moment, i.e. taking into account the dipole operator before carrying out the cross-correlation (Dietrich et al., 1994). A semi-classical model is developed based on the equations of motion 1.8, 1.9, 1.10. With $E_x = E \cdot \cos(\arctan(\epsilon))$ and $E_y = E \cdot \sin(\arctan(\epsilon))$ the transverse displacement of the electron is:

$$y(t) = -\frac{E_y}{\omega_0^2}[\sin(\omega_0 t_{flight}) - \sin(\omega_0 t_i)] + \frac{E_y}{\omega_0}\cos(\omega_0 t_i)(t - t_i) \tag{4.7}$$

Calculation of the decay rate $\beta$ is well established for generation in atoms (Dietrich et al., 1994; Dudovich et al., 2006; Khan et al., 2011). With equation 1.6 the initial electron wave packet is established after tunneling out of an atom. The electron wave packet spreads in the continuum according to equation 1.14. The recombination probability at each different ellipticity $\epsilon$ is obtained by convoluting the electron wavefunction with the wavefunction of the parent parent ion[3]. A fit to $exp(-\beta\epsilon^2)$ delivers the decay rate $\beta$. Figure 4.18(a) displays the calculations for different electron trajectories. These results are quantitatively in good agreement with those from Dietrich, Dudovich and coworkers (Dietrich et al., 1994; Dudovich et al., 2006). The case is different for clusters however. The following assumption is made: The initial size of the electron wave packet tunneling out of the cluster is the same as the delocalization of the electron cloud in the cluster. The size of the electron wave packets at recombination is calculated according to equation 1.14 for the cutoff trajectory at each ellipticy. The electron wave packet is convoluted with the initial ground state wavefunction (size of the delocalized electron cloud) at each transverse displacement. Figure 4.17 displays the decay rate $\beta$ extracted from such a convolution for different delocalized electron cloud sizes.
A comparison of the results from this calculation with the experimental data from figure 4.14 shows that two different trends might be responsible for the increase of the decay rate $\beta$. The observed maximum results from an optimal size of the recolliding wavefunction and the delocalized electron cloud in the cluster leading to maximum for the cross-correlation. The delocalization of the electron wave packet (radius in $1/e^2$) can either increase from 2.3 Å for $\beta = 40$ to 3.1 Å for $\beta = 60$ or decrease from 8.0 Å for $\beta = 40$ to 6.4 Å for $\beta = 60$. The band structure observed in the photoelectron spectra from krypton clusters gains in importance with increasing cluster size: The band becomes broader and the signal inceases (Carnovale et al., 1991). Thus the size of the delocalized electron clouds are expected to decrease as the average cluster size diminishes with increasing nozzle temperature. We therefore exclude the delocalization increase of the electron wavepacket from 2.3 Å to 3.1 Å.

In a first approximation the simple model of Cluster-to-Itself recombination shows that the average radius ($1/e^2$) of the delocalized electron cloud decreases from 8.0 Å to 6.4 Å when decreasing the average cluster size from $\bar{N} \approx 14000$ to $\bar{N} \approx 4000$. The average volume of the delocalized wave packet is thus divided by about two. This measurement

[3] 0.88 Å is taken as the radius of the krypton atom (Clementi et al., 1967).

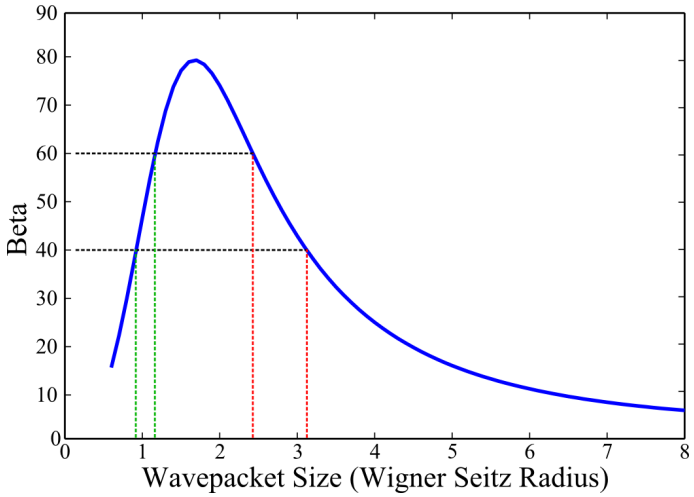


**Figure 4.17.:** Beta as a function of initial electron wave packet size (radius in $1/e^2$) in the cluster for the cutoff trajectory at an intensity of $10^{14}\,W/cm^2$. The units are given in Wigner-Seitz radii of krypton clusters: 2.57 Å.

is the first demonstration that electron correlation length in clusters can be characterized by HHG. This method can certainly be useful in other cases of HHG in inhomogenous media, like metal plasma (Ganeev et al., 2007; Suzuki et al., 2007; Ganeev et al., 2009) or water droplets (Kurz et al., 2012). The disadvantage of this method for determining electron correlation length is evident however, only the average value of a big ensemble of samples can be determined.
The second important feature which is uncovered in figure 4.15(c) is the decrease of $\beta$ with a rising nozzle temperature. It suggests that the overall signal in this region, is produced both by monomers and clusters. There are two possible scenarios imaginable. In the first one, large clusters disintegrate and more monomers might be present at higher temperatures. The monomer signal dominates in this region at higher temperature. If $\beta$ is smaller for krypton atoms than for krypton clusters for harmonic 15 on axis, a decrease of the overall decay rate $\beta$ might be plausible. Figure 4.18 shows however that this would not be expected. Another explication might hold however.

This emission might also be attributed to clusters emission. Taking into account figure 4.17 this could be assigned to low electron correlation lengths in clusters ($< 2.57$ Å), but would rather be unlikely. Correlation lengths should be independent from harmonic order. Another possibilty might be a generation mechanism from another species of clusters. The signal of this region is increasing when decreasing the nozzle temperature (see figure 4.11(b)). The signal might thus stem from small clusters such as dimers, trimers etc. . A possible recombination mechanism could be recombination from one atomic site directly to another site. In such a process the electron does not need to be driven back to the parent ion. Electrons that are emitted before the laser field reaches the extremum of the laser cycle would be able to recombine. Such a process would not be very sensitive to

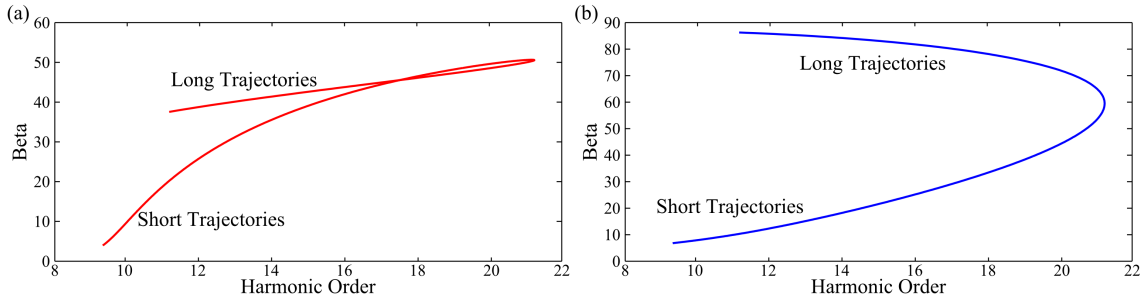


**Figure 4.18.:** (a) Beta for krypton atoms as a function of harmonic order at an intensity of $10^{14}\,\mathrm{W/cm^2}$. (b) Beta for krypton clusters (radius $(1/e^2)$ of the initial wave packet: 6.4 Å) as a function of harmonic order at an intensity of $10^{14}\,\mathrm{W/cm^2}$

the decay rate $\beta$. On the one hand the electron wave packet has only very little time to spread transversally. On the other hand the electron trajectory can neither be significantly deviated in such a short time. As already observed for the short trajectories in figure 4.18, we expect that the second process is dominating. Also the decrease of $\beta$ with temperature is plausible. The high harmonic signal from monomers and small clusters is competing in this spatio-spectral region. As the temperature is increased the large clusters dissociate and the density of the small clusters increases. Thus the relative weight of the small clusters becomes more important at higher temperatures and the overall signal in this spatio-spectral region, is dominated by them. As $\beta$ is higher for HHG from monomers than for small cluster a decrease of $\beta$ is expected.

### 4.3.4. Polarization Measurement: Degree of linear Polarization

In order to further characterize the different generation mechanisms at play a polarimetry measurement was performed (Antoine et al., 1997). We used an unprotected silver mirror in combination with a gold grating as a fixed polarizer (see figure 4.19) and rotated the laser polarization with a zero-order half waveplate.

Figure 4.20 depicts the evolution of the signal for harmonic 15 on axis and harmonic 25 off axis as a function of the half waveplate angle. A Malus' law with a $\cos^2$ dependence is observed. The signal from harmonic 15 clearly shows a strong modulation of the signal. The contrast of this modulation is $\approx 1.8$. A contrast of 2.8 is expected however (see figure 4.19(b)). There might be several reasons for this disagreement. The background might be underestimated or a silver oxide layer might change the reflectivity for the silver mirror, leading to a shift in contrast.

After subtracting the background, a Fourier transform is performed to extract the amplitude of the oscillatory component, which is then normalized to the sum of the Fourier transform. This procedure provides the amplitude of the oscillation and therewith the degree of linear polarization. Only elliptically polarized generation pulses can lead to elliptically polarized harmonic emission. Figure 4.21(a) presents the spatio-spectrally re-

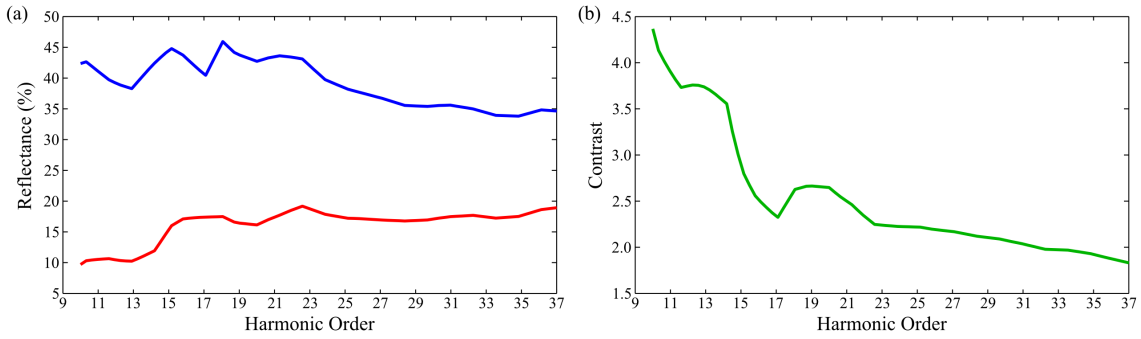


**Figure 4.19.:** (a) Calculated reflectance of the unprotected silver mirror (AOI = 70°) in combination with the gold grating (AOI = 87°) for s-polarized (blue) and p-polarized light (red). (b) Contrast (s-polarized/p-polarized) of the combined polarizer.

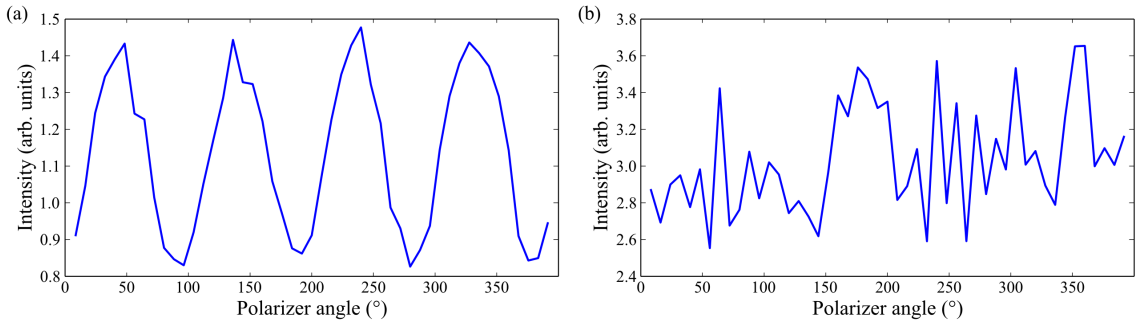


**Figure 4.20.:** Malus law for (a) harmonic 15 on axis and (b) harmonic 25 off axis. The background is subtracted in order to compare the contrast of the signal.

solved degree of linear polarization obtained at 80 °C. As expected, the plasma lines are linearly depolarized. More surprisingly, the same region that is attributed to cluster emission in figure 4.15(b) shows a remarkably low degree of linear polarization. A low degree of linear polarization is very surprising for high harmonic generation by a linear laser field. A high degree of polarization should be observed for all harmonic orders (Antoine et al., 1997). This low degree of linear polarization is systematically observed in different conditions. Figure 4.21 illustrates this measurement performed at different temperatures (80 °C, 160 °C and 240 °C) in krypton cluster and in various species: carbon dioxide and argon.

### 4.3.5. Linearly depolarized High Harmonic Generation from Clusters

A linear depolarization for HHG from clusters might however be plausible. The polarization direction of the high harmonics is set by the recollision direction of the electrons and the electronic structure of the wavefunction of the ground state to which these electrons recombine. Within the strong field approximation, in linear polarization, the recollision direction is parallel to the laser field. In a centrosymmetric medium the harmonics are thus necessarily polarized along this direction. To go beyond the strong field approximation CTMTC-QUEST has been applied (see section 1.4) for the calculation of the recollision angles in atoms at intensities of $1.2 \times 10^{14}$ W/cm$^2$. These calculations take into account the influence of the ionic core on the electron trajectories (Shafir et al., 2012a), which broadens the distribution of recollision angles. Figure 4.22 illustrates the recollision angle distribution peaked around $\pm 6°$ after summing the recolliding electrons over the polar angle. In clusters, due to the high charge states observed in our experiments, the ionic potential is expected to play a more important role (Fukuda et al., 2006). Furthermore screening effects can inhomogenize the electric field over the cluster (Skopolová et al., 2010). These two effects will lead to a broader recollision angle distribution.

For understanding the origin of the apparent depolarization of harmonic emission, simple simulations of the macroscopic generation process assuming an infinitely thin medium were performed. N emitters were randomly distributed on a square grid of 100 $\mu$m $\times$ 100 $\mu$m which represent the generating medium. Each emitter located in $(x,y)$ radiates an electric field $\vec{E}_q(x,y) = I_0(x,y)^{q_{Eff}/2} e^{i\alpha_q I_0(x,y)} \vec{u}(x,y)$, where $I_0(x,y)$ is the fundamental intensity distribution, $q_{Eff}$ the effective non-linearity of the harmonic emission (typically 5), $\alpha_q$ the intensity dependence of the harmonic phase ($\alpha \approx 10 \times 10^{-14}$ cm$^2$/W for the end of the plateau), and $\vec{u}(x,y)$ is a unit vector with a direction randomly picked in the distribution of recolliding angles. For clusters the latter is assumed to be three times broader than the one obtained for atoms by using CTMC. We calculate the electric field resulting from the coherent sum of the contributions from the N emitters in the far field by Fourier transforming the near field profile. Two extreme cases are considered: emission from an ensemble of clusters and from an ensemble of monomers with a density of $10^{18}$ cm$^{-3}$. Assuming that only one atom out of $10^5$ emits high harmonics (due to the recombination

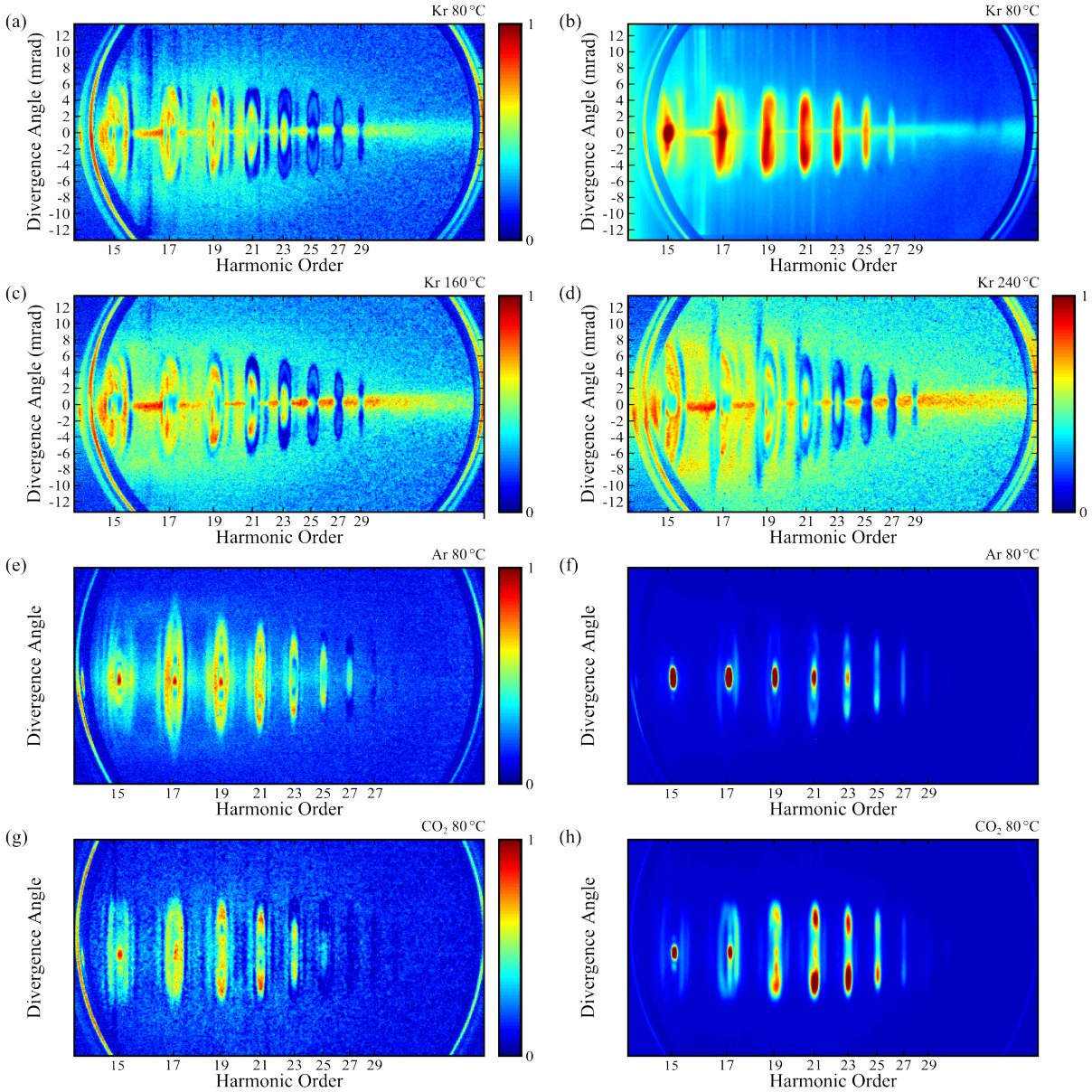


**Figure 4.21.:** Polarimetry maps generated in krypton clusters at (a) 80 °C, (c) 160 °C and (d) 240 °. (b) Spectrum at a temperature of 80 °C. (e) Polarimetry map in argon clusters at 80 °C and 20 bar with (f) its corresponding spectrum. (g) Polarimetry map in carbon dioxide clusters at 80 °C and 20 bar with (h) its corresponding spectrum.

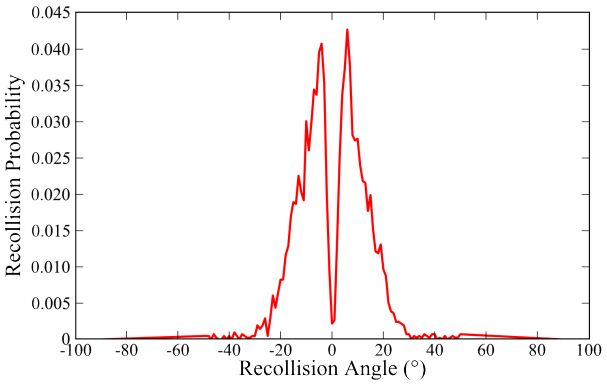


**Figure 4.22.:** Electron recollision probability as a function of recollision angle.

probability) and a medium thickness of 100 $\mu$m, we get $10^7$ atoms to distribute on our grid. For clusters, the density is much lower: assuming a medium with 80 % of the atoms forming clusters of 30000 monomers, the density is $\approx 3 \times 10^{13}$ cm$^{-3}$ (Dorchies et al., 2003), which leads to a few hundred to thousand emitters with an emission probability which is the same or higher than that for atoms. In the following, we will consider 1000 emitters and we checked that the results were qualitatively similar using 100 to 10000 emitters.

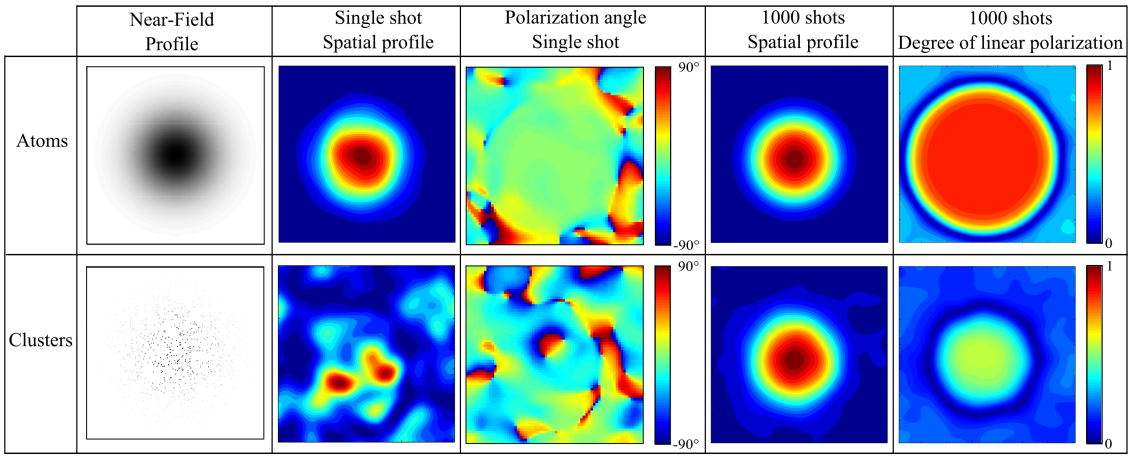


**Figure 4.23.:** Simulations for many atoms or few large clusters leading to a substantially different degree of polarization.

These simulations show that while in the case of atomic emission the harmonic far field profile is well defined in a single laser shot, the profile obtained from clusters is very inhomogeneous and fluctuates significantly from shot to shot because there are too few emitters to obtain a nice constructive interference on axis and destructive off axis (see figure 4.23). The polarization state from clusters is also very inhomogeneous,

showing important ellipticities and polarization angles partially very different from zero. When averaging over 1000 shots, the spatial intensity profile becomes much smoother and the polarization angle is quasi homogeneously equal to zero. The degree of linear polarization of the resulting light is calculated, by defining a Malus law out of the Stokes parameters and extracting its normalized oscillatory component. While the polarization appears perfectly linear in monomers, the emission from clusters appears depolarized. These results show that unpolarized emission might be a fingerprint of HHG from large clusters, which have a low density in the jet and thus produce inhomogeneous harmonic emission. As a linearly depolarized high harmonic emission needs to be confirmed in further measurement depolarized HHG might also be used as an indicator for other low density sources such as metal plasma (Ganeev et al., 2007; Suzuki et al., 2007; Ganeev et al., 2009) or water droplets (Kurz et al., 2012)

### 4.3.6. Polarization Measurement: Polarization Angle

Polarimetry at different laser ellipticities proves to be sensitive probe of the high harmonic generation mechanism shedding light on the role of the ionic potential (Shafir et al., 2012a). Such a measurement should also give further insight in the case of clusters. The phase of the Malus' law gives information about the main axis of polarization. Figure 4.24 depicts the polarization angle for each pixel at different ellipticities. It seems that the plasma line between harmonic 15 and harmonic 17 is not randomly polarized but has polarization which changes with that of off axis cutoff harmonics. The polarization of the plasma emission should however be completely unpolarized. It might be possible that the intensity changed with the angle of the half waveplate, slightly modulating the plasma emission. This might lead to a periodic dependency of plasma emission and harmonic emission which can be extracted as polarization angle.

In the regions where polarization is well defined the electron recollision angle can be extracted from the the polarization angle. At zero ellipticity this angle should be zero but it should increase with increasing ellipticity. The sign of theses angles is however inverse for long and short trajectories in argon atoms (Shafir et al., 2012a). Figure 4.25 shows such a study for five different ellipticities in krypton clusters for harmonic 15. Obviously the sign is not changing for short and long trajectories. Also the polarization angle is huge for short trajectories at high ellipticities. This is not at all expected and might be an artifact of the laser polarization that is not controlled as it is supposed to be. It might also be the contribution of HHG from clusters that is changing the recollision angle significantly. The experiment needs to be reproduced in krypton atoms for ruling out any cluster contribution.

Figure 4.26 finally illustrates the extracted polarization angle at an ellipticity of 0.21 extracted for a fit of each pixel. The depolarized regions gives fits with zero slope even though the polarization angle can vary significantly between an ellipticity of -0.21 and 0.21. The 2D maps nicely illustrate the different polarization angles for short and long electron trajectories. When heating up the nozzle the structure of these maps does not

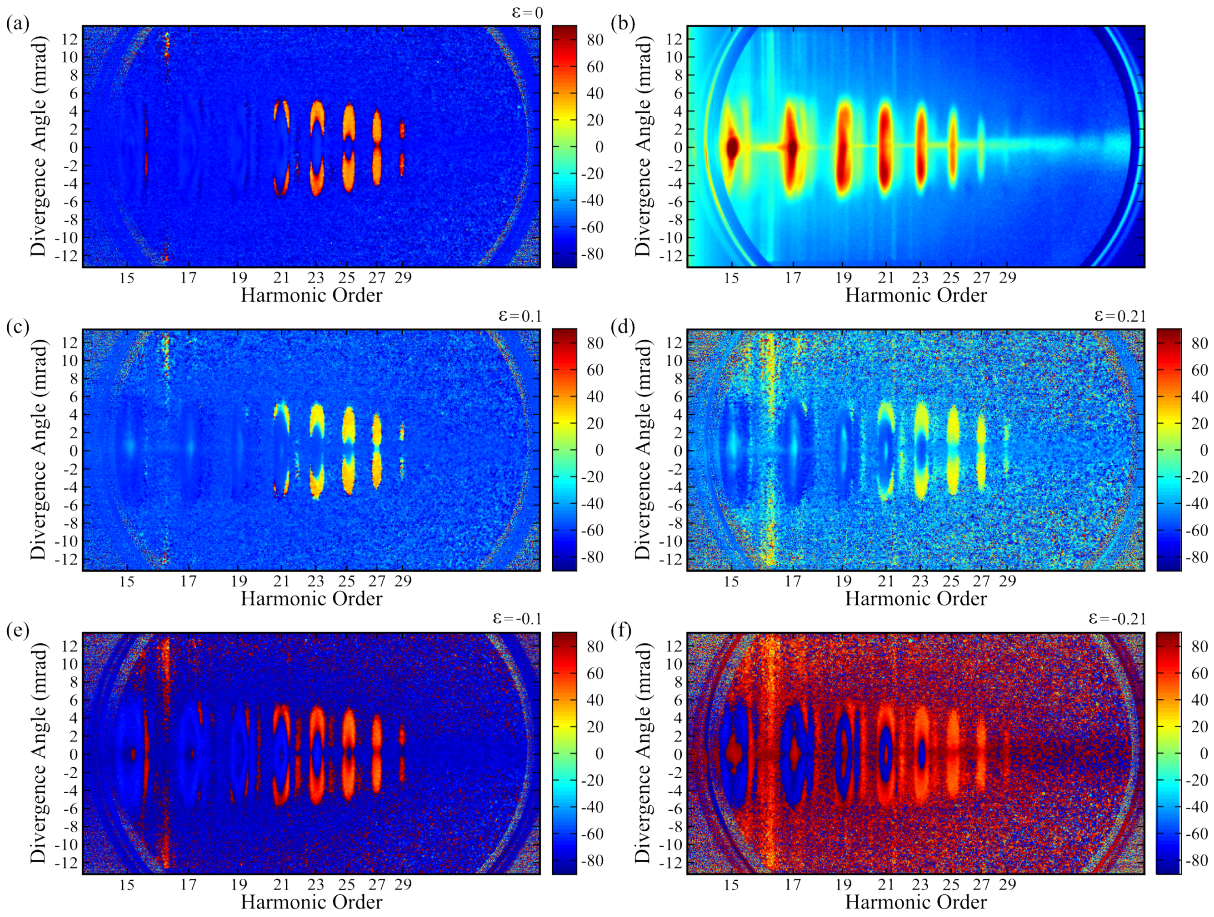


**Figure 4.24.:** High harmonic polarization angle for krypton clusters produced at 20 bar and a temperature of 80 °C at (a) linear polarization, (c) laser ellipticity of 0.1, (d) laser ellipticity of 0.21, (e) laser ellipticity of -0.1 and (f) laser ellipticity of -0.21. (b) Spectrum at linear laser polarization.

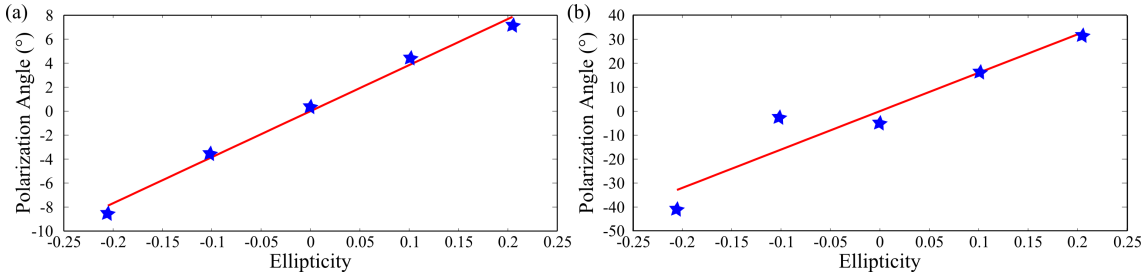


**Figure 4.25.:** Polarization angle as a function of laser ellipticity at 20 bar and a temperature of 80 °C in krypton. (a) Long trajectory signal for harmonic 15 and (b) short trajectory signal for harmonic 15.

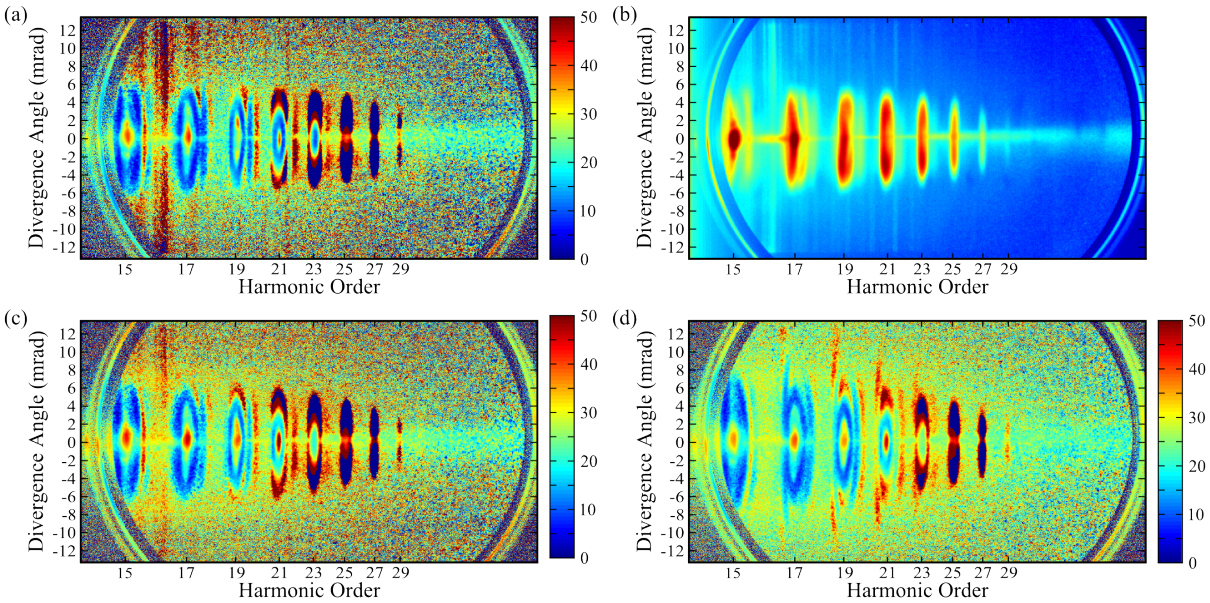


**Figure 4.26.:** Polarization angle extracted from a fit as displayed in figure 4.25 at an ellipticity of 0.21 for each pixel. Harmonic emission from krypton clusters was performed at (a) 80 °C, (c) 160 °C and (d) 240 °C. (b) Spectrum at linear laser polarization at 80 °C.

change significantly. The high polarization angles of $\pm 40°$ are not expected from first CTMC-QUEST calculations[4] in krypton atoms. The experiments have to be repeated in krypton atoms making sure that the laser polarizaton is well controlled.

### 4.3.7. Polarization Measurement in Krypton Atoms

Figure 4.27 displays the polarimetry maps at different ellipticities. A different behaviour is observed for different signs of ellipticity. This should not be the case, there is no physical explanation why the response from an isotropic generation medium should reveal such a result. The more probable explanation is a different polarization of the fundamental laser beam at the two ellipticities. The waveplates are not perfect over a broad wavelength range and thus do not allow an absolute control. A rotating three-mirror polarizer would supersede the linear polarization control by the zero-order half waveplate (see paragraph 5.1) in the future. The source for the different behaviour to ellipticities from opposite sign might also originate from another uncertainty as demonstrated in the following paragraph.

In order to investigate a possible artifact from polarimetry in clusters, measurements have been performed in a static-cell, i.e. in krypton atoms. Figure 4.29(g) depicts this measurement and also reveals depolarized cutoff harmonics in krypton atoms. When testing the experimental setup a $MgF_2$ plate (Melles Griot) at the exit of the compressor

[4] Performed by Fabre and Pons.

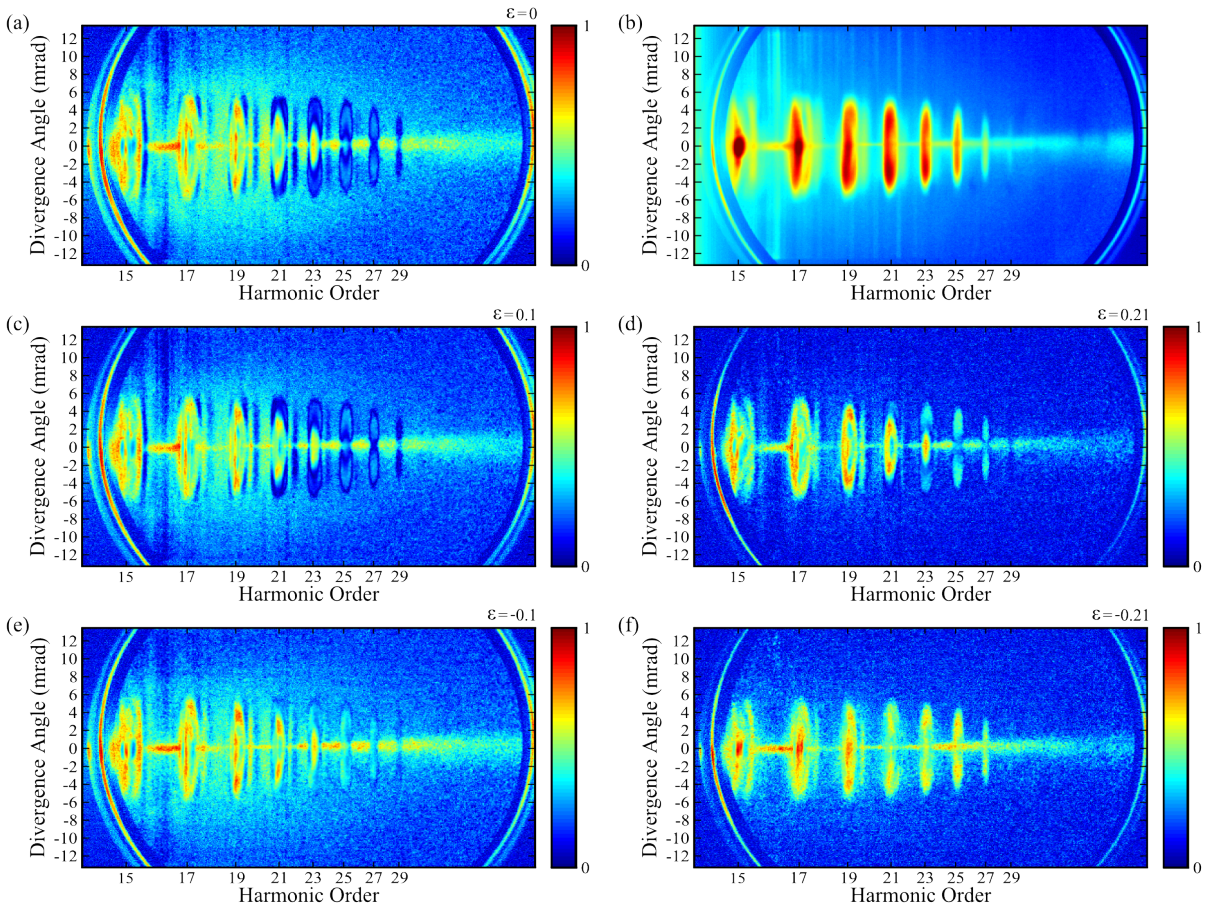


**Figure 4.27.:** Polarimetry maps generated in krypton clusters at (a) linear polarization, (c) laser ellipticity of 0.1, (d) laser ellipticity of 0.21, (e) laser ellipticity of -0.1 and (f) laser ellipticity of -0.21. (b) Spectrum at linear laser polarization.

was found which was not exactly autocollimated. $MgF_2$ is an anisotropic material and birefringent. According to manufacturer information the optical axis is perpendicular to the surface of the plate. If the beam is tilted by an angle $\alpha$ with respect to the perpendicular line of the $MgF_2$ plate, the refractive index of the extraordinary axis has to be considered:

$$\frac{1}{n_e^2(\alpha)} = \frac{\cos^2\alpha}{n_o^2} + \frac{\sin^2\alpha}{n_e^2} \tag{4.8}$$

with $n_e$ and $n_o$ the extraordinary and ordinary index of refraction respectively. The group refractive indices are calculated from a three-term Sellmeier-type dispersion equation. They are calculated from two different references: first the manufacturer information (Melles Griot) $n_e = 1.3952$, $n_o = 1.3831$ and second the reference (Dodge, 1984) $n_e = 1.3943$, $n_o = 1.3822$. Even though the results are slightly different the calculated phase difference between ordinary and extraordinary beam depicted in figure 4.28 is the same within $10^{-6}\,\pi$. Also the angle of the optical axis with respect to laser polarization plays an important role. Only if the projection of the optical axis onto a plane perpendicular to propagation direction is parallel or perpendicular to laser polarization the beam is not split in an ordinary or extraordinary one. If this projection, exhibits an angle of 45° with respect to laser polarization, the extraordinary and ordinary components are separated in equal parts. In a first approximation the phase difference $\phi$ between the two beams is:

$$\phi = \frac{2\pi}{\lambda}(n_e(\alpha) - n_o)\frac{d}{\cos\alpha} \tag{4.9}$$

with d = 5 mm the thickness of the $MgF_2$ plate. Figure 4.28 illustrates the phase difference between the ordinary and the extraordinary beam as a function of angle of incidence (AOI) on the $MgF_2$ plate. The angle does probably not exceed more than 5° due to the poor autocollimation. Thus the phase difference is not larger than three optical cycles, i.e. the ordinary and extraordinary beam still overlap almost completely leading to an elliptical beam.

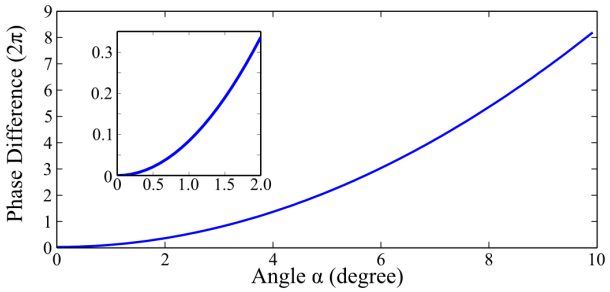


**Figure 4.28.:** Phase difference between the ordinary and extraordinary beam as a function of AOI on the $MgF_2$ plate.

Thus this window might have created an elliptically polarized pulse. After six reflections

on the silver mirrors this elliptical polarization increases due to different phases for the reflection of s- and p-polarization. The beam finally passes a broadband zero-order half-wave plate (ellipticity control), a fixed broadband zero-order quarter-wave plate, a broadband zero-order half-wave plate (polarization control) and the entrance window of the vacuum chamber. The waveplates are probably not perfect over the spectral bandwidth of the laser pulses. Polarimetry was performed in different configurations. The waveplates for the ellipticity control were removed and different half-waveplates were tried out. The result remained the same, a very low degree of linear polarization for the off-axis cutoff harmonics.
A last uncertainty that is not controlled are nonlinear effects that induce a polarization rotation. Nonlinear elliptical polarization rotation (NER) is an nonlinear ellitpic effect attributed to third order susceptiblities in isotropic materials (Minkovski et al., 2002; Jullien, 2006). Even cross polarized wave (XPW) generation (Minkovski et al., 2004) which is especially strong in anisotropic media (Jullien et al., 2005) plays a role. Also the mount of the entrance window and the mechanical stress applied on the window have to be considered. If the stress is too high anisotropic effects can be signifcantly enhanced. We tested different configurations, assembling the focussing mirror inside or outside of the vacuum chamber, thus changing the intensity on the entrance window by a factor of four. Again the polarimetry maps did not change.

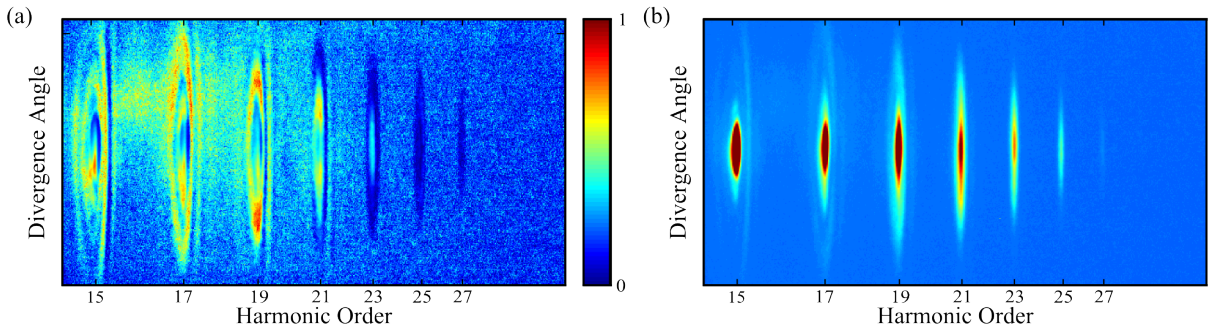


**Figure 4.29.:** (a) Polarimetry map generated in a static-gas cell at linear polarization, i.e. krypton atoms with (b) the corresponding spectrum.

It is thus difficult to conclude on the polarization state of the laser on the gas target, we can only conclude that it is certainly not perfectly linear. Elliptical radiation does not produce linearly depolarized HHG, so what is the origin of this effect? And why are only the regions in the maps that are attributed to cluster emission linearly depolarized? Even though there are no answers to these open questions, these results do not discredit the conclusion from section 4.3.2. If the laser polarization is not exactly linear, a different decay rate $\beta$ can be be attributed to HHG from clusters revealed by an increasing decay rate with a rising temperature. For being sure of the quantitative values, this measurement has to be reproduced however.

## 4.4. Cluster Dynamics

The extension of HHG to the case of clusters allows the investigation of strong field processes in many-body systems, the role of multielectron effects and monitoring of cluster dynamics through the harmonic signal. An experimental work performed by Chen and coworkers demonstrated the enhancement of HHG in clusters and characterization of cluster vibrations (Chen et al., 2007). A theoretical study performed by Strelkov and coworkers followed four years later and suggested the characterization of the cluster properties by the harmonic spectra. Also an enhancement is predicted for certain harmonics (Strelkov et al., 2011). These results motivated the study of HHG from clusters in a pump-probe laser scheme. Two different experimental results are presented in the following. The first one was conducted in Milano pumping at 1460 nm and probing at 800 nm. The second one was performed at Bordeaux probing and pumping at the same wavelength, namely 800 nm.

### 4.4.1. Cluster Explosion triggered by Pulses centered at 1460 nm

The following experiments were performed at the Politecnico di Milano in collaboration with the group of Vozzi and Stagira. Even though the repetition rate of the laser was only 10 Hz we had the great advantage of using a few-optical-cycle infrared parametric source (Vozzi et al., 2007, 2008). The high harmonics were generated in a supersonic gas jet, employing the Even-Lavie valve in the same configuration as described in paragraph 4.2.3, but a repetition rate of 10 Hz. A collinear pump-probe setup was used, employing 20 fs pump pulses at a center wavelength of 1460 nm and 100 fs probe pulses at a center wavelength of 800 nm. The on target intensity was $10^{14}\,\mathrm{W/cm^2}$ for the pump and $0.5 \times 10^{13}\mathrm{W/cm^2}$ for the probe pulse. The harmonic spectrum cannot be resolved spatially as a torroidal mirror is used for imaging the source on the MCPs.

Transien XUV emission from krypton clusters are shown on a 2D spectrogram 4.30. High harmonic emission can only be observed at negative delays, i.e. when the sample is excited by the 800 nm and probed by the near infrared light. At negative delays below -2.5 ps the harmonic signal disappears (see figure 4.31(a)). HHG is not visible any more already before zero delay, strong ionization from the overlapped beams might destroy phase-matching. At lower delays cluster expansion is triggered by the 800 nm pump pulses. It seems that after 2.5 ps of expansion high harmonic generation by the 1460 nm pulses is not supported any more. Again high ionization due to impact ionization might play a role and destroy phase matching conditions. The transient signal from plasma emission shows a maximum around 5 ps and is neglible at negative delays. A study performed by Dorchies and coworkers already investigated the x-ray production in a pump-probe scheme with argon clusters at intensities of $10^{17}\,\mathrm{W/cm^2}$ at 800 nm. Their results suggest that the maximum plasma emission can be attributed to an optimal average electron density during cluster expansion which efficiently heats the cluster (Dorchies et al., 2005). The same mechanism might be at play in our case, with one difference however. The pump

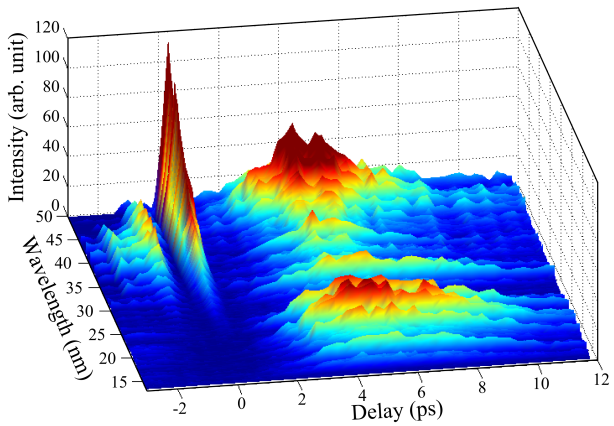


**Figure 4.30.:** 2D transient in krypton clusters at 30 bar and a nozzle temperature of 27 °C as a function of wavelength and pump-probe delay. The signal below 0 ps corresponds to high harmonic emission. Four-wave mixing is observed at 0 ps and the plasma emission above 0 ps.

intensity is three orders of magnitude smaller at 1460 nm what might suggest that cluster expansion is triggered more efficiently at this wavelength than at 800 nm.

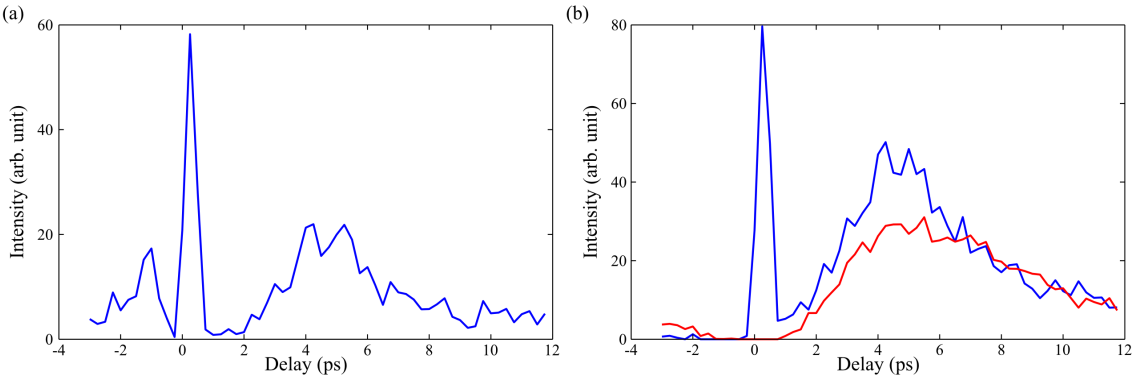


**Figure 4.31.:** Transient in krypton clusters at 30 bar and a nozzle temperature of 27 °C. (a) The evolution of harmonic 35 ($<0$ ps), the four-wave mixing signal (0 ps) and the plasma emission ($>0$ ps). (b) Evolution of plasma emission at 45.0 nm (blue) and 15.1 nm (red).

Fukuda and coworkers calculated the contribution of different ionic species during cluster explosion at intensities of $10^{18}$ W/cm$^2$. They state that lower charged ionic state are produced by field ionization only whereas highly charged ions are produced by field and impact ionization (Fukuda et al., 2006). The time evolution of the charged states is very different for the two mechanisms. We therefore tried to assign the plasma lines to different electronic transitions in krypton ions in order to decouple possibly different ionization mechanisms. It was hard however to assign the plasma lines to different states,

the spectral calibration is not accurate enough. Also the time evolution of the plasma lines is not fundamentally different as illustrated in figure 4.31(b). We were not able yet to define a method quantifying the different time evolutions of the plasma lines.

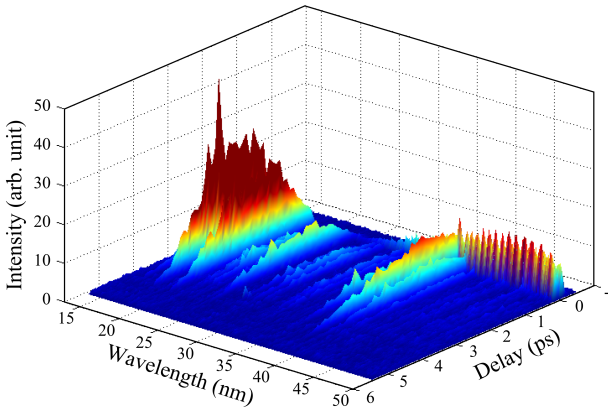


**Figure 4.32.:** 2D transient in carbon dioxide clusters at 30 bar and a nozzle temperature of 34 °C as a function of wavelength and pump-probe delay.

The same experiments as described in krypton clusters were also performed in carbon dioxide clusters. Figure 4.32 depicts such a transient scan. High harmonic emission as in the case of krypton clusters was not observed even at delays of -2 ps (not shown). The plasma emission shows however an evolution that is different and are illustrated in figure 4.33. The qualitative behaviour of the three different subfigures is quite different, each one has a trend of its own. It is even more difficult to assign these lines in molecular clusters to specific electronic transitions as it is not clear what host to take: oxygen, carbon, carbon dioxide or carbon monoxide? Emission from oxygen atoms/ions was almost impossible to assign to any plasma lines. The same holds for carbon dioxide and carbon monoxide, as it is tedious to find the corresponding data. It seemed however that the six lines shown in figure 4.33 can be assigned to different transitions in carbon ions (database: http://spectr-w3.snz.ru/splines.phtml). The emission shown in figure 4.33 can be attributed to (a) $C^{2+}$, (b) to $C^{3+}$ and (c) $C^{4+}$. If this identification is right, this measurement can be used for decoupling two different mechanisms at play: field and impact ionization.

### 4.4.2. Cluster Explosion triggered by Pulses centered at 800 nm

Similar experiments were repeated in Bordeaux with a non collinear pump probe scheme with both pulses centered at 800 nm. Pump and probe energy were at 2.2 mJ (diameter $(1/e^2)$: 7.8 mm) and 240 $\mu$J (diameter $(1/e^2)$: 19.5 mm clipped by an iris of 5.6 mm) respectively which were both focussed by a spherical mirror with a focal length of 37.5 cm onto the gas jet. The repetition rate of the valve was changed to 100 Hz for reaching nozzle temperatures of 50 °C. Figure 4.34 depicts the transients taken at different nozzle temperatures and thus different average cluster sizes. Again plasma lines show a maximum

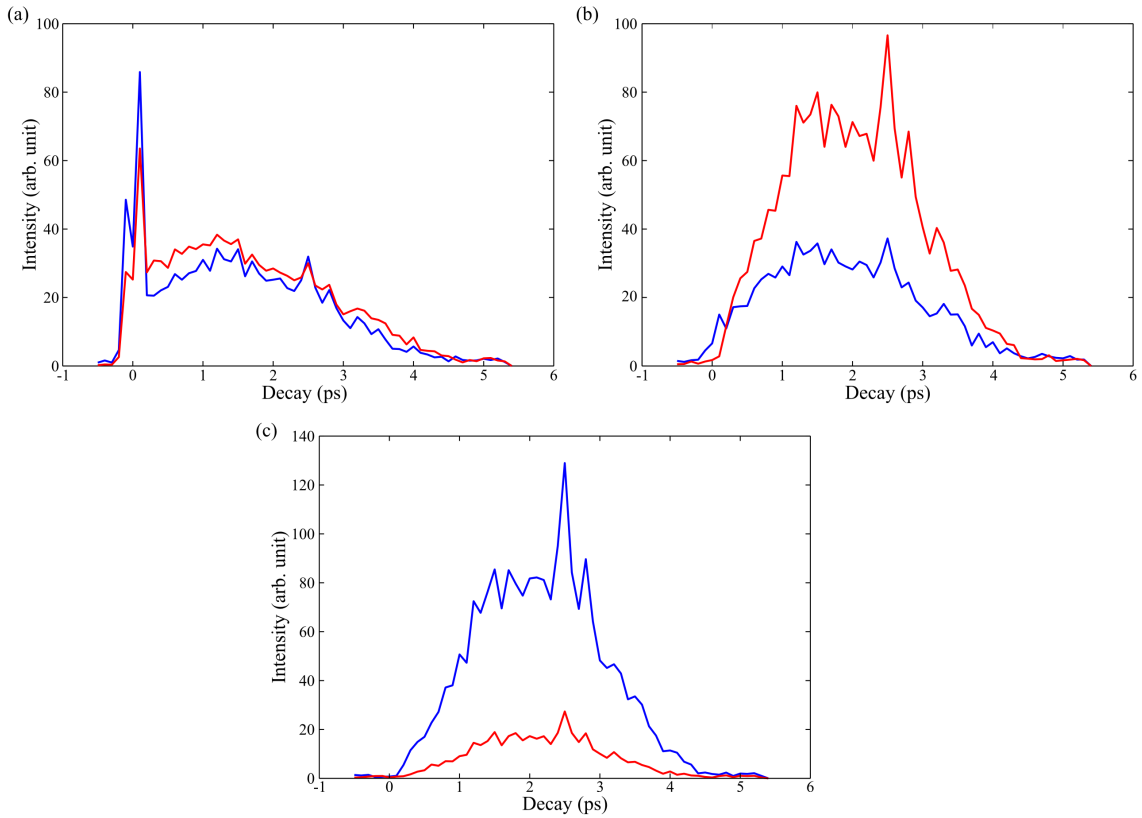


**Figure 4.33.:** Evolution of plasma emission from carbon dioxide clusters at 30 bar and a nozzle temperature of 34 °C. Plasma emission at a wavelength of (a) 38.9 nm (blue), 37.8 nm (red), (b) 24.2 nm (blue), 19.6 nm (red), (c) 17.5 nm (blue) and 15.3 nm (red).

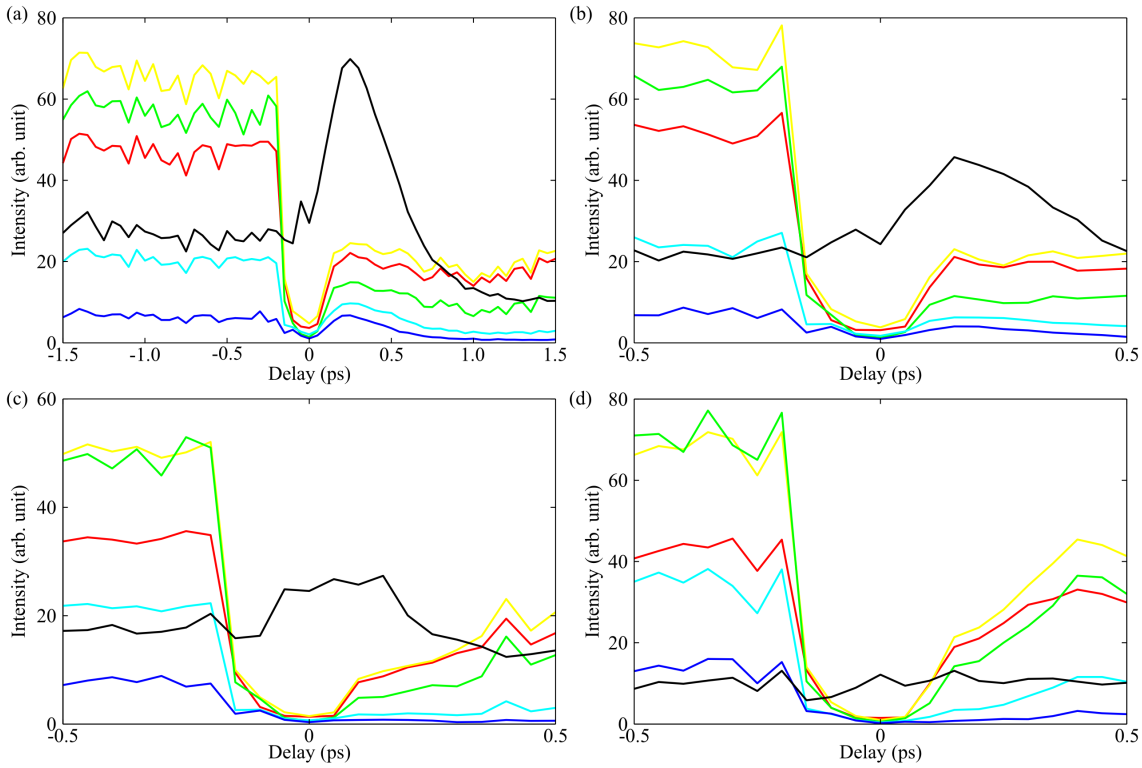


**Figure 4.34.:** Pump probe scan in carbon dioxide clusters. The transients of the total signal for harmonic 15 (red) to harmonic 23 (blue) are depicted. The evolution of the strongest plasma signal at 47.7 nm is shown in black. The nozzle temperature is increased for the sequent subfigures: (a) 50 °C, (b) 80 °C, (c) 150 °C and (d) 80 °C.

after the incident pump pulse. The plasma signal drops to a level that is below the pre-pump level. This difference is probably due to the exploded clusters that do not emit plasma emission long enough after pumping. The maximum is not very distinct at high nozzle temperatures (figure 4.34(b) and figure 4.34(c)). Also the signal difference before and after pumping is almost negligible. This indicates probably the lack of large clusters at these temperatures. In the four cases the harmonic signal drops significantly. Again this can probably be attributed to the free electrons that are created during cluster explosion, which destroy phase matching conditions. Interestingly the cutoff harmonics (harmonic 21 and harmonic 23) reveals stronger dynamics than the plateau harmonics between 0 ps and 0.5 ps. It is not clear yet if this different evolution can be attributed to the varying cluster density or the electron density. We also performed similar experiments in sulfur hexafluoride clusters but could not reproduce the oscillations from cluster vibrations, that were detected by Chen and coworkers (Chen et al., 2007).

## 4.5. The Role of Clusters for HHG in a cold Carbon Dioxide Gas Jet

Let's return to the initial question that triggered the study of HHG in clusters (see chapter 2, paragraph 2.3): What is the role of clusters for HHG in a cold Carbon Dioxide Gas Jet? At the time when the alignment scans have been performed, a temperature study has been conducted. Two conclusions were drawn from such a measurement (see paragraph 4.3). First the off-axis cutoff signal is significantly stronger at low nozzle temperatures than at high nozzle temperatures. Second the signal from the on axis plateau harmonics increases with nozzle temperature.
Figure 4.35 depicts the differential measurement in the alignment conditions (80 °C, 9 bar). In argon the overall signal is going down with increasing temperature as expected from heating up the nozzle (Scoles et al., 1988; Beijerinck and Verster, 1981). Xenon which has a much higher tendency to clusterize (see equation 4.5 and table 4.1) already shows a different behaviour: A stronger signal from the short trajectory harmonics at higher temperatures. The same effect, not as pronounced however, is observed for carbon dioxide. It has a stronger tendency than argon but lower than xenon to clusterize. Such a behaviour has not been observed for short trajectory harmonics (see chapter 4.35). One has to point out that the valve was operated at 9 bar, a backing pressure that is usually insufficient for the Even-Lavie valve. The experiments performed in clusters were performed at backing pressures above 10 bar and might thus show different characteristics in the high harmonic spectra. A significant contribution from clusters to HHG can therefore be excluded.
As presented in paragraph 4.4 clusters explose after exposure to a strong pump pulse either through hydrodynamic expansion or Coulomb explosion. The pump-pulse used for molecular alignment at an intensity of $6 \times 10^{13}\,\mathrm{W/cm^2}$ probably destroys the largest clusters. Smaller clusters probably survive at these intensities. Therefore the presence of

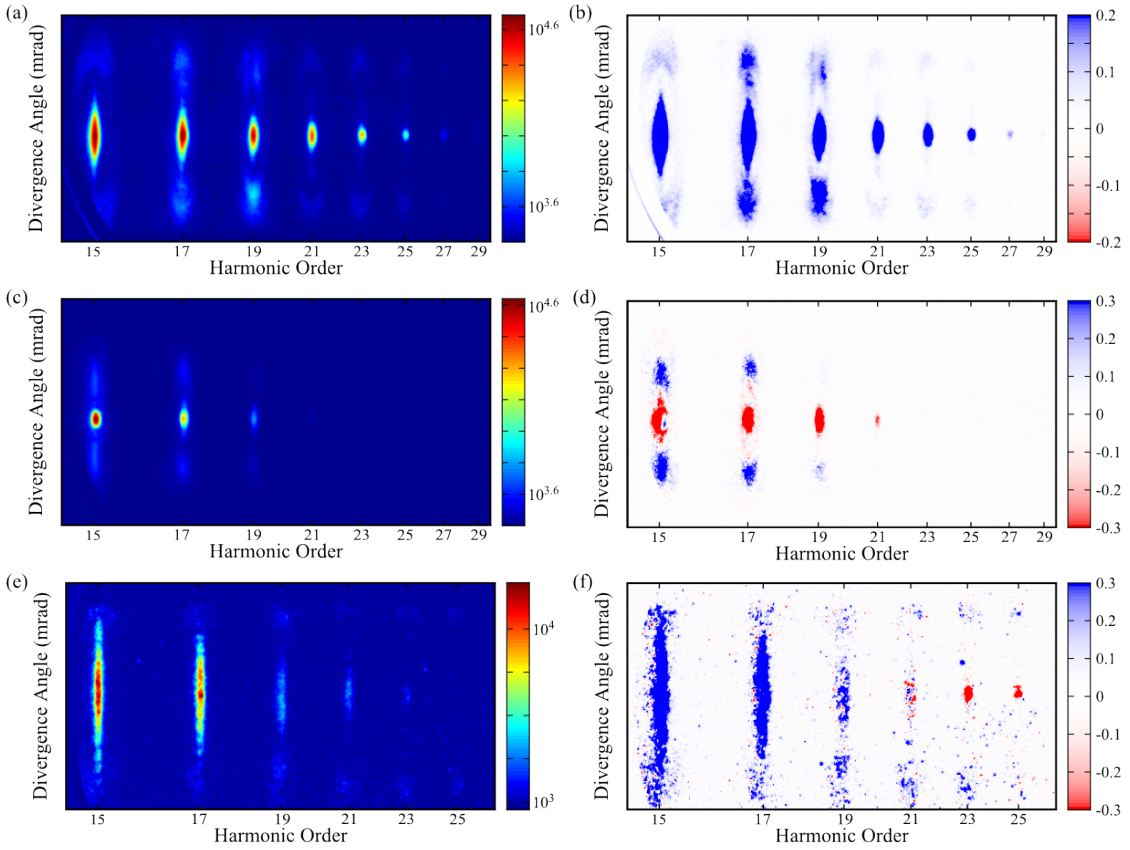


**Figure 4.35.:** Spectra in (a) argon, (c) xenon and (e) carbon dioxide at a backing pressure of 9 bar. Subfigures (b), (d) and (f) illustrate the respective difference signal of spectra $S_{200}$ taken at 200 °C subtracted from spectra $S_{80}$ taken at 80 °C $((S_{80} - S_{200})/(S_{80} + S_{200}))$ and then normalized by the sum of the two spectra.

clusters cannot be ruled out in a cold carbon dioxide gas jet.

## 4.6. Conclusion and Outlook

The most striking results of this chapter are certainly presented in paragraph 4.3: By performing a 2D spectro-spatial analysis, we are able to disentangle several contributions to the harmonic signal from a mixture of clusters and monomers. The off-axis emission shows three clear features: an extended cutoff with increasing average cluster size, an increasing decay rate with ellipticity when the average cluster size is reduced and a very low degree of linear polarization. We attribute the first two effects to a high harmonic generation mechanism in which delocalized electrons tunnel out from a cluster and recollide coherently to the whole cluster. This hypothesis needs to be further investigated using the appropriate theoretical tools. An open question remained until the defence of this thesis: Can it really be attributed to low density sources or is it purely an artifact due to an uncontrolled polarization change induced by one of the optics along the laser beam path?
Further experiments were performed without the $MgF_2$ window at the exit of the compressor. Also the strain on the entrance window was minimized. The off-axis cutoff harmonics could not be observed however. Figure 4.36 displays microscope images which were taken at different distance from the nozzle throat after the experiment. A foreign object is clearly visible. It certainly disturbs the gas expansion and thus prevents an efficient cooling of the jet. Shortly before submission of this manuscript the object could be removed and the initial results reproduced confirm the following: High harmonic emission featuring a very low degree of linear polarization can only be observed in the presence of clusters in the gas jet. A low density source as in the case for clusters is the reason for the linearly depolarized light (see section 4.3.5).

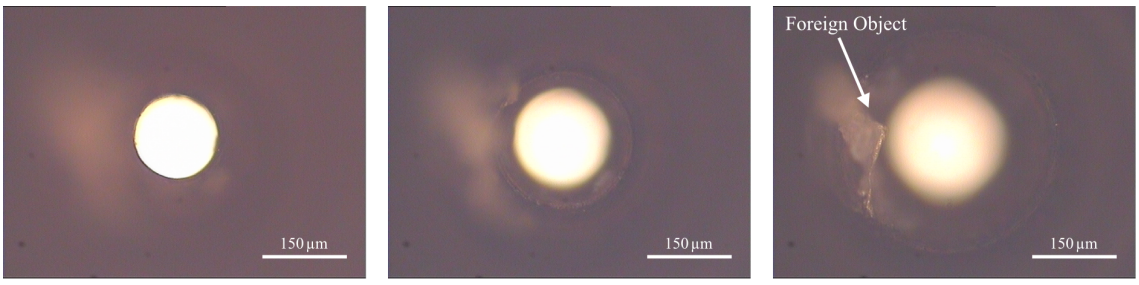


**Figure 4.36.:** Microscope images at different distances from the nozzle throat. At z = -7.107 mm the throat is well imaged. With decreasing z the image plane is moved to wider nozzle diameters.

This work could be extended by performing a complete polarimetry study of the harmonic emission in elliptical laser fields, which was recently shown to be a sensitive probe of

the influence of the ionic potential in HHG (Shafir et al., 2012a). This would enable us to determine the process responsible for the generation of the lowest harmonics and possibly further differentiate the contribution from monomers and from atom-to-atom emission in clusters. The use of advanced 2D experimental characterization should allow us to disentangle contributions from different classes of emitters and different mechanisms. It could be applied to many situations in high harmonic spectroscopy, and should in particular be useful for other cases of HHG in inhomogeneous media, such as metal plasma (Ganeev et al., 2007; Suzuki et al., 2007; Ganeev et al., 2009) or water droplets (Kurz et al., 2012). Field enhancement in nano metal tips was recently demonstrated, revealing carrier-envelope phase dependent electron spectra (Krüger et al., 2011). High harmonics could however not be observed. Either the number of emitters is too low or the hole in the tip might recombine non-radiatively. Vozzi and coworkers made an attempt to produce HHG in metal clusters at 10 Hz, but did not succeed. The field enhancement is expected to be even higher at spherical than at peaked nanostructures, such that relatively low laser intensities could be used to efficiently generate high harmonics. Thus complex amplified laser systems might be superseded and fiber lasers at megahertz repetition rate might find another application (Boullet et al., 2009). Also the properties of HHG from completely delocalized electrons in such a cluster might be very interesting. However the production of a high density metal cluster jet seems to be technically very challenging.

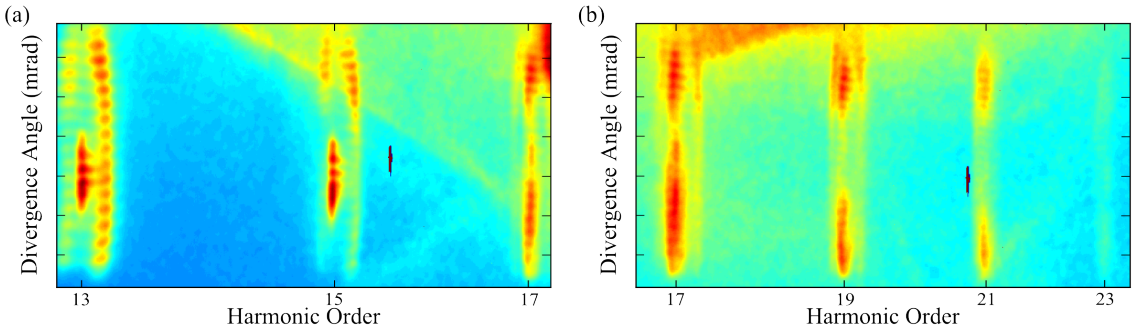


**Figure 4.37.:** Spectra from a two spatially separated harmonic sources in argon clusters at backing pressure of 70 bar and a nozzle temperature of 30 °C.

In collaboration with the atto group at Saclay further experiments were conducted in clusters: probing spatial coherence of high-harmonics from clusters. These measurements are not performed with a Michelson interferometer as has been done in one of the first measurements (Bellini et al., 1998; Lynga et al., 1999) but with a phase waveplate. The phase of the beam on the upper half of the plate is shifted by $\pi/2$ with respect to the lower half. At focus this leads to two focal spots with the advantage of higher stability than with a Michelson interferometer. Figure 4.37 presents one of the first measurements performed with this plate in argon clusters. Again it seems that the cutoff harmonics in figure 4.37(b) are more divergent than the lower harmonics. This might be an indication that the signal originates from clusters but still needs to be verified by the measurements performed

in paragraph 4.3. Also a different dipole phase from cluster emission is expected, as it appears to be divergent on the 2D images in the cutoff (e.g. figure 4.11). A measurement as performed by Corsi and coworkers might be feasible (Corsi et al., 2006). Depending on this phase clusters might provide a tool for controlling the phase of attosecond light pulses, i.e. the attosecond chirp (Mairesse et al., 2003).

## Résumé du Chapitre

*La quatrième chapitre est consacré à la génération d'harmonique dans les agrégats. Cette étude a été motivée par les expériences de la génération dans un jet de gaz de dioxyde de carbone à des températures basses où des agrégats peuvent se former et éventuellement contribuer à la GHOE . Les agrégats sont généralement considérés comme une source prometteuse de rayonnement XUV permettant d'augmenter la fréquence de coupure (Donnelly et al., 1996; Vozzi et al., 2005b). Le mécanisme de génération dans des agrégats n'est pas clairement établi à ce jour.*

*D'un point de vue expérimental la difficulté consiste à différencier les harmoniques produites par différentes espèces dans le milieu de la production: les monomères et les agrégats dont la taille est répartie sur une large distribution. Une mesure différentielle est réalisée en fonction de la température ainsi qu'une étude du taux de décroissance du signal harmonique avec ellipticité laser à différentes tailles des agrégats moyens dans le jet. A l'aide d'une analyse spatio-spectrale du signal harmonique, nous avons été capable d'identifier le rôle des agrégats dans la GHOE. Nous avons attribué un mécanisme de recombinaison recollisionnel à GHOE dans des agrégats ("cluster-to-itself"): ionisation à partir et recombinaison vers un nuage d'électrons délocalisé dans un agrégat. La longueur de corrélation à l'intérieur d'un agrégat peut être estimée, comme le paquet d'ondes recollisionnel constitue une excellente sonde avec la résolution nécessaire. L'estimation de la longueur de corrélation électronique est basée sur un modèle simple, mais une analyse théorique plus profonde est nécessaire pour une meilleure compréhension de celle-ci. L'utilisation de la caractérisation 2D devrait permettre de distinguer les contributions des différentes émetteurs et des différents mécanismes. Elle pourrait être appliquée à de nombreuses situations en spectroscopie harmonique élevé et devrait en particulier être utile pour d'autres cas de la GHOE dans des milieux hétérogènes, tels que des plasmas métalliques (Ganeev et al., 2007; Suzuki et al., 2007; Ganeev et al., 2009) ou des gouttelettes d'eau (Kurz et al., 2012).*

*Les résultats expérimentaux de la polarimétrie étaient ambigus au début, une émission harmonique linéairement dépolarisé était mesurée pour la GHOE dans des agrégats et des atomes. Les mesures étaient répétées et ont confirmé que l'émission harmonique linéairement dépolarisé est seulement observé si des agrégats sont présents dans le jet. Comme dans les atomes d'argon la mesure de la polarisation est une sonde sensible du mécanisme de génération d'harmoniques élevés et devrait apporter de nouvelles idées, et notamment élucider le rôle de la recombinaison du potentiel ionique dans des agrégats (Shafir et al., 2012a). Cela nous permettrait de différencier la contribution des monomères et l'émission d'atome à atome des agrégats.*

*Des expériences supplémentaires ont été réalisées en collaboration avec le groupe atto à Saclay pour sonder la cohérence temporelle des harmoniques. Une faible cohérence temporelle pour les agrégats uniquement pourrait être un signe que les collisions d'électrons à l'intérieur de l'agrégat jouent un rôle important à l'échelle de l'attoseconde. L'échelle*

*de temps du mouvement collectif des électrons dans un plasma est du même ordre de grandeur que le processus de recollision dans la GHOE (Krausz and Ivanov, 2009). Ces mesures pourraient donc être très utiles pour comprendre les processus de collisions qui déclenchent la fusion nucléaire dans les agrégats (Ditmire et al., 1999; Grillon et al., 2002).*

# 5. Development of a Table-Top XUV Light Source

So far atomic, molecular and condensed matter have been studied in a self probing scheme. The spectrum of the high harmonic emission originating from radiative recombination of an electron reveals important structural and dynamical information of these systems. In this chapter another approach is followed, the photons generated by HHG are used to probe the sample of study (see figure 5.1).

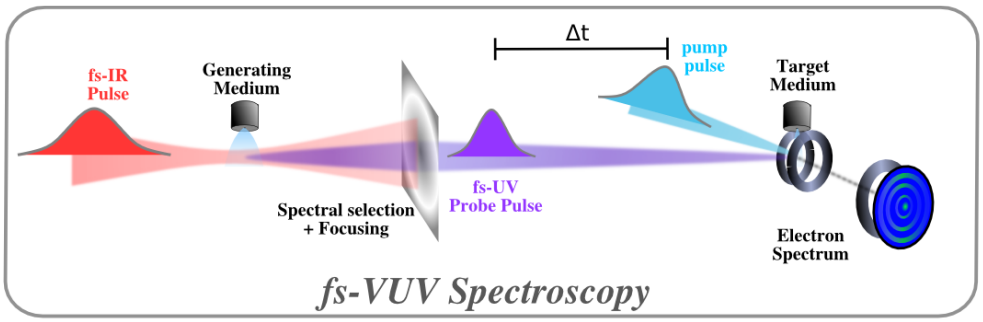


**Figure 5.1.:** Scheme of fs-XUV spectroscopy. HHG is not used in a self-probing scheme but deliver the probe beam for photofragment imaging.

Before the discovery of HHG only discharge tubes and synchrotrons were able to reach photon energies up to several hundred of eV. Discharge tubes however do not reach a sufficent photon flux at a low repetition rate and synchrotrons are very big, cost-intensive machines. HHG opened a side entrance to access these photon energies by means of table-top systems. HHG has been proved to provide pulses in the microjoule range (Hergott et al., 2002; Takahashi et al., 2002). Even though achieved photon fluxes are weaker than in synchrotrons, the emission from HHG is temporally and spatially coherent (Zerne et al., 1997; Bellini et al., 1998; le Déroff et al., 2000). Another advantage of HHG is their short pulse duration, allowing highest possible temporal resolutions down to the attosecond time scale (Paul et al., 2001; Hentschel et al., 2001; Mairesse et al., 2003; Tzallas et al., 2003).
Different experimental schemes have been developped for HHG as a XUV light source using grating monochromators for spectral selection. The grating monochromator at the Artemis facility uses four different gratings with the grooves almost parallel to the incident and diffracted wave vector (Poletto et al., 2009). The overall monochromator transmission varies between 21 % and 28 %. XUV pulses with $1.6\times10^7$ photons per pulse for harmonic 21 at 1 kHz were measured after the monochromator. Pulse durations between 20 fs and 30 fs were measured (Frassetto et al., 2011). Another setup employing two torroidal

gratings with a transmission of 2.6 % was used in Japan (Ito et al., 2010). $4.2\times10^6$ photons per pulse for harmonic 21 at 1 kHz with a pulse duration of 47 fs was measured after the monochromator. When compensating the pulse tilt-front the high harmonic pulses were compressed down to 11 fs (Igarashi et al., 2012). A much simpler setup was implemented by Wernet and coworkers (Wernet et al., 2011). Only one torroidal grating was used, leading to $10^7$ photons per pulse at 1 kHz for harmonic 13 or harmonic 15 when generating in xenon. The duration of the monochromized XUV pulses determined at around 120 fs. The tunability of harmonic order for the different setups is respectively from the first to the third setup: harmonic 11 to harmonic 25, harmonic 15 to harmonic 29 and harmonic 11 to harmonic 27.
It is clear that the new setup designed and built at CELIA must fulfill the following criteria: spectral selectivity between harmonic 9 and harmonic 17, short time resolution, low-budget, a photon flux of $10^6$ on target per pulse and harmonic and an easy switching to ENLOS setup (extreme non-linear optical spectroscopy). The samples of interest are pumped by 266 -2000 nm tunable pulses. Two different configurations are required for the probe beam in the fs-XUV setup. Either the full harmonic spectrum is used as a probe employing filters cutting out undesirable wavelengths in the spectrum or a grating monochromator is used for selecting a single harmonic. The fragments of the ionized sample can be captured in a simple time of flight spectrometer or by the recently built velocity map imaging spectrometer (VMI) (Handschin, 2012).

## 5.1. Design of the new Vacuum Chamber

There is one requirement the new vacuum chamber has to fulfill, it shall be used in three different configurations. The first configuration shall allow the direct measurement of high harmonic spectra. Optionally a three-mirror polarizer shall be introduced in this configuration allowing us to probe the state of polarization of HHG directly. In the two other cases the XUV-photon shall probe the samples in the VMI. The challenge is the wavelength selection in this energy regime. Conventional dielectric mirrors have a low reflectivity around 100 nm and are generally cost-intensive in the XUV range. Thus different solutions are applied in this regime. One possibility for spectral selectivity is a grating monochromator. However employing a grating monochromator brings along two important disadvantages: the XUV pulses are temporally broadened and the first order diffraction efficiency is very low in terms of reflectivity. For this reason an alternative optical path can be chosen which avoids reflections with an acute angle. This ensures that the photon loss is minimized by avoiding reflections with pointed angles, but the spectral selection of a given harmonic cannot be ensured any more. Filters can be used in order to ensure a higher spectral selectivity. The layout of the chamber was calculated with the ABCD matrix formalism, which is summarized in appendix A. Several assumptions are made, which are not perfeclty fulfilled in experimental conditions. This formalism is however accurate enough for the purpose of calculating a first chamber layout.

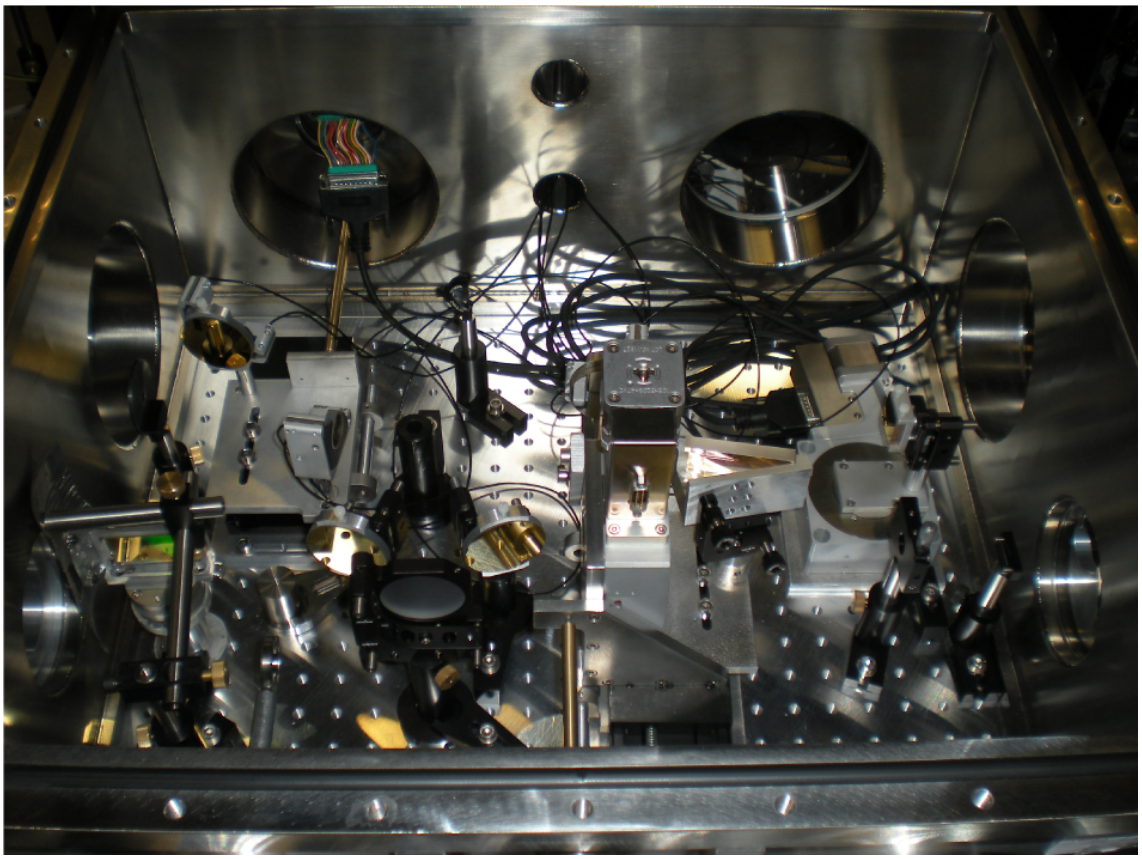

**Figure 5.2.:** The new chamber in the ENLOS configuration with a fixed three mirror polarizer. Apart from the electrical rotation stage each part of the setup was completely unmounted and the grease was removed with acetone. Molybdenum disulphide (Caburn-MDC) was used as a lubricant instead. This procedure is necessary to avoid the deposit of thin films on the optics under vacuum.

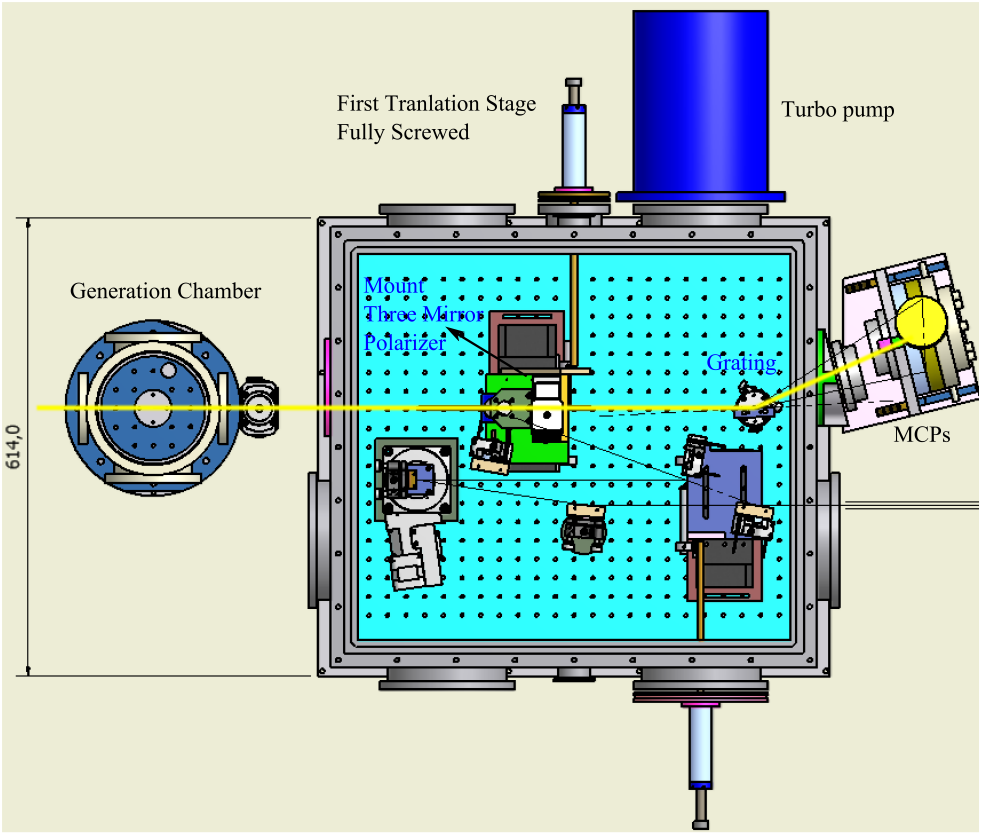


**Figure 5.3.:** First chamber configuration. The harmonic beam goes directly on the grating and then the MCPs. The width of the main chamber is 614 mm.

### 5.1.1. ENLOS Beamline

In the first configuration the vacuum chamber needs to fulfill the spectral imaging of the high harmonics. Figure 5.3 depicts this first possible configuration. The XUV beam goes directly onto a flat aberration corrected concave gold grating for flat-field spectrographs (Hitachi: Part No. 001-0437*1,2) which images and resolves the generated harmonics spectrally onto MCPs. The distance between the position of HHG and the grating is 806 mm.
The flat field image is achieved by a varying groove spacing. It has $\sigma_0 = 1200$ grooves per mm at its central region, a radius of curvature of R = 5649 mm and a blaze angle of 3.2°. According to the manufacturer instruction, the grating must be used at an AOI of 87° with an object distance of r = 237 mm and an imaging distance of r' = 235.3 mm for obtaining a flat field image in a wavelength range of 5-20 nm.

We have already observed under experimental conditions that the image quality of the high harmonic spectrum does not change significantly if the imaging distance is changed by 1 cm when moving the MCPs. The imaging conditions of the grating have to be

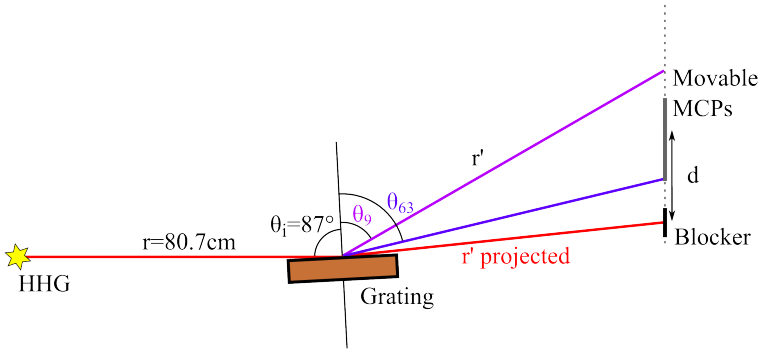


**Figure 5.4.:** Geometrical configuration of the grating. The angle range between $\theta_9$ and $\theta_{63}$ corresponds to the diffracted spectral region that has to be imaged. As the MCPs are not big enough they need to be moved for if the whole spectral range shall be covered.

established for setting up the grating in a different optical configuration as the object distance used in this setup is significantly increased compared to those recommended in the manufacturer information. The line spacing between each groove is not constant and is controlled as follows (Kita et al., 1983):

$$\sigma = \sigma_0 \Big/ \left(1 + \frac{2b_2}{R}w + \frac{3b_3}{R^2}w^2 + \frac{2b_4}{R^3}w^3\right) \tag{5.1}$$

with $w$ the distance from the center of the grating, and $b_2$, $b_3$ and $b_4$ the varied-spacing ruling parameters. When considering only the highest order of equation 5.1 and calculating the image of infinitesimal small angles the image distance can be calculated (Depret, 2010):

$$r' = \frac{rR\cos^2\theta_r}{r(\cos\theta_i + \cos\theta_r) - R\cos^2\theta_i - 2rb_2(\sin\theta_i + \sin\theta_r)} \tag{5.2}$$

where $\theta_i = 87°$ is the angle of incidence on the grating, $\theta_r$ the reflection angle and $b_2$ = -19.9751. The plane of the flat field image is perpendicular to the surface of the gold grating. For calculating the $m^{th}$ order of refraction, the reflection angle of the reflective gratings is given by:

$$m\sigma\lambda = \sin\theta_i + \sin\theta_r \tag{5.3}$$

Figure 5.5(a) shows the position of the image at $r'$ projected (see figure 5.4) as a function of wavelength. In case of an object to grating distance of 23.7 cm a good flat field image can be produced for wavelengths between 5 nm and 30 nm. As already noted this accuracy is not necessary under experimental conditions and stronger discrepancies of focal distances are acceptable. This experiment aims to image harmonic 9 to 63 which corresponds to wavelengths between 12.7 nm and 88.9 nm. At an object distance

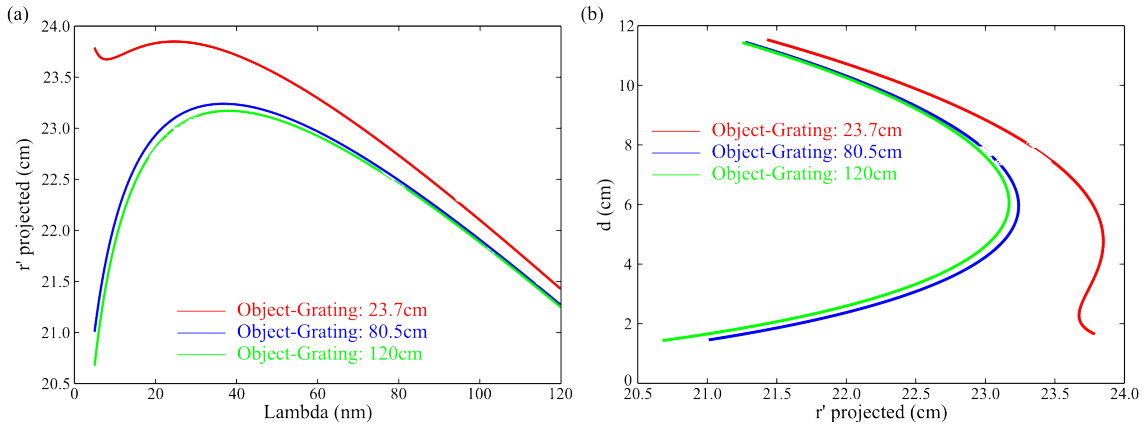


**Figure 5.5.:** Illustration of the image distance, r' projected (see figure 5.4), under different diffraction angles. (a) The projected distance as a function of wavelength for different object-grating distances. (b) d the distance on the MCPs from infrared reflection (see figure 5.4) as a function of r' projected.

of 120 mm the image position varies by 2 cm in this wavelength range. When placing the MCPs at a distance (r' projected) of 22.5 cm the image still has a good quality. The image position $d$ on the MCPs in the desired spectral range is between 3 cm and 10 cm (see figure 5.5 (b)). The MCPs which have only a diameter of 4 cm therefore have to be moved if the whole spectrum shall be recorded. This is feasible as the MCPs are connected by a bellow with an interior diameter of 63 mm to the main vacuum chamber.

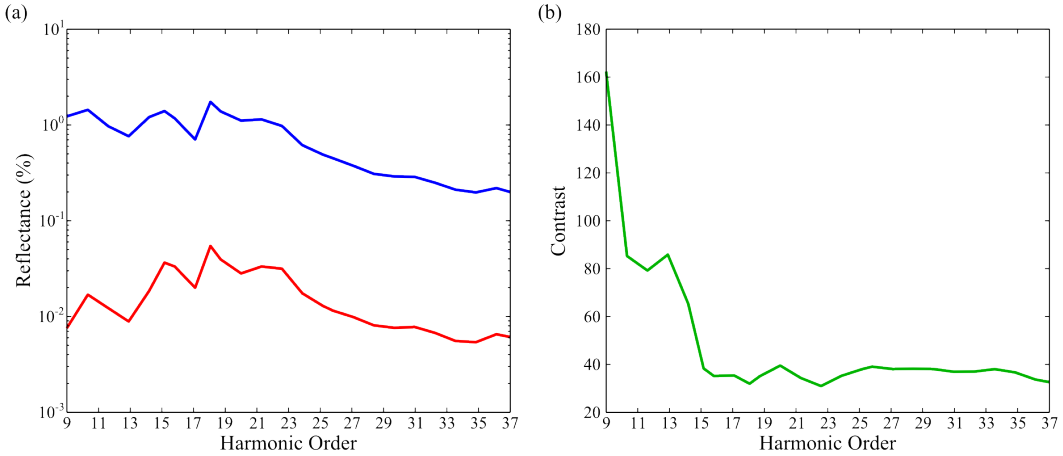


**Figure 5.6.:** (a) Reflectance of the three mirror polarizer for s-polarized (blue) and p-polarized light (red). (b) Contrast (s-polarized/p-polarized) as a function of harmonic order between s- and p-polarized light.

A three mirror polarizer is planned in the ENLOS beamline as indicated in figure 5.3. As the polarizer is rotated the beam must not shift and stays on axis. Therefore the

precision of the mechanical mount for the polarizer is crucial, the rotation axis has to be exactly overlapped with the beam axis. However this overlap has not yet been achieved, an adjustable mechanical high precision mount is required. This polarizer allows us to probe the polarization of the high harmonic emission directly without employing $\lambda/2$ plates. Moreover the contrast of the polarimetry measurement would be extremely enhanced for such a polarizer. Two of the mirrors are under an AOI of 60° and one under an AOI of 30° which leads to a contrast as depicted in figure 5.6(b). Depending on the position of the polarizer the fixed gold grating which is under an AOI of 87° further increases or decreases the contrast (see figure 5.7). The fact that the gold grating does not rotate with the polarizer is problematic, but can be neglected as the contrast induced by the three mirror polarizer is much higher than the contrast of the gold grating. The three mirror polarizer will allow a high precision polarimetry measurement in the future once the precision problem of its mechanical mount is resolved.

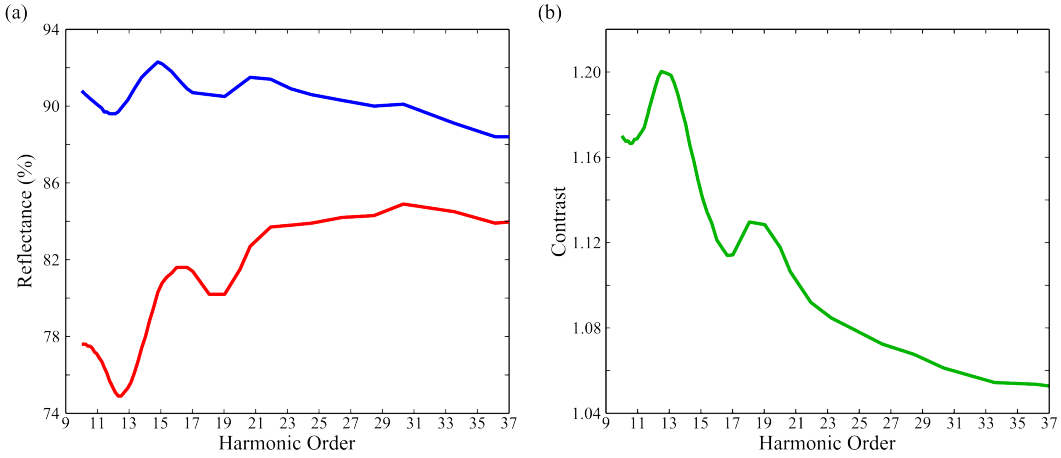


**Figure 5.7.:** (a) Reflectance gold grating for s-polarized (blue) and p-polarized light (red). (b) Contrast as a function of harmonic order between s- and p-polarized light.

### 5.1.2. fs-XUV Beamline

Two different options are possible for using the generated harmonics in the fs-XUV setup. In the first configuration the full high harmonic spectrum is sent on target. The second one allows a spectral selection of one harmonic by a grating monochromator.

Figure 5.8 illustrates the first configuration. The beam is sent onto a $SiO_2$ plate under an AOI of 10° which has an anti-reflective coating (AR coating) at 800 nm with a last layer of $SiO_2$. The distance between the harmonic source and the $SiO_2$ plate, which determines the size of the diverging infrared beam on the plate and therewith possible damage, is 450 mm. The reflectivity of the AR coating is approximately 10 % at 800 nm. Then the beam is reflected towards a plane gold mirror, a torroidal gold mirror and again on a plane gold mirror before being focussed into the VMI. The AOI is for each mirror 80°, 85° and

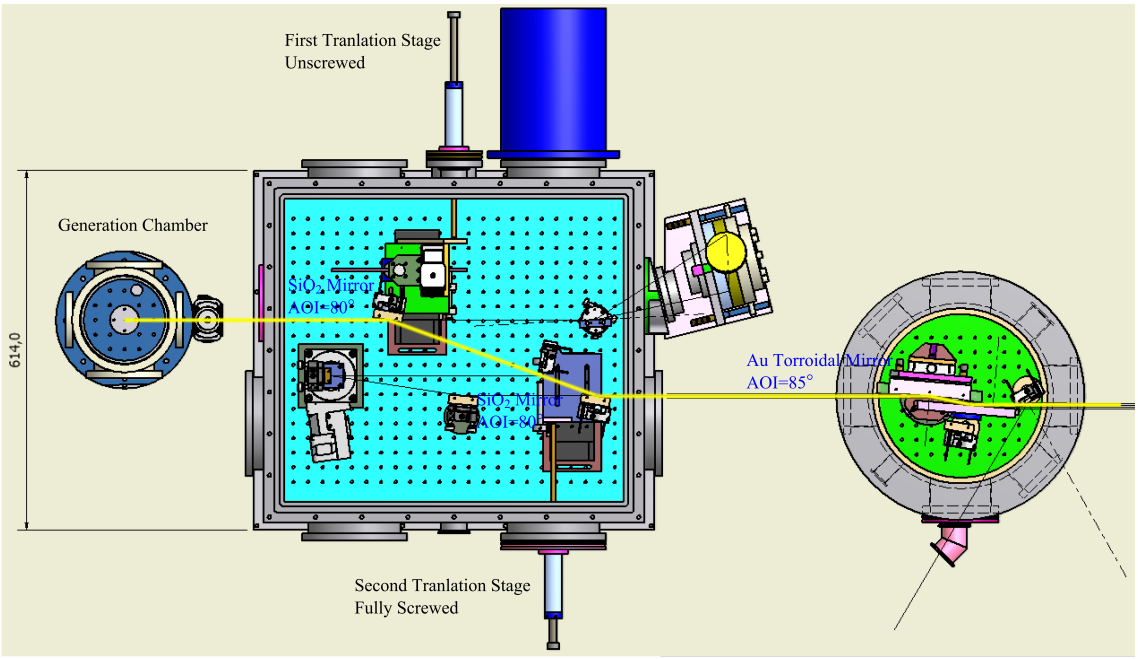


**Figure 5.8.:** Metallic filter configuration. The full harmonic spectrum is sent on target and possibly filtered.

85° respectively. The calculated reflectivities for the different optics at different AOIs are show in figure 5.9

The torroidal mirror images the source of the high harmonic radiation directly inside the VMI. The focii of the torroidal mirror for the tangential and sagittal rays are given by equation A.10 of Appendix A. With a focal length of f = R/2 = 0.5 m, the required radii are: $R_{tan}$ = -11.474 m and $R_{sag}$ = -0.087 m. The alignment of the torroidal mirror is crucial and very sensitive. The mirror is mounted on a high precision rotation mount. It is first autocollimated and rotated by 85°. The fine alignement is finally done by adjusting horizontal and vertical tilt of the mirror for compensating the astigmatism at the focus. Thus the beam direction is fixed by the torroidal mirror but can still be adjusted by the flat gold mirror which follows. The distance between high harmonic generation and the torroidal mirror is 1475 mm which leads to an imaging distance of 753 mm always assuming a perfect Gaussian beam with a $M^2 = 1.5$.
Figure 5.10 shows the propagation of the beam at its waist. The beam propagation is calculated by the ABCD-matrix formalism of appendix A, which assumes a perfect Gaussian beam for propagation. It can clearly be seen that it is important to align the torroidal mirror up to a precision of one-tenth of a degree. Note that the absolute values of the beam radius are only a rough estimation. The waist of the infrared beam in the generating medium is estimated in appendix B to 115 $\mu$m and to 57.5 $\mu$m for the XUV beam. For filtering out the 800 nm light and only transmitting harmonic 11 to 49 an aluminium filter is used.

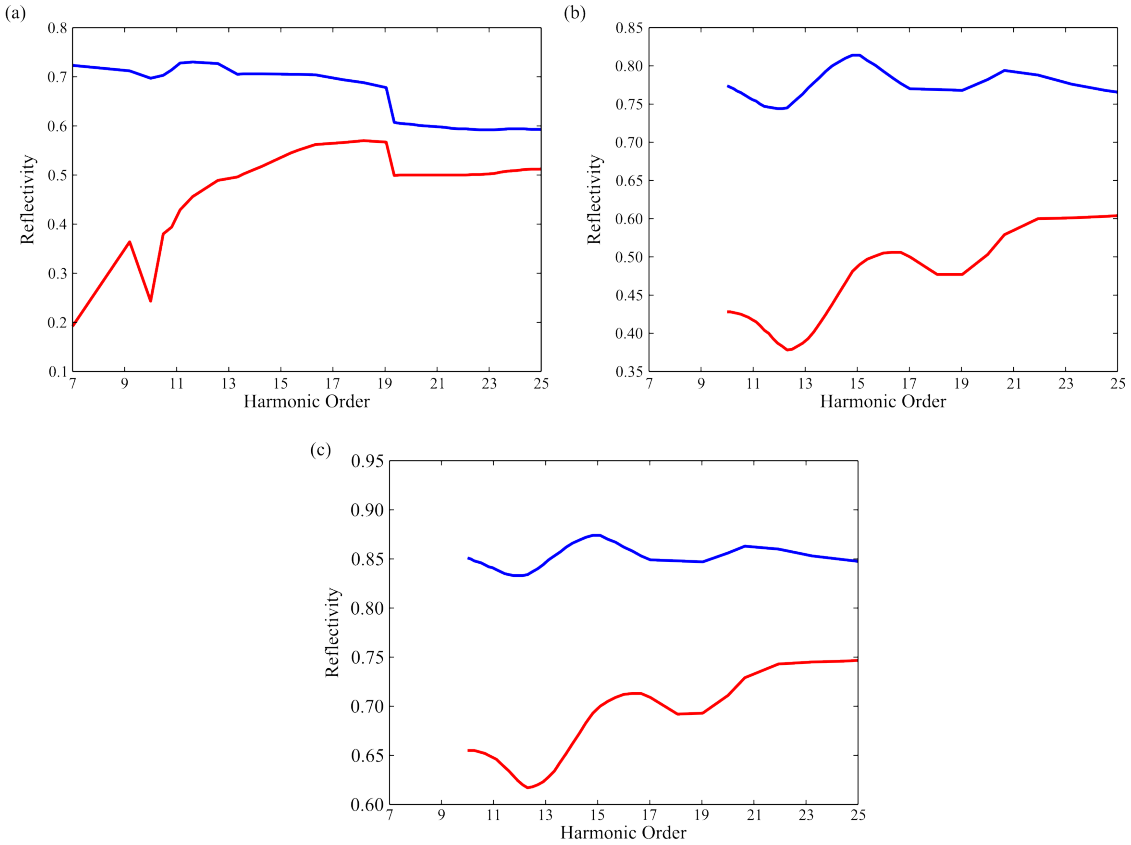


**Figure 5.9.:** Reflectivity as a function of harmonic order for (a) $SiO_2$ with an AOI of 80°, (b) gold with an AOI of 80° and (c) with an AOI of 85°. The blue solid (red dashed) line corresponds to s-polarized (p-polarized) light.

In the monochromator configuration of the fs-XUV pump-probe setup a grating is integrated in the beam path for selection of a single harmonic (see figure 5.11). The grating however decreases temporal resolution of the pump probe setup. Each groove induces a delay $\Delta t = \lambda/c$ for the first diffracted order, due to the path difference between two neighbouring interfering rays. Therefore it is of interest to illuminate as few grooves as possible what is accomplished here by focussing the beam. The smallest laserspot size on the grating is limited by the damage threshold of the gold grating (Bödefeld et al., 2010) which is about 15 mJ/cm$^2$. A compromise has to be found between the induced delay and the maximal fluence of the generation beam on the grating. A slit is placed after the grating for spectrally selecting different harmonic orders and blocking all the others. Different harmonic orders are chosen by turning the grating.

A spherical mirror with a radius of curvature of R = 550 mm is used for decreasing the beam diameter on the grating. The distance between high harmonic generation and the first curved mirror is set by 730 mm. The focus of the curved mirror is approximately 440 mm behind the curved mirror and thus 80 mm after the grating. The beam diameter

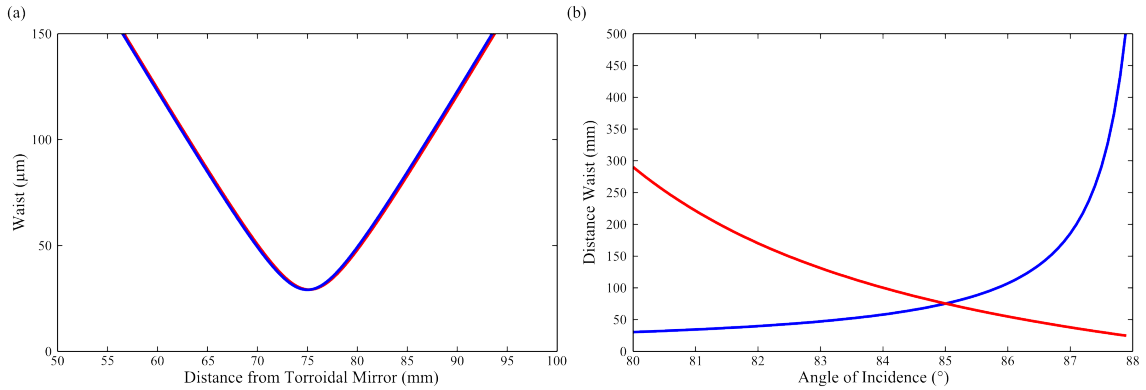


**Figure 5.10.:** (a) Waist for the sagittal (blue line) and tangential rays (red line) for an AOI of 85° of the torroidal mirror as function of distance from the mirror for harmonic 11. The sagittal (blue line) and tangential (red line) beam waist overlap very well. (b) Position of the sagittal and tangential beam waist as function of AOI on the torroidal mirror. The waist overlap only at an AOI of exactly 85°.

of the fundamental beam on the grating is calculated with the ABCD matrix formalism assuming a waist of 115 $\mu$m at HHG (see appendix B). Gaussian beam propagation results in a beam radius of 268 $\mu$m in the tangential and 331 $\mu$m in the sagittal plane at the grating. For estimating the fluence on the grating, the reflectivities of the $SiO_2$ plate and the curved $B_4C$ mirror are assumed to be respectively 10 % and 20 %. At focus the fluence is 177 mJ/cm$^2$ which is clearly above the damage threshold of 15 mJ/cm$^2$. When placing the grating 80 mm before the focus as done in the setup the maximal fluence is below this value at around 12.6 mJ/cm$^2$. The AOI on the curved mirror is 10° and has therewith an acute angle what is undesirable for reflections in the XUV regime. A $B_4C$ coating still ensures a reflectivity of up to 20 % for harmonic orders below 15 (see figure 5.12).

The delay induced by the grating is evalutated applying the following formula:

$$\Delta t = \frac{d\lambda_0}{gcn} \tag{5.4}$$

with $n$ the harmonic order, $\lambda_0 = 800$ nm the frequency of the fundamental beam, $d$ the beam diameter on the grating calculated by the ABCD matrix formalism and $c$ the speed of light. The grating (Spectrogon) consists of $\sigma = 600$ grooves/mm, i.e. it has of groove spacing of $g = 1.67\mu m$. One great advantage of the grating is its low cost of 600 € which is very low as compared to the gratings used in the setups mentioned in the introduction of this chapter (10000 € to 30000 €). The blazing angle of the grating is optimized at an AOI of 6° for a wavelength of 100nm, leading to a deviation angle of 8.56°. Table 5.1 shows the induced delay by the grating for the calculated waist size for the sagittal and tangential ray bundle. The waist size of the XUV-beam is extracted from appendix B where it is approximated to 57.5$\mu$m. The ABCD matrix formalism thus

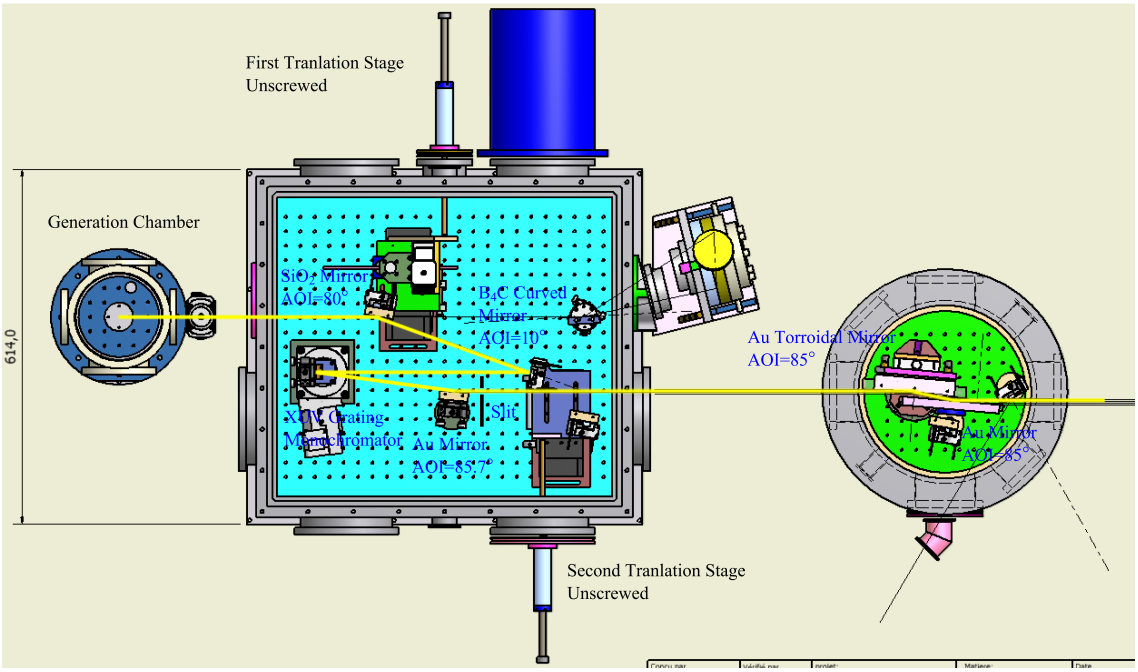


**Figure 5.11.:** Monochromator configuration. The spectral selection is done by a XUV grating monochromator before the beam is sent onto a torroidal mirror.

predicts an induced delay by the grating monochromator which is beyond 20 fs for the harmonic orders considered here.

| harmonic order | Tan 80 mm $w_0/\Delta t$ | Sag 80 mm $w_0/\Delta t$ |
|---|---|---|
| 7 (114.3 nm) | 78 $\mu$m/14 fs | 96 $\mu$m/18 fs |
| 9 (88.9 nm) | 62 $\mu$m/11 fs | 75 $\mu$m/14 fs |
| 11 (72.7 nm) | 52 $\mu$m/10 fs | 62 $\mu$m/11 fs |
| 13 (61.5 nm) | 45 $\mu$m/8 fs | 54 $\mu$m/10 fs |
| 15 (53.3 nm) | 40 $\mu$m/7 fs | 47 $\mu$m/9 fs |
| 17 (47.1 nm) | 36 $\mu$m/7 fs | 42 $\mu$m/8 fs |

**Table 5.1.:** Induced delay and calculated beam radius at the grating position of 80 mm before the focus of the $B_4C$ mirror for different harmonic orders.

The simulation of the focus is depicted in figure 5.12(b) for the fundamental beam. The focii of the sagittal and the tangential beam are clearly shifted because the curved mirror creates astigmatism at an AOI of 10°.
The spectral resolution of the grating has to be sufficient for resolving the different harmonics. The resolving power $R$ of a grating is given by (Born and Wolf, 1991):

$$R = \frac{\lambda}{\Delta\lambda} = mN \tag{5.5}$$

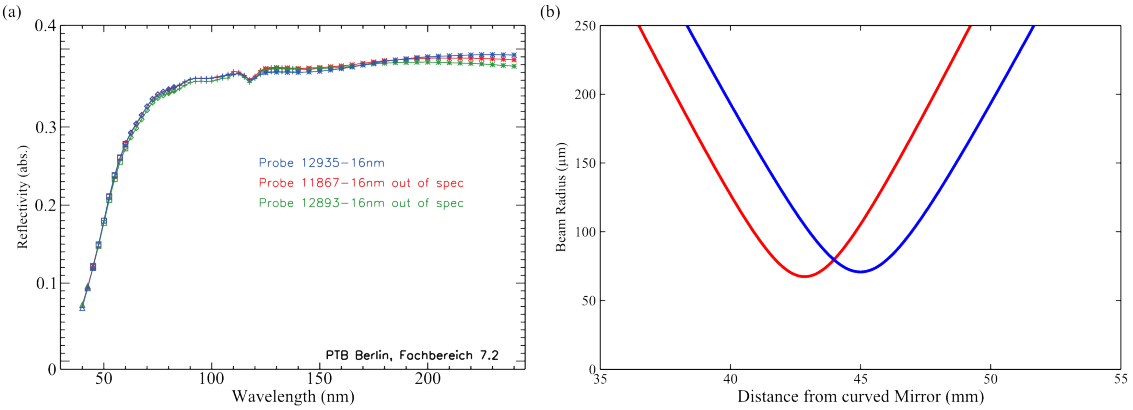


**Figure 5.12.:** (a) Reflectivity of the $B_4C$ coated mirror as a function of wavelength at an AOI of 10°. (b) Radius of fundamental beam after the focus of the curved $B_4C$ coated mirror for the sagittal (blue line) and tangential beam (red line).

where $N$ is the number of illuminated grooves, $m$ the diffracted order and $\Delta\lambda$ the minimal wavelength difference that can be separated, defined by the Rayleigh criterion. Considering harmonic 7 and harmonic 17 a resolution of $\Delta\lambda = 0.70\,nm$ and $\Delta\lambda = 0.31\,nm$ is achieved for the two respective harmonic orders. This resolution is certainly sufficient for the required application.

| Harmonic Order | $\theta_i$ | $\theta_m$ | sep. on slit |
|---|---|---|---|
| 7 (114.3 nm) | 6.25° | 2.31° | 4.6 mm |
| 9 (88.9 nm) | 5.81° | 2.74° | 2.9 mm |
| 11 (72.7 nm) | 5.53° | 3.02° | 2.0 mm |
| 13 (61.5 nm) | 5.34° | 3.22° | 1.5 mm |
| 15 (53.3 nm) | 5.20° | 3.36° | 1.1 mm |
| 17 (47.1 nm) | 5.09° | 3.46° | 0.9 mm |

**Table 5.2.:** Incident angle $\theta_i$, deviation angle $\theta_m$ and separation on the slit to neighbouring higher order.

One further issue is the spatial separation of the harmonics on the slit, once the angle of the grating is adjusted for a certain harmonic. The slit size can be varied very precisely with a $\mu$m screw. It is placed 300 mm after the grating. The distance between the selected harmonic and the one that is closest is calculated as displayed in table 5.2. The slit blocks the neighbouring order harmonics when chosing a slit size of 1.5 mm. By imaging the harmonics on a pair of MCPs the spatial selection of the slit up to harmonic 19 has been experimentally tested. As a matter of fact the spatial selection of the slit works even for second order diffracted harmonics.
Again the focussing of the high order harmonics is done with a torroidal mirror which images the focus of the curved $B_4C$ mirror into the VMI. The torroidal mirror does a 1:1

image of the focus with a object to image distance of 2 m. If the VMI is used in this configuration it has to be moved by 250 mm away from the torroidal mirror.

## 5.2. Characterization of the New Setup

The big question mark of this experiment is the photon number per pulse on target and thus also the diffraction efficiency of the grating monochromator. In a first setup a 2 cm long gas cell with a lens of 80 cm focal length was used for HHG in krypton. An iris was used for controlling intensity at HHG. Variation of the diameter of the iris which is located in front of the focussing lens is used for controlling the intensity of the fundamental laser field at focus. The gas pressure in the cell is optimized too. The photon flux of each harmonic, utilizing the grating monochromator, is measured with a calibrated photodiode. Also the overall photon flux is measured when generating in krypton using a lens with an focal length of 1 m.

### 5.2.1. Transmission of the Grating Monochromator

The photon transmission is calculated for the monochromator configuration assuming the theoretical reflectivities for the different surfaces. A comparison between the signal from the monochromator configuration and the metallic filter configuration is made for extracting the transmission of the grating monochromator.

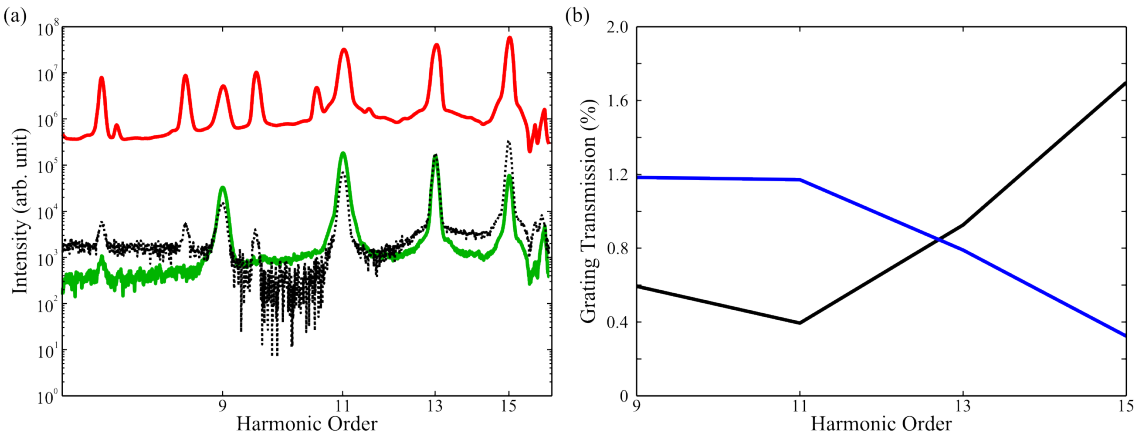


**Figure 5.13.:** (a) Spectra taken in different configurations. The red solid line shows a spectrum taken in the metallic filter configuration (without metallic filter). The other two spectra are taken passing the grating monochromator. The zero order diffraction is depicted by the green solid line and the black dotted line illustrates the first order diffraction of the grating. (b) The grating transmission for the zero (black solid line) and first diffracted order (blue solid line) obtained from the spectra on the left. These were calculated by taking into account the different theoretical reflectivities of the optical elements in the two configurations.

Figure 5.13(a) shows spectra taken in the different configurations, with and wihtout the grating monochromator. The zero and first order diffraction of the grating monochromator is recorded on the MCPs. In the first case the grating is in reflection configuration (AOI = 4.3°). The spectrum of the first order diffraction is a sum over four spectra corresponding to harmonic 9-15 taken at the four respective incident angles (see table 5.2). Note that also second order diffracted harmonics of the grating monochromator are recorded. It is strange that the first order diffraction is stronger for harmonic 15 than the zero order. This might be justified to a stronger background signal for the first order spectrum as it is summed over four scans at four different angles. This implies that the background signal from scattered light is different for the different angles. The measurement of the diffraction efficiency needs to be repeated with a better blocker of the scattering signal. The diffraction efficiency has been calculated[1] however for such a grating monochromator, it drops from 3.7 % for harmonic 9 to 0.7 % for harmonic 13.
The transmission of the grating can be estimated, by assuming that the reflectivities of all the other optical elements are well known. Figure 5.13(b) illustrates the transmission taking into account the different overall reflectivities for the two different configurations. The transmission of the grating is between 0.5 % and 1.6 % depending on the harmonic order and therewith on the diffracted order.

### 5.2.2. Photon Flux Optimization

The photon flux is optimized in a 2 cm long gas cell filled with krypton. An optimal interaction length equal to the Rayleigh length was found (Tamaki et al., 2000). It is difficult to calculate the Rayleigh length analytically in this configuration because a clipped Gaussian beam is focussed into the cell. A crude approximation can be done by assuming a Gaussian with a beam radius of 2.5 mm if the iris before the lens has a diameter of 6 mm. Following the ABCD matrix formalism this leads to a Rayleigh length of approximately 2.5 cm and would thus be far from the optimal condition. Different cells with different lenses still need to be studied. A lens with a focal length of 80 cm and the focus 0.5 cm - 1 cm before the center of the cell was utilized.
The focal length was found to be critical. The intensity of the infrared on the first $SiO_2$ plate seemed to be too high and caused damage on this plate. Therefore the distance between the interaction chamber and the $SiO_2$ plate was increased in a later setup employing a different lens (f = 1 m).

The further experiments are conducted with a lens of shorter focal length (80 cm) with a focus moved slighty before the generation medium. This supports phase matching for harmonics generated by the short trajectories and thus on-axis emission. Still the gas pressure in the cell and the generation intensity need to be optimized. As depicted in figure 5.14(a) a too high pressure limits and even decreases the intensity of HHG. This effect can be attributed to reabsorption in the medium. A maximum signal is obtained

[1] Calculated by Dr. Olaf Schwarzkopf at Berliner Elektronenspeicherring-Gesellschaft für Synchrotronstrahlung (Bessy).

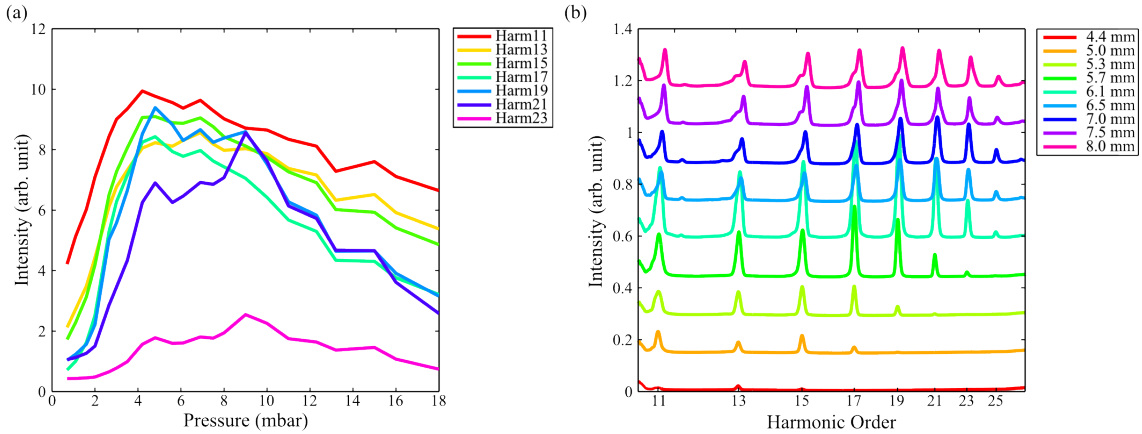


**Figure 5.14.:** (a) Signal as a function of gas pressure for different harmonic orders generated in krypton. The iris diameter is 6 mm. (b) Harmonic spectra at different iris diameters. Each spectrum is shifted with respect to zero intensity and scaled logarithmically. All spectra are measured on the MCPs.

at cell pressures around 5 mbar. Assuming a photoionization cross section of 15 Mb[2] (Kennedy and Manson, 1972) an absorption length of 5.5 mm is calculated (see chapter 1 section 1.5.2). With a cell length of 2 cm this corrpesponds well to the optimizing conditions predicted in section 1.5.2, equation 1.38: $L_{med} > 3L_{abs}$.

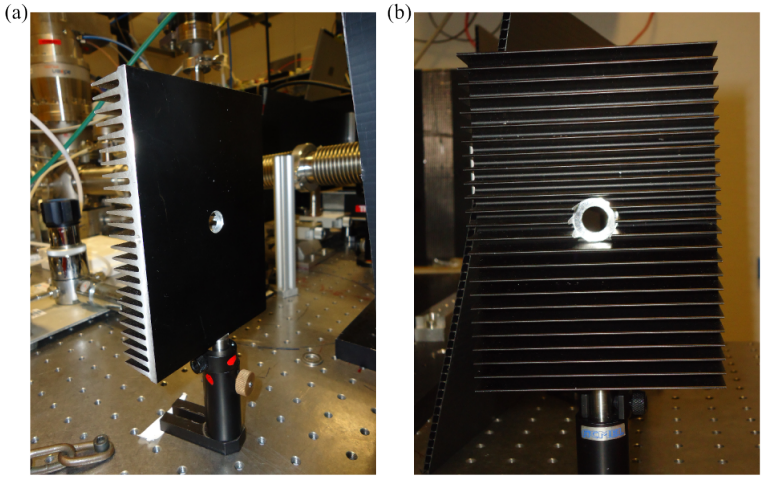


**Figure 5.15.:** Front (b) and back (b) of the metal radiator that absorbs the beam energy which would be blocked by the iris otherwise.

The intensity plays a crucial role for ionization and therewith phase matching conditions. It is controlled by the opening diameter of an iris. If the iris absorbs the energy that is blocked it heats up and creates thermal airflow around it. An unstable high harmonic

[2] $1b = 10^{-24} cm^2$

spectrum was observed due to this airflow around the iris. A large metal radiator with cooling ribs and a circular opening of 1 cm diameter was therefore introduced in the beampath (see figure 5.15). The spectrum was stabilized with this cooler. Figure 5.14(b) illustrates harmonic spectra at different iris diameters. An iris diameter around 6.1 mm optimizes the harmonic spectrum.

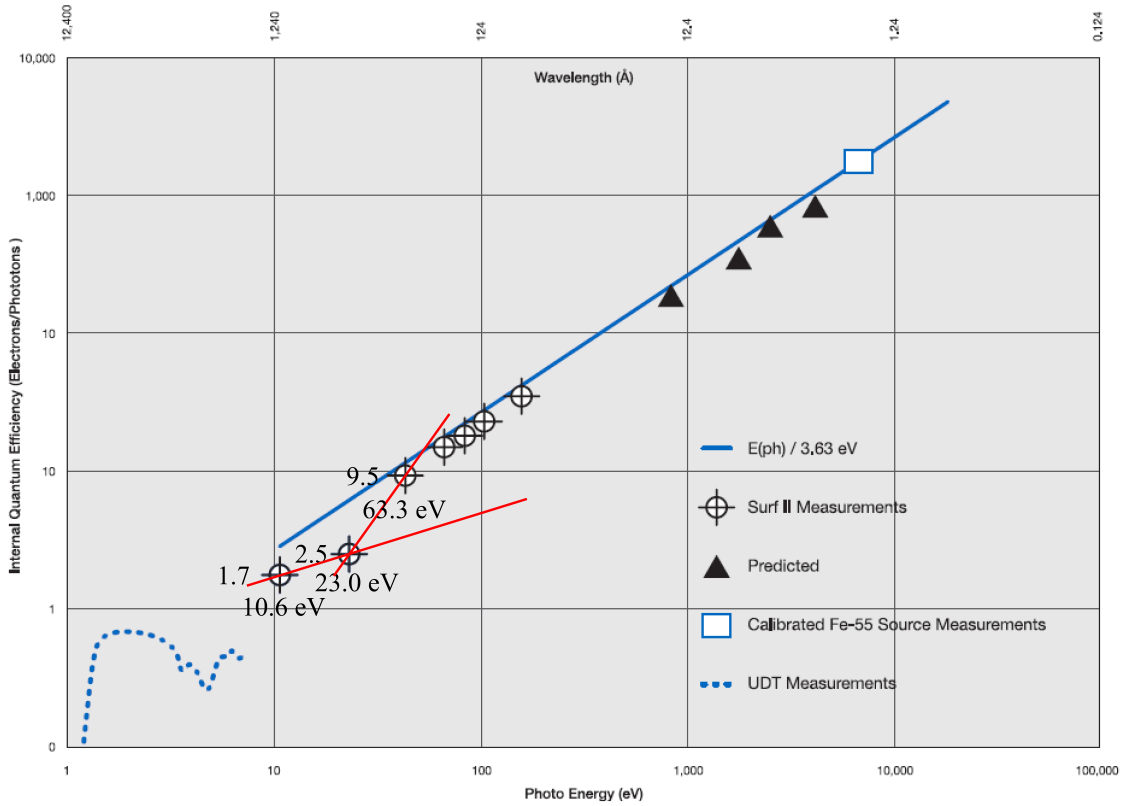


**Figure 5.16.:** Calibration curve of the photodiode. The red line depicts the extrapolation of the two points measured at lowest energy.

### 5.2.3. Photon Flux of Single Harmonics

The number of photons per shot on target is the crucial value which is a limitting factor for the number of events that are measured with the VMI. Too few photon numbers would lead to an unfeasible experiment. Typical photoionisation cross sections for hydrogen and oxygen are around 5 Mb. For detecting reasonable signals in the VMI 100 events per shot are desirable. It is difficult to calculate the number of required photons per shot as interaction volume and gas density are difficult to determine. A first rough estimation predicts required $10^7$ photons per shot.
HHG was performed in krypton in this experiment. The photon number was measured with a calibrated photodiode (OSI Systems Company; XUV-100). The calibration for the

internal quantum efficiency (IQE) curve is depicted in figure 5.16. Unfortunately there are very few points measured in the spectral region of interest. The experimental points in the spectral region of interest have a lower internal quantum efficiency than predicted by the linear fit (blue line). The last three points are closest/within the spectral region of harmonic 11 to harmonic 27. These points are therefore extrapolated for extraction of the internal quantum efficiency for each harmonic order (see table 5.3).

| Harmonic Order | IQE |
|---|---|
| 11 (17.05 eV) | 2.17 |
| 13 (20.15 eV) | 2.35 |
| 15 (23.25 eV) | 2.52 |
| 17 (26.35 eV) | 3.40 |
| 19 (29.45 eV) | 4.23 |
| 21 (32.55 eV) | 5.26 |
| 23 (35.65 eV) | 6.33 |
| 25 (38.75 eV) | 7.52 |
| 27 (41.85 eV) | 8.81 |

**Table 5.3.:** Internal quantum efficiency of the photodiode for different harmonic orders.

A first measurement, which resolves the different harmonics spectrally, is done with the MCPs by rotating the grating monochromator (see figure 5.18(a)). Second order diffraction is still quite strong for harmonic 13 and 15. The harmonic orders were resolved spectrally with the Hitachi grating. Only harmonic orders between 9 and 15 could be observed on the MCPs. The other harmonic orders cannot be measured as they do not reach the MCPs. Figure 5.18(b) depicts the same scans on two different days, showing a clear shift of the harmonic spectra depending on a day to day alignment. The MCP signal is comprared to the photodiode signal in order to assign a current measured by each harmonic order.

An aluminium filter with a thickness of d = 167 nm (Luxel) is employed in order to filter out the infrared beam. It also absorbs completely the harmonic 9. Aluminium oxide is also strongly absorbing the XUV-light and needs to be considered. The exact thickness of the $Al_2O_3$ layer is not known but is assumed to be d = 5 nm thick on each side of the aluminium filter (Mott, 1940). Table 5.4 displays the corresponding transmission at different wavelengths. The photocurrent is measured by the photodiode with a pico-amperemeter. The signal at angles higher than 5.65° is attributed to second order diffraction from harmonic 19 and harmonic 17. It might be the case that higher second order diffraction also contributes to angles below 5.65°, but this shall be neglected because harmonic 21 and harmonic 23 are already in the cutoff. The theoretically calculated AOIs for the grating monochromator from table 5.2 agree well with the main value averaged over measurements on different days. The extracted photocurrents $I_{photon}$ corresponding to these values are extracted and illustrated in table 5.4. The photon number per shot

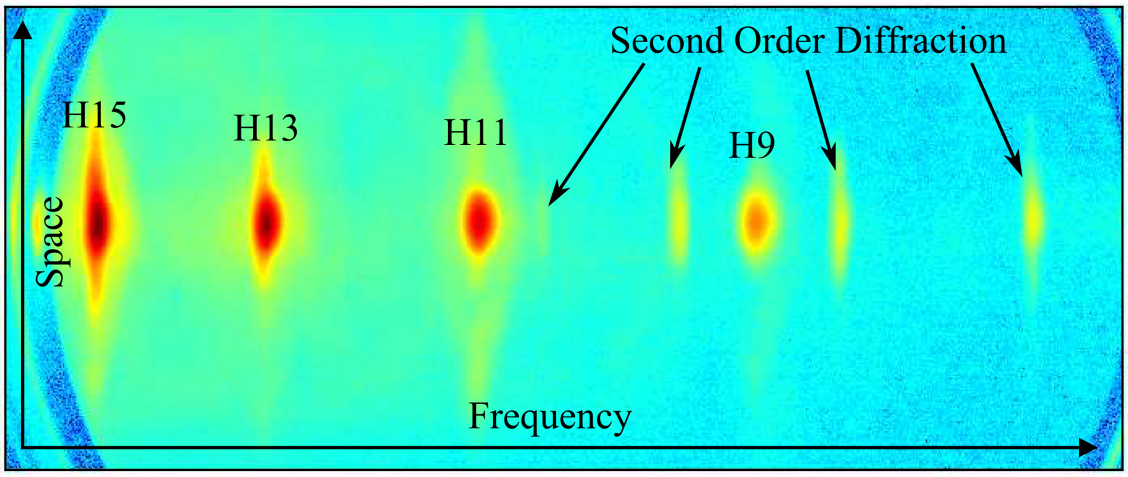


**Figure 5.17.:** High harmonic spectrum after having passed the grating monochromator in zero order configuration. Also the second order diffraction of the Hitachi grating is still detected on the MCPs.

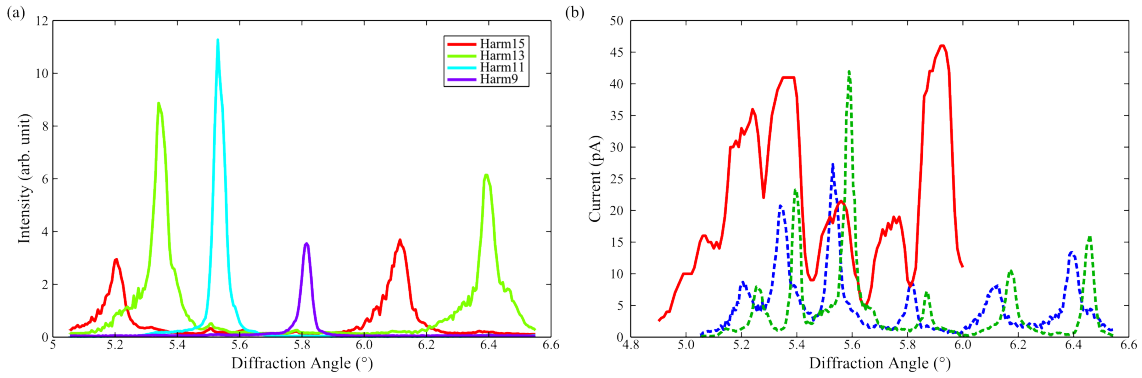


**Figure 5.18.:** (a) Harmonic spectrum spectrally resolved by the Hitachi grating as a function of AOI on the grating monochromator. Also second order diffraction from the grating monochromator is observed from harmonic 15 and harmonic 13. (b) Angular scan of the grating monochromator recording the signal with the photodiode (red solid line) and measuring the current with a pico-amperemeter. The two other scans (dashed lines) are recorded with the MCPs on two different days.

$N_{photon}$ is calulated by:

$$N_{photon} = \frac{I_{photon}}{e \cdot IQE \cdot t_{Al} \cdot t_{Al_2O_3}} \times 10^{-3} \tag{5.6}$$

| Harmonic Order | $I_{photon}$ (pA) | $t_{Al}$ d = 167 nm | $t_{Al_2O_3}$ d = 10 nm | Photon Number |
|---|---|---|---|---|
| 11 (17.05 eV) | 21.5 | 0.45 | 0.60 | $2.3 \times 10^5$ |
| 13 (20.15 eV) | 41.0 | 0.68 | 0.39 | $4.1 \times 10^5$ |
| 15 (23.25 eV) | 36.0 | 0.69 | 0.40 | $3.3 \times 10^5$ |
| 17 (26.35 eV) | 31.0 | 0.67 | 0.43 | $2.0 \times 10^5$ |
| 19 (29.45 eV) | 16.0 | 0.67 | 0.45 | $0.8 \times 10^5$ |

**Table 5.4.:** Photocurrent $I_{photon}$, transmission for aluminium $t_{Al}$ and aluminium oxide $t_{Al_2O_3}$ for the corresponding material thicknesses (CXRO, 2012) and output photon number. The on target photon number has to be divided by a factor 1.38, as the XUV beam still goes on two gold surfaces with a reflectivity of 85 % on each surface for the harmonic orders concerned.

The order of magnitude for the different harmonics is calculated to $10^5$ photons per shot on target. Note that this is only a rough estimation, there are several parameters that might have been over- or underestimated. The photodiode calibration illustrated in figure 5.16 is not very accurate in the wavelength range investigated. The photodiode should therefore be better calibrated. Also the thickness of the aluminium oxide layer is crucial as transmission is very sensitive to its thickness. As described in the section 5.2.4, the overall transmission of the aluminium filter has been determined in a measurement to: 0.27. This value agrees quite well with the average value calculated in table 5.4: $t_{Al_2O_3} \times t_{Al} = 0.48 \times 0.65 = 0.31$. The overall photon number on target per shot is calculated by summing up the photon numbers for each harmonic. Taking into account the respective reflectivities of the different optical element the total on target photon number is $9.0 \times 10^5$ and $9.9 \times 10^8$ at generation. With a laser energy of 1.23 mJ per pulse a conversion efficiency[3] of $3.0 \times 10^{-6}$ is determined for the measured photon flux. Note however that this conversion efficiency is underestimated as harmonic orders below 11 were not measured and could therefore not be considered. There should still be potential to increase the conversion efficiency, efficiencies of $3.0 \times 10^{-5}$ have already been measured when generating in argon (Kazamias-Moucan, 2003). It will be challenging to create sufficient events per shot for a reasonable measurement in the VMI, future experiments will show (Handschin, 2012). Table 5.5 illustrates the photon number on target and at high harmonic generation for the individual harmonics.

[3] Ratio between input and output energy.

| Harmonic Order | Photon Number HHG | Photon Number Target |
|---|---|---|
| 11 (17.05 eV) | $1.1 \times 10^8$ | $1.6 \times 10^5$ |
| 13 (20.15 eV) | $2.4 \times 10^8$ | $2.9 \times 10^5$ |
| 15 (23.25 eV) | $2.6 \times 10^8$ | $2.5 \times 10^5$ |
| 17 (26.35 eV) | $2.4 \times 10^8$ | $1.4 \times 10^5$ |
| 19 (29.45 eV) | $1.4 \times 10^8$ | $0.6 \times 10^5$ |

**Table 5.5.:** Photon number on target and at high harmonic generation calculated from the theoretical values of the reflectivities and assuming grating transmission of 1 % for all harmonic orders.

### 5.2.4. Overall Photon Flux

The overall photon flux is measured in the metallic filter configuration, the XUV beam is directed only on the $SiO_2$ plate and the gold mirror. We changed to a different focussing lens with a focal length of f = 1 m and a different cell with a length of 1 cm to increase the signal. In order to prevent damage on the first $SiO_2$ plate the distance between this plate and the generation chamber has been increased from 450 mm up to 550 mm. Two different aluminium filters are employed, one with a thickness of 167 $\mu$m and one with a thickness of 250 $\mu$m. The signal of the photodiode is not measured with the pico-amperemeter, but with an oscilloscope with an uptstream pre-amplifier which has a gain of 5. The signal is integrated. The photon number measured by the photodiode can then be calculated by:

$$N_{photon} = \frac{\int U dt}{5 \cdot R \cdot e \cdot \ IQE \cdot t_{Al-Filter}} \tag{5.7}$$

where $R = 50\,\Omega$ is the electrical resistance and $e$ the elementary charge. The voltage $U$ is integrated over time within the red frame as depicted in figure 5.19(a).

With the two filters in the integrated signal is 7.8 nVs. If the thinner of the two filters is removed a signal of 28.8 nVs is measured what leads to a tranmission of 0.27 for the removed filter. This value agrees well with the average transmission[4] (CXRO, 2012): $t_{Al-Filter} = \sum_{i=11}^{27} t^i_{Al_2O_3} \times t^i_{Al} \times w_i = 0.300$. Assuming that the theoretical values also hold for the thicker filter an average transmission of $t_{Al-Filter} = \sum_{i=11}^{27} t^i_{Al_2O_3} \times t^i_{Al} \times w_i = 0.242$ is taken for this filter. The weighted average value for the IQE (see table 5.6) amounts to 4.1, again taking the average of the different harmonic orders concerned. Inserting these values in equation 5.7 the measurement only with the thicker filter delivers $7.2 \times 10^8$ photons per shot. It has to be emphasized that this is only a rough estimation as the IQE of the photodiode is not very accurate in the required wavelength range and might be

[4] In the following the average values are taken between harmonic 11 and harmonic 27 considering the weight $w_i$ (see table 5.6) of each harmonic (see figure 5.19(b)). The weights are calculated by summing the signal over the individual harmonics normalized by its sum. Note that the generated harmonic orders 11 and below are completely blocked by the filter.

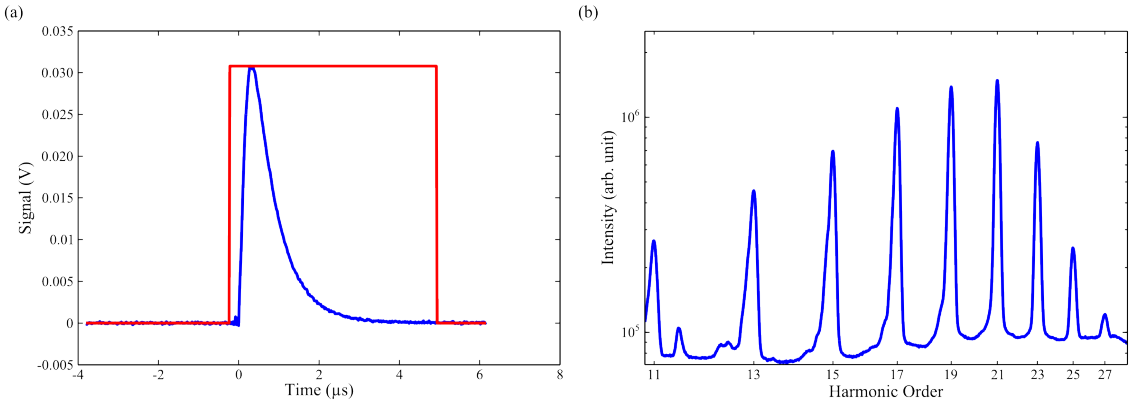


**Figure 5.19.:** (a) Oscilloscope signal (solid blue line) from the photodiode using a pre-amplifier with a gain of 5. (b) Harmonic spectrum generated in krypton in logarithmic scale measured with the Hitachi grating directly after HHG as displayed in figure 5.3.

very different from the assumed linear interpolation. Furthermore the aluminium filters clipped a part of the beam in this measurement. The on target photon number per shot after the torroidal mirror and the flat gold mirror is thus estimated to $7.6 \times 10^8$. From this result the overall photon number on target per shot is calculated to $4.2 \times 10^8$ and $1.2 \times 10^9$ at generation by taking into account the respective reflectivities of the different optical elements.

| Harmonic Order | Weights $w_i$ | Photon Number HHG | Photon Number Target |
|---|---|---|---|
| 11 (17.05 eV) | 4.6 % | $0.6 \times 10^8$ | $1.9 \times 10^7$ |
| 13 (20.15 eV) | 8.9 % | $1.1 \times 10^8$ | $3.8 \times 10^7$ |
| 15 (23.25 eV) | 13.2 % | $1.6 \times 10^8$ | $5.6 \times 10^7$ |
| 17 (26.35 eV) | 18.1 % | $2.2 \times 10^8$ | $7.7 \times 10^7$ |
| 19 (29.45 eV) | 21.3 % | $2.6 \times 10^8$ | $9.0 \times 10^7$ |
| 21 (32.55 eV) | 20.9 % | $2.5 \times 10^8$ | $8.9 \times 10^7$ |
| 23 (35.65 eV) | 10.1 % | $1.2 \times 10^8$ | $4.3 \times 10^7$ |
| 25 (38.75 eV) | 2.5 % | $0.3 \times 10^8$ | $1.0 \times 10^7$ |
| 27 (41.85 eV) | 0.4 % | $0.1 \times 10^8$ | $0.2 \times 10^7$ |

**Table 5.6.:** Photon numbers calculated from the overall photon flux on target and at high harmonic generation. The theoretical reflectivities were assumed for the respective harmonic orders and lead to the values shown above. The weights refer to the respective contribution of each harmonic compared to the overall signal (see figure 5.19).

With a laser pulse energy of 670 $\mu$J a conversion efficiency of $8.2 \times 10^{-6}$ is calculated which is higher than in the previous configuration. Increasing the focal length of lens

to 1 m and decreasing the length of the generation medium to 1 cm certainly improved the efficiency. This conversion efficiency is underestimated. Harmonic orders below 11 could not be measured and are therefore not considered. Table 5.6 illustrates the photon numbers on target and at high harmonic generation for the individual harmonics. The photon fluxes for single harmonic orders should meet the requirements of $10^7$ photons per shot on target for sufficient events per shot in the VMI.

## 5.3. Conclusion on the fs-XUV Beamline

We built a new beamline, that fulfills three different requirements. First the high harmonic spectrum can easily be imaged on the MCPs. Second the full harmonic spectrum can be used as a probe employing metallic filters for a spectral selection. Third a grating monochromator can be utilized for selecting a single harmonic. The setup has the great advantage to switch easily between the first and the two other configurations. It is however time-consuming to do this switch between the monochromator and the metallic filter configuration. A great advantage of the setup is the low cost of the grating monochromator.

| Harmonic Order | 11 | 13 | 15 | 17 | 19 | 21 | 23 | 25 | 27 | $\Delta$t (fs) |
|---|---|---|---|---|---|---|---|---|---|---|
| Berlin (Ar) | 0.9 | 1.6 | 1.4 | 1.8 | 1.6 | 1.0 | 0.7 | 0.3 | - | 120 |
| Rutherford (Ar) | 10 | 8 | 5 | 6 | 6 | 5 | 2 | 5 | - | 20 - 30 |
| Hokkaido (Ar) | - | - | 7 | 21 | 32 | 42 | 30 | 13 | 7 | 47 |
| Bordeaux (Kr) | 1.6 | 2.9 | 2.5 | 1.4 | 0.6 | - | - | - | - | $*$ |

**Table 5.7.:** Comparison of the on target photon number ($\times 10^5$) and pulse durations at different sites in monochromator configuration: Berlin (Wernet et al., 2011), Rutherford (Poletto et al., 2009; Frassetto et al., 2011) and Hokkaido (Ito et al., 2010; Igarashi et al., 2012). $*$ means that the measurement still needs to be accomplished.

Table 5.7 compares the setup to three other experiments at different sites. It is evident that the one from Bordeaux delivers the lowest on target photon flux. But we also believe that the pulse-front tilt caused by the grating monochromator will induce only a very low additional temporary pulse broadening (see table 5.1). Relatively speaking, the on target intensities are higher when drawing a comparison to the other setups due to the expected short pulses. In order to increase the harmonic flux, xenon can be utilized, it shows a stronger high harmonic generation efficiency, but has the disadvantage of being expensive. If spectral selectivity is not as important also the metallic filter configuration can be employed and thus increasing the flux by two orders of magnitude (see table 5.6).

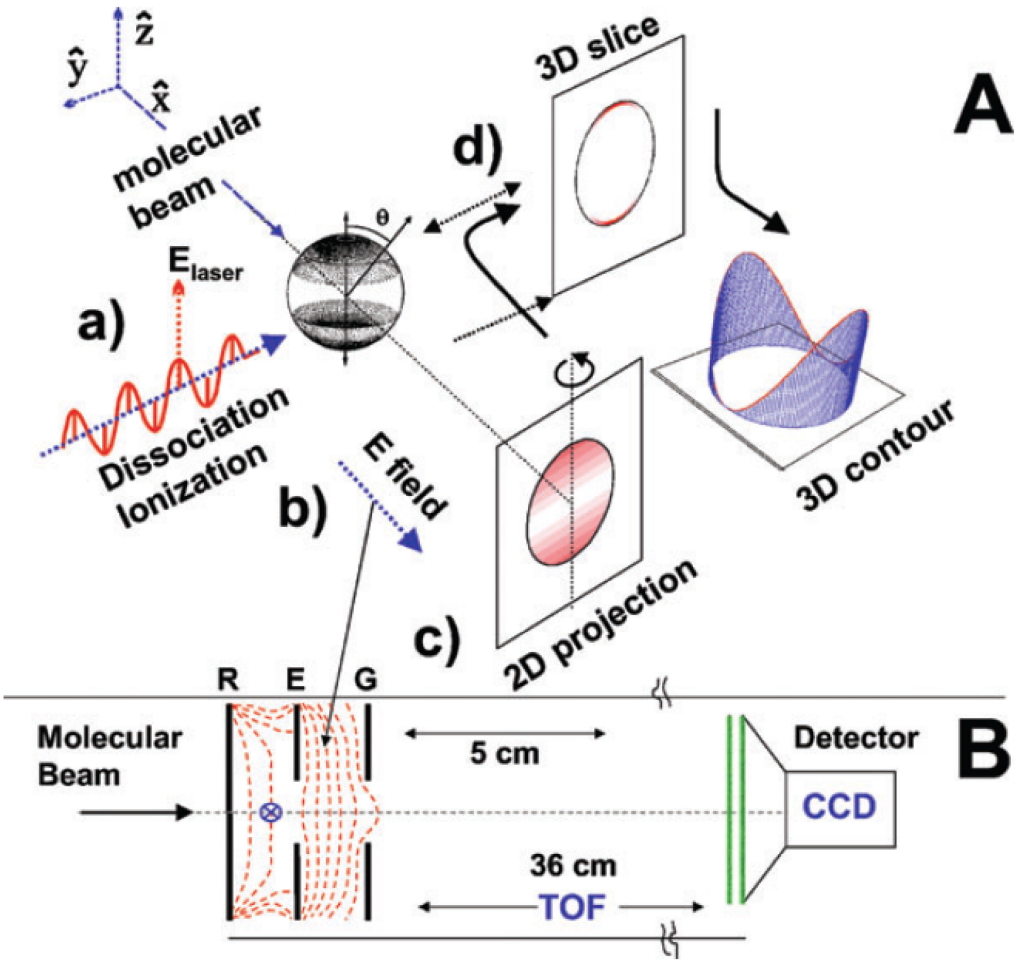


**Figure 5.20.:** A: Measurement and analysis of a Newton sphere. (a) Photoionization of molecules/atoms in a gas jet using a linearly polarized laser with the polarization direction parallel to the detector face. (b) Photofragments fly radially away forming Newton spheres. (c) Projection of the Newton sphere on a 2D surface (MCPs) by an electric field. (d) Abel transformation from a 2D image back to the 3D distribution. A slice through the center of the sphere displays the particle momentum and angular distribution. B: Layout of a VMI spectrometer in the x-y plane. The photofragments are accelerated y the repellller plate (R) towards the detector. Particles of same momentum are imaged on the same point of the detector by the electrostatic lens (E) and (G) (figure adopted from (Ashfold et al., 2005)).

## 5.4. Outlook: Velocity Map Imaging

The radial photofragment distribution after ionization has always been of interest for photochemists and was first realized by Solomon (Solomon, 1967) applying photochemical

etching inside a glass hemisphere. The next step forward followed twenty years later using ion imaging (Chandler and Houston, 1987) which also shed light on the quantitative kinetic energy of the photoproducts. This technique has been further improved through the use of an electrostatic lens (Eppink and Parker, 1997) what lead to velocity map imaging (VMI), which consitutes a state-of-the-art spectroscopy method. This paragraph shortly presents first results of the VMI technique, the PhD thesis of Handschin is recommended however for a deeper understanding and technical detail of the spectrometer built in Bordeaux (Handschin, 2012).

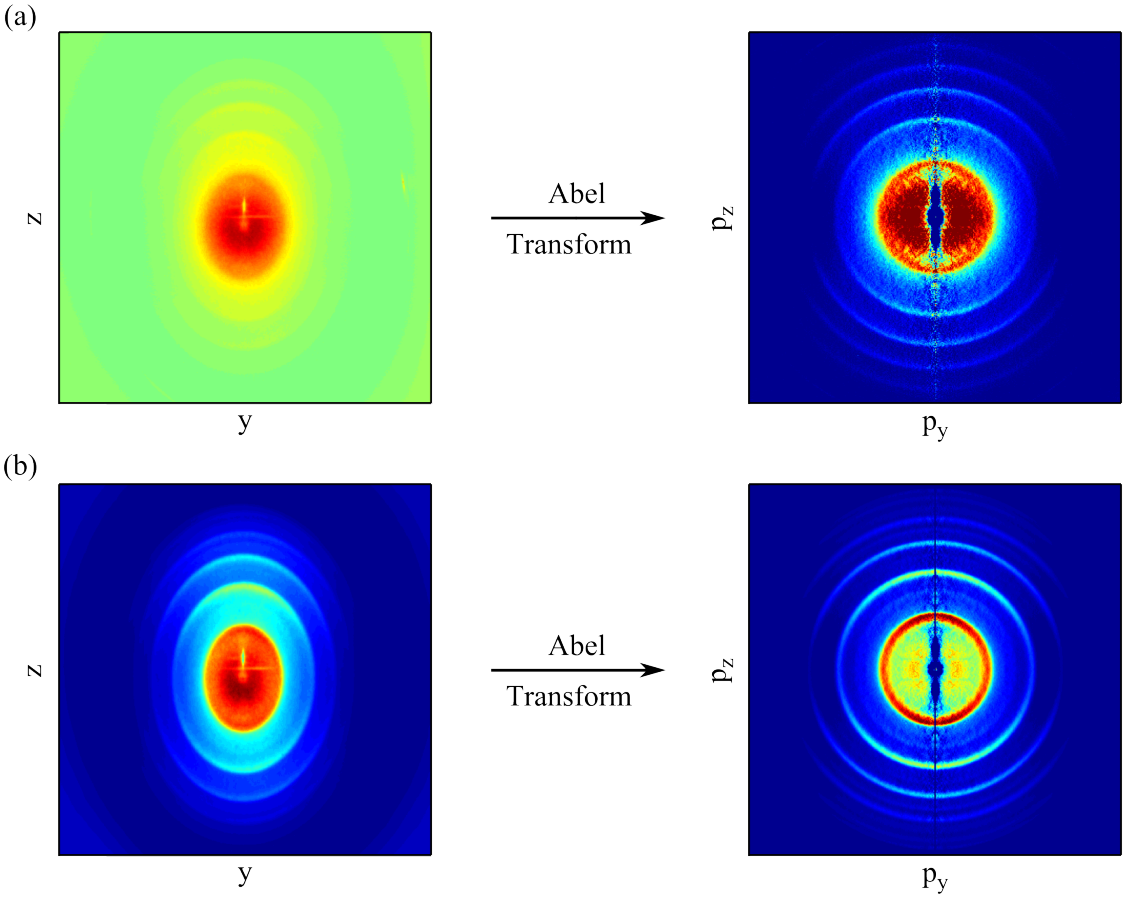


**Figure 5.21.:** (a) VMI image and its Abel transform of photoelectrons ionized by the harmonic spectrum only. (b) VMI image and its Abel transform of photoelectrons ionized by the harmonic spectrum and the fundamental laser beam at 800 nm.

### 5.4.1. First Experimental Results with the VMI Spectrometer

The basic principle of the VMI spectrometer is shortly described in figure 5.20, further details of this technique are found in the following references: (Parker et al., 2000; Chandler et al., 2003; Parker, 2000; Ashfold et al., 2005). The sample of interest, i.e. an

atom or a molecule, is photoionized by a linearly polarized laser pulse. The fragments are flying away in different directions. The sum of these fragments results in a Newton sphere, which contains ideally all the statistically averaged photofragments with different velocities. The ions or the electrons of this Newton sphere are accelerated by a repeller plate towards the two dimensional detector whose surface is parallel to the laser polarization. This corresponds to the projection of the Newton sphere onto a 2D surface. The original symmetry of the sphere allows a back transformation recovering the third dimension. This Abel inversion (Heck and Chandler, 1995) delivers the angular and kinetic momentum resolved photofragment distribution.
The type of photofragments, i.e. ions or electrons, is selected by the sign of the voltage on the repeller plate. By pulsing the detector (MCPs and phosphorscreen) particles with a certain mass are detected as a time window is selected. The time of flight $t_{TOF}$ is proportional to the square root of the fragments' mass:

$$t_{TOF} \propto d \cdot \sqrt{\frac{m}{2qU}} \tag{5.8}$$

with U the applied voltage on the repeller plate, d the flight distance between the interaction region and the detector, q the charge and m the mass of the fragment. The VMI at Bordeaux is able to resolve fragments which have a mass lower than that of protons.

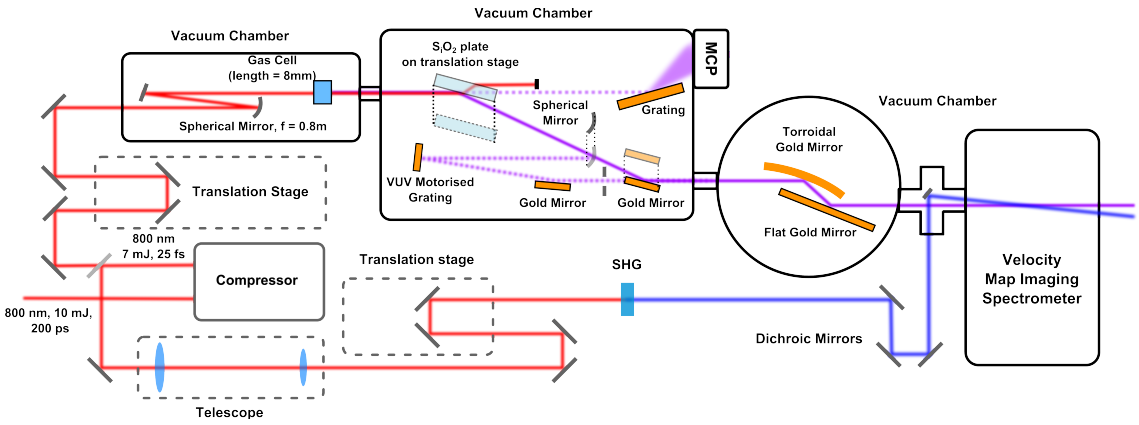


**Figure 5.22.:** Fs-VUV pump probe setup.

Figure 5.21(a) illustrates two VMI images recorded from the photoionization in argon. The Abel transform of the VMI image reveals rings. The square of the radius of these rings is proportional to the kinetic energy of the photofragments. Here a positive voltage was applied on the repeller plates what leads to the detection of photoelectrons. Thus each ring can be attributed to photoionization from a certain harmonic order. If the fundamental laser beam is not blocked by an aluminium filter, sidebands can be detected (see figure 5.21(b)). These are visible as intermediate rings.

In a next step femtosecond dynamics are resolved in a pump probe experiment, studying the photodissociation of acetylene with the VMI spectrometer. The setup of this experiment is quite elaborate, it is depicted in figure 5.22. The pump pulse centered at 400 nm excites the acetylene molecule. The probe pulse is, given by the XUV emission, triggers the photodissocation. Further details of this experiment can be found in the thesis of Handschin (Handschin, 2012).

## Résumé du Chapitre

*Jusqu'à présent les atomes et les molécules et la matière condensée ont été étudiées dans un régime d'auto sondage. Le spectre de l'émission d'harmoniques élevés provenant de la recombinaison radiative d'un électron révèle des informations structurales et dynamiques de ces systèmes. Dans ce chapitre, une autre approche est suivie pour les étudier, les photons générés par la GHOE sont utilisés pour sonder l'échantillon.*

*Avant la découverte de la GHOE seuls des tubes à décharge électronique et des synchrotrons ont été en mesure d'atteindre des énergies de photon jusqu'à plusieurs centaines d'eV. Les tubes à décharge ne parviennent pas à produire un flux de photons suffisant et les synchtrotons sont des machines très grandes et très coûteuses. La GHOE a permis d'accéder à des énergies de photons au moyen de systèmes "table-top". La GHOE permet de produire des impulsions dans la gamme microjoule (Hergott et al., 2002; Takahashi et al., 2002). Même si des flux de photons sont plus faibles que dans les synchrotrons, l'émission de la GHOE est temporellement et spatialement cohérente (Zerne et al., 1997; Bellini et al., 1998; le Déroff et al., 2000) et permet seule d'accéder à une résolution temporelle femtoseconde à attoseconde. Différents schémas expérimentaux ont été développés pour des lignes de lumière XUV utilisant des monochromateurs pour une sélection spectrale (Poletto et al., 2009; Frassetto et al., 2011; Ito et al., 2010; Igarashi et al., 2012; Wernet et al., 2011).*

*Ce dernier chapitre résume la planification, la construction et une première analyse de la ligne de lumière produite par GHOE. Un des avantages de cette ligne de lumière est la possibilité de permuter facilement entre des configurations différentes: l'imagerie spatio-spectrale du spectre harmonique sur les MCPs, la spectroscopie fs-XUV utilisant un filtre métallique pour la sélection spectrale ou la spectroscopie fs-XUV utilisant une seule harmonique sélectionnée par un monochromateur à réseau. Le flux atteint jusqu'à $9 \times 10^7$ photons par harmonique sur cible dans la configuration utilisant le filtre métallique et jusqu'à $3 \times 10^5$ photons par harmonique sur cible dans la configuration monochromateur à réseau. Dans une première expérience, la photodissociation de l'acétylène est étudiée dans un spectromètre VMI en utilisant l'émission XUV comme sonde (Handschin, 2012). Le spectromètre VMI peut également effectuer des mesures de temps de vol et donc être utilisé comme un spectromètre de masse.*

# Conclusion and future Challenges

The work presented in this manuscript was aimed at resolving electronic structure and dynamics at an Angström resolution and attosecond time scale. We especially employed high harmonic generation (HHG) in a self-probing scheme for studying the different samples of interest. Finally a XUV beamline was implemented provided by HHG. In the following a brief summary of each chapter is given, followed by an outlook on future challenges.

In a first experiment we demonstrated HHG from argon with a parametric amplifier delivering pulses at 1800 nm. We observed the Cooper minimum in argon which is well known from the total photoionization cross section. This minimum originates from the electronic structure of the argon atom. In our experiment the position of the Cooper minimum is measured at $53.8 \pm 0.7$ eV. In order to reproduce this minimum, Fabre and Pons developped a new method, classical trajectory Monte Carlo quantum electron scattering theory (CTMC-QUEST), which is based on a semiclassical approach, taking into account the core potential. With a position for the theoretical Cooper minimum of 53.7 eV this model reproduces the experimentally observed position of the minimum very well.
In another study CTMC-QUEST was applied for calculating high harmonic polarization angle at different laser ellipticities in argon (Shafir et al., 2012a). These are only in good agreement with the experimental results if the ionic potential, in particular Coulomb focussing, is considered in the recombination step. CTMC-QUEST thus proves to be a suitable approach for simulating HHG in argon, but can it also be extended to other atomic or even molecular systems? The group from Lin is using a similar approach which is already extended from atoms to molecules, but does not take the ionic core into account (Le et al., 2009). CTMC-QUEST still has to take this hurdle for the recombination step and prove its general application. CTMC-QUEST has especially one great advantage with respect to quantum calculations, it is computationally not as demanding and is thus suited to numerical calculations of larger molecules. If a similar agreement with the experiment can be established in more complex systems as in the case of argon, CTMC-QUEST will be a powerful method for the future understanding of atomic and molecular structure.

This lead us to the second experimental campaign: the study of small linear molecules, such as nitrogen and carbon dioxide. An Even-Lavie valve permits a strong alignment of the molecules, reaching an estimated rotational temperature of 5 K. Owing to the improved alignment distribution we are able to resolve new features in the high harmonic spectra as a function of alignment angle. These two molecules are good examples for demonstrating structural and dynamical effects. On the one hand we observe the shape

resonance in nitrogen, a structural feature, for the first time. It has recently been predicted by calculations of the high harmonic spectra (Jin et al., 2012). On the other hand a dynamical minimum is observed in carbon dioxide. This minimum is a result of the interference from different ionization channels. Harvey, Smirnova and Ivanov are currently performing calculations in order to reproduce the experimental results in carbon dioxide. These indicate the interplay of four channels. A dynamical minimum is also observed in the experiments performed in nitrogen. Further calculations are necessary for confirming multichannel interference in this case. Indeed only the improved alignment distribution at high gas densities delivered by the Even-Lavie valve permitted the high resolution in the alignment angle dependent measurements. We expect that this tool will not only set standards for the imaging of molecular dynamics, but also for orbital tomography.

The third chapter extends our approach to a nonlinear molecule, nitrogen dioxide, studying its photodissociation and vibronic dynamics at the crossing of a conical intersection with a sophisticated experimental method: HHG combined with transient grating spectroscopy. Two experimental campaigns were performed, the first in Ottawa and the second in Bordeaux. Photodissociation dynamics measured in the two setups agree well with each other. The vibronic dynamics, traced by an electronic fs-relaxation, were assigned in a first interpretation to the population transfer between two different potential energy surfaces (PES). The dynamics recorded in Bordeaux with higher statistics differ slightly with the experimental results from Ottawa. In order to reproduce these dynamics theoretically Halvick and coworkers performed 3D calculations based on trajectory surface hopping (TSH). HHG was then calculated from the electron wave packets provided from TSH. The simulation of HHG could only be implemented in a 1D model as the ionic potential curves and the dipole moments were not available at different stretch coordinates. Still our 1D calculation was in good agreement with our experimental result, leading to a different interpretation of the observed femtosecond transients. Oscillations of the bending wave packet and the coupling between the two PES are responsible for the fs-dynamics. An extension to a 3D model likely rules out last ambiguities of this interpretation.
Even though the Bordeaux interpretation implies that the benefit of high harmonic transient grating spectroscopy depends on the molecular system, two great advantages remain: extraction of phase information and suppression of the background signal. Ozone might be another species worth being studied by high harmonic transient grating spectroscopy. The Hartley band of ozone is responsible for the absorption of the hard UV radiation in the stratosphere. This band could be accessed by photoexcitation at 266 nm[5] leading to dissociation of ozone and the production of oxygen atoms. The challenge lies however in the availability of this gas in a sufficient quantity. One possibility is the production of ozone with generator using oxygen as a base delivering 10 % to 15 % vol.[6] of ozone. This

[5]The absorption cross section of oxygen is several order of magnitude lower at 266 nm than for ozone.
[6]Janssen from LPMAA, Paris can provide such an ozone generator.

gas mixture has to be injected then by a mechanical valve into the vacuum chamber and might explose or react during expansion into the chamber. If a sufficient quantity of ozone survives this gas expansion, high harmonic transient grating spectroscopy could be the ideal tool for tracing dissociation dynamics. First tests of the such a gas jet elucidating its composition with a time of flight spectrometer will reveal the feasibility of such an experiment.

HHG from clusters has not been extensively studied so far, only few experiments have been performed in the past. The harmonic spectrum from clusters exhibits an extended cutoff, the generation mechanism from clusters remains however debated. From an experimental point of view the difficulty consists in disentangling the harmonics produced by different species in the generation medium: monomers and clusters whose size is spread over a large distribution. A differential temperature measurement was performed and the decay rate of the harmonic signal with laser ellipticity at different average cluster sizes in the jet was studied. Owing to a 2D spatio-spectral analysis of the harmonic signal, we were able to identify the role of HHG in clusters. We assigned a recollisional recombination mechanism to HHG from clusters (cluster-to-itself): ionization from and recombination to a delocalized electron cloud in the cluster. Even the electron correlation length within such a cluster could be estimated, remember the recolliding wave packet constitutes an excellent probe with the necessary resolution. The estimation of the electron correlation length are based on a crude model. Further theoretical analysis is necessary for a deeper understanding.
Experimental results from polarimetry were ambiguous at first. Before submission of this manuscript we could confirm that linearly depolarized harmonic emission can only be observed in the presence of clusters in the gas jet. Clusters constitute a low density source which explains the very low degree of polarization of harmonic emission. As in argon atoms the polarization measurement is a sensitive probe of the high harmonic generation mechanism and is expected to give further insight, especially shedding light on the role of the ionic potential at recombination in clusters (Shafir et al., 2012a).
Further experiments are also necessary for determining other properties of HHG from clusters. In collaboration with the atto group at Saclay experiments were conducted in clusters probing the spatial coherence of high-harmonics. First measurements were performed in Saclay with the Even-Lavie valve but a strong background from scattered light on the detector prevents a decent analysis of the signal. Modifying the mount for the Even-Lavie valve and its translation stage and a better screening of scattered light will probably solve this problem. Thus the identification of HHG from clusters and atoms should be permitted and finally allow the determination of the high-harmonic spatial coherence from clusters. A lower spatial coherence as for atoms might be an indication that electron collisions inside the cluster play an important role on the attosecond time scale. The time scale of the collective motion of electrons in a plasma is on the same order of magnitude as the recollision process in HHG (Krausz and Ivanov, 2009). Thus a decrease of spatial coherence might be observed for the cluster signal which is emitted from longer

electron trajectories. These measurements might be extremely helpful for understanding collision processes that trigger nuclear fusion in clusters (Ditmire et al., 1999; Grillon et al., 2002). We also expect a different dipole phase for HHG from clusters than from atoms. A measurement as performed by Corsi and coworkers might shed light on this phase (Corsi et al., 2006). It might be possible that a different dipole phase partially contributes to a further compression of attosecond light pulses.
Clusters might also help generating high harmonics at lower intensity but higher repetition rate lasers. How is this possible? Field enhancement in metal nanostructures recently revealed carrier-envelope phase dependent electron spectra (Krüger et al., 2011). A stronger field enhancement is even expected for metallic spheres. This field enhancement should allow HHG in metal clusters at lower generation intensities. Intensities delivered by fiber lasers at megahertz repetition rate should be sufficient, with the great advantage of increasing the sampling rate. Vozzi and coworkers already attempted HHG in metal clusters at 10 Hz, but did not succeed. It seemed that the supply of a high density metal cluster jet is technically very challenging.

Last but not least the design, construction and first characterization of a XUV beamline based on HHG is presented. One advantage of this beamline is the possibilty to easily switch between different setups: spatio-spectral imaging of the high harmonic spectrum on the MCPs, fs-XUV spectroscopy using a metallic filter for spectral selection or fs-XUV spectroscopy using a single harmonic selected by a grating monochromator. The photon flux reaches up to $9 \times 10^7$ photons per harmonic on target in the metallic filter configuration and up to $3 \times 10^5$ photons per harmonic on target in the grating monochromator configuration. In a first experiment the photodissociation of acetylene is studied in a VMI spectrometer using the XUV-light as a probe (Handschin, 2012). The VMI specrometer can also perform time of flight measurements and can thus be used as a mass spectrometer.
The VMI spectrometer might especially be helpful for analyzing the ingredients of gas jets. The cluster size distribution and atom to cluster ratio in such a jet might be estimated. After ionization the clusters would need to hit the detector before dissociation. This difficulty might prevent a reasonable measurement. Another application might be the characterization of the ozone to oxygen ratio in the gas jet, which is supplied by a gas mixture from an ozone generator. This test is inevitable for continuing further experiments in such a jet. From a femtochemist's point of view there exist numerous other molecules that are worth being studied in the VMI spectrometer.

# A. The ABCD Matrix Formalism

The layout of the chamber and the optical propagation is based on the ABCD matrix formalism. Within the context of this formalism the propagtion of light rays is described by transfer matrices (Kogelnik and Li, 1966; Milonni and Eberly, 1988; Fowles, 1989; Ruf, 2008). The strength of this formalism is that it can be transferred from paraxial rays to Gaussian beams. Paraxial rays are rays which have only a small angle $x_2$ to the optical axis and therefore fulfill the following conditions well enough: $x_2 \approx \sin x_2 \approx \tan x_2$. A ray is fully characterized by its location and angle towards the optical axis (see figure A.1).

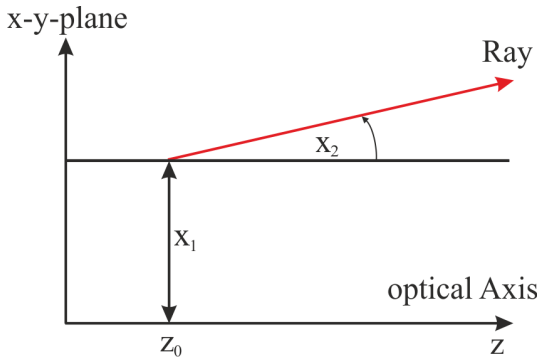


**Figure A.1.:** A ray is fully characterized at the point $z_0$ by the two parameters $x_1$ and $x_2$.

When putting an optical element in the beam path, these parameters are changed. In the paraxial approximation all ray transfomations are linear and can therefore conveniently be described by the transfer matrix notation:

$$\begin{bmatrix} x^2 \\ y^2 \end{bmatrix} = \begin{bmatrix} A & B \\ C & D \end{bmatrix} \begin{bmatrix} x^1 \\ y^1 \end{bmatrix} \tag{A.1}$$

with $x_1$ and $y_1$ the ray parameters before passing the optical element and $x_2$ and $y_2$ the ray parameters after passing the optical element. The optical element itself is displayed by the ABCD transfer matrix. This formalism allows the calculation of the beam propagation in terms of geometrical optics. Some examples of transfer matrices are depicted in table A.1.

The knowledge of the transfer matrices of optical elements is the condition for calculating the propagation of the beam in the vacuum chamber. When combining $n$ optical elements the propagtion is calulated by multiplication of the matrices $\mathbf{M_1}$,$\mathbf{M_2}$,...,$\mathbf{M_n}$. Since multiplication of transfer matrices is not commutative the order has to be considered. The final matrix $\mathbf{M}$ combining all optical elements has the following form:

| Optical Element | Transfer Matrix | Comment |
|---|---|---|
| free path | $\begin{bmatrix} 1 & d \\ 0 & 1 \end{bmatrix}$ | $d \mathrel{\widehat{=}}$ covered distance |
| thin lens | $\begin{bmatrix} 1 & 0 \\ -\frac{1}{f} & 1 \end{bmatrix}$ | $f \mathrel{\widehat{=}}$ focal length |
| curved dielectric element | $\begin{bmatrix} 1 & 0 \\ \frac{1}{r}\left(\frac{n_1}{n_2}-1\right) & \frac{n_1}{n_2} \end{bmatrix}$ | $r \mathrel{\widehat{=}}$ radius of curvature<br>$n_1$,$n_2 \mathrel{\widehat{=}}$ index of refraction |

**Table A.1.:** Examples of different transfer matrices.

$$\mathbf{M} = \begin{bmatrix} A & B \\ C & D \end{bmatrix} = \begin{bmatrix} A_n & B_n \\ C_n & D_n \end{bmatrix} \cdot \ldots \cdot \begin{bmatrix} A_2 & B_2 \\ C_2 & D_2 \end{bmatrix} \cdot \begin{bmatrix} A_1 & B_1 \\ C_1 & D_1 \end{bmatrix} \tag{A.2}$$

This formalism has to be translated to Gaussian beams. To simplify matters the electric field is not treated vectorially, polarization effects shall be neglected. Also the time dependence is left out and a position-dependent field in vacuum is described by the scalar wave equation. In the regime of linear optics the electric field form can be written by means of the superposition principle, namely the sum of monochromatic light with differing wave vectors $\vec{k}$. The Helmoltz-equation describes such a monochromatic light field:

$$(\nabla^2 + k^2)E(\vec{r}) = 0 \tag{A.3}$$

Two prominent solutions are described either by a plane wave or by a speherical wave (Milonni and Eberly, 1988). Both solutions do not describe a laser beam very well due to their infinite extension. Therefore the following Ansatz is made:

$$E(\vec{r}) = E_0(\vec{r})e^{ikz} \tag{A.4}$$

It is assumed that the amplitude $E_0$ of the electric field only varies slowly in z-direction with respect to the wavelength. The field is thus considered in the paraxial equation what applies very well for laser beams. Within this approximation the paraxial wave equation describes the electric field:

$$\left(\frac{\partial^2}{\partial x^2} + \frac{\partial^2}{\partial y^2}\right)E_0(\vec{r}) + 2ik\frac{\partial E_0(\vec{r})}{\partial z} = 0 \tag{A.5}$$

The easiest solution of the equation A.5 having a Gaussian profile is the following (Milonni and Eberly, 1988):

$$E_0(\vec{r}) = A\, e^{ik(x^2+y^2)/2q(z)}\, e^{ip(z)} \tag{A.6}$$

with A the the electric field amplitude and the complex parameters q(z) and p(z):

$$\frac{1}{q(z)} = \frac{1}{R(z)} + \frac{i\lambda}{\pi w^2(z)}$$

$$e^{ip(z)} = \frac{1}{1 + iz/z_0}$$

$$R(z) = z + \frac{z_0^2}{z}$$

$$w(z) = w_0\sqrt{1 + z^2/z_0^2} \tag{A.7}$$

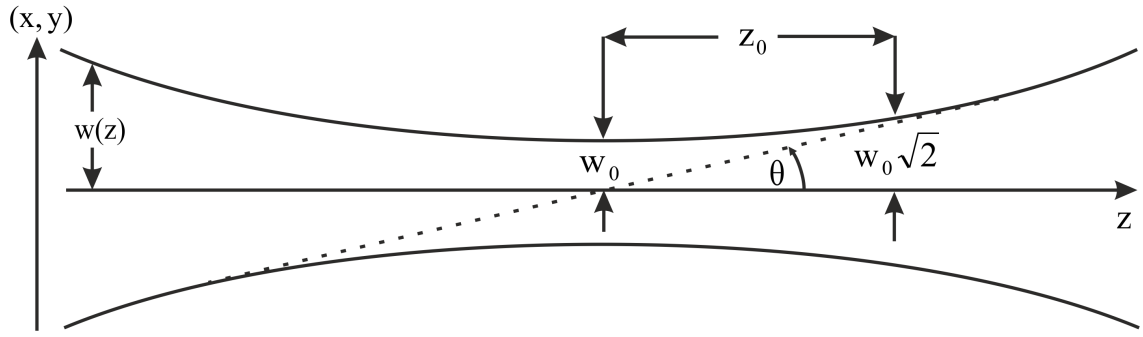


**Figure A.2.:** Propagation of the Gaussian beam around its waist $w_0$, indicating the Rayleigh-length and the divergence angle.

The beam propagation (see figure A.2) is thus completely determined by the wavelength $\lambda$ and the Rayleigh-length $z_0 = \pi w_0^2/\lambda$. $R(z)$ denotes the radius of curvature being infinty at the focal point $z_0$. The shorter the Rayleigh-length, the more important the divergence angle $\theta$. The beam radius $w(z)$ is defined as the distance to the optical axis which correponds to an intensity of $1/e^2 \approx 13.5\,\%$ of the maximal value on axis. The beam waist $w_0$ is the beam radius at the focal point $z_0$.
At a position $z$ a Gaussian beam is fully described by its phase, the electric field amplitude $A$, the radius of curvature $R$ and the beam radius $w$. Both the radius of curvature $R$ and the beam radius $w$ are connected to the complex beam parameter $q(z)$ which itself is modified through an optical element by the ABCD-matrix as follows (Milonni and Eberly, 1988):

$$q_f = \frac{Aq_i + B}{Cq_i + D} \tag{A.8}$$

with A,B,C and D the matrix elements. $q_i$ and $q_f$ are respectively the complex beam parameters before and after the propagation through the optical system.
There also exist other solutions to the paraxial wave equation A.5 that can be described by spherical symmetric Laguerre-Gaussian functions or Hermite-Gaussian functions $H_{mn}$ of $m^{th}$ or $n^{th}$ order (Kogelnik and Li, 1966). The transverse modes of higher orders are also labelled as $TEM_{mn}$-modes of the electric field. In case of the Hermite polynomials the order of $TEM_{mn}$-modes assigns the number of knots in the x-y directions.
Consider that under experimental conditions beam profiles appear often Gaussian-like but cannot be described by a perfect Gaussian mode $TEM_{00}$. Such profiles are mixtures of higher transverse order modes. The beam quality factor $M^2$ characterizes the mode purity of $TEM_{00}$ beams. The divergence angle of a Gaussian beam can therewith be redefined by a higher divergence angle (Eichler et al., 2004):

$$\theta = M^2 \frac{\lambda}{\pi w_0} \tag{A.9}$$

If $M^2 = 1$ is fulfilled only the ground mode is present but with $M^2 > 1$, the beam profile will contain higher order transverse modes. The beam profile of the XUV-beam certainly depends on the generating conditions. For ideal refocussing in the VMI only harmonics produced by the short trajectory electrons are desirable. A measurement of the beam quality factor under vacuum would need a setup of its own, but is feasible for the future. In the following a perfect Gaussian mode with $M^2$ is assumed, which gives at least lowest limits for refocussing conditions.
The focussing in the vacuum chamber (see chapter 5) is done by a spherical or a torroidal mirror which has a focal distance defined by half the radius of curvature of the mirrors. Only a focal spot with a symmetric shape on target ensures highest possible intensities. A spherical mirror will always introduce astigmatism if the angle of incidence (AOI) is not zero. In the same way a torroidal mirror is only designed for a certain angle, mostly an obtuse one. However a spherical mirror can still be used under different AOIs if aberration is not too high. With an AOI of $\gamma$ the effective focal distances are given for the sagittal and tangential plane (Hanna, 1969):

$$f_{sag.} = f/\cos(\gamma)$$

$$f_{tan.} = f \cdot \cos(\gamma) \tag{A.10}$$

The sagittal (tangential) plane is perpendicular (parallel) to the plane of incidence[1] of the mirror. For a spherical mirror with $\gamma \neq 0$ one expects the sagittal focal length always to be longer than tangential focal length. A torroidal mirror has two different radii of curvature for the sagittal and tangential plane and can therewith be adapted for a well defined AOI.

[1] The plane of incidence is the plane spanned by the propagation vectors of incoming and outgoing radiation.

# B. Intensity at Focus in High Harmonic Generation

Determination of the intensity at focus in high harmonic generation is challenging. The laser intensity of high harmonic generation is obtained by the cutoff from a spectrum in rare gases (see equation 1.26). Why can this intensity not be estimated by measuring the pulse energy and calculating waist at the focus? Here is an example.

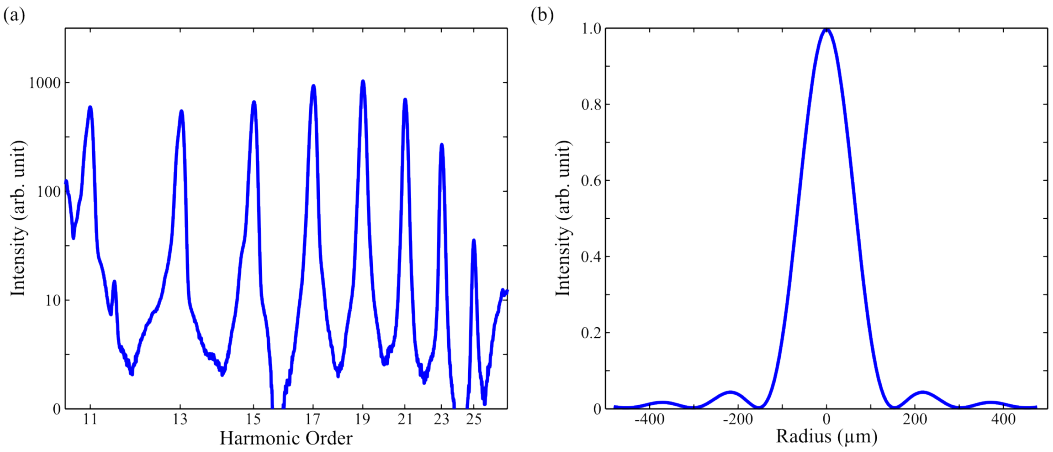


**Figure B.1.:** (a) High harmonic spectrum in Krypton. (b) Fourrier transform of Gaussian beam with a diameter of 19.5 mm ($1/e^2$) cut by an iris with a diameter of 6.1 mm.

Figure B.1(a) shows a spectrum generated in krypton. The cutoff is at harmonic 21 what corresponds to an intensity of $1.1 \times 10^{14}\,\mathrm{W/cm^2}$. The energy of 1.95 mJ per pulse is reduced to 0.89 mJ after the iris (d = 6.1 mm) and then focussed by a lens with focal distance $f = 80\,\mathrm{cm}$. A beam propagation factor of $M^2 = 1.5$ has been measured for the laser beam. The Fourrier transform of this clipped Gaussian beam gives the shape of the beam at focus which is illustrated in figure B.1(b). 91.6% of the energy remains in the central part, 8.4% of the energy is lost in the wings. The Gaussian fit of the central part gives a waist of 115 $\mu$m. Assuming that HHG scales with $I^4$ (Wahlström et al., 1993), a waist of 57.5 $\mu$m is taken for the XUV beam.
For calculating the maximum intensity $I_{max}$ of the beam, the beam profile, expressed as a function of spatial and temporal parameters needs to be calculated. Assuming a radial beam symmetry the following relationship between power and maximum intensity can be established in radial coordinates:

$$P = \int_0^\infty \int_0^{2\pi} r e^{-2r^2/w^2} dr d\varphi = \frac{\pi}{2} w^2 I_{max} \tag{B.1}$$

The maximum intensity can be calculated similarly as a function of pulse duration $\Delta T$ (FWHM). With a pulse profile of $I(t) = I_{max}e^{-t^2/t_0^2}$ and $t_0 = \Delta T/\sqrt{4ln2}$ the fluence $F$ can be expressed in terms of the maximum intensity:

$$F = \int_{-\infty}^{\infty} I_{max}e^{-t^2/t_0^2}dt = I_{max}\sqrt{\pi}t_0 \tag{B.2}$$

With a pulse duration of $\Delta T = 25\,\text{fs}$ a maximum intensity of $5.9 \times 10^{14}\,\text{W/cm}^2$ is found which is clearly higher than the maximum intensity derived from the cutoff. First of all a perfect phasefront is assumed in the calculation, what is not true. Approximately 50% of the beam energy is lost additionally in the wings due to the imperfect phase front. Another factor that needs to be considered: The intensity of $1.1 \times 10^{14}\,\text{W/cm}^2$ needs to be reached in a certain volume of the generation medium. This condition can only be fulfilled if the center intensity exceeds the cutoff intensity.
This example clearly shows that a pure simulation of the laser intensity at focus does not work if phase front and effective interaction volume for HHG are unknown.

# C. Calibration of the Microchannel Plates

The gain of the MCPs as a function of voltage is established in this appendix. Even the absolute photon number could be extracted from the signal obtained by the MCPs. A measurement on the MCPs and the photodiode would need to be done synchronously. This is possible with the setup presented in chapter 5, but there is one circumstance which prevents such a measurement. The objective and the camera which images the phosphor screen behind the MCPs must never be touched again for maintaining the same image size as for the calibration measurement. However the voltage scaling with photonnumber is an important information for the experiment. The established scaling law is independent of harmonic order.

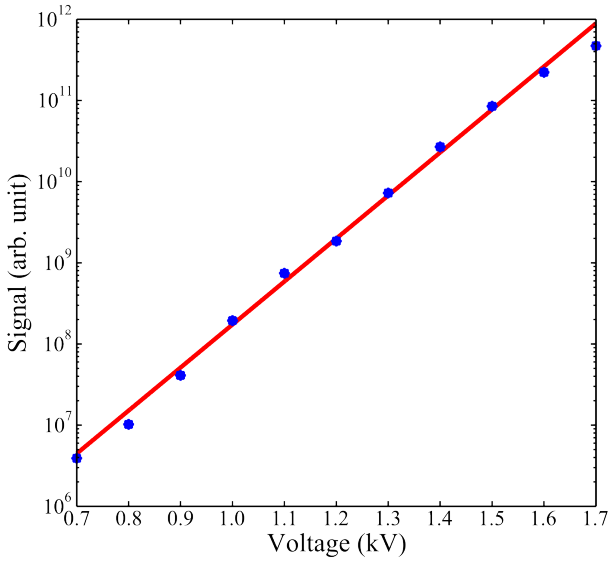


**Figure C.1.:** Signal of harmonic 13 (blue dots) in logarithmic scale as a function of MCP voltage with the fitted logarithmic scaling law (red solid line).

Figure C.1 illustrates the measured harmonic signal as a function of applied MCP voltage $U_{MCP}$. The measured values show a very good agreement with a logarithmic scaling law:

$$S_{Harm} = 869 \times 10^{5.3 U_{MCP}} \tag{C.1}$$

The harmonic signal is given as a function of MCP voltage in kV. This formula allows us to make a comparison between signals taken at different MCP voltages.

# Bibliography


Abrines, R. and Percival, I. C. (1966). Classical theory of charge transfer and ionization of hydrogen atoms by protons. *Proc. Phys. Soc.*, 88:861.

Agostini, P., Fabre, F., Mainfray, G., Petite, G., and Rahman, N. K. (1979). Free-free transitions following six-photon ionization of xenon atoms. *Phys. Rev. Lett.*, 42(17):1127–1130.

Akagi, H., Arissian, L., Bertrand, J. B., Corkum, P. B., Gertsvolf, M., Pavicic, D., Rayner, D. M., Smeenk, C., Staudte, A., Villeneuve, D. M., and Wörner, H. J. (2009). An STM for Molecules and Wide-Bandgap Crystal. *Laser Physics*, 19:1697.

Ammosov, M. V., Delone, N. B., and Krainov, V. P. (1986). Tunnel ionization of complex atoms and of atomic ions in an alternating electromagnetic field. *Sov. Phys. JETP*, 64:1191.

Antoine, P., Carré, B., L'Huillier, A., and Lewenstein, M. (1997). Polarization of high-order harmonics. *Phys. Rev. A*, 55(2):1314.

Antoine, P., L'Huillier, A., and Lewenstein, M. (1996). Attosecond Pulse Trains Using High-Order Harmonics. *Phys. Rev. Lett.*, 77(7):1234–1237.

Arasaki, Y. and Takatsuka, K. (2007). Quantum wavepacket dynamics for time-resolved photoelectron spectroscopy of the $NO_2$ conical intersection. *Chem. Phys.*, 338:275.

Arasaki, Y., Takatsuka, K., Wang, K., and McKoy, V. (2010). Time-resolved photoelectron spectroscopy of wavepackets through a conical intersection in $NO_2$. *J. Chem. Phys.*, 132:124307.

Arefiev, A. V., Gao, X., Tushentsov, M. R., Wang, X., Shim, B., Breizman, B. N., and Downer, M. C. (2010). Size distribution and mass fraction of microclusters in laser-irradiated plasmas. *High Energy Density Physics*, 6:121.

Ashfold, M. N. R., Nahler, N. H., Orr-Ewing, A. J., Vieuxmaire, O. P. J., Toomes, R. L., Kitsopoulos, T. N., Garcia, I. A., Chestakov, D. A., Wu, S.-M., and Parker, D. H. (2005). Imaging the dynamics of gas phase reactions. *Phys. Chem. Chem. Phys.*, 8:26.

Ashkin, A., Boyd, G. D., and Dziedzic, J. M. (1963). Observation of Continuous Optical Harmonic Generation with Gas Masers. *Phys. Rev. Lett.*, 11:14.

Augst, S., Strickland, D., ans S. Chin, D. M., and Eberly, J. (1989). Tunneling ionization of noble gases in a high intensity laser field. *Phys. Rev. Lett.*, 63:2212.

Balazs, N. L. and Voros, A. (1990). Wigner's function and tunneling. *Ann. Phys.*, 199:123.

Balcou, P., Salières, P., L'Huillier, A., and Lewenstein, M. (1997). Generalized phase-matching conditions for high harmonics: The role of field-gradient forces. *Phys. Rev. A*, 55(4):3204–3210.

Bandrauk, A. D. and Yu, H. (1999). High-order harmonic generation by one- and two-electron molecular ions with intense laser pulses. *Phys. Rev. A*, 58:1.

Beijerinck, H. and Verster, N. (1981). Absolute Intensities and Perpendicular Temperatures of Supersonic Beams of Polyatomic Gases. *Physica B & C*, 111:327.

Bellini, M., Lynga, C., Tozzi, A., Gaarde, M. B., Hänsch, T. W., L'Huillier, A., and Wahlstrom, C.-G. (1998). Temporal Coherence of Ultrashort High-Order Harmonic Pulses. *Phys. Rev. Lett.*, 81(2):297–300.

Bertrand, J. B., Wörner, H. J., Bandulet, H.-C., Bisson, E., Spanner, M., Kieffer, J.-C., Villeneuve, D. M., and Corkum, P. B. (2011). Ultrahigh-Order Wave Mixing in Noncollinear High Harmonic Generation. *Phys. Rev. Lett.*, 106(2):023001.

Björneholm, O., Federmann, F., Fössing, F., and Möller, T. (1995). Core Level Photoelectron and X-Ray Absorption Spectroscopy of Free Argon Clusters: Size-Dependent Energy Shifts and Determination of Surface Atom Coordination. *Phys. Rev. Lett.*, 74:3017–3020.

Björneholm, O., Federmann, F., Fössing, F., Möller, T., and P., S. (1996). Core level binding energy shifts and polarization screening: A combined experimental and theoretical study of argon clusters. *J. Chem. Phys.*, 104:5.

Blaga, C. I., Xu, J., DiChiara, A. D., Sistrunk, E., Zhang, K., Agostini, P., Miller, T. A., DiMauro, L. F., and Lin, C. D. (2012). Imaging ultrafast molecular dynamics with laser-induced electron diffraction. *Nature*, 483:194.

Blanchet, V., Zgierski, M. Z., Seideman, T., and Stolow, A. (1999). Discerning vibronic molecular dynamics using time-resolved photoelectron spectroscopy. *Nature*, 401:52–54.

Bödefeld, R., Theobald, W., Schreiber, J., Gessner, H., Welsch, E., Feurer, T., and Sauerbrey, R. (2010). Damage threshold measurements of gold and dielectric coated optical components at 50 fs - 5 ns. Technical report, Universität Jena.

Bohr, N. (1913). On the constitution of atoms and molecules. *Philosophical Magazine*, 26:1.

Born, M. and Wolf, E. (1991). *Principles of Optics*. Pergamon Press.

Botheron, P. and Pons, B. (2009). One-electron atom in a strong and short laser pulse: Comparison of classical and quantum descriptions. *Phys. Rev. A.*, 80:023402.

Boullet, J., Zaouter, Y., Limpert, J., Petit, S., Mairesse, Y., Fabre, B., Higuet, J., Mével, E., Constant, E., and Cormier, E. (2009). High-order harmonic generation at a megahertz-level repetition rate directly driven by an ytterbium-doped-fiber chirped-pulse amplification system. *Opt. Lett.*, 34:1489.

Boyd, R. W. (1992). *Nonlinear Optics*. Academic Press.

Brumer, P. and Shapiro, M. (1989). One photon mode selective control of reactions by rapid or shaped laser pulses: An emperor without clothes? *Chem. Phys.*, 139:221.

Buck, U. and Krohne, R. (1996). Cluster size determination from diffractive He atom scattering. *J. Chem. Phys.*, 105:5408.

Busani, R., Folkers, M., and Cheshnovsky, O. (1998). Direct Observation of Band-Gap Closure in Mercury Clusters. *Phys. Rev. Lett.*, 81:3836–3839.

Campargue, R. (1983). Progress in Overexpanded Supersonic Jets and Skimmed Molecular Beams in Free-Jet Zones of Silence. *J. Chem. Phys.*, 88:4466.

Carnovale, F., Peel, J. B., and Rothwell, R. (1991). Photoelectron spectroscopy of krypton and xenon clusters. *J. Chem. Phys.*, 95:3.

Cha, C. Y., Ganteför, G., and Eberhard, W. (1993). Photoelectron spectroscopy of $Cu_n^-$ clusters: Comparison with jellium model predictions. *J. Chem. Phys.*, 99:6308.

Chan, W. F., Cooper, G., Guo, X., Burton, G. R., and Brion, C. E. (1992). Absolute optical oscillator strengths for the electronic excitation of atoms at high resolution: the photoabsorption of argon, krypton, and xenon. *Phys. Rev. A*, 46:149.

Chandler, D. W., Chichinin, A. I., Einfeld, T. S., Eppink, A. T. J. B., Gericke, K.-H., Heber, O., Helm, H., Houston, P. L., Kitsopoulos, T. N., Lorenz, K. T., Maul, C., Müller, U., Parker, D. H., Rakitzis, T. P., Springfield, J. L., Strasser, D., Suzuki, T., Wade, E. A., Whitaker, B. J., Wu, S.-M., and Zajfman, D. (2003). *Imaging in Molecular Dynamics*. Cambridge University Press.

Chandler, D. W. and Houston, P. L. (1987). Two-dimensional imaging of State-Selected Photodissociation Products by Multiphoton ionizaiton. *J. Chem. Phys.*, 87:1445.

Chang, Z. (2011). *Fundamentals of Attosecond Optics*. CRC Press, Taylor & Francis Group.

Chen, Y.-M., Hsu, M.-Y., Hsieh, Y.-H., Lin, J.-Y., Wang, J., and Chen, S.-Y. (2007). Enhancement of high-harmonic generation by laser-induced cluster vibration. *Opt. Lett.*, 32:2714.

Cireasa, R., Hamard, J.-B., Maury, C., and Blanchet, V. (2009). Imaging fast relaxation dynamics of $NO_2$. *Phys. Scr.*, 80:048106.

Clementi, E., Raimondi, D. L., and Reinhardt, W. P. (1967). Atomic Screening Constants from SCF Functions. II. Atoms with 37 to 86 Electrons. *J. Chem. Phys.*, 47:1300.

Cohen-Tannoudji, C., Diu, B., and Laloe, F. (1996). *Mécanique Quantique II*. Hermann, éditeurs des sciences et des arts.

Cohen-Tannoudji, C., Diu, B., and Laloe, F. (1998). *Mécanique Quantique I*. Hermann, éditeurs des sciences et des arts.

Constant, E., Garzella, D., Breger, P., Mével, E., Dorrer, C., Blanc, C. L., Salin, F., Agostini, P., and Carré, B. (1999). Optimizing High Harmonic Generation in Absorbing Gases: Model and Experiment. *Phys. Rev. Lett.*, 82:1668.

Cooper, J. W. (1962). Photoionization from outer atomic subshells. A model study. *Phys. Rev.*, 128:681.

Corkum, P. B. (1993). Plasma perspective on strong field multiphoton ionization. *Phys. Rev. Lett.*, 71(13):1994.

Corsi, C., Pirri, A., Sali, E., Tortora, A., and Bellini, M. (2006). Direct Interferometric Measurement of the Atomic Dipole Phase in High-Order Harmonic Generation. *Phys. Rev. Lett.*, 97:023901.

CXRO (2012). Center for X-Ray Optics. *http://www-cxro.lbl.gov/*.

Danil'chenko, A. G., Kovalenko, S. I., and Samovarov, V. N. (2009). Cluster formation in supersonic $CO_2$ and $CO_2$-Kr jets. *Low Temp. Phys.*, 35:12.

de Aldana, J. R. V. and Roso, L. (2001). High-order harmonic generatin in atomic clusters with a two-dimensional model. *J. Opt. Soc. Am. B*, 18:325.

de Broglie, L. (1923). Ondes et quanta. *Comptes rendus*, 177:507.

de Nalda, R., Heesel, E., Lein, M., Hay, N., Velotta, R., Springate, E., Castillejo, M., and Marangos, J. P. (2004). Role of orbital symmetry in high-order harmonic generation from aligned molecules. *Phys. Rev. A*, 69:031804.

Depret, M. (2010). Studying optical properties of a flat-field grating with variable line spacing. Technical report, Commissariat à l'Énergie Atomique.

Dietrich, P., Burnett, N., Ivanov, M., and Corkum, P. B. (1994). High-harmonic generation and correlated two-electron multiphoton ionization with elliptically polarized light. *Phys. Rev. A*, 50:3585.

Dillon, A. C., Jones, K. M., Bekkedahl, T. A., Kiang, C. H., Bethune, D. S., and Heben, M. J. (1997). Storage of hydrogen in single-walled carbon nanotubes. *Nature*, 386:377–379.

Ditmire, T., Zweiback, J., Yanovsky, V., Cowan, T., Hays, G., and Wharton, K. (1999). Nuclear fusion from explosions of femtosecond laser-heated deuterium clusters. *Nature*, 398:489.

Diveki, Z., Camper, A., Haessler, S., Auguste, T., Ruchon, T., Carré, B., Salières, P., Guichard, R., Caillat, J., Maquet, A., and Taïeb, R. (2012). Spectrally resolved multichannel contributions to the harmonic emission in $N_2$. *New J. Phys.*, 14:023062.

Dodge, M. J. (1984). Refractive properties of magnesium fluoride. *Appl. Opt.*, 23:1980.

Donnelly, T. D., Ditmire, T., Neuman, K., Perry, M. D., and Falcone, R. W. (1996). High-Order Harmonic Generation in Atom Clusters. *Phys. Rev. Lett.*, 76:2472–2475.

Dooley, P. W., Litvinyuk, I. V., Rayner, K. F. L. D. M., Spanner, M., Villeneuve, D. M., and Corkum, P. B. (2003). Direct imaging of rotational wave-packet dynamics of diatomic molecules. *Phys. Rev. A*, 68:023406.

Dorchies, F., Blasco, F., Caillaud, T., Stevefelt, J., Stenz, C., Boldarev, A. S., and Gasilov, V. A. (2003). Spatial distribution of cluster size and density in supersonic jets as targets for intense laser pulses. *Phys. Rev. A*, 68:023201.

Dorchies, F., Caillaud, T., Blasco, F., Bonté, C., Jouin, H., Micheau, S., Pons, B., and Stevefelt, J. (2005). Investigation of laser-irradiated Ar cluster dynamics from K-shell x-ray emission measurements. *Phys. Rev. E*, 71:066410.

Doyle, J. P. K. and Calvo, F. (2002). Entropic effects on the structure of Lennard-Jones clusters. *J. Chem. Phys.*, 116:19.

Dudovich, N., Levesque, J., Smirnova, O., Zeidler, D., Comtois, D., Ivanov, M. Y., Villeneuve, D. M., and Corkum, P. B. (2006). Attosecond Temporal Gating with Elliptically Polarized Light. *Phys. Rev. Lett.*, 97:253903.

Echt, O., Sattler, K., and Recknagel, E. (1981). Magic Numbers of Sphere Packings: Experimental Verification in Free Xenon Clusters. *Phys. Rev. Lett.*, 47:16.

Eichler, J., Dünkel, L., and Eppick, B. (2004). Die Strahlqualität von Lasern. *LTJ*, 2:63.

Eppink, A. and Parker, D. (1997). Velocity map imaging of ions and electrons using electrostatic lenses: Application in photoelectron and photofragment ion imaging of molecular oxygen. *Rev. Sci. Instrum.*, 68:3477.

Farges, J., de Feraudy, M. F., Raoult, B., and Torchet, G. (1983). Noncrystalline structure of argon clusters. I. Polyicosahedral structure of $Ar_n$ clusters, 20<N<50. *J. Chem. Phys.*, 84:6.

Farges, J., de Feraudy, M. F., Raoult, B., and Torchet, G. (1986). Noncrystalline structure of argon clusters. II. Multilayer icosahedral structure of $Ar_n$ clusters 50<N<750. *J. Chem. Phys.*, 84:6.

Farges, J., Feraudy, M. F. D., Raoult, B., and Torchet, G. (1981). Structure and Temperature of Rare Gas Clusters in a Supersonic Expansion. *Surface Science*, 106:95.

Farrell, J. P., Spector, L. S., McFarland, B. K., Bucksbaum, P. H., and Gühr, M. (2011). Influence of phase matching on the Cooper minimum in Ar high-order harmonic spectra. *Phys. Rev. A*, 83:023420.

Feifel, R., Tchaplyguine, M., Öhrwall, G., Salonen, M., Lundwall, M., Marinho, R. R. T., Gisselbrecht, M., Sorensen, S. L., de Brito, A. N., Karlsson, L., Martensson, N., Svensson, S., and Björneholm, O. (2004). From localised to delocalised electronic states in free Ar, Kr and Xe clusters. *Eur. Phys. J. D*, 30:343–351.

Feng, X., Gilbertson, S., Mashiko, H., Wang, H., Khan, S. D., Chini, M., Wu, Y., Zhao, K., and Chang, Z. (2009). Generation of Isolated Attosecond Pulses with 20 and 28 Femtosecond Lasers. *Phys. Rev. Lett.*, 103:183901.

Ferrari, F., Calegari, F., Lucchini, M., Vozzi, C., Stagira, S., Sansone, G., and Nisoli, M. (2010). High-energy isolated attosecond pulses generated by above-saturation few-cycle fields. *Nature Photonics*, 4:875.

Ferray, M., L'Huillier, A., Li, X. F., Lompré, L. A., Mainfray, G., and Manus, C. (1988). Multiple-harmonic conversion of 1064 nm radiation in rare gases. *J. Phys. B*, 21:L31.

Fittinghoff, D. N., Bolton, P. R., Chang, B., and Kulander, K. C. (1992). Observation of Nonsequential Double Ionization of Helium with Optical Tunneling. *Phys. Rev. Lett.*, 69:2642.

Fork, R., Cruz, C. B., Becker, P. C., and Shank, C. V. (1987). Compression of optical pulses to six femtoseconds by using cubic phase compensation. *Opt. Lett.*, 12:483.

Fort, E., Pradère, F., Martino, A. D., Vach, H., and Châtelet, M. (1997). Diagnostics of mixed van der Waals clusters. *Eur. Phys. J. D*, 1:79.

Fowles, G. R. (1989). *Introduction to Modern Optics*. Dover Publications.

Franken, P. A., Hill, A. E., Peters, C. W., and Weinreich, G. (1961). Generation of Optical Harmonics. *Phys. Rev. Lett.*, 7:118.

Frassetto, F., Cacho, C., Froud, C. A., Turcu, I. E., Villoresi, P., Bryan, W. A., Springate, E., and Poletto, L. (2011). Single-grating monochromator for extreme-ultraviolet ultrashort pules. *Opt. Express*, 19:19169.

Friedrich, B. and Herschbach, D. (1995). Alignment and Trapping of Molecules in Intense Laser Fields. *Phys. Rev. Lett.*, 74:4623.

Frumker, E., Hebeisen, C. T., Kajumba, N., Bertrand, J. B., Wörner, H. J., Spanner, M., Villeneuve, D. M., Naumov, A., and Corkum, P. B. (2012). Oriented Rotational Wave-Packet Dynamics Studies Via High Harmonic Generation. *Phys. Rev. Lett.*, 109:113901.

Fukuda, Y., Kishimoto, Y., Masaki, T., and Yamakawa, K. (2006). Structure and dynamics of cluser plasmas created by ultrashort intense laser fields. *Phys. Rev. A*, 73:3.

Gaarde, M. B., Salin, F., Constant, E., Balcou, P., Schafer, K. J., Kulander, K. C., and L'Huillier, A. (1999). Spatiotemporal separation of high harmonic radiation into two quantum path components. *Phys. Rev. A*, 59(2):1367–1373.

Ganeev, R. A., Bom, L. E., Kieffer, J.-C., and Ozaki, T. (2007). Systematic investigation of resonance-induced single-harmonic enhancement in the extreme-ultraviolet range. *Phys. Rev. A*, 75:063806.

Ganeev, R. A., Suzuki, M., Baba, M., and Kuroda, H. (2009). Extended high-order harmonics from laser-produced Cd and Cr plasmas. *Appl. Phys. Lett.*, 94:051101.

Georges, R., Delon, A., and Jost, R. (1995). The visible excitation spectrum of jet cooled $NO_2$: The chaotic behavior of a set of $^2B_2$ vibronic levels. *J. Chem. Phys.*, 103:1732.

Ghimire, S., DiChiara, A. D., Sistrunk, E., Agostini, P., DiMauro, L. F., and Reis, D. A. (2011). Observation of high-order harmonic generation in a bulk crystal. *Nature Phys.*, 7:138–141.

Goulielmakis, E., Schultze, M., Hofstetter, M., Yakovlev, V. S., Gagnon, J., Uiberacker, M., Aquila, A. L., Gullikson, E. M., Attwood, D. T., Kienberger, R., Krausz, F., and Kleineberg, U. (2008). Single-Cycle Nonlinear Optics. *Science*, 320:1614.

Grillon, G., Balcou, P., Chambaret, J.-P., Hulin, D., Martino, J., Moustaizis, S., Notebaert, L., Pittman, M., Pussieux, T., Rousse, A., Rousseau, J. P., Sebban, S., Sublemontier, O., and Schmidt, M. (2002). Deuterium-Deuterium Fusion Dynamics in Low-Density Molecular-Cluster Jets Irradiated by Intense Ultrafast Laser Pulses. *Phys. Rev. Lett.*, 89:065005.

Grunwaldt, J. D. and Baiker, A. (1999). Gold/Titania Interface and Their Role in Carbon Monoxide Oxidation. *J. Phys. Chem. B*, 103:1002–1012.

Haessler, S. (2009). *Generation of Attosecond Pulses in Atoms and Molecules*. PhD thesis, Université Paris-Sud XI.

Haessler, S., Caillat, J., Boutu, W., Giovanetti-Teixeira, C., Ruchon, T., Auguste, T., Diveki, Z., Breger, P., Maquet, A., Carré, B., Taïeb, R., and Salières, P. (2010). Attosecond imaging of molecular electronic wavepackets. *Nature Physics*, 6:200–206.

Hagena, O. and Obert, W. (1972). Cluster Formation in Expanding Supersonic Jets: Effect of Pressure, Temperature, Nozzle Size, and Test Gas. *J. Chem. Phys.*, 56:5.

Hagena, O. F. (1987). Condensation in Free Jets: Comparison of Rare Gases and Metals. *Z. Phys. D*, 4:291–299.

Halvick, P., Boggio-Pasqua, M., Bonnet, L., Voronin, A. I., and Rayez, J. C. (2002). Trajectory surface hopping study of the C+CH reaction. *Phys. Chem. Chem. Phys.*, 4:2560.

Hamard, J. B., Cireasa, R., Chatel, B., Blanchet, V., and Whitaker, B. J. (2010). Quantum Interference in $NO_2$. *J. Phys. Chem. A*, 114:3167.

Handschin, C. (2012). *Dynamique moléculaire par spectroscopie VUV femtoseconde et attoseconde*. PhD thesis, Université de Bordeaux.

Hanna, D. C. (1969). Astigmatic Gaussian Beams Produced by Axially Asymmetric Laser Cavities. *IEEE J. Quant. Elec.*, 5:483.

Haruta, M. (1997). Size- and support-dependency in the catalysis of gold. *Catalysis Today*, 36:153–166.

Haynes, W. M. (2007). *Handbook of Chemistry and Physics 88th edition*. CRC Press Inc.

Hecht, E. (2002). *Optics*. Pearson Education.

Heck, A. J. R. and Chandler, D. W. (1995). Imaging Techniques for the Study of Chemical Reaction Dynamics. *Annu. Rev. Phys. Chem.*, 46:335.

Hentschel, M., Kienberger, R., Spielmann, C., Reider, G. A., Milosevic, N., Brabec, T., Corkum, P., Heinzmann, U., Drescher, M., and Krausz, F. (2001). Attosecond metrology. *Nature*, 414:509.

Hergott, J.-F., Kovacev, M., Merdji, H., Hubert, C., Mairesse, Y., Jean, E., Breger, P., Agostini, P., Carre, B., and Salières, P. (2002). Extreme-ultraviolet high-order harmonic pulses in the microjoule range. *Phys. Rev. A*, 66(2):021801.

Heyl, C. M., Güdde, J., Höfer, U., and L'Huillier, A. (2011). Spectrally Resolved Maker Fringes in High-Order Harmonic Generation. *Phys. Rev. Lett.*, 107:033903.

Higuet, J. (2010). *Études structurelles et dynamiques de systèmes atomiques ou moléculaires par génération d'harmoniques d'ordre élevé*. PhD thesis, Université de Bordeaux.

Higuet, J., Ruf, H., Thiré, N., Cireasa, R., Constant, E., Cormier, E., Descamps, D., Mével, E., Petit, S., Pons, B., Mairesse, Y., and Fabre, B. (2011). High-order harmonic spectroscopy of the Cooper minimum in argon: Experimental and theoretical study. *Phys Rev A*, 83:053401.

Hu, S. X. and Xu, Z. Z. (1997). Dynamics of an intense laser-driven multiwell system: A model of ionized clusters. *Phys. Rev. A*, 56:3916–3922.

Huismans, Y., Rouzée, A., Gijsbertsen, A., Jungmann, J. H., Smolkowska, A. S., Logman, P. S. W. M., Lépin, F., Cauchy, C., Zamith, S., Marchenko, T., Bakker, J. M., Berden, G., Redlich, B., van der Meer, A. F. G., Muller, H. G., Vermin, W., Schafer, K. J., Spanner, M., an O. Smirnova, M. Y. I., Bauer, D., Popruzhenko, S. V., and Vrakking, M. J. J. (2011). Time-Resolved Holography with Photoelectrons. *Science*, 331:61.

Igarashi, H., Makida, A., Ito, M., and Sekikawa, T. (2012). Pulse compression of phase-matched high harmonic pulses from a time-delay compensated monochromator. *Opt. Express*, 20:3725.

Ihee, H., Lobastov, V. A., Gomez, U. M., Goodson, B. M., Srinivasan, R., Ruan, C. Y., and Zewail, A. H. (2001). Direct Imaging of Transient Molecular Structures with Ultrafast Diffraction. *Science*, 291:458.

Ionov, S., Brucker, G. A., Jaques, C., Chen, Y., and Wittig, C. (1993). Probing the $NO_2NO+O$ transition state via time resolved unimolecular decomposition. *J. Chem. Phys.*, 99:3420.

Itatani, J., Levesque, J., Zeidler, D., Niikura, H., Pepin, H., Kieffer, J. C., Corkum, P. B., and Villeneuve, D. M. (2004). Tomographic imaging of molecular orbitals. *Nature*, 432(7019):867.

Ito, M., Kataoka, Y., Okamoto, T., Yakashita, M., and Sekikawa, T. (2010). Spatiotemporal characterization of single-order high harmonic pulses from time-compensated toroidal-grating monochromator. *Opt. Express*, 6:6071.

Ivanov, M. Y., Spanner, M., and Smirnova, O. (2005). Anatomy of strong field ionization. *J. Mod. Opt.*, 52:165.

Jin, C., Bertrand, J. B., Lucchese, R. R., Wörner, H. J., Corkum, P. B., Villeneuve, D. M., Le, A.-T., and Lin, C. D. (2012). Intensity dependence of multiple orbital contributions and shape resonance in high-order harmonic generation of aligned $N_2$ molecules. *Phys. Rev. A*, 85:013405.

Joffre, M. (2007). Comment on "Coherent Control of Retinal Isomerization in Bacteriorhodopsin". *Science*, 317:453.

Jullien, A. (2006). *Génération d'impulsions laser ultra-brèves et ultra-intenses à constraste temporel élevé*. PhD thesis, École Polytechnique.

Jullien, A., Albert, O., Chériaux, G., Etchepare, J., Kourtev, S., Minkovski, N., and Saltiel, S. M. (2005). Nonlinear polarization rotation of elliptical light in cubic crystals, with application to cross-polarized wave generation. *J. Opt. Soc. Am. B*, 22:2635.

Kakar, S., Björneholm, O., Weigelt, J., de Castro, A. R. B., Tröger, L., Frahm, R., and Möller, T. (1997). Size-dependent K-edge EXAFS study of the structure of free Ar clusters. *Phys. Rev. Lett.*, 78:1675–1678.

Kanai, T., Minemoto, S., and Sakai, H. (2005). Quantum interference during high-order harmonic generation from aligned molecules. *Nature*, 435:470.

Kanai, T., Takahashi, E. J., Nabekawa, Y., and Midorikawa, K. (2007). Destructive Interference during High Harmonic Generation in Mixed Gases. *Phys. Rev. Lett.*, 98(15):153904.

Kazamias, S., Douillet, D., Weihe, F., Valentin, C., Rousse, A., Sebban, S., Grillon, G., Augé, F., Hulin, D., and Balcou, P. (2003). Global Optimization of High Harmonic Generation. *Phys. Rev. Lett.*, 90:193901.

Kazamias-Moucan, S. (2003). *Optimisation d'une source d'harmoniques d'ordres élevés pour l'optique non-linéaire dans l'extrême UV*. PhD thesis, École Polytechnique.

Keldysh, L. (1965). Ionization in the field of a strong electromagnetic wave. *Sov. Phys. JETP*, 20:1307.

Kennedy, D. J. and Manson, S. T. (1972). Photoionization of the Noble Gases: Cross Secions and Angular Distributions. *Phys. Rev. A*, 5:227.

Keshavamurthy, S. and Miller, W. H. (1994). Semi-classical correction for quantum mechanical scattering. *Chem. Phys. Lett.*, 218:189.

Khan, S. D., Cheng, Y., Möller, M., Zhao, K., Zhao, B., Chini, M., Paulus, G. G., and Chang, Z. (2011). Ellipticity dependence of 400 nm-driven high harmonic generation. *Appl. Phys. Lett.*, 99:161106.

Kita, T., Harada, T., Nakano, N., and Kuroda, H. (1983). Mechanically ruled aberration-corrected concave gratings for a flat-field grazing-incidence spectrograph. *Appl. Opt.*, 22:512.

Kittel, C. (2005). *Introduction to Solid State Physics*. John Wiley & Sons.

Knoll, M. and Ruska, E. (1932). Das Elektronenmikroskop. *Z. Physik*, 78:318.

Ko, D. H., Kim, K. T., Park, J., lee, J.-H., and Nam, C. H. (2010). Attosecond chirp compensation over broadband high-order harmonics to generate near transform-limited 63 as pulses. *New J. Phys.*, 12:063008.

Kogelnik, H. and Li, T. (1966). Laser Beams and Resonators. *Appl. Opt.*, 5:1550.

Krainov, V. P. and Smirnov, M. B. (2002). Cluster beams in the super-intense femtosecond laser pulse. *Phy. Rep.*, 370:237–331.

Kraus, P. M., Arasaki, Y., Bertrand, J. B., Patchkovskii, S., Corkum, P. B., Villeneuve, D. M., Takatsuka, K., and Wörner, H. J. (2012). Time-resolved high-harmonic spectroscopy of nonadiabatic dynamics in $NO_2$. *Phys. Rev. A*, 85:043409.

Kraus, P. M. and Wörner, H. J. (2012). Time-resolved high-harmonic spectroscopy of valence electron dynamics. *Chem. Phys., in print*.

Krause, J. L., Schafer, K. J., and Kulander, K. C. (1992). High-Order Harmonic Generation from Atoms and Ions in the High Intensity Regime. *Phys. Rev. Lett.*, 68:3535.

Krausz, F. and Ivanov, M. (2009). Attosecond physics. *Rev. Mod Phys.*, 81:164.

Krüger, M., Schenk, M., and Hommelhoff, P. (2011). Attosecond control of electrons emitted from a nanoscale metal tip. *Nature*, 475:78.

Kulander, K. C., Schafer, K. J., and Krause, J. L. (1992). *Atoms in Intense Laser Fields*. Academic Press, San Diego.

Kumarappan, V., Bisgaard, C. Z., Viftrup, S. S., Holmegaard, L., and Stapelfeldt, H. (2006). Role of rotational temperature in adiabatic molecular alignment. *J. Chem. Phys.*, 125:194309.

Kurkal, V., Fleurat-Lessard, P., and Schinke, R. (2003). $NO_2$ : Global potential energy surfaces of the ground ($1\ ^2A_1$) and the first excited ($1\ ^2B_2$) electronic states. *J. Chem. Phys.*, 119:1489.

Kurz, H. G., Steingrube, D. S., Ristau, D., Lein, M., Morgner, U., and Kovacev, M. (2012). Transient Phase Matching during High-Order Harmonic Generation in Water Droplets. In *XVIII International Conference On Ultrafast Phenomena*.

Lavorel, B., Faucher, O., Morgen, M., and Chaux, R. (2000). Analysis of femtosecond Raman-induced polarization spectroscopy (RIPS) in $N_2$ and $CO_2$ by fitting and scaling laws. *Journal of Raman spectroscopy*, 31:77.

Le, A.-T., Lucchese, R. R., Tonzani, S., Morishita, T., and Lin, C. D. (2009). Quantitative rescattering theory for high-order harmonic generation from molecules. *Phys. Rev. A.*, 80:013401.

le Déroff, L., Salières, P., Carré, B., Joyeux, D., and Phalippou, D. (2000). Measurement of the degree of spatial coherence of high-order harmonics using a Fresnel-mirror interferometer. *Phys. Rev. A*, 61:043802.

Lee, K. F. (2006). *Controlling Molecular Alignement*. PhD thesis, McMaster University.

Lein, M. (2005). Mechanisms of ultrahigh-order harmonic generation. *Phys. Rev. A*, 72:053816.

Lein, M., Hay, N., Velotta, R., Marangos, J. P., and Knight, P. L. (2002). Interference effects in high-order harmonic generation with molecules. *Phys. Rev. A*, 66(2):023805.

Leonardi, E., Petrongolo, C., Hirsch, G., and Buenker, R. J. (1996). Ab inition study of $NO_2$. V. Nonadiabatic vibronic states and levels of the $X^2A_1/\tilde{A}^2B_2$ conical intersection. *J. Chem. Phys.*, 105:9051.

Levesque, J., Mairesse, Y., Dudovich, N., Pépin, H., Kieffer, J.-C., Corkum, P. B., and Villeneuve, D. M. (2007). Polarization state of high-order harmonic emission from aligned molecules. *Phys. Rev. Lett.*, 99(24):243001.

Lewenstein, M., Balcou, P., Ivanov, M. Y., LHuillier, A., and Corkum, P. B. (1994). Theory of high-harmonic generation by low-frequency laser fields. *Phys. Rev. A*, 49:2117.

L'Huillier, A., Balcou, P., Candel, S., Schafer, K. J., and Kulander, K. C. (1992). Calculations of high-order harmonic-generation processes in xenon at 1064 nm. *Phys. Rev. A*, 46:2778.

L'Huillier, A., Lompré, L. A., Mainfray, G., and Manus, C. (1983). Multiply charged ions ionduced by multiphoton absorption processes in rare-gas atoms at 1.064 $\mu$m. *J. Phys. B*, 16:1363.

Li, W., Zhou, X., Lock, R., Patchkovskii, S., Stolow, A., Kapteyn, H. C., and Murnane, M. M. (2008). Time-resolved dynamics in $N_2O_4$ probed using high harmonic generation. *Science*, 322:1207–1211.

Li, X. F., L'Huillier, A., Ferray, M., A.Lompré, L., and Mainfray, G. (1989). Multiple-harmonic generation in rare gases at high laser intensity. *Phys. Rev. A*, 39:5751.

Lock, R. M., Zhou, X., Li, W., Murnane, M. M., and Kapteyn, H. C. (2009). Measuring the intensity and phase of high-order harmonic emission from aligned molecules. *Chem. Phys.*, 366:22.

Lundwall, M. (2007). *Rare-gas Clusters Studied by Electron Spectroscopy*. PhD thesis, Uppsala Universitet.

Luria, K., Christen, W., and Even, U. (2011). Generation and Propagation of Intense Supersonic Beams. *J. Phys. Chem. A*, 115:7362–7367.

Lynga, C., Gaarde, M. B., Delfin, C., Bellini, M., Hansch, T. W., L'Huillier, A., and Wahlstrom, C.-G. (1999). Temporal coherence of high-order harmonics. *Phys. Rev. A*, 60(6):4823–4830.

Mairesse, Y., de Bohan, A., Frasinski, L. J., Merdji, H., Dinu, L. C., Monchicourt, P., Breger, P., Kovacev, M., Taïeb, R., Carré, B., Muller, H. G., Agostini, P., and Salières, P. (2003). Attosecond Synchronization of High-Harmonic Soft X-rays. *Science*, 302:1540.

Mairesse, Y., Dudovich, N., Levesque, J., Ivanov, M., Corkum, P., and Villeneuve, D. (2008a). Electron wavepacket control with elliptically polarized laser light in high harmonic generation from aligned molecules. *New J. Phys.*, 10:025015.

Mairesse, Y., Haessler, S., Fabre, B., Higuet, J., Boutu, W., Breger, P., Constant, E., Descamps, D., Mével, E., Petit, S., and Salières, P. (2008b). Polarization-resolved pump-probe spectroscopy with high harmonics. *New J. Phys.*, 10:025028.

Mairesse, Y., Higuet, J., Dudovich, N., Shafir, D., Fabre, B., Mével, E., Constant, E., Patchkovskii, S., Walters, Z., Ivanov, M., and Smirnova, O. (2010). High Harmonic Spectroscopy of Multichannel Dynamics in Strong-Field Ionization. *Phys. Rev. Lett.*, 104:213601.

Mairesse, Y., Zeidler, D., Dudovich, N., Spanner, M., Levesque, J., Villeneuve, D. M., and Corkum, P. B. (2008c). High-Order Harmonic Transient Grating Spectroscopy in a Molecular Jet. *Physical Review Letters*, 100(14):143903.

Maker, P. D., Terhune, R. W., Nisenoff, M., and Savage, C. M. (1962). Effects of Dispersion and Focusing on th Production of Optical Harmonics. *Phys. Rev. Lett.*, 8:21.

Marr, G. V. and West, J. V. (1976). Absolute photoionization cross-section tables for helium, neon, argon, and krypton in the VUV spectral regions. *At. Data Nucl. Data Tables*, 18:497.

Mauritsson, J., Johnsson, P., Lopez-Martens, R., Varju, K., Kornelis, W., Biegert, J., Keller, U., Gaarde, M. B., Schafer, K. J., and L'Huillier, A. (2004). Measurement and control of the frequency chirp rate of high-order harmonic pulses. *Phys. Rev. A*, 70(2):021801.

McFarland, B. K., Farrel, J. P., Bucksbaum, P. H., and Gühr, M. (2008). High harmonic generation from multiple orbitals in $N_2$. *Science*, 322:1232.

McPherson, A., Gibson, G., Jara, H., Johann, U., Luk, T. S., McIntyre, I., Boyer, K., and Rhodes, C. K. (1987). Studies of multiphoton production of vacuum-ultraviolet radiation in the rare gases. *J. Opt. Soc. Am. B*, 4:595.

Meckel, M., Comtois, D., Zeidler, D., Staudte, A., Pavicić, D., Bandulet, H. C., Pépin, H., Kieffer, J. C., Dörner, R., Villeneuve, D. M., and Corkum, P. B. (2008). Laser-Induced Electron Tunneling and Diffraction. *Science*, 320:1478.

Meier, C. and Engel, V. (2002). Time-resolved photoelectron spectroscopy of molecular dissociation: Classical trajectory versus quantum wave-packet calculations. *Phys. Chem. Chem. Phys.*, 4:5014.

Mével, E., Breger, P., Trainham, R., Petite, G., Agostini, P., Migus, A., Chambaret, J.-P., and Antonetti, A. (1993). Atoms in strong optical fields: Evolution from multiphoton to tunnel ionization. *Phys. Rev. Lett.*, 70:406.

Mével, E., E.Constant, Garzella, D., Breger, P., Dorrer, C., LeBlanc, C., Salin, F., and Agostini, P. (2000). Optimizing high order harmonic generation in absorbing gases. In DiMauro, L. F., Freeman, R. R., and Kulander, K. C., editors, *Multiphoton Processes : ICOMP VIII, 8th International Conference*, page 373.

Milonni, P. W. and Eberly, J. H. (1988). *Lasers*. John Wiley & Sons.

Minkovski, N., Petrov, G. I., Saltiel, S. M., Albert, O., and Etchepare, J. (2004). Nonlinear polarization rotation and orthogonal polarization generation experienced in a single-beam configuration. *J. Opt. Soc. Am. B*, 21:1659.

Minkovski, N., Saltiel, S. M., Petrov, G. I., Albert, O., and Etchepare, J. (2002). Polarization rotation induced by cascaded third-order processes. *Opt. Lett.*, 27:2025.

Moreno, M., Plaja, L., and Roso, L. (1994). High-Order Harmonic Geration by Electron-Proton Recombination. *Europhys. Lett.*, 28:9.

Moreno, P., Plaja, L., and Roso, L. (1997). Ultrahigh harmonic generation from diatomic molecular ions in highly excited vibrational states. *Phys. Rev. A*, 55:3.

Mott, N. F. (1940). Oxidation of Metals and the Formation of Protective Films. *Nature*, 145:996.

Muller, H. G. (1999). Numerical simulation of high-order above-threshold-ionization enhancement in argon. *Phys. Rev. A*, 60:1341.

Murray, R., Spanner, M., Patchovskii, S., and Ivanov, M. Y. (2011). Tunnel Ionization of Molecules and Orbital Imaging. *Phys. Rev. Lett.*, 106:173001.

Muth-Böhm, J., Becker, A., and Faisal, F. H. M. (2000). Suppressed Molecular Ionization for a Class of Diatomics in Intense Femtosecond Laser Fields. *Phys. Rev. Lett.*, 85(11):2280.

NIST (2012). National Institute of Standards and Technology. *http://www.nist.gov/index.html*.

Nolting, W. (2002). *Grundkurs Theoretische Physik 6*. Springer-Verlag.

Nugent-Glandorf, L., Scheer, M., Samuels, D. A., Mulhisen, A. M., Grant, E. R., Yang, X., Bierbaum, V. M., and Leone, S. R. (2001). Ultrafast time-resolved soft x-ray photoelectron spectroscopy of dissociating $Br_2$. *Phys Rev Lett*, 87(19):193002.

Numico, R., Giulietti, D., Giulietti, A., Gizzi, L. A., and Roso, L. (2000). High-order harmonic generation from a linear chain of ions. *J. Phys. B*, 33:2605–2615.

Parker, D. H. (2000). Laser Photochemistry. *Acc. Chem. Res.*, 33:563.

Parker, D. H., Gordon, R. J., Zhu, L., Hayden, C. C., Stolow, A., Radloff, W., Rosmus, P., Chambaud, G., Kimura, K., Johnson, P. M., Morioka, Y., Ng, C., Weitzel, K.-M., Ogawa, T., Faubel, M., Larsson, M., Continetti, R. E., Boesl, U., Bässmann, C., Schlag, E. W., Wang, L.-S., Simons, J., Pratt, S. T., Ellenberger, E., Lin, C. D., Morishita, T., Berrah, N., Southworth, S. H., Young, L., Kanter, E. P., and LeBrun, T. (2000). *Photoionization and Photodetachment*. World Scientific Publishing.

Pastirk, I., Comstock, M., and Dantus, M. (2001). Femtosecond ground state dynamics of gas phase $N_2O_4$ and $NO_2$. *Chem. Phys. Lett.*, 349:71.

Patchkovskii, S., Zhao, Z., Brabec, T., and Villeneuve, D. M. (2006). High Harmonic Generation and Molecular Orbital Tomography in Multielectron Systems: Beyond the Single Active Electron Approximation. *Phys. Rev. Lett.*, 97:123003.

Paul, P. M., Toma, E. S., Breger, P., Mullot, G., Balcou, P., Muller, H. G., and Agostini, P. (2001). Observation of a Train of Attosecond Pulses from High Harmonic Generation. *Science*, 292:1689.

Paulus, G. G., Nicklich, W., Xu, H., Lambropoulos, P., and Walther, H. (1994). Plateau in Above Threshold Ionization Spectra. *Phys. Rev. Lett.*, 72:2851.

Poletto, L., Bonora, S., Frassetto, F., Villoresi, P., Springate, E., Froud, C. A., Turcu, I. C. E., Wolff, D. S., Collier, J. S., and Roper, M. (2009). The XUV monochromator for ultrashort pulses at the Artemis facility. Technical report, STFC Rutherford Appleton Laboratory.

Popmintchev, T., Chen, M.-C., Popmintchev, D., Arpin, P., Brown, S., Brown, S., Ališauskas, S., Andriukaitis, G., Balciunas, T., Mücke, O. D., Pugzlys, A., Baltuska, A., Shim, B., Schrauth, S. E., Gaeta, A., Hernández-García, C., Plaja, L., Becker, A., Jaron-Becker, A., Murnane, M. M., and Kapteyn, H. C. (2012). Bright Coherent Ultrahigh Harmonics in the keV X-ray Regime from Mid-Infrared Femtosecond Lasers. *Science*, 336:1287.

Qu, Z. W., Zhu, H., Grebenshchikov, S. Y., and Schinke, R. (2005). The photodissociation of ozone in the Hartley band: A theoretical analysis. *J. Chem. Phys.*, 123:074305.

Quéré, F., Thaury, C., Monot, P., Dobosz, S., Martin, P., Geindre, J. P., and Audebert, P. (2006). Coherent Wake Emission of High-Order Harmonics from Overdense Plasmas. *Phys. Rev. Lett.*, 96:125004.

Raković, M. J., Schultz, D. R., Stancil, P. C., and Janev, R. K. (2001). On quantum-classical correspondence in classical studies of atomic processes. *J. Phys. A*, 34:4753–4770.

Ramos, A., Fernández, J. M., Tejeda, G., and Montero, S. (2005). Quantitative study of cluster growth in free-jet expandsions of $CO_2$ by Rayleigh and Ramand scattering. *Phys. Rev. A*, 72:053204.

Ratner, M. A. (1999). Kinetics of cluster growth in expanding rare-gas jets. *Low Temp. Phys.*, 25:266.

Reiss, H. R. (1980). Effect of an intense electromagnetic field on a weakly bound system. *Phys. Rev. A*, 22:1786.

Renard, V., Renard, M., Rouzée, A., Guérin, S., Jauslin, H. R., Lavorel, B., and Faucher, O. (2004). Nonintrusive monitoring and quantitative analysis of strong laser-field-induced impulsive alignment. *Phys. Rev. A*, 70:033420.

Richter, A., Burrows, J. P., Nüss, H., Granier, C., and Niemeier, U. (2005). Increase in tropospheric nitrogen dioxide over China observed from space. *Nature*, 437:129.

Rosca-Pruna, F. and Vrakking, M. J. J. (2001). Experimental Observation of Revival Structures in Picosecond Laser-Induced Alignment of $I_2$. *Phys. Rev. Lett.*, 87:153902.

Roscoe, H. K. and Hind, A. K. (1993). The equilibrium constant of $NO_2$ with $N_2O_4$ and the temperature dependence of the visible spectrum of $NO_2$: A critical review and the

implications for measurements of $NO_2$ in the polar stratosphere. *Journal atmospheric chemistry*, 16:257.

Rouzée, A. (2007). *Alignement uni et tridimensionnel de molécules par impulsion laser femtoseconde*. PhD thesis, Université de Bourgogne.

Rouzée, A., Renard, V., Guérin, S., Faucher, O., and Lavorel, B. (2007). Optical gratings induced by field-free alignment of molecules. *Phys. Rev. A*, 75:013419.

Ruf, H. (2008). Untersuchung eines tmho-dotierten festkörperlasers. Master's thesis, Universität Konstanz.

Ruf, H., Handschin, C., Ferré, A., Thiré, N., Bertrand, J. B., Bonnet, L., Cireasa, R., Constant, E., Corkum, P. B., Descamps, D., Fabre, B., Higuet, J., Larregaray, P., Mével, E., Petit, S., Pons, B., Staedter, D., Wörner, H. J., Villeneuve, D. M., Mairesse, Y., Halvick, P., and Blanchet, V. (2012). High-harmonic transient grating spectroscopy of $NO_2$ electronic excitation. *J. Chem. Phys., accepted*.

Rundquist, A., Durfee, C., Chang, Z., Herne, C., Backus, S., Murnane, M. M., and Kapteyn, H. C. (1998). Phase-Matched Generation of Coherent Soft X-rays. *Science*, 280:1412.

Saalmann, U. (2006). Resonant energy absorption of rare-gas clusters in strong laser pulses. *J. Mod. Opt.*, 53:173.

Sakurai, J. J. (2005). *Modern Quantum Mechanics*. Pearson Education (Singapore).

Salières, P., Carré, B., Déroff, L. L., Grasbon, F., Paulus, G. G., Walther, H., Kopold, R., Becker, W., Miloevic, D. B., Sanpera, A., and Lewenstein, M. (2001). Feynman's Path-Integral Approach for Intense-Laser-Atom Interactions. *Science*, 292:902–905.

Salières, P., L'Huillier, A., Antoine, P., and Lewenstein, M. (1999). Study of the spatial and temporal coherence of high-order harmonics. *Adv. At. Mol. Opt. Phys.*, 41:83.

Salières, P., L'Huillier, A., and Lewenstein, M. (1995). Coherence control of high-order harmonics. *Phys. Rev. Lett.*, 74(19):3776–3779.

Samson, J. and Stolte, W. (2002). Precision measurements of the total photoionization cross-sections of He, Ne, Ar, Kr, and Xe. *Jour.of Electron Spec. and Relat. Phen.*, 123:265.

Sanchez, A., Abbet, S., Heinz, U., Schneider, W. D., Häkkinen, H., Barnett, R. N., and Landman, U. (1999). When Gold Is Not Noble: Nanoscale Gold Catalysts. *J. Phys. Chem. A*, 103:9573–9578.

Sanrey, M. and Joyeux, M. (2007). Slow periodic oscillations in time domain dynamics of $NO_2$. *The Journal of Chemical Physics*, 126(7):074301.

Santoro, F. and Petrongolo, C. (1999). Nonadiabatic radiative lifetimes and fluorescence spectra of $NO_2$. *J. Chem. Phys.*, 111:9651.

Santoro, F., Petrongolo, C., Granucci, G., and Persico, M. (2000). Quantum and semiclassical dynamics of the Franck-Condon wave packet on the coupled potential surfaces of the $\tilde{X}^2A'/\tilde{A}^2A'$ conical intersection. *Chem. Phys.*, 259:193.

Schafer, K. J. (2009). *Strong Field Laser Physics*, chapter Numerical Methods in Strong Field Physics, page 111. Springer Series in Optical Sciences.

Schafer, K. J., Yang, B., DiMauro, L. F., and Kulander, K. C. (1993). Above threshold ionization beyond the high harmonic cutoff. *Phys. Rev. Lett.*, 70(11):1599–1602.

Scoles, G., Bassi, D., Buck, U., and Lainé, D. (1988). *Atomic and Molecular Beam Methods*. Oxford University Press, New York.

Seideman, T. (1995). Rotational excitation and molecular alignment in intense laser fields. *J. Chem. Phys.*, 103:7887.

Seideman, T. (1999). Revival structure of aligned rotational wave packets. *Phys. Rev. Lett.*, 83:4971.

Shafir, D., Fabre, B., Higuet, J., Soifer, H., Dagan, M., Descamps, D., Mével, E., Petit, S., Wörner, H. J., Pons, B., Dudovich, N., and Mairesse, Y. (2012a). Role of the Ionic Potential in High Harmonic Generation. *Phys. Rev. Lett.*, 108:203001.

Shafir, D., Soifer, H., Brunner, B. D., Dagan, M., Mairesse, Y., Patchkovskii, S., Ivanov, M. Y., Smirnova, O., and Dudovich, N. (2012b). Resolving the time when an electron exits a tunneling barrier. *Nature*, 485:343.

Shan, B., Tong, X.-M., Zhao, Z., Chang, Z., and Lin, C. D. (2002). High-order harmonic cutoff extension of the $O_2$ molecule due to ionization suppression. *Phys. Rev. A*, 66:061401.

Shiner, A. D., Trallero-Herrero, C., Kajumba, N., Bandulet, H.-C., Comtois, D., Légaré, F., Giguere, M., Kieffer, J.-C., Corkum, P. B., and Villeneuve, D. M. (2009). Wavelength Scaling of High Harmonic Generation Efficiency. *Phys. Rev. Lett.*, 103:073902.

Siegmann, A. E. (1986). *Lasers*. University Science Books, Sausalito, CA.

Skopolová, E., El-Taha, Y. C., Zaïr, A., Hohenberger, M., Springate, E., Tisch, J. W. G., Smith, R. A., and Marangos, J. P. (2010). Pulse-Length Dependence of the Anisotropy of Laser-Driven Cluster Explosions: Transition to the Impulsive Regime for Pulses Approaching the Few-Cycle Limit. *Phys. Rev. Lett.*, 104:203401.

Smirnova, O., Mairesse, Y., Patchkovskii, S., Dudovich, N., Villeneuve, D., Corkum, P., and Ivanov, M. Y. (2009a). High harmonic interferometry of multi-electron dynamics in molecules. *Nature*, 460:972.

Smirnova, O., Patchkovskii, S., Mairessea, Y., Dudovich, N., and Ivanov, M. Y. (2009b). Strong-field control and spectroscopy of attosecond electron-hole dynamics in molecules. *Proceedings of the National Academy of Sciences*, 106:16556.

Smith, R. A., Ditmire, T., and Tisch, J. W. G. (1998). Characterization of a cryogenically cooled high-pressure gas jet for laser/cluster interaction experiments. *Rev. Sci. Instrum.*, 69:11.

Soifer, H., Botheron, P., Shafir, D., Diner, A., Raz, O., Bruner, B. D., Mairesse, Y., Pons, B., and Dudovich, N. (2010). Near-Threshold High-Order Harmonic Spectroscopy with Aligned Molecules. *Phys. Rev. Lett.*, 105(14):143904.

Solomon, J. (1967). Photodissociation as studied by Photolysis Mapping. *J. Chem. Phys.*, 47:889.

Stapelfeldt, H. and Seideman, T. (2003). Colloquium: Aligning molecules with strong laser pulses. *Rev. Mod. Phys.*, 75:543.

Stolow, A. (1998). Applications of wavepacket methodology. *Phil. Trans. R. Soc. Lond. A*, 356:345.

Stolyarov, D., Polyakova, E., Bezel, I., and Wittig, C. (2002). Rate coefficients for photoinitiated $NO_2$ unimolecular decomposition: energy dependence in the threshold regime. *Chem. Phys. Lett.*, 358:71.

Strelkov, V. (2010). Role of Autoionizing State in Resonant High-Order Harmonic Generation and Attosecond Pulse Production. *Phys. Rev. Lett.*, 104:123901.

Strelkov, V., Saalmann, U., Becker, A., and Rost, J. M. (2011). Monitoring Atomic Cluster Expansion by High-Harmonic Generation. *Phys. Rev. Lett.*, 107:113901.

Strikland, G. and Mourou, G. (1985). Compression of amplified chirped optical pulses. *Opt. Com.*, 56:219.

Suzuki, M., Ganeev, R. A., Bom, L. B. E., Baba, M., Ozaki, T., and Kuroda, H. (2007). Extension of cutoff in high harmonic by using doubly charged ions in a laser-ablation plume. *J. Opt. Soc. Am. B*, 24:2847.

Takahashi, E., Nabekawa, Y., and Midorikawa, K. (2002). Generation of 10-$\mu$j coherent extreme-ultraviolet light by use of high-order harmonics. *Opt. Lett.*, 27:1920.

Tamaki, Y., Itatani, J., Obara, M., and Midorikawa, K. (2000). Optimization of conversion efficiency and spatial quality of high-order harmonic generation. *Phys. Rev. A*, 62:063802.

Tang, K. T. and Toennies, J. P. (1986). New Combining Rules for Well Parameters and Shapes of the van der Waals Potential of Mixed Rare Gas Systems. *Z. Phys. D: At., Mol. Clusters*, 1:91–101.

Tate, J., Auguste, T., Muller, H. G., Salières, P., Agostini, P., and L. F. DiMauro, L. F. (2007). Scaling of Wave-Packet Dynamics in an Intense Midinfrared Field. *Phys. Rev. Lett.*, 98:013901.

Tchaplyguine, M., Marinho, R. R., Gisselbrecht, M., Schulz, J., Martensson, N., Sorensen, S. L., de Brito, A. N., Feifel, R., Öhrwall, G., Lundwall, M., Svensson, S., and Björneholm, O. (2004). The size of neutral free clusters as manifested in the relative bulk-to-surface intensity in core level photoelectron spectroscopy. *J. Chem. Phys.*, 120:1.

Tempea, G. and Brabec, T. (2000). Optimization of high-harmonic generation. *Appl. Phys. B*, 70:S197.

Tisch, J. W. G., Ditmire, T., Fraser, D. J., Hay, N., Mason, M. B., Springate, E., Marangos, J. P., and Hutchinson, M. H. R. (1997). Investigation of high-harmonic generation from xenon atom clusters. *J. Phys. B: At. Mol. Opt. Phys.*, 30:709.

Tong, X. M., Zhao, Z. X., and Lin, C. D. (2002). Theory of molecular tunneling ionization. *Phys. Rev. A*, 66:033402.

Torres, R., de Nalda, R., and Marangos, J. P. (2005). Dynamics of laser-induced molecular alignment in the impulsive and adiabatic regimes: A direct comparison. *Phys. Rev. A*, 72:023420.

Tully, J. C. (1990). Molecular dynamics with electronic transitions. *J. Chem. Phys.*, 93:1061.

Tzallas, P., Charalambidis, D., Papadogiannis, N. A., Witte, K., and Tsakiris, G. D. (2003). Direct observation of attosecond light bunching. *Nature*, 426:267–271.

Vandaele, A. C., Hermans, C., Fally, S., Carleer, M., Mérienne, M. F., Jenouvrier, A., and Colin, R. (2003). Absorption cross-sections of $NO_2$: simulation of temperature and pressure effects. *Journal of Quantitative Spectroscopy and Radiative Transfer*, 76:273.

Varju, K., Mairesse, Y., Carré, B., Gaarde, M. B., Johnsson, P., Kazamias, S., Lopez-Martens, R., Mauritsson, J., Schafer, K. J., Balcou, P., L'Huillier, A., and Salières., P. (2005). Frequency chirp of harmonic and attosecond pulses. *Journal of Modern Optics*, 52:379.

Velotta, R., Hay, N., Mason, M., Castillejo, M., and Marangos, J. (2001). High-Order Harmonic Generation in Aligned Molecules. *Phys. Rev. Lett.*, 87:183901.

Velten, A., Willwacher, T., Gupta, O., Veeraraghavan, A., Badwendi, M., and Raskar, R. (2012). Recovering Three-Dimensional Shape around a Corner using Ultra-Fast Time-of-Flight Imaging. *Nat. Commun.*, 3:101038.

Véniard, V., Taïeb, R., and Maquet, A. (2001). Atomic clusters submitted to an intense short laser pulse: A density-functional approach. *Phys. Rev. A*, 65:013202.

Vincenti, H. and Quéré, F. (2012). Attosecond Lighthouses: How To Use Spatiotemporally Coupled Light Fields To Generate Isolated Attosecond Pulses. *Phys. Rev. Lett.*, 108:113904.

Vozzi, C., Calegari, F., Benedetti, E., Caumes, J.-P., Sansone, G., Stagira, S., Nisoli, M., Torres, R., Heesel, E., Kajumba, N., Marangos, J. P., Altucci, C., and Velotta, R. (2005a). Controlling Two-Center Interference in Molecular High Harmonic Generation. *Phys. Rev. Lett.*, 95:153902.

Vozzi, C., Calegari, F., Benedetti, E., Gasilov, S., Sansone, G., Cerullo, G., Nisoli, M., Silvestri, S. D., and Stagira, S. (2007). Millijoule-level phase-stabilized fe-optical-cycle infrared parametric source. *Opt. Lett.*, 32:2957.

Vozzi, C., Manzoni, C., Calegari, F., Benedetti, E., Sansone, G., Cerullo, G., Nisoli, M., Silvestri, S. D., and Stagira, S. (2008). Characterization of a high-energy self-phase-stabilzed near-infrared parametric source. *J. Opt. Soc. Am. B*, 25:112.

Vozzi, C., Negro, M., Calegari, F., Sansone, G., Nisoli, M., Silvestri, S. D., and Stagira, S. (2011). Generalized molecular orbital tomography. *Nature Phys.*, 7:822.

Vozzi, C., Nisoli, M., Caumes, J.-P., Sansone, G., Stagira, S., Silvestri, S. D., Vecchiocattivi, M., Bassi, D., Pascolini, M., Poletto, L., Villoresi, P., and Tondello, G. (2005b). Cluster effects in high-order harmonics generated by ultrashort light pulses. *Appl. Phys. Lett.*, 86:111121.

Wagner, N., Wüest, A., Christov, I., Popmintchev, T., Zhou, X., Murnane, M., and Kapteyn, H. (2006). Monitoring molecular dynamics using coherent electrons from high harmonic generation. *Proc. Natl. Acad. Sci.*, 103:13279–13285.

Wagner, N., Zhou, X., Lock, R., Li, W., Wüest, A., Murnane, M., and Kapteyn, H. (2007). Extracting the phase of high-order harmonic emission from a molecule using transient alignment in mixed samples. *Phys. Rev. A*, 76:061403.

Wahlström, C.-G., Larsson, J., Persson, A., Starczewski, T., Svanberg, S., Salieres, P., Balcou, P., and L'Huillier, A. (1993). High-order harmonic generation in rare gases with an intense short-pulse laser. *Phys. Rev. A*, 48(6):4709–4720.

Walker, B., Sheehy, B., DiMauro, L. F., Agostini, P., Schafer, K. J., and Kulander, K. C. (1994). Precision Measurement of Strong Field Double Ionization of Helium. *Phys. Rev. Lett.*, 73:1227.

Walters, Z. B., Tonzani, S., and Greene, C. H. (2007). High harmonic generation in $SF_6$: Raman-excited vibrational quantum beats. *J. Phys. B: At. Mol. Opt. Phys.*, 40:277.

Weber, S. (2007). Alignement de molécules pour la génération d'harmoniques d'ordre élevé. Master's thesis, Université Pierre et Marie Curie.

Wernet, P., Gaudin, J., Godehusen, K., Schwarzkopf, O., and Eberhardt, W. (2011). Femtosecond time-resolved photoelectron spectroscopy with a vacuum-ultraviolet photon-source based on laser high-order harmonic generation. *Rev. Sci. Instrum.*, 82:063114.

Whitaker, B. J. (2011). Shining Light on Diabolic Points. *Science*, 334:187.

Wong, M. C. H., Brichta, J. P., and Bhardwaj, V. R. (2010). High-harmonic generation in $H_2O$. *Opt. Lett.*, 35:1947.

Wörner, H. J., Bertrand, J. B., Fabre, B., Higuet, J., Ruf, H., Dubrouil, A., Patchkovskii, S., Spanner, N., Mairesse, Y., Blanchet, V., Mével, E., Constant, E., Corkum, P. B., and Villeneuve, D. M. (2011). Conical Intersection Dynamics in $NO_2$ Probed by Homodyne High-Harmonic Spectroscopy. *Science*, 334:208.

Wörner, H. J., Bertrand, J. B., Hockett, P., Corkum, P. B., and Villeneuve, D. M. (2010). Controlling the Interference of Multiple Molecular Orbitals in High-Harmonic Generation. *Phys. Rev. Lett.*, 104(23):233904.

Wörner, H. J., Bertrand, J. B., Kartashov, D. V., Corkum, P. B., and Villeneuve, D. M. (2010). Following a chemical reaction using high-harmonic interferometry. *Nature*, 466:604.

Wörner, H. J., Niikura, H., Bertrand, J. B., Corkum, P. B., and Villeneuve, D. M. (2009). Observation of Electronic Structure Minima in High-Harmonic Generation. *Phys. Rev. Lett.*, 102:103901.

Xie, J., Northby, J., Freeman, D., and Doll, J. (1989). Theoretical studies of the energetics and structures of atomic cluster. *J. Chem. Phys.*, 91:1.

Yarkony, D. R. (1996). Diabolic conical intersections. *Rev. Mod. Phys.*, 68:985.

Yoshii, K., Miyaji, G., and Miyazaki, K. (2011). Retrieving Angular Distributions of High-Order Harmonic Generation from a Single Molecule. *Phys. Rev. Lett.*, 106:013904.

Yu, H. and Bandrauk, A. D. (1995). Three-dimensional Cartesian finite element method for the time dependent Schrödinger equation of molecules in laser fields. *J. Chem. Phys.*, 102:1257.

Zaïr, A., Holler, M., Guandalini, A., Schapper, F., Biegert, J., Gallmann, L., Keller, U., Wyatt, A. S., Monmayrant, A., Walmsley, I. A., Cormier, E., Auguste, T., Caumes, J. P., and Salières, P. (2008). Quantum Path Interferences in High-Order Harmonic Generation. *Phys. Rev. Lett.*, 100:143902.

Zaretsky, D. F., Korneev, P., and Becker, W. (2010). High-order harmonic generation in clusters irradiated by an infrared laser field of moderate inensity. *J. Phys. B*, 43:105402.

Zerne, R., Altucci, C., Bellini, M., Gaarde, M. B., Hänsch, T. W., L'Huillier, A., Lynga, C., and Wahlström, C. G. (1997). Phase-Locked High-Order Harmonic Sources. *Phys. Rev. Lett.*, 79:1006.

Zewail, A. (2000). Femtochemistry: atomic-scale dynamics of the chemical bond (adapted from the Nobel Lecture). *J. Phys. Chem. A*, 104:56605694.

Zhao, K., Zhang, Q., Chini, M., Wu, Y., Wang, X., and Chang, Z. (2012). Tailoring a 67 attosecond pulse through advantageous phase-mismatch. *Opt. Lett.*, 37:3891.

Zhao, Y., Kim, Y.-H., Dillon, A. C., Heben, M. J., and Zhang, S. B. (2005). Hydrogen Storage in Novel Organometallic Buckyballs. *Phys. Rev. Lett.*, 94:155504.

**Résumé:**

Depuis sa première observation, la génération d'harmoniques d'ordre élevé (GHOE) dans les gaz a demontré son importance, ouvrant la voie à la science attoseconde. Cette technique produit un rayonnement impulsionnel XUV qui s'étend dans le domaine spectral intermédiaire entre l'ultraviolet et les rayons X. Ces impulsions attosecondes donnent accès à des résolutions temporelles extrêmes, permettant ainsi d'observer des dynamiques électroniques dans des atomes ou des molécules. En effet le processus de génénération d'harmonique repose sur l'oscillation de paquets d'électrons attosecondes issus des molécules, accélérés par le champ de laser intense et se recombinant radiativement avec leurs ions moléculaires parents. Ainsi, le rayonnement harmonique émis lors de la recombinaison permet d'encoder l'information structurale sur le ou les orbitales impliquées avec une résolution spatiale de l'ordre l'Angström et temporelle femtoseconde ou attoseconde. La génération d'harmonique peut être utilisée comme signal de sonde dans des expériences de spectroscopie pompe-sonde résolue en temps. Ces expériences de spectroscopie harmoniques permettent d'étudier la structure des orbitales et les dynamiques moléculaires ultra-rapides.

L'objectif de cette thèse est d'utiliser le processus de la GHOE, pour sonder les processus fondamentaux qui interviennent dans les atomes, les molécules et la matière condensée. Tout d'abord, pour comprendre comment extraire des informations dynamiques ou structurelles sur les orbitales à partir du signal harmonique nous avons étudié un système simple et connu: l'argon. Une nouvelle approche théorique développée par Fabre et Pons a permis de reproduire fidèlement l'expérience. Nous avons continué à étudier la structure et la dynamique moléculaire dans $N_2$ et $CO_2$. Les molécules issues d'un jet supersonique Even-Lavie qui permettait d'obtenir des températures rotationelles de moins de 10 K ont été alignées par laser avec un fort degré d'alignement. Ce type de jet permet d'améliorer la sensibilité à la structure des orbitales impliquées et d'identifier la contribution de plusieurs orbitales. Ensuite nous avons utilisé la sensibilité de la génération des harmoniques d'ordre élevé à la structure des orbitales moléculaires pour sonder la dynamique complexe du $NO_2$ excité autour d'une intersection conique. Nous avons appliqué la méthode du réseau d'excitation transitoire qui permet d'améliorer la sensibilité aux molécules excitées. Nous avons donc mené une étude dans les agrégats. A l'aide d'une étude différentielle en température et d'une méthode de cartographie spectrale et spatiale, nous avons pu isoler la contibution des grands agrégats. Notre analyse suggère un nouveau mécanisme de génération par des agrégats et permet même une estimation de la longeur de corrélation des électrons dans les agrégats. Ce manuscrit se termine avec la présentation d'une ligne de lumière XUV. Cette technique consiste à utiliser le rayonnement XUV fs produit par la GHOE comme impulsion sonde pour ioniser des fragments de dissociation moléculaire à l'aide d'une transition à un photon.

**Mots-cléfs:**
Génération d'harmoniques d'ordre élevé; Spectrocopie harmonique; Interaction laser-matière; Physique atomique, moléculaire et des agrégats; Alignement moléculaire; Jet supersonique; Dynamique moléculaire; Intersection conique; Impulsions attosecondes; Spectroscopie XUV-fs